Strong Field Ionization in Two-Color Fields

Dissertation

zur Erlangung des Doktorgrades der Naturwissenschaften

vorgelegt beim Fachbereich Physik der Johann Wolfgang Goethe-Universität in Frankfurt am Main von

Sebastian Gereon Eckart
aus Frankfurt am Main

Frankfurt 2019 (D30)

vom Fachbereich Physik der
Johann Wolfgang Goethe-Universität als Dissertation angenommen.

Dekan:	Prof. Dr. Michael Lang
Gutachter:	Prof. Dr. Reinhard Dörner
	Prof. Dr. Till Jahnke

Datum der Disputation: 9.7.2019

Die vorliegende Version unterscheidet sich geringfügig von der Version, die in der Universitätsbibliothek veröffentlicht wurde. Einige Tippfehler etc. wurden korrigiert und der Lebenslauf ist nicht enthalten.
Datum der aktuellen Version: 10.9.2019

Meiner Familie.

Contents

1. Introduction **1**

2. Atomic Units and useful Definitions **5**

3. Basic Physical Ideas in Strong Field Ionization **6**

3.1. Multi-Photon Ionization 6

3.2. Adiabatic Tunnel Ionization 7

3.2.1. Negative Vector Potential and the Simple Man's Model 9

3.3. Keldysh-Parameter 10

3.4. Non-Adiabatic Tunnel Ionization 10

4. Experimental Methods **13**

4.1. Experimental Setup 13

4.1.1. Laser System 14

4.1.2. Fully Automated Interferometric Two-Color Setup 15

4.1.3. Electron and Ion Momentum Imaging 21

4.1.4. Data Acquisition and Control of the Experimental Protocol 26

4.1.5. Comissioning: Generating well-defined Two-Color Fields 30

5. Theoretical Methods to Simulate Strong Field Ionization **33**

5.1. Saddle Point Strong Field Approximation - Method 34

5.2. Saddle Point Strong Field Approximation - Examples 36

5.3. Semi-Classical Two-Step Model 38

5.3.1. Semi-Classical Trajectories 43

6. Non-Sequential Double Ionization **45**

6.1. State of the Art: Non-Sequential Double Ionization 47

6.2. Single Ionization of Argon in Counter-Rotating Two-Color Fields 49

6.3. Non-Sequential Double Ionization - Experimental Protocol 51

6.4. Controlling Inelastic Recollisions using Counter-Rotating Two-Color Fields . 55

6.4.1. Intensity Dependence of Non-Sequential Double Ionization 58

6.5. Electron Momentum Distributions for Non-Sequential Double Ionization of Argon 60

6.5.1. Non-Sequential Double Ionization: The First Electron 61

6.5.2. Tomographic Reconstruction of the Second Electron 63
6.6. Three-Dimensionality of the Measured Momentum Distribution 67

7. Three-Dimensional Electron Momentum Distributions 69
7.1. State of the Art: Sub-Cycle Interferences 70
7.2. Single Ionization of Helium in Counter-Rotating Two-Color Fields 71
7.3. Low Energy Electrons 75
7.4. Interference in the Plane of Polarization 77
7.5. Sub-cycle Interference along the Light Propagation Direction 78
7.5.1. Sub-cycle Interference: Fringe Visibility 80
7.6. Conclusion: Sub-cycle Interference 85
7.7. Comparing the Ionization of Helium and Neon 86
7.7.1. 2D Maps of the Electron's Angle in Momentum Space 91
7.7.2. Conclusion: Comparing the Ionization of Helium and Neon 95

8. Non-Adiabatic Tunneling: Offsets of the Initial Momentum Distribution 97
8.1. State of the Art: Non-Adiabatic Tunneling and the Initial Momentum Distribution 100
8.2. Single Ionization of Argon in Counter- and Co-Rotating Two-Color Fields . . 104
8.2.1. Direct Access to Non-Adiabatic Offsets 107
8.2.2. Analysis of Coulomb Interaction after Tunneling 112
8.3. Non-Adiabatic Offsets upon Ionization by a Single-Color Field 114
8.4. The Effective Keldysh-Parameter for Non-Adiabatic Offsets 118
8.5. Mechanistic Picture of Non-Adiabatic Tunneling 119
8.6. Conclusion: Non-Adiabatic Offsets 122

9. Non-Adiabatic Tunneling: The Magnetic Quantum Number 123
9.1. State of the Art: Non-Adiabatic Tunneling and the Magnetic Quantum Number 125
9.2. Sequential Double Ionization of Argon using a Pump-Probe-Scheme 127
9.3. Setting up the Pump-Pulse 128
9.4. Setting up the Probe-Pulse 131
9.5. Setting up the Temporal Overlap and the Spatial Overlap of Pump and Probe-Pulse 134
9.6. Distinguish First and Second Electron 138
9.7. Random Coincidences 141

9.8. Detailed Model of the Pump-Probe-Scheme . . . 145
9.9. Qualitative Results . . . 148
9.10. m-Dependent Electron Momentum Distributions . . . 150
9.10.1. Comparison of the Results with Theory . . . 156
9.11. Temporal Evolution of the Electron-Hole . . . 159
9.12. m-Dependent Electron Momentum Distributions . . . 162
9.12.1. Comparison with Theory and m-Dependent Release Time of the Electron . . . 164
9.13. Conclusion: The Magnetic Quantum Number . . . 167

10. Evidence for Non-Adiabatic Over-The-Barrier Ionization 169
10.1. Non-Zero Initial Momentum in the Tunneling Direction . . . 170
10.2. Non-Adiabatic Over-The-Barrier Ionization . . . 175
10.3. Conclusion: Initial Momentum in the Tunneling Direction . . . 180

11. Summary, Conclusion and Outlook 181
11.1. In Short: Boiling all Observations Down to One Model . . . 182
11.2. Limitations and Shortcomings . . . 183
11.3. Perspective . . . 184

A. Appendix 187
A.1. The Laser Intensity in the Interaction Region . . . 187
A.2. Offline Compensation of the Drifts of the Relative Phase . . . 191
A.3. Two-Color Fields Composed of Non-Circularly Polarized Single-Color Fields 196
A.4. Active Stabilization of the Relative Phase . . . 202
A.4.1. Active Stabilization: Proof of Concept . . . 203
A.4.2. Active Stabilization: Implementation . . . 208
A.5. Appendix for Non-Sequential Double Ionization . . . 211
A.5.1. Absolute Yield of Ar^{2+} and Ar^{1+} . . . 211
A.5.2. False Electron-Ion Coincidences and Momentum Conservation . . . 213
A.5.3. Tomographic Reconstruction - Validating the Method . . . 217
A.5.4. Tomographically Reconstructed Second Electron - Details . . . 219
A.6. Supplementary 2D Maps of the Electron's Angle in Momentum Space . . . 222
A.7. Uncertainty of the Experimentally Determined Two-Color Ratio . . . 225

A.8. The Effective Angular Frequency in Circularly Polarized Two-Color Fields . 226
A.8.1. The Effective Keldysh-Parameter 231
A.8.2. Alternative Derivation of the Effective Angular Frequency 232

References **235**

Deutsche Zusammenfassung **249**

Acknowledgments **257**

Publications **260**

Contributions to Conferences **263**

Practical Experience related to Atomic Physics **264**

1. Introduction

Everything we touch, see, hear, smell, and taste in daily life is composed of atoms. Understanding the building blocks of our world is at the very heart of science.

In atoms the **electrostatic force** binds the electrons to the atomic nucleus. An electron that is bound in a spherical symmetric potential has a defined **energy** and a defined **angular momentum**. What happens to this electron if one applies an **external electric field** that (partially) compensates for the electrostatic force that binds the electron to its atom? If ionization occurs: is the ionization dynamics sensitive to the temporal structure and the polarization of the external electric field?

If a strong electric field significantly distorts the atomic potential, then tunnel ionization can occur [1]. The very nature of tunneling in itself motivates to study ionization processes in strong laser[1] fields; because the knowledge gained from these experiments further increases the understanding of this fundamental quantum mechanical process. Of particular interest are non-trivial tunneling processes, such as tunneling through a time-dependent barrier. The insight that is gained might not be limited to atoms or molecules, because tunneling occurs in a variety of physical systems: e.g. optical evanescent waves are a textbook[2] example of a tunneling process. Nevertheless, the question of how long it takes a wave packet to transverse a (time-dependent) potential barrier is the subject of an ongoing debate [4–13]. Further examples for the relevance of tunneling are the scanning tunneling microscope [14, 15], Fowler-Nordheim tunneling [16] in transistors which are used in flash-drives [17, 18] and the modeling of alpha decay [19, 20]. Hence, one can hope that insight regarding tunneling might trigger future applications in neighboring fields.

For this thesis several experiments were conducted in order to study scenarios in which the electric field (and thus the tunneling barrier) are time-dependent. This is the regime of non-adiabatic tunnel ionization [21, 22]. What influences the dynamics of non-adiabatic tunnel-ionization? To this end light-matter interaction has to be modeled in detail and the entire process of how a bound electron is liberated has to be understood: Initially, long before the light pulse arrives and tunneling occurs, the atom is a time-independent entity that is perfectly stable and will remain so forever. For the sake of the argument a p-electron is considered. A p-electron possesses an orbital angular momentum of one and the magnetic quantum number can possess the values minus one, zero and one. In a semi-classical picture the magnetic quantum number defines the direction of rotation of the electron that is orbiting

[1] LASER is an acronym for *Light Amplification by Stimulated Emission of Radiation*.
[2] Examples are found in Ref. [2], p. 306-309 and Ref. [3], p. 498.

its ionic core. Further, the electron also possesses a spin which can be either up or down. When the atom is hit by a tightly focused femtosecond light pulse with a pulse energy of about 10 µJ, this can lead to the ejection of an electron.[3] For a photon energy of about $E_{ph} = 1.6\,\mathrm{eV}$ the light pulse consists of approximately $4 \cdot 10^{13}$ photons. Since most of the photons arrive in a very short period of time of only 40 fs, the peak electric field of the light pulse is on the order of $6 \cdot 10^{8}\,\mathrm{V\,cm^{-1}}$. In any photo-ionization process the energy transfer from the light field to the atom is quantized. The transferable energy packets are determined by the photon energy E_{ph}. In this thesis cases are studied in which up to several dozen photons are absorbed by the atom from one laser pulse.

Peak electric fields on the order of $6 \cdot 10^{8}\,\mathrm{V\,cm^{-1}}$ are extremely high. Such a field would result if one connected 50 million 12 V car batteries and then placed the cathode and the anode at a distance of 1 cm. Fortunately, there are better and safer ways of applying very high electric fields to atoms. Employing femtosecond laser pulses, such electric fields can be created and the properties of the time-dependent electric fields can be tailored with high precision. For the experimental work of this thesis, the light pulses are synthesized combining two separate laser pulses. The first pulse has a central wavelength of 780 nm and the second laser pulse has a central wavelength of 390 nm. The intensity, the ellipticity and the orientation of the main axis of the ellipse can be adjusted. Additionally, the relative time delay of the two laser pulses can be controlled. This leads to seven degrees of freedom that can be tuned to experimentally synthesize a tailored two-color laser pulse.[4]

These tailored, time-dependent light fields serve a double purpose. Firstly, they create time-dependent potential barriers and thus, a scenario in which the tunnel exit positions and the probabilities for tunneling are time-dependent as well. Secondly, after the electron emerges at the tunnel exit, it is steered by the tailored two-color laser electric field and the electron is only slightly influenced by the long-range potential of the remaining ion. The three-dimensional final momentum of this liberated electron can be measured using COLTRIMS[5]. The most important experimentally measured quantity in this thesis is the final momentum of the liberated electron. Combining many measured electron momenta leads to an electron momentum distribution. The control parameters in the performed experiments are the tailored two-color femtosecond laser pulses that impinge the single atoms. In order to unveil the properties of light-matter interaction in the strong field regime, the properties of the experimentally produced laser field are varied and the changes in the experimentally

[3] The basic ideas of strong field ionization are discussed in chapter 3.
[4] The two-color setup is described in chapter 4.1.2.
[5] COLTRIMS is an acronym for “COLd Target Recoil Ion Momentum Spectroscopy”and explained in chapter 4.1.3.

measured quantities are observed.

An important category of two-color fields are counter-rotating circularly polarized two-color laser fields (CRTC fields). CRTC fields are composed of two circularly polarized laser pulses that are counter-rotating, co-propagating and overlap in time. One pulse has the frequency ω while the other has the frequency 2ω.

This thesis is based on four peer-reviewed publications by Eckart et al. [23–26] and in addition to the published results many further details are presented and some important new results are shown.

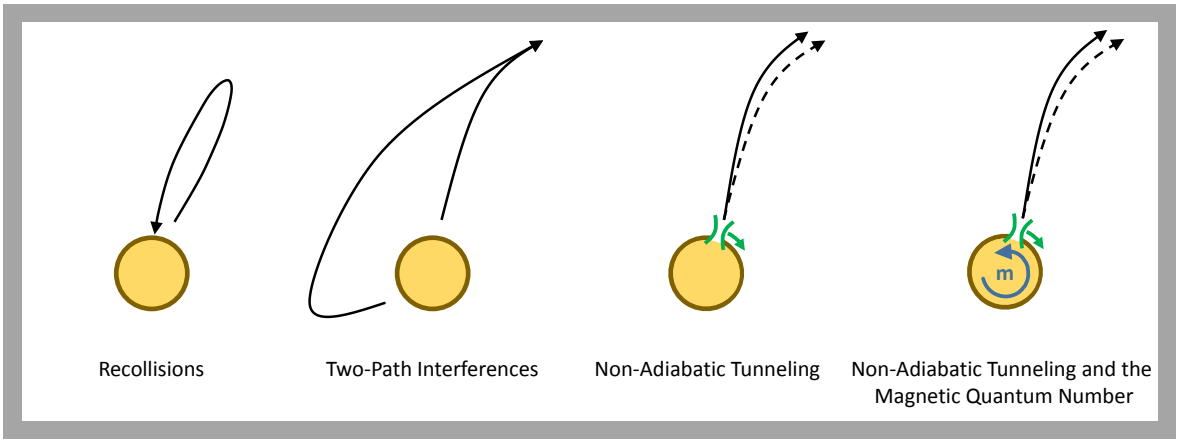


Figure 1.1: Illustration of the four main topics of this thesis (see bullets for details).

Fig. 1.1 illustrates the key scientific questions of this thesis:

- Under which conditions can the electron re-encounter its parent ion after it has exited the tunnel in a CRTC field? Fig. 1.1(a) illustrates the process (see chapter 6).
- Is it possible to observe two-path-interference in final momentum space as a result of two different initial tunneling directions using CRTC fields? Fig. 1.1(b) illustrates the process (see chapter 7).
- How does the temporal evolution of the laser's electric field at the instance of tunneling affect the final electron momentum? Fig. 1.1(c) illustrates the process. The answer is that the temporal evolution of the laser's electric field offsets the initial momentum distribution at the exit of the tunnel (see chapter 8).
- How does the magnetic quantum number m of the bound electron influence the tunneling dynamics? Fig. 1.1(d) illustrates the process. The answer is that the ionization probability and the final momentum of the electron depend on m (see chapter 9).

The first two projects deal with the propagation of the liberated electron (see chapter 6 and chapter 7). The other two deal with the tunneling process itself (see chapter 8–10).

2. Atomic Units and useful Definitions

Tab. 2.1 introduces atomic units and lists several useful definitions to describe the dynamics of atoms. It can be seen that atomic units are defined on different time and length scales compared to the dynamics of the macroscopic world. Here, ε_0 is the influence constant which has a value of $8.85419 \cdot 10^{-12}\,\mathrm{A\,s\,V^{-1}\,m^{-1}}$ in SI units and $1/(4\pi)$ in atomic units[6].

Table 2.1: The table is inspired and the vales are copied from Ref. [27].

dimension	expression	value in atomic units	value in SI units
mass	m	1 a.u.	$9.10938 \cdot 10^{-31}\mathrm{kg}$
charge	e	1 a.u.	$1.60218 \cdot 10^{-19}\mathrm{C}$
length	a_0	1 a.u.	$5.29177 \cdot 10^{-11}\mathrm{m}$
velocity	v_0	1 a.u.	$2.18769 \cdot 10^{6}\,\mathrm{m\,s^{-1}}$
time	a_0/v_0	1 a.u.	$2.41888 \cdot 10^{-17}\mathrm{s}$
momentum	$m \cdot v_0$	1 a.u.	$1.99285 \cdot 10^{-24}\mathrm{kgms^{-1}}$
angular momentum	$\hbar = a_0 \cdot m \cdot v_0$	1 a.u.	$1.05457 \cdot 10^{-34}\mathrm{kgm^2s^{-1}}$
energy	$\mathrm{e}^2/(4\pi\varepsilon_0 \cdot a_0)$	1 a.u.	$27.2116\mathrm{eV} = 4.3598 \cdot 10^{-18}\,\mathrm{J}$
action	$\hbar = \mathrm{e}^2/(4\pi\varepsilon_0 \cdot v_0)$	1 a.u.	$1.05457 \cdot 10^{-34}\mathrm{J\,s}$
electric field	$\mathrm{e}/\left(4\pi\varepsilon_0 \cdot a_0^2\right)$	1 a.u.	$5.14221 \cdot 10^{11}\,\mathrm{V\,m^{-1}}$

Time, length and energy scales, which are typical for the dynamics that are studied in this thesis, are shown in Tab. 2.2.

Table 2.2

dimension	typical value in atomic units
mass	mass of the electron is 1 a.u.
charge	charge of the electron is -1 a.u.
momentum	momenta of the measured electrons are typically between 0.0 a.u. and 1.5 a.u.
time	pump probe delay in chapter 9 is about 8300 a.u. (200 fs)
energy	ionization potential of argon for single ionization is 0.57915 a.u. (15.7596 eV) [28]
electric field	peak electric fields are typically between 0.05 a.u. and 0.11 a.u.

[6] The value is copied from Ref. [27].

3. Basic Physical Ideas in Strong Field Ionization

How to ionize an atom with light? One option is single photon absorption (photoelectric effect [29]). In this case the photon energy has to be larger than the ionization potential ($E_{ph} > I_p$) and for single ionization the excess energy manifests itself as the kinetic energy of the liberated electron. Is it also possible to ionize atoms if the photon energy is smaller than the ionization potential ($E_{ph} < I_p$)? In 1931, it was already predicted that for very high light intensities, it should be possible to absorb two photons (two-photon absorption) [30]. About 30 years later this was observed experimentally [31]. Generally it is possible to absorb not only two, but multiple photons. However, very high photon densities (high light intensities) are needed to allow for such processes.

3.1. Multi-Photon Ionization

Multi-photon ionization [32] can be illustrated as shown in Fig. 3.1. The probability for an ionization event in which n photons are involved is

$$\omega_{\text{rate}} \propto I^n \tag{1}$$

where I is the light intensity. The reason for this dependence is that the photon density is linear in the light intensity. Thus, the probability for n photons to exist simultaneously in the same volume in space scales with I^n.

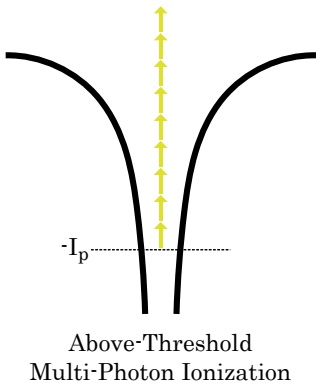


Figure 3.1: Schematic model of a bound electron which is liberated by absorbing multiple photons.

A similar insight is gained regarding the electron energy spectrum. Because of energy conservation, the final electron energy spectrum is expected to show narrow peaks that are separated by the photon energy. This is called above-threshold ionization (ATI), because in addition to the photons that are needed to overcome the ionization potential, an arbitrary

additional number of photons can be absorbed [33, 34]. One could expect that the final electron energy is given by $E_{\text{kin}} = n \cdot \hbar\omega - I_p$. However, this is only true for laser pulses that are long enough to allow the electron to leave the laser focus while the laser pulse is still on. In contrast, for short laser pulses it is important that the electron describes a quivering motion in the continuum after it has absorbed the photons [35]. The quivering motion is due to the time-dependent electric field. The average energy of this quivering motion is the ponderomotive energy U_p. If the laser pulse fades out while the electron is still in the laser focus, the quivering motion fades out as well. Thus, the final electron energy is given by [35]:

$$E_{\text{kin}} = n \cdot \hbar\omega - I_p - U_p \tag{2}$$

For a linearly polarized, time-dependent electric field with frequency ω and amplitude E_0, the acceleration of the electron is

$$\ddot{x} = \frac{\mathrm{e} \cdot E_0}{m} \cos(\omega t) \tag{3}$$

where m is the mass of an electron and e is the elementary charge. Thus, for a linearly polarized electric field the expectation value of the electron's kinetic energy[7] is:

$$U_p = \frac{\mathrm{e}^2 \cdot E_0^2}{4 \cdot \omega^2 \cdot m} \tag{4}$$

e and m both have the value of 1 in atomic units.[8]

In conclusion, multi-photon ionization scales non-linearly with the light intensity and is only relevant for high intensities. Instead of using photons, a light field can be described as a time-dependent electric field.

3.2. Adiabatic Tunnel Ionization

If a static electric field is applied to an atom, the photon energy can be considered to be zero (infinitesimal slow time evolution of the electric field). In this case ionization is also possible, but has to be described differently. Fig. 3.2(a) illustrates the electric potential for the outermost electron of argon which has an ionization potential of $I_p = 15.76\,\text{eV}$. The electron is bound because there is only a small region in position space (close to $r = 0\,\text{a.u.}$) where the electron's energy is higher or equal to the potential energy (classically allowed

[7] The arguments on how to derive Eq. 4 are taken from Ref. [36].

[8] For clarity the symbols e and m are shown here, but in the other chapters they will sometimes be omitted for brevity (also see chapter 2).

region, marked as a green bold line in Fig. 3.2(a)). If a strong static electric field $F = 0.05\,\text{a.u.} = 2.6 \cdot 10^8 \text{V}\,\text{cm}^{-1}$ is applied, then the potential well is distorted and a potential barrier is formed (see Fig. 3.2(b)). The barrier separates two regions in position space where the electron's energy is higher or equal to the potential energy (see green bold lines in Fig. 3.2(b)). In other words: the two classically allowed regions are separated by a classically forbidden region (the bound electron's energy is lower than the potential energy). The electron can transverse[9] the classical forbidden region by tunneling [37]. The tunneling probability, which governs the ionization rate, decreases exponentially with increasing thickness of the tunneling barrier.

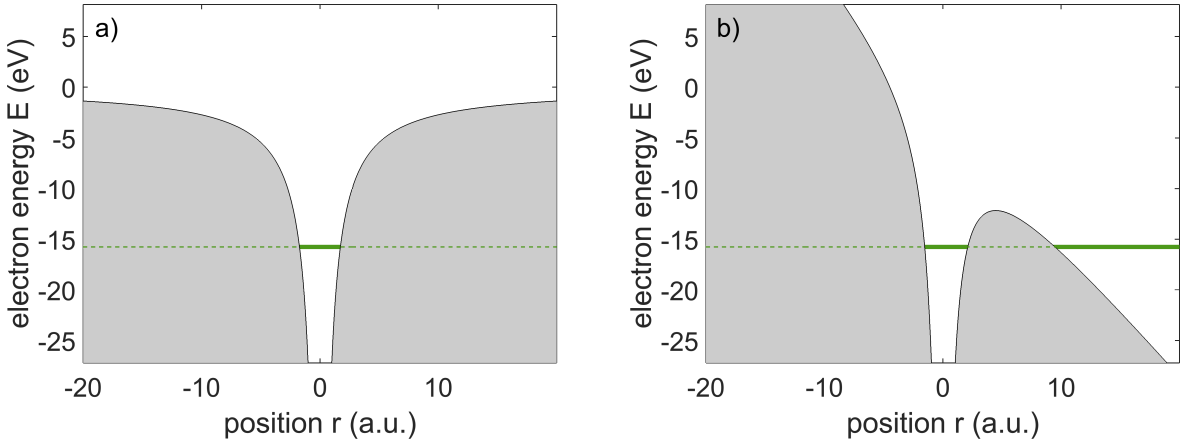


Figure 3.2: The black line in a) shows a Coulomb potential $V(r) = -1/r$. The classically forbidden region ($E(r) < V(r)$) is shaded in gray. The dashed green line indicates the ionization potential corresponding to the single ionization of argon of $I_p = 15.76\,\text{eV}$. The bold green line indicates the allowed region for an electron with an energy of $E = -I_p$. (b) shows the same as (a) but with $V(r) = -1/r - F \cdot r$ and $F = 0.05\,\text{a.u.}$ This representation ignores the temporal evolution of the laser field completely (regime of adiabatic tunneling).

The tunnel ionization rate[10] can be approximated by:

$$\omega_{\text{rate}} \approx \exp\left(-\frac{2\cdot(2\cdot I_p)^{\frac{3}{2}}}{3\cdot|E(t_0)|}\right)\cdot\exp\left(-\frac{v_\perp^2\cdot\sqrt{2\cdot I_p}}{|E(t_0)|}\right) \tag{5}$$

From Eq. 5 it is evident that the tunnel ionization rate increases with the absolute value of the electric field $|E(t_0)|$ and decreases with the ionization potential I_p and the absolute value of the initial momentum at the tunnel exit $|v_\perp|$. The initial momentum at the tunnel exit

[9] The description of tunneling as a process in which a particle traverses a classical forbidden region is commonly used. Alternatively, the same process can be viewed as the projection of a wave function: a bound state in a potential with finite binding energy has long-range tails of the wave function's density. This means that there is a non-zero probability for the electron to exist at classical forbidden positions. If an external field bends the potential, a part of the density that was formerly located in the classical forbidden region is no longer forbidden. Hence, the electron can be observed to exist at this position for a finite time. The position with the smallest value for r that was forbidden without an external field and is allowed with the external field can be considered as the "tunnel exit".

[10] Eq. 5 is taken from Ref. [38]. Ref. [38] cites Refs. [39–41].

$|v_\perp|$ is perpendicular to the tunneling direction. For adiabatic tunneling there is no initial momentum component along the tunneling direction (see chapter 8 and 10.2). Moreover, the mean of the initial momentum is zero in all directions. After tunneling, for a truly static electric field the electron would be accelerated continuously until it leaves the region in space where the external field is present. The situation changes if a time-dependent electric field acts on the electron after it has left the tunnel. In this case the electron is accelerated in a time-dependent electric field (e.g. determined by a laser pulse and the ionic potential).

For completeness it should be mentioned that for single ionization and an electric field E_{OBI} that fulfills

$$E_{\mathrm{OBI}} > \frac{I_p^2}{4} \tag{6}$$

the maximum of the potential barrier is lower than the energy level of the bound electron [42]. This scenario is called "over-the-barrier ionization" (OBI).

3.2.1. Negative Vector Potential and the Simple Man's Model

Let t_0 be the "instance of tunneling" (or "birth-time") which is the time at which the electron emerges at the tunnel exit with zero initial momentum. The time integral of all forces that act upon an electron that leaves the tunnel at t_0 determines the electron's final momentum[11] $\vec{p}_{\mathrm{final}}$. Neglecting the ionic potential one obtains:

$$\vec{p}_{\mathrm{final}} = -\mathrm{e}\int_{t_0}^{\infty} \vec{E}(t')\mathrm{d}t' = \left[\mathrm{e}\cdot\vec{A}(t')\right]_{t_0}^{\infty} = -\mathrm{e}\cdot\vec{A}(t_0) \tag{7}$$

Here, $\vec{E}(t)$ is the time-dependent electric field, $\vec{A}(t)$ is the corresponding vector potential[12] and e is the elementary charge. This model, in which the trajectories of single electrons are described classically after they have left the tunnel, is commonly known as the "simple man's model". In the simple man's model the final momentum $\vec{p}_{\mathrm{final}}$ is the same as the negative vector potential at the instance of tunneling. Using the simple man's model one can predict recolliding electrons [44]. A recollision occurs if the time-dependent field drives the electron back to its ionic core (see chapters 5.3, 6 and 6.1).

[11] In Eq. 7 it is assumed that the vector potential vanished for infinite time.

[12] The vector potential is assumed to be independent of the position in space. This is equivalent to ignoring the laser magnetic field. This is a good approximation since the influence of the laser magentic field is very small compared to the influence of the laser electric field in strong field ionization (see e.g. Ref. [43]).

3.3. Keldysh-Parameter

Multi-photon ionization and adiabatic tunnel-ionization both allow for photo-ionization although $E_{ph} < I_p$. Which of the two models is the more accurate description depends on the parameters of the system that is to be described. To this end the Keldysh-parameter γ can be used [1]:

$$\gamma = \frac{\omega}{\mathrm{e} \cdot E_0} \sqrt{2 \cdot m \cdot I_p} \tag{8}$$

e and m both have the value of 1 in atomic units. Here, for clarity, the symbols e and m are shown, but in the other chapters they will sometimes be omitted for brevity (also see chapter 2). Using Eq. 4 the expression for the Keldysh-parameter can be rewritten as (see e.g. [22, 45]):

$$\gamma = \sqrt{\frac{I_p}{2 \cdot U_p}} \tag{9}$$

Eq. 9 is very useful since it compares the ionization potential[13] I_p, which is a property of the atom that is to be ionized, to the ponderomotive energy[14] U_p, which characterizes the driving electric field (see e.g. [46]):

- For $\gamma \gg 1$ the ionization potential I_p is very large compared to the energy which an electron possesses that performs a quivering motion in the driving electric field. In this case the ionization process can be described as a multi-photon absorption.
- For $\gamma \ll 1$ the ionization potential I_p is very small compared to U_p. In this case the ionization process can be described as a tunneling process.

3.4. Non-Adiabatic Tunnel Ionization

How can strong field ionization with $\gamma \approx 1$ be treated? One would expect tunneling and MPI to seamlessly merge for $\gamma \approx 1$. But the two pictures are very different: one describes everything using photons and the other uses the light's electric field. The issues are resolved by accepting that MPI and tunneling are complementary processes that "very well co-exist peacefully" [22]. This concept is the basis of further theoretical work by Klaiber et al. which is discussed in chapter 8.1 [47, 48]. The general idea that follows for this thesis is that non-adiabatic tunneling occurs in two steps. In a first step a multi-photon process promotes the

[13] In this thesis, typical values for the ionization potential I_p are between $I_p = 0.58$ a.u. (single ionization of argon) and $I_p = 1.01$ a.u. (double ionization of argon).

[14] In this thesis, typical values for the ponderomotive energy U_p are between $U_p = 0.05$ a.u. (peak electric field of 0.05 a.u. at 390 nm, see discussion of Fig. 9.4) and $U_p = 0.89$ a.u. (peak electric field of 0.11 a.u. at 780 nm, see discussion of Fig. 9.10).

bound electron to a virtual intermediate state. In a second step the electron adiabatically tunnels from the virtual intermediate state. The first step increases the energy of the bound electron which decreases the width of the tunnel barrier in the second step. This interplay of multi-photon absorption and adiabatic tunneling can increase the ionization probability (see chapter 9.13). During the first step the shape of the wave function changes. This can modify the initial momentum distribution at the tunnel exit in the second step (see chapter 8).

In summary, Fig. 3.3(a) illustrates adiabatic tunneling as a process in which the position (horizontal axis) of the electron is changed first (green arrow) while the electron energy is not changed. Afterwards, the electron energy (vertical axis) is changed by the interaction with the time-dependent laser field. In contrast, multi-photon ionization (see Fig. 3.3(c)) is illustrated as a process in which the electron's energy changes in a first step by the absorption of several photons (yellow vertical arrows). Obviously, the position changes later because otherwise the electron could not be separated from its parent ion in position space. Non-adiabatic tunneling shows vertical as well as horizontal transitions. It is important to note that both steps cannot be separated in time (see Fig. 3.3(b)).

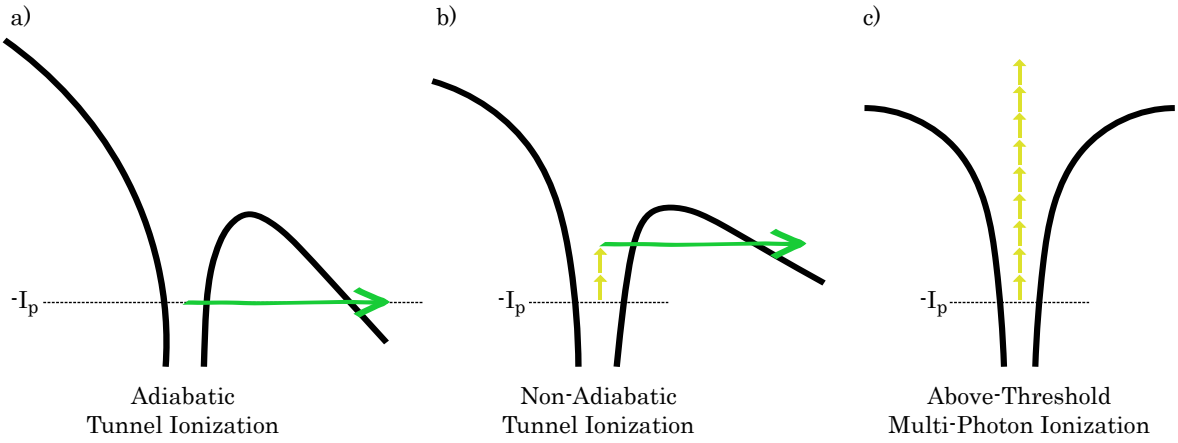


Figure 3.3: (a) schematically shows adiabatic tunneling (occurs for $\gamma \ll 1$). (b) illustrates non-adiabatic tunneling ($\gamma \approx 1$) and is based on an idea by Klaiber et al. [47] but a similar idea is already found in Ref. [22]. (c) schematically shows above-threshold multi-photon ionization as in Fig. 3.1 (occurs for $\gamma \gg 1$).

Finally, all this can be summarized as follows:

- "adiabatic tunneling": position changes first and energy changes later
- "non-adiabatic tunneling": position and energy change simultaneously (see discussion of Fig. 8.14(b) for details)
- "multi-photon ionization": energy changes first and position changes later

4. Experimental Methods

This chapter explains the components of the experimental setup and provides a short description of the experimental methods which were used for this thesis.

4.1. Experimental Setup

The experimental setup consists of four main components which are schematically shown in Fig. 4.1.

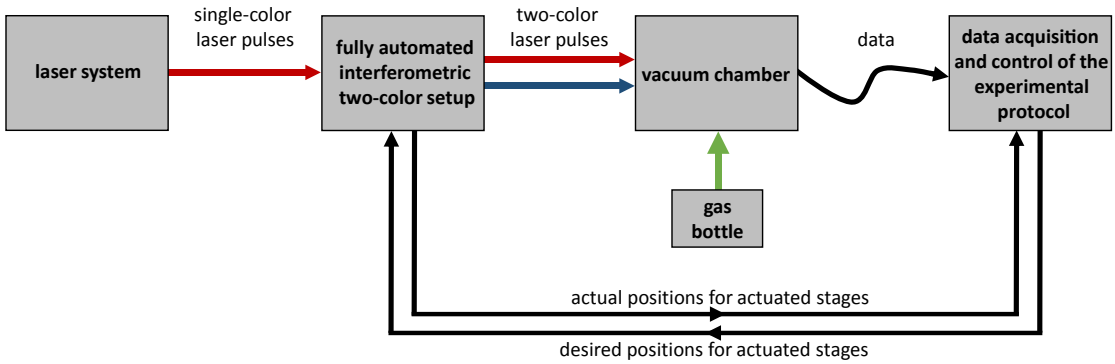


Figure 4.1: Schematic overview of the experimental setup (see text for details).

The central part of the setup is the vacuum chamber in which the ionization of the target atoms occurs and the momenta of the produced ions and electrons are measured. The target atoms are supplied from a gas bottle. In order to ionize the target atoms, strong laser pulses are used. The laser pulses are produced by the laser system and modified by the fully automated interferometric two-color setup. The data acquisition system is used to store the settings for the fully automated interferometric two-color setup for each detected ionization event together with the information which is needed to calculate the momenta of all detected particles. Moreover, the data acquisition system is also used to set the positions of the motorized stages.

4.1.1. Laser System

The laser system "dragon" is based on Ti:Sa technology and a commercial product from KMLabs. The laser system produces 40-fs laser pulses at a central wavelength of 780 nm. The laser system is the same as in Ref. [36]. The maintenance of the laser system was carried out by Maksim Kunitski. Further relevant information concerns the characteristics of the

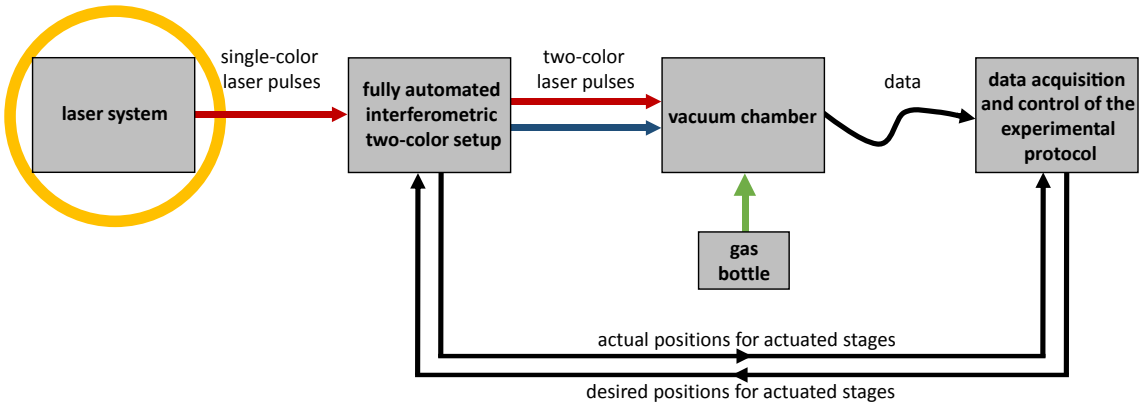


Figure 4.2: Schematic overview of the experimental setup. The laser system is highlighted.

laser pulses at the exit of the laser system:

- The repetition rate is 8 kHz.
- The average output power has been up to 2.8 W.
- The beam diameter at the exit of the laser system is about 4 mm (full width at half maximum).
- The spectral width is about 40 nm (full width at half maximum) with a central wavelength of 780 nm.

In addition, directly in front of the output of the laser, there is an adjustable grating that can be used to change the spectral chirp of the laser pulses. Before a measurement campaign was started, the grating was set so that the ionization rate was highest for the corresponding experimental setting. When two-color fields were used or several settings of the automated interferometric two-color setup were used, the grating was adjusted using a typical two-color field for the planned measurement campaign. The output of the laser system and the input of the fully automated interferometric two-color setup (see chapter 4.1.2) were connected by two dielectric turning mirrors with low group delay dispersion and high reflectivity at 780 nm. In some cases a neutral density filter was placed in between these two turning mirrors to adjust the intensity at the input of the fully automated interferometric two-color setup.

4.1.2. Fully Automated Interferometric Two-Color Setup

The development of the fully automated interferometric two-color setup was the first important step in the project that led to this thesis. The setup links the laser system and the vacuum chamber.

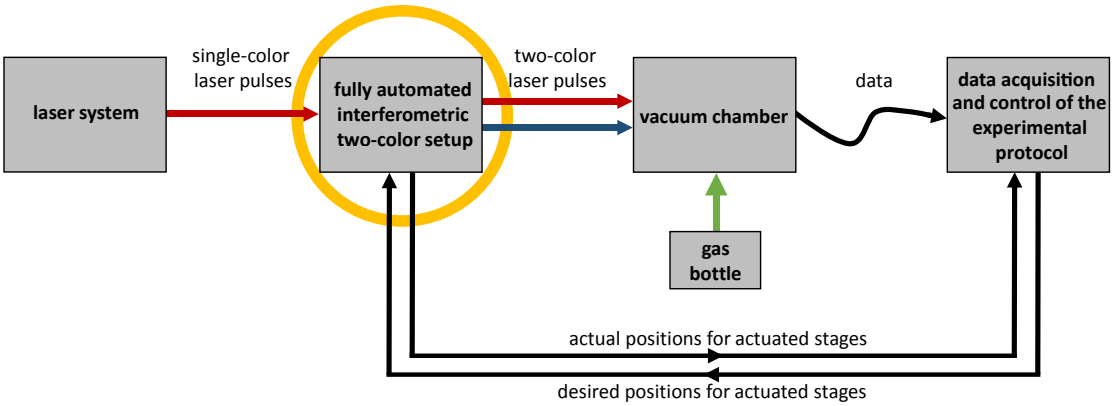


Figure 4.3: Schematic overview of the experimental setup. The fully automated interferometric two-color setup is highlighted.

The goal was to allow for the generation of different tailored two-color fields as the superposition of two laser pulses. In order to achieve this, one laser pulse remains at the fundamental wavelength of 780 nm and one laser pulse is frequency-doubled by a non-linear crystal (beta barium borate). Both laser pulses are femtosecond laser pulses of variable ellipticity, intensity and orientation of the main axis of the polarization ellipse. Hence, each laser pulse can be tailored using three degrees of freedom. The temporal delay between the two pulses is controllable with sub-cycle precision. As a result, there are seven degrees of freedom that can be used to tailor the two-color field. In order to set the properties of the tailored two-color field in a reproducible and automated way another criterion was high thermal and vibrational stability. All seven degrees of freedom can be set using motorized stages.

The fully automated interferometric two-color setup was built[15] on a separate breadboard[16] using posts with heights of about 45 mm and a diamter of 1 inch. All components were selected to allow for excellent stability. At the beginning of the design process the digital model shown in Fig. 4.4 was created. The model is close to the setup that has finally been realized. A photograph of the fully automated interferometric two-color setup is shown in Fig. 4.5.

[15] Before the fully automated interferometric two-color setup was built, the author of Ref. [36] had built a similar setup which was not automated (see Ref. [36]) and less stable since it was built using mostly aluminum components. For the setup, which was constructed for this thesis, longer and thinner posts for the mirror mounts and metallic instead of dielectric mirrors were used.

[16] The product "M-SG-22-2" from Newport Spectra-Physics GmbH was chosen.

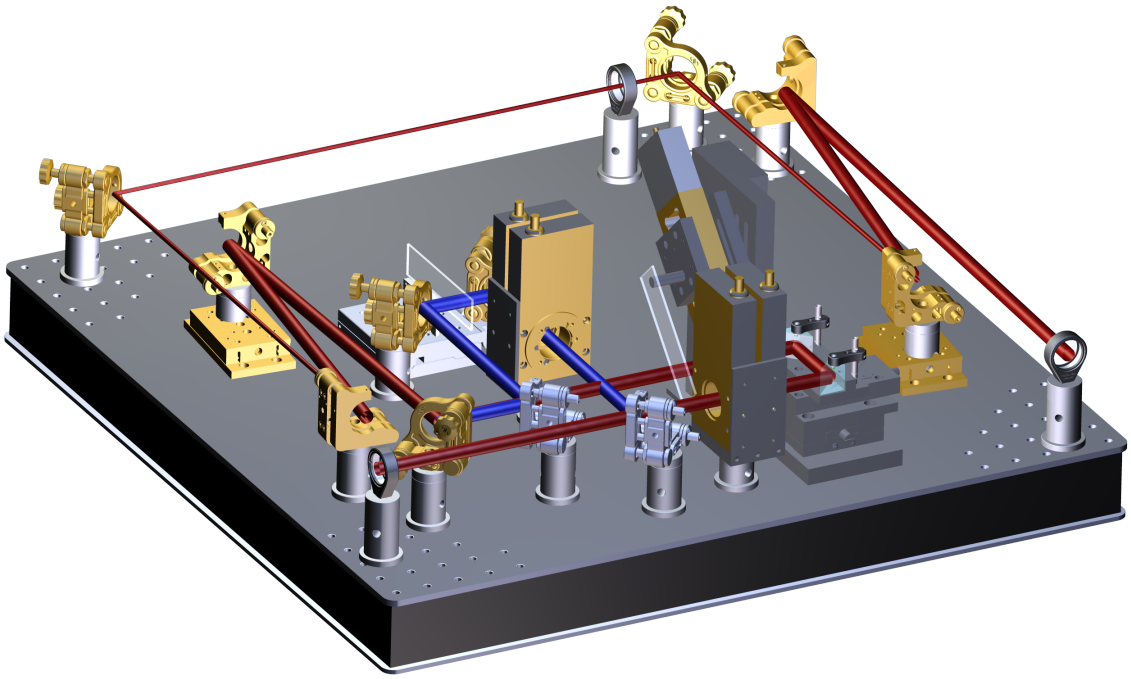


Figure 4.4: This figure was created as part of the design process for the experimental setup. It shows the digital model of the interferometric two-color setup that was used to decide which components could be bought and which would have to be custom-made. The geometry of the setup shown is not identical to the final setup. The digital model was created using Autodesk Inventor Professional 2015.

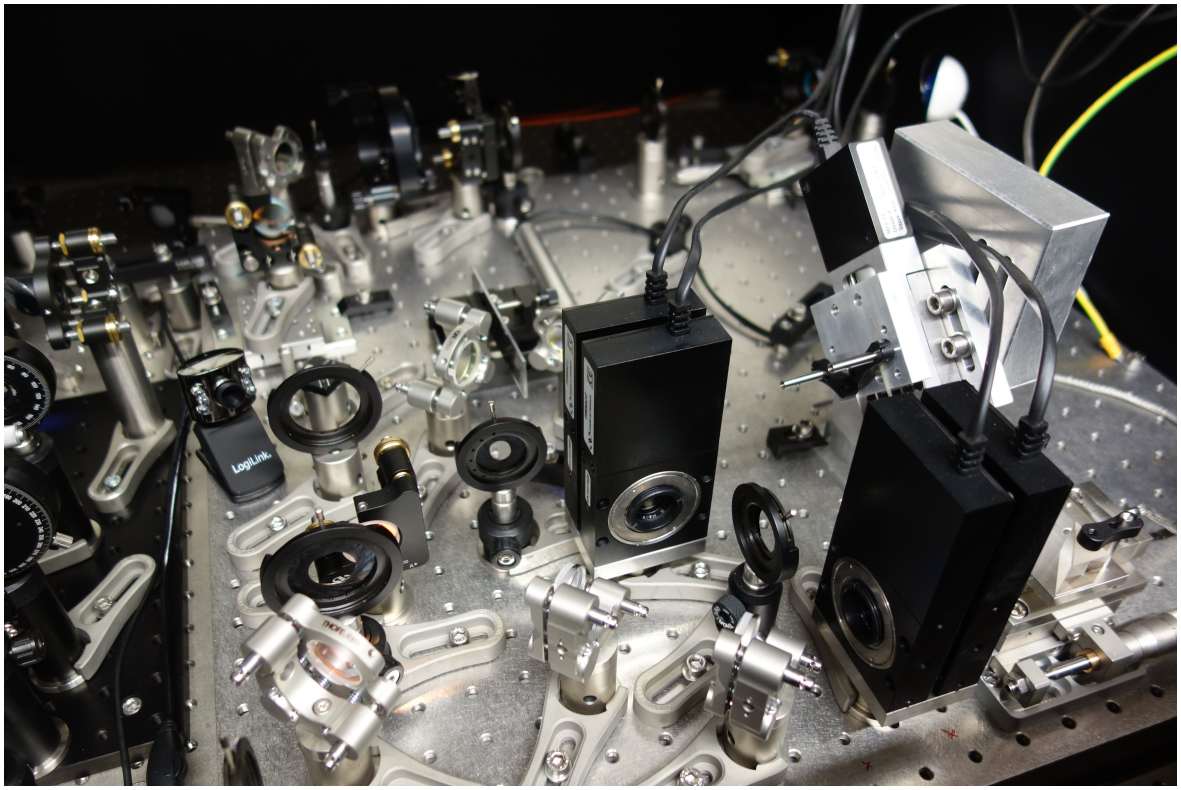


Figure 4.5: Photograph of the final interferometric two-color setup.

Fig. 4.6 shows a scheme of the fully automated interferometric two-color setup. The details are described in the caption of Fig. 4.6. The basic idea is to start with linearly polarized (p-polarized) femtosecond laser pulses with a central wavelength of 780 nm that are frequency-doubled in a BBO[17]. In order to increase the efficiency of the generation of the second harmonic in the BBO two telescopes are used. After the BBO both single color laser pulses propagate co-linearly until they are separated by a dielectric beamsplitter (BS1 in Fig. 4.6). Before they are recombined using a beam combiner (BS1 in Fig. 4.6), both single-color laser pulses can be tailored independently. To this end, neutral density filters, quarter wave plates and half wave plates are used. The temporal delay of the two single-color pulses can be adjusted using a delay stage (DS in Fig. 4.6). After the beam combiner the diameter of the two-color beam is widened using a 1:4 telescope. Finally, the tailored two-color laser pulses enter the vacuum chamber through a window made of fused silica[18] which is transparent for 390 nm. Inside the vacuum chamber a spherical silver mirror ($f = 80$ mm) focuses the beam. The focal point intersects with the incident beam. The mirror's position can be adjusted in three-dimensions to move the focus position. For the experiments the laser focus also has to intersect the gas jet. The intersecting volume of the laser focus and the gas jet defines the interaction region in which the ionization occurs (see Fig. 4.8).

All components are carefully chosen to allow for the manipulation of the seven-dimensional parameter space as completely as possible but without compromising the desired reproducibility of the experimental settings and the stability of the relative phase of the two single-color laser pulses.

- All four wave plates[19] are mounted in motorized rotation stages[20].
- The two continuously variable, metallic neutral density filters[21] are mounted on motorized delay stages[22] with travel ranges of 25 mm.
- The neutral density filter for the beam at 390 nm moves parallel to the surface of the breadboard and the surface of the neutral density filter is almost perpendicular to the laser propagation direction. The moving-direction of the neutral density filter for the beam at 780 nm is tilted by 45°with respect to the surface of the breadboard (see Fig.

[17] The thickness of the p-coated BBO (beta barium borate) is 200 µm and the cut angle is $\theta = 29.8°$ (type 1 phase-matching).
[18] In some cases a second fused silica window between the beam combiner and the entrance window to the vacuum chamber was used to reflect part of the laser beam for beam-analysis (see e.g. chapter A.4).
[19] The wave plates are zero order air-gap wave plates from Bernhard Halle Nachfl. GmbH with an aperture of 14.5 mm and an anti-reflective coating on all surfaces.
[20] The motorized rotation stages are all "CONEX-PR50CC" by Newport Spectra-Physics GmbH. The repeatability is 0.1°.
[21] The filters are "NDL-25C-4" by Thorlabs GmbH. The filters allow for an attenuation of upto four orders of magnitude.
[22] The actuator from Newport Spectra-Physics GmbH for moving the neutral density filter in the beam at 780 nm (390 nm) has the product name "MFA-PPD" ("TRA25PPD").

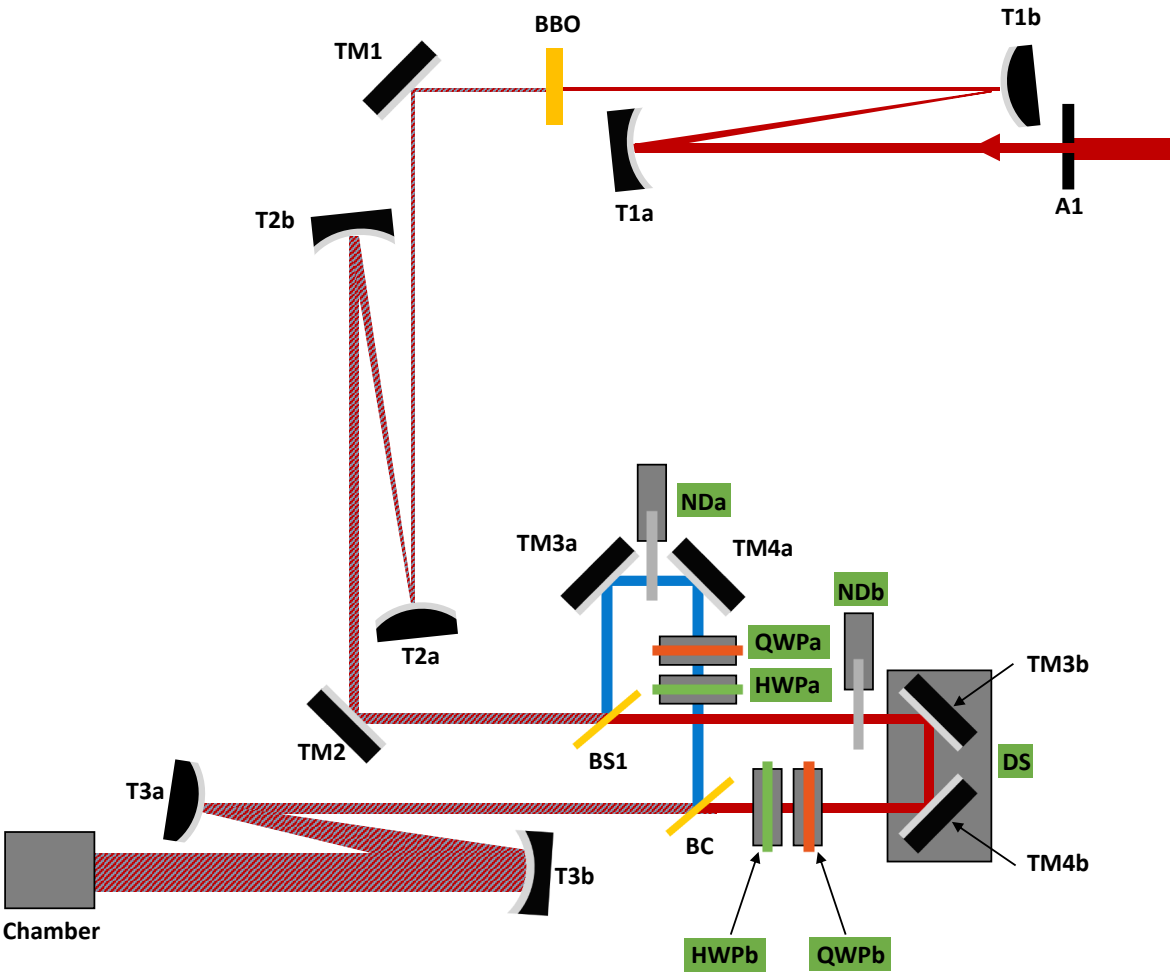


Figure 4.6: Schematic overview of the interferometric two-color setup. The femtosecond laser pulses at 780 nm enter the setup at the top-right corner. The beam at 780 nm (390 nm) is depicted in red (blue). The two-color beam is illustrated as a blue and red striped line. The beam diameter is indicated by the thickness of the line. The seven automated stages that are used to tailor the two-color laser pulses are highlighted in green (see text). First, the femtosecond laser pulses at 780 nm pass a diaphragm to crop the edges of the collimated beam in order to clean up the beam profile. The diameter of the aperture is usually set to below 5 mm. The diameter of the cropped beam is reduced using a 3:1 telescope consisting of a concave spherical mirror with a focus length of $f = 450$ mm (T1a) and a convex spherical mirror with a focus length of $f = -150$ mm (T1b). Due to the reduction of the beam diamter by a factor of three, the peak intensity of the laser beam is increased by a factor of nine. This increases the intensity of the second harmonic which is generated during the subsequent passage of the BBO (beta barium borate) by a factor of 81 and is the reason why the telescope is used. From here on, the beam is a two-color beam. The beam is reflected by a turning mirror (TM1) and afterwards a 1:3 telescope is used to widen the beam diameter. The reason why the beam diameter is widened is to not damage the neutral density filter or the wave plates. The 1:3 telescope is built from a convex spherical mirror with a focus length of $f = -150$ mm (T2a) and a concave spherical mirror with a focus length of $f = 450$ mm (T2b). After the 1:3 telescope, a turning mirror (TM2) reflects the beam. A beamsplitter (BS1) reflects the beam at 390 nm and transmits the beam at 780 nm. The beam at 390 nm hits a turning mirror (TM3a), a neutral density filter, another turning mirror (TM4a), a quarter wave plate and a half wave plate before it is recombined with the beam at 780 nm by the beam combiner (BC). The beam at 780 nm passes through a neutral density filter before it is reflected by two silver mirrors (TM3b and TM4b) that are mounted on a delay stage (DS). Afterwards, the beam at 780 nm passes through a quarter wave plate and a half wave plate before it reaches the beam combiner (BC). The tailored two-color laser pulses are reflected by a convex spherical mirror with a focus length of $f = 150$ mm (T3a) and a concave spherical mirror with a focus length of $f = 600$ mm (T3b) which act as a 1:4 telescope before they enter the vacuum chamber.

4.5). The surface of the neutral density which is used for the beam at 780 nm filter, is almost perpendicular to the laser propagation direction. The reflected light from the neutral density filters is blocked on diaphragms.

- The turning mirrors TM1 and TM2 (see Fig. 4.6) were bought from Layertec GmbH and were coated upon request. For an angle of incidence of 45°, the mirrors are designed to have a reflectivity greater than 99.9% in the wavelength range from 740 nm to 860 nm and a reflectivity greater than 99.7% in the wavelength range from 380 nm to 400 nm. The absolute value of the group delay dispersion (GDD) is designed to be below 70 fs^2 (30 fs^2) for (p-polarized) s-polarized light in the wavelength range from 710 nm to 800 nm (380 nm to 400 nm).
- The mirrors T1a, T1b, T2a, T2b, T3a, T3b (see Fig. 4.6) have a different coating and were also bought from Layertec GmbH. For an angle of incidence of 0°-10°, the mirrors are designed to have a reflectivity greater than 99.9% in the wavelength range around 390 nm and 780 nm. The absolute value of the GDD is designed to be below 40 fs^2 for p-polarized and s-polarized light.
- The mirrors TM3a and TM4a (see Fig. 4.6) also have a special coating and were also bought from Layertec GmbH. For an angle of incidence of 45°, the mirrors are designed to have a reflectivity greater than 99.9% in the wavelength range from 370 nm to 420 nm. The absolute value of the GDD is designed to be below 20 fs^2 for p-polarized and s-polarized light.
- The beam combiner and the beam splitter (see BC1 and BC in Fig. 4.6) are identical dielectric beam splitters and were bought from Layertec GmbH. For an angle of incidence of 45°, they are designed to have a reflectivity greater (less) than 99.9% (2%) in the wavelength range around 390 nm (780 nm). The absolute value of the GDD is designed to be below 50 fs^2 for p-polarized and s-polarized light in the relevant spectral regions for transmission and reflection. The shortcoming of this beam splitter is that about 2% of the light at 780 nm is reflected[23].
- The mirrors TM3b and TM4b (see Fig. 4.6) are protected silver mirrors from Thorlabs GmbH (product name “MRA20-P01”).
- The delay stage (see DS in Fig. 4.6) is a stack of two delay stages. A piezo actuated,

[23] At the beam combiner approximately 2% of the light at 780 nm is also reflected. Hence, in the worst case 0.04% of the light at 780 nm before the beam splitter (BS1) is transmitted through the beam combiner (BC). This parasitic contribution can be relevant if the neutral density filter (NDb) is close to the maximal attenuation of 4 orders of magnitude. A possible improvement of the setup might be to replace TM3a and TM4a with dielectric mirrors identical to BC1.

high-precision nanopositioning stage from Physik Instrumente (PI) GmbH & Co. KG (product name “P-752.2CD”) with a travel range of 30 µm and a repeatability of 2 nm is mounted on a manual, linear translation stage made of stainless steel (product name “9063-X-M” from Newport Spectra-Physics GmbH) with a travel range of 25 mm. The manual delay stage is used to extend the range of nm-delay stage.

For the control of the fully automated interferometric two-color setup a modular control scheme was developed. How the software works is explained in chapter 4.1.4. In the following subchapter the COLTRIMS reaction microscope is explained.

4.1.3. Electron and Ion Momentum Imaging

The COLTRIMS[24] reaction microscope is able to measure the momenta of all fragments of ionization events that occur in a localized region in position space [49, 50]. The vacuum chamber is highlighted in Fig. 4.7.

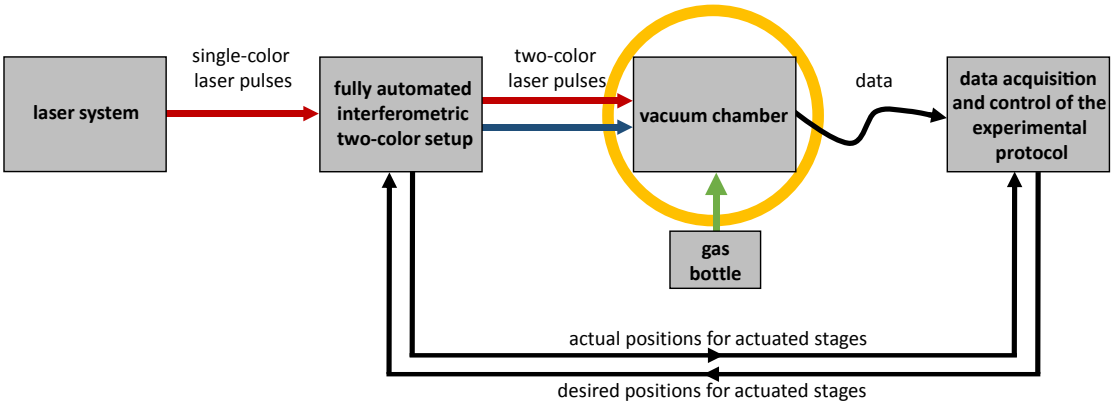


Figure 4.7: Schematic overview of the experimental setup. The vacuum chamber is highlighted.

The vacuum chamber and the COLTRIMS reaction microscope which are used for this thesis are the same as the ones which were used for the thesis by Martin Richter (see Ref. [36]) and will not be explained in detail. Here, the principle of the COLTRIMS reaction microscope is explained using Fig. 4.8 as schematic overview. A gas target is created by supersonic gas expansion through a nozzle with a diameter of 30 µm [36]. The inlet of the nozzle is connected to a gas bottle and the inlet pressure is usually at about 1.3 bar (absolute pressure) for the experiments presented in this thesis. After the nozzle a skimmer with a diameter of 300 µm is inserted into the zone-of-silence of the supersonic gas expansion [36]. This leads to a jet consisting of cold gas atoms (see e.g. Ref. [51]). Along the jet propagation direction the momentum distribution is not as narrow as it is along the other two directions. This is relevant because any uncertainty regarding the knowledge of the initial velocity of the target atoms affects the momentum resolution of the detected fragments. For the experiments performed for this thesis, the measurement of the electron's momenta are not limited significantly by the velocity distribution of the target atoms. For the measurement of the ions only the direction along the jet propagation direction (y-direction) is blurred by the velocity distribution of the target atoms. This is irrelevant because the spectrometer setting used does not allow for any significant momentum resolution along the x-direction and the y-direction (see discussion

[24] COLTRIMS is an acronym for COLd Target Recoil Ion Momentum Spectroscopy.

of Fig. 4.9). The laser beam[25] is focused into the gas jet using a concave spherical silver mirror[26] ($f = 80\,\text{mm}$) inside the vacuum chamber (see Fig. 4.8).

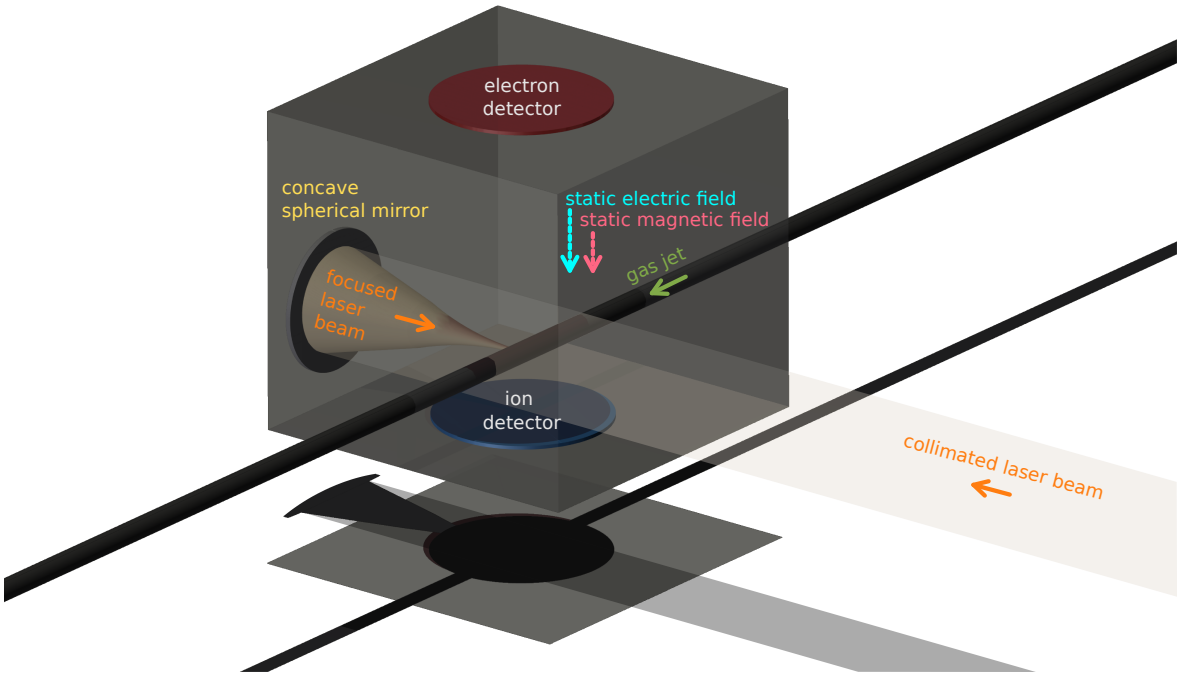


Figure 4.8: The collimated laser beam is focused by a concave spherical mirror. The laser beam that is leaving the interaction region is not shown for clarity. In the spectrometer of a COLTRIMS reaction microscope there are homogeneous electric and magnetic fields that guide charged particles, which are created in the interaction volume (volume in which the focused laser beam and the gas jet overlap), towards position and time sensitive detectors. The gray box highlights the volume in which the charged particles propagate on their way from the interaction region towards the electron or the ion detector.

The volume in which the focused laser beam and the gas jet overlap is called interaction region. If a laser pulse ionizes an atom in the interaction region, the fragments (ion and up to several electrons) are accelerated by a static homogeneous electric field (a typical electric field for this thesis is 11 Vcm^{-1}) into opposite directions. In both directions there are time and position sensitive detectors. One detector acts as ion detector and one acts as electron detector. In addition, a static homogeneous magnetic field (typically about 8 G=0.8 mT), which is parallel to the electric field, prevents the electrons from moving too far away in the directions perpendicular to the time-of-flight direction. The detectors are position sensitive microchannel plate (MCP) detectors with three layer delay-line anodes [36, 49]. The diameter of the MCP is 120 mm (80 mm) for the electron (ion) detector.

[25] Since the collimated beam has about 6 order of magnitudes less peak intensity it does not interact significantly with the atoms inside the vacuum chamber.

[26] The silver mirror can be set to an arbitrary electric potential to prevent electrons from escaping the silver mirror's surface by the photoelectric effect. In order to not cause inhomogeneities in the electric field, the electric potential of the mirror is adjusted so that it is as close to the electric potential of the corresponding region in the spectrometer as possible, but attractive enough for electrons to prevent them from leaving the silver surface.

All signals that are produced by the detectors and the photodiode are analogue signals (for details see Ref. [36, 52]) that encode the occurrence of an event as a short electrical pulse. The signals are amplified[27] and converted to NIM-signals[28] before they are recorded by a time-to-digital converter[29] that is connected to a computer. Any NIM-signal can be used as a trigger signal[30]. All NIM-signals in a certain time window before and after the trigger signal are interpreted as one event and stored by the program that is used for the data-acquisition. The software used is the CoboldPC software from the RoentDek Handels GmbH. During each measurement the CoboldPC software counts the number of events that have already been recorded. This number is made available in the analysis as the variable "eventcounter". This leads to a situation in which:

- The start time of all fragments (electrons and ions) is known with a precision of about 100 ps.[31]
- The start position of all fragments (electrons and ions) is known with micrometer precision, since the laser focus has a diameter of several micrometers (see chapter A.1).
- The detection time of all fragments (electrons and ions) is known with a precision of about one nanosecond.
- The detection position[32] of all fragments (electrons and ions) is known with a precision of about 250 µm.
- The distances of the start position to the detectors are known. The distance is about 378 mm for electrons and 68 mm for ions.
- The static electric and magnetic fields are known.[33]
- The mass of the atoms in the gas target is known.

This knowledge can be used to calculate the three-dimensional momentum of all particles detected (electrons and ions) individually by solving the equations of motion for each particle

[27] As amplifier a commercial product from the RoentDek Handels GmbH with the name "FAMP6b" is used.

[28] The analogue signals are converted to NIM signals by a constant fraction discriminator from the RoentDek Handels GmbH with the product name "CFD4b". NIM is an acronym for "Nuclear Instrumentation Standard".

[29] The time-to-digital converter is a "TDC8HP" from RoentDek Handels GmbH.

[30] If not stated otherwise the signal from the front-side of the MCP of the electron detector is used as the trigger signal.

[31] A photodiode is used to measure the time the laser pulses exit the laser system. Performing a "wiggle-run" the temporal difference the photodiodes signal is received and the time the laser interacts with the target atoms can be inferred (see Fig. 3.11 in Ref. [36]).

[32] In front of the electron detector and the ion detector a mesh with a lattice spacing of 250 µm is used to be able to accelerate the partiles before they hit the MCP (see Ref. [36] for details).

[33] The energy resolution of the measured electrons depends on the chosen electric and magnetic fields. Usually the resolution worsens as the electric field is increased. The energy resolution depends on the electron's kinetic energy and is at least 1.3 eV (2.5 eV) for electrons with a kinetic energy smaller than 20 eV (40 eV).

(see e.g. Refs. [27, 36, 52, 53] for details). To calculate the momenta accurately, calibration measurements are performed using arrangements which produce precisely known features[34]. The calibration measurements are used to systematically fine-tune the values of the spectrometer settings that are used to calculate the three-dimensional momenta (see chapter 3.3.1 in Ref. [27] and chapter 3.3.3 in Ref. [36]).

Since all fragments can be recorded for a given laser shot and usually there is only one reaction per laser shot, this allows for the coincidence detection of electron(s) and ion(s). If the momenta of all fragments are obtained, this is referred to as a "kinematically complete experiment". In general, coincidence detection creates a plethora of possibilities regarding the data analysis. For example, an experiment using argon as gas target can be performed and the electron momentum distributions for the single ionization and the double ionization of argon can be distinguished from one another. Fig. 4.9(a) shows the time-of-flight spectrum of the detected ions.

Besides the singly (at a time-of-flight of about 7085 ns) and doubly (at a time-of-flight of about 5000 ns) charged argon ions, it is evident that other gas atoms were ionized from residual gas atoms inside the vacuum chamber[35]. The singly charged argon ions hit a narrow spot (compared to a position resolution of about 250 µm) on the MCP (see Fig. 4.9(b) and 4.9(c)). As a consequence no momentum resolution is achieved along the x-direction and the y-direction for ions. Along the time-of-flight direction the spot is broad having a width of several tens of nanoseconds (compared to a time resolution which is below 1 ns). What are the other features[36] seen in the panels of Fig. 4.9? For example, the blurred peak at about 4800 ns in Fig. 4.9(b) and 4.9(c) is due to water molecules from the residual gas in the vacuum chamber. Since these water molecules are not at low temperatures they have a broad initial momentum distribution which manifests as a broad distribution for the position on the detector and the distribution in the time-of-flight direction.

[34] An obvious example for a calibration measurement is the measurement of ATI (above-threshold ionization) spectra (see chapter 3.1). The observed spheres in the three-dimensional final momentum space are all separated by multiples of the photon energy.

[35] This also shows why it is so important to have a low pressure inside the vacuum chamber. For all measurements presented in this thesis, the pressure inside the main vacuum chamber was $1.4 \cdot 10^{-10} \pm 0.2 \cdot 10^{-10}$ mbar.

[36] The origin of the peak at around 7140 ns is not understood by the author of this thesis. The time-of-flight corresponds to a singly charged particle with 40.5 amu and no jet-offset is observed. The peak at about 1000 ns is due to protons and the peak at round 3700 ns is caused by detector problems. The peak around 3700 ns vanishes if all particles that have a reconstruction method bigger than 0 are omitted. The reconstruction method indicates the quality of the detected signals on the delay-line anode on the single particle level. Details are described in Ref. [54] on page 110 and onwards.

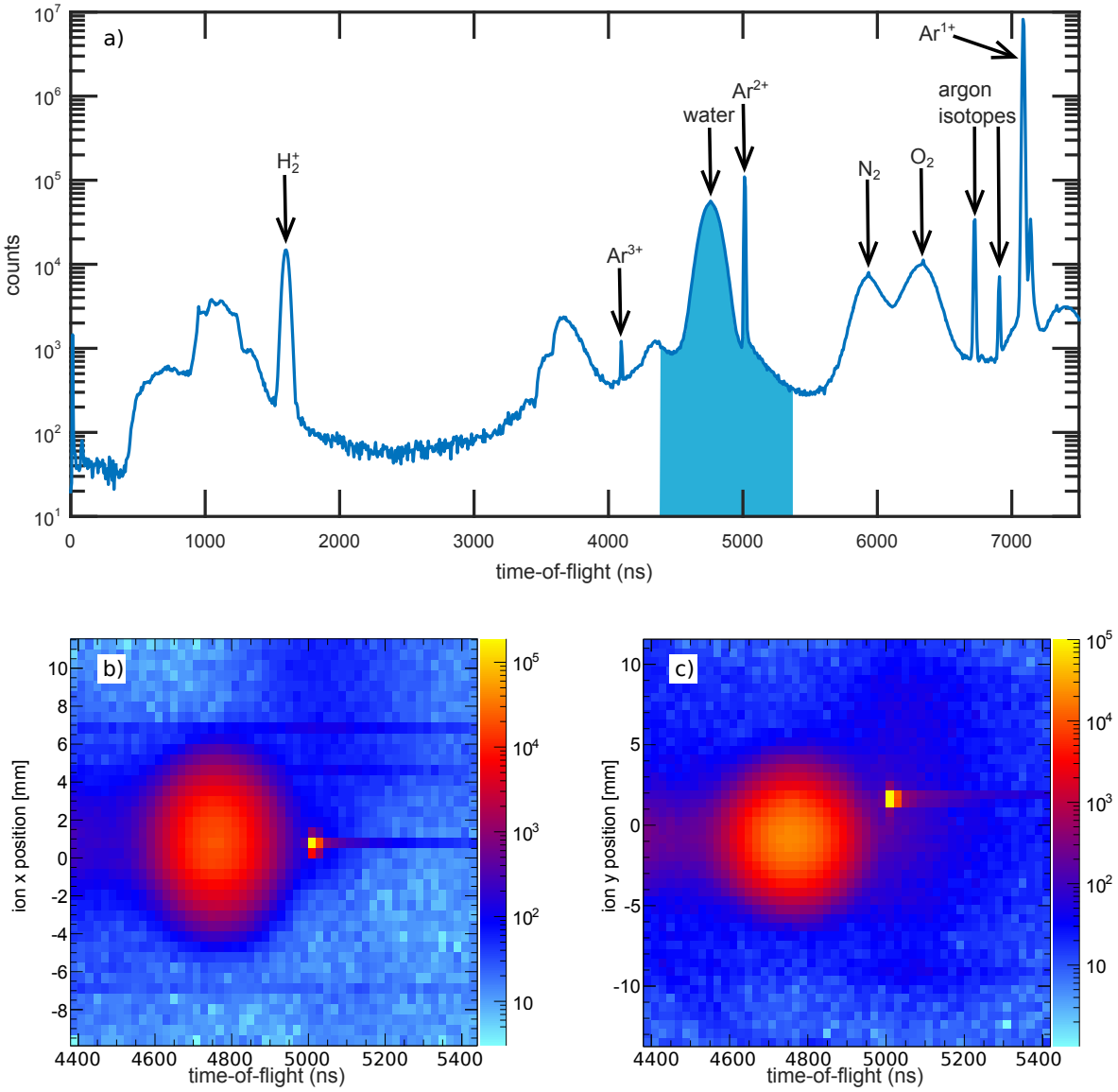


Figure 4.9: (a) shows the time-of-flight spectrum of the detected ions. The corresponding species are indicated. The peak from singly charged argon dominates. The peak from double charged argon is close to the peak from water. It can be seen that the peaks from argon are sharp and the peak from water is broad. This is because the argon ions are cooled by the supersonic gas expansion, and water is residual gas at room temperature. The events that are shaded in (a) are shown in (b) and (c). In (b) the position in the direction of the laser propagation direction is shown (x-position) additionally. (c) shows the same as (b) but for the position along the jet-propagation direction (y-position). The offset of the sharp argon peak to the broad water peak in (c) is due to the finite velocity offset of the jet in the jet-propagation direction. The peak from water is broad compared to the peak from doubly charged argon in (b) and (c) for the same reason as in (a). All data shown is based on the same data set as Fig. 6.11.

4.1.4. Data Acquisition and Control of the Experimental Protocol

In chapter 4.1.3 it was explained that the CoboldPC software was used to record the data. The availability of seven motorized stages in the fully automated interferometric two-color setup demands for a concept to control the experimental protocol. For the data analysis and the interpretation of the experimental results it is very important to know the positions of all motorized stages for every event. Moreover, it is important to not record data while the stages are moving. To achieve these two goals the stages are controlled by the CoboldPC software. This approach minimizes the risk that the recorded data is inconsistent[37]. Hence, the data acquisition and the communication with the controllers of the motorized stages are both carried out by the CoboldPC software (see Fig. 4.10).

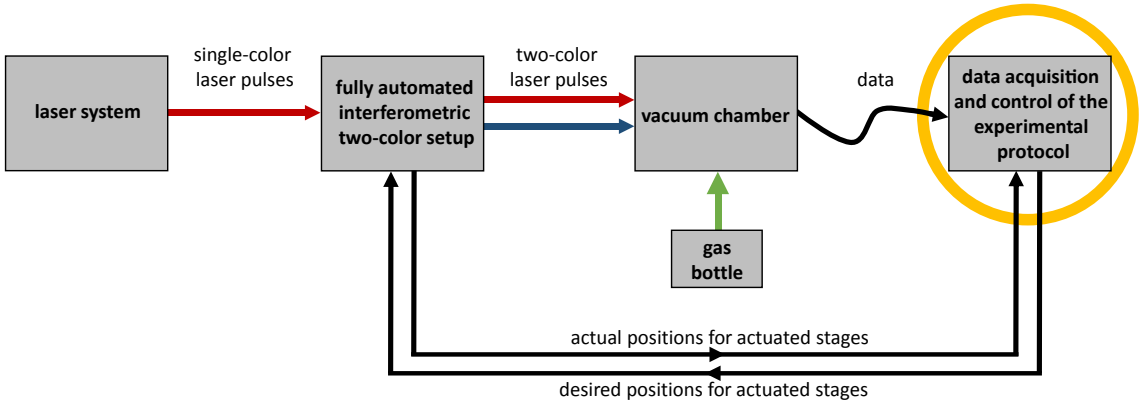


Figure 4.10: The data acquisition and the control of the experimental protocol are both done by the CoboldPC software. The desired positions for the motorized stages are set and the actual positions are read by the CoboldPC software. During the movement of the stages the CoboldPC software does not record data.

This software was modified by implementing a coordinating thread that manages six sub-threads[38]. Each sub-thread manages the communication with one stage-controller[39]. All stage-controllers are connected to the computer using one USB-hub. The advantage of having one thread for each stage-controller is that several stages can be managed simultaneously without any restrictions. This software architecture is very robust and appears to be ideal for performing predefined movements. However, there are two disadvantages to this approach:

- Each time the experimental protocol is changed (a different sequence of stage movements is desired) the CoboldPC software has to be re-compiled.

[37] An alternative approach would be to use another program to manage the motorized stages. This way, any problems regarding the communication of the two programs might lead to recorded data which is inconsistent.

[38] These modifications were done with the help of the RoentDek Handels GmbH. The project benefited from previous work by Maksim Kunitski who used one single thread to perform predefined movements using the CoboldPC software.

[39] A stage-controller is an electronic device that is usually delivered together with the actuator for the motorized stage. Here, all stage-controllers have an USB-interface and the communication is performed sending ASCII commands using a virtual COM-port.

- The approach is very impractical to quickly try different settings for the motorized stages. This is a common procedure that is done before the real measurement campaign is started to find the ideal experimental settings.

Both disadvantages are elegantly overcome by implementing a shared memory interface into the CoboldPC software. This allows one to set desired stage positions using an independent application with a graphical user interface (GUI). At the same time the shared memory interface can be used by the GUI to display the current stage positions. Fig. 4.11 illustrates how the shared memory acts as an interface connecting the two independent applications. Fig. 4.12 shows a screenshot of the GUI.

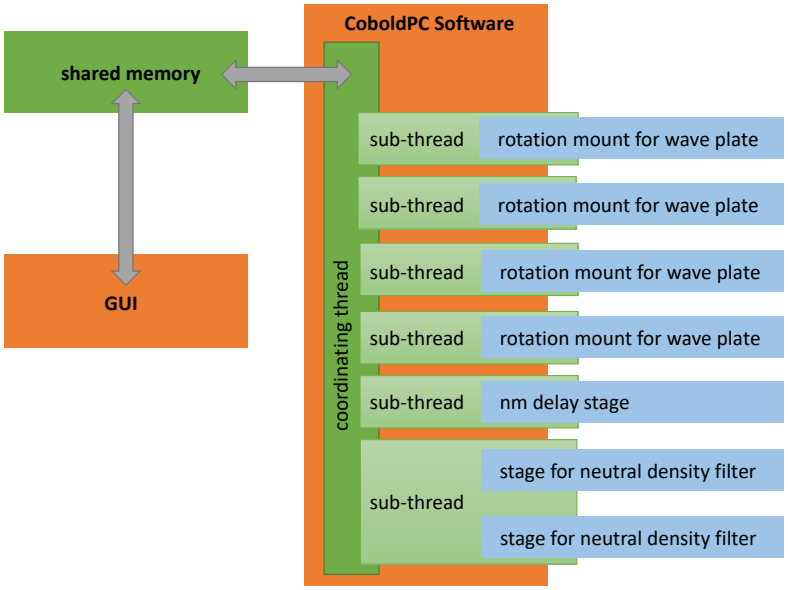


Figure 4.11: The CoboldPC software is the program that is used to record the data during the experiments. A coordinating thread which is part of the CoboldPC software manages six sub-threads. Each sub-thread communicates with one stage-controller using a USB-interface. Both stages that are used to actuate the neutral density filters are controlled by the same stage-controller. Therefore, those two stages are managed by the same sub-thread.

The use of an independent application with a GUI has two advantages:

- Each time the experimental protocol is changed (a different sequence of stage movements is desired) only the independent application with the GUI has to be re-compiled. This allows one to keep the data acquisition running while the application with the GUI is recompiled.
- This approach is very practical to quickly try different settings for the motorized stages.

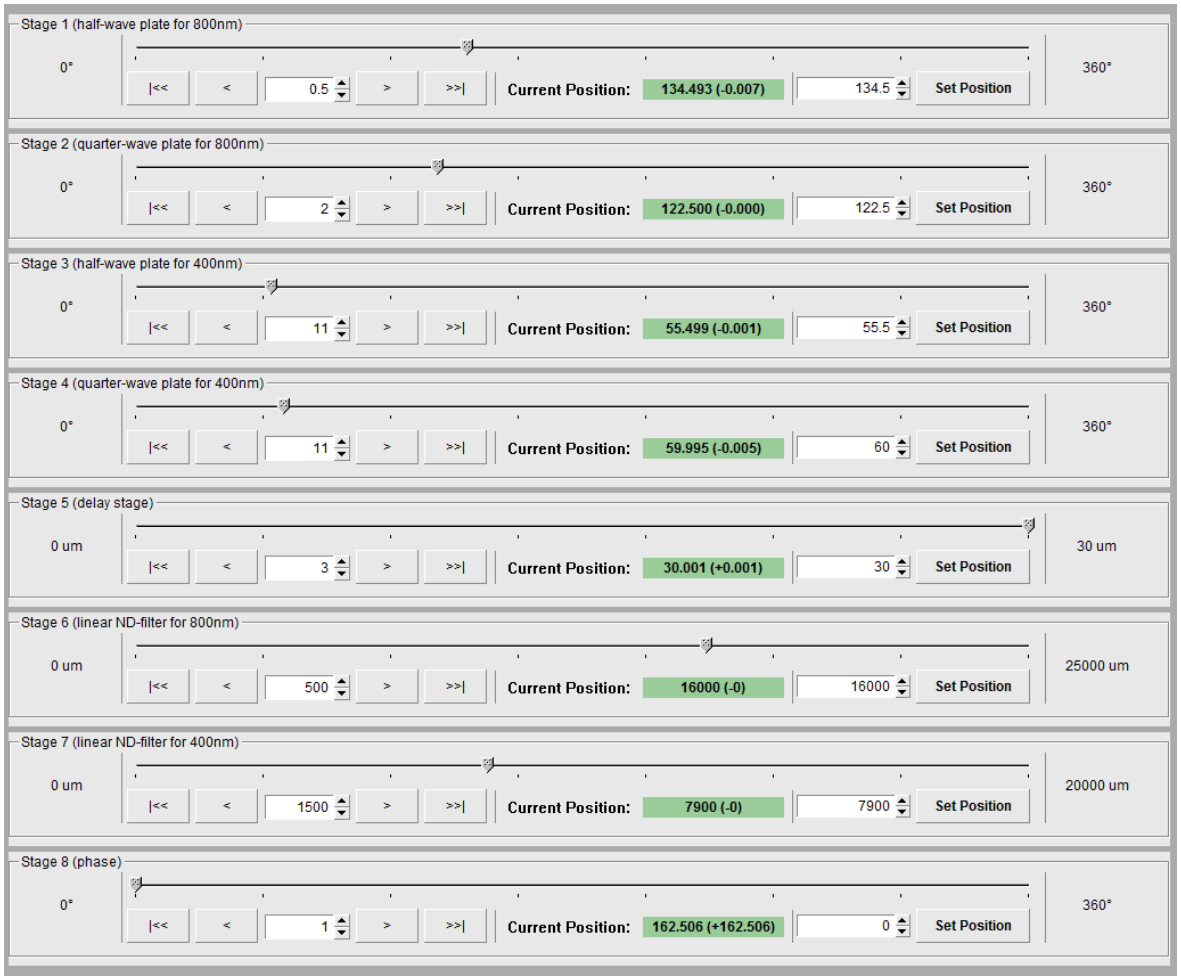


Figure 4.12: Screenshot of the GUI of the program that is used to define the experimental protocol. Each row corresponds to one controllable degree of freedom. The first four rows are used to set the desired positions of the motorized rotation mounts used to actuate the wave plates. The fifth row is assigned to the nm-delay stage. The sixth and the seventh row are used to control the position of the neutral density filters. The numbers on the very left and the very right indicate the minimum and the maximum values that can be set. "Stage 8 (phase)" is a field that only works if the active stabilization of the two-color phase is running (see chapter A.4 for details).

The buttons and text fields in the GUI can be used to set the desired positions in the shared memory. If this is done the green background color of the label that shows the current stage position turns red. If the coordinating thread of the CoboldPC software detects that a stage movement is desired by reading the shared memory, the coordinating thread stops the data acquisition and passes the command to the responsible sub-thread. The sub-thread manages the movement of the stage and determines the final stage position. Afterwards, the sub-thread indicates that the movement is finished and the coordinating thread reenables the data acquisition. Afterwards, the current stage position and a boolean flag, signaling that the movement is completed, is updated in the shared memory by the coordinating thread. Finally, the program of the GUI reads the shared memory, sets the background color of the label that

shows the current stage position back to green and updates the current stage position which is displayed in the GUI.

4.1.5. Comissioning: Generating well-defined Two-Color Fields

To gain physical insight, the properties of the two-color laser field inside the interaction region have to be known. To this end, the interferometric two-color setup and the vacuum chamber cannot be threaded independently, because the polarization of the tailored two-color laser field in front of the entrance window cannot be assumed to be identical to the polarization of the two-color field inside the interaction region. Thus, the interferometric two-color setup and the vacuum chamber have to be understood as one setup that determines the two-color laser field in the interaction region (see Fig. 4.13). This has two reasons:

- The transmittance of the entrance window and the focusing by the spherical mirror inside the vacuum chamber can have wavelength-dependent and polarization-dependent properties.
- For non-linear light matter interaction the most central cycles of fs-laserpulses are more important than the rising and falling edge of fs-laserpulse (or the temporally averaged laser pulse).[40]

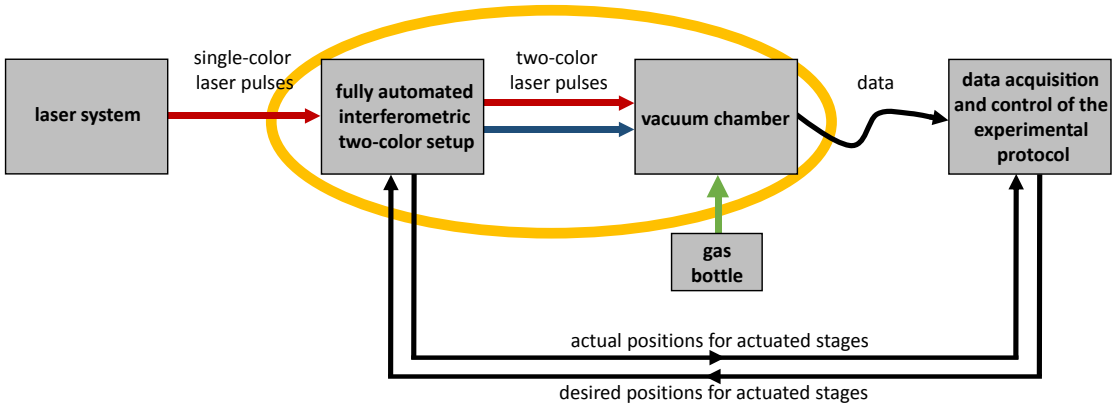


Figure 4.13: Schematic overview of the experimental setup. The combination of the interferometric two-color setup and the vacuum chamber is highlighted. The properties of both elements are relevant for the two-color field parameters that govern the ionization of the studied target atoms.

Due to these two limitations it is very difficult to precisely know the ellipticity in the interaction region. Fortunately, there are two polarization states that are easy to identify:

- Perfect linearly polarized light results in efficient non-sequential double ionization (see Fig. 4.8 in Ref. [55]). Slightly elliptical polarization already results in a strongly

[40] This can be illustrated by using a sequence of two laser pulses with the same pulse energy, but different pulse durations (e.g. 1000 fs and 10 fs) and a delay of 2000 fs. Both laser pulses are linearly polarized and the polarization vectors are orthogonal to each other. The longer pulse will not contribute to the tunneling probability and all that is relevant in the interaction region is the linearly polarized 10 fs-laserpulse. Trying to measure the polarization in front of the vacuum chamber using a linear polarizer might lead to the conclusion that circularly polarized light was used for the experiment. Not realizing that there are two laser pulses, the pulse energy might be estimated to be twice as high as it really is.

decreased recollision-probabilty compared to perfect linearly polarized light (see also chapter 6).

- The nonlinear dependence of the ionization rate (comp. Eq. 5) on the laser electric field is very helpful. Only perfect circular polarization leads to electron momentum distributions that are independent of the angle in the plane of polarization (e.g. see Fig. 8.10(a)). Small deviations from perfect circularly polarized light manifest as electron momentum distributions that strongly depend on the angle in the plane of polarization.

As a result, it is not easy to use driving fields in the interaction region that are other than linearly or circularly polarized and have a defined ellipticity. Systematic approaches to overcome this limitation are described in Refs. [55, 56]. Ref. [55] is the master thesis of Nikolai Schlott who was supervised by the author of this thesis. The polarization is affected by the individual optical components which are modeled using Jonas matrices. For both single-color beams it is possible to find mapping functions that link the angles of the wave plates with the ellipticity in the interaction region. A model incorporating the transmission for s-polarized and p-polarized light as well as the phase shift of both polarization components is used to map the polarization state behind the wave plates to the polarization state inside the interaction region. The model can be fitted using experimentally observable properties of the setup. This is done by finding all combinations of positions for the half-wave plate and the quarter-wave plate for which the light in the interaction region is linearly polarized.

The light intensity in the interaction region is also of interest. Several methods to calibrate the laser intensity are found in the literature (see e.g. Refs. [57–59]). If not stated otherwise, for this thesis the single-color intensity of the laser pulse at 780 nm is determined using the following precedure. Using circularly polarized light in the absence of above-threshold ionization peaks, the most probable radial electron momentum in the plane of polarization p is linked to the electric field amplitude E by the relation $p = \mathrm{e} \cdot E/\omega$, where ω is the frequency of the driving field (see chapter 3.2.1) and e is the elementary charge. This is used to determine E which defines the peak intensity. The uncertainty of the absolute laser intensity in the interaction region, that is determined using this method, is estimated to be 10%. An obvious, but significant problem of this in situ intensity calibration method is that it relies on an accurate calibration of the electron momentum measurement. Another systematic error is due to the non-adiabaticity of tunnel ionization. As shown in chapter 8 the non-adiabatic offset of the initial momentum distribution leads to a higher radial momentum and thus a systematic overestimation of the in situ intensity. A second systematic contribution partially

cancels this systematic overestimation: the long range Coulomb interaction slows down the escaping electron which leads to a reduced final radial momentum (see also chapter 7). If the procedure which is described above is not applicable due to the presence of above-threshold ionization (ATI) peaks (which is often the case for 390 nm) another method is usually used: the shift of the ATI peaks is measured as a function of the average power of the laser pulses which is measured with a power meter in front of the vacuum chamber. The shift of the ATI peaks in energy is due to the ponderomotive energy U_p. Fortunately, U_p is a function of the laser intensity (see Eq. 5). Thus, the intensity can be obtained in situ (see also chapter 3.1 and Ref. [36]). The uncertainty of the absolute laser intensity in the interaction region, which is determined using this method, is estimated to be 20%. An advantage of these two approaches to calibrate the laser intensity in the interaction region is that focal averaging for single ionization is intrinsically included (see chapter A.1).

For most projects that are described in this thesis, both individual single-color fields are circularly polarized. As has been described above, it is possible to determine the intensity of both single-color laser pulses in the interaction region. The two-color field is a superposition of the two single-color fields. Two further parameters, which have not yet been discussed, are the helicities of the single-color fields. It will be shown that the relative helicity[41] of the two single-color laser pulses (one laser pulse at a central wavelength of 390 nm and the other at a central wavelength of 780 nm) manifests itself in the symmetry of the observed electron momentum distribution (see Fig. 8.4). For the sake of the argument, one can assume that both single-color fields have the same helicity. How can the absolute helicity of the laser pulse at 780 nm be determined? An elegant procedure that can be used is to change the position of the nm-delay stage and observe the rotation of the electron momentum distribution in the plane of polarization.

[41] If both single-color laser pulses have the same helicity the electric field vectors of the single-color fields are rotating in the same direction with time. If both single-color laser pulses have opposite helicities the electric field vectors of the single-color laser fields are rotating in opposite directions taking the temporal evolution into account.

5. Theoretical Methods to Simulate Strong Field Ionization

During the work for this thesis two complementary methods have proven to be extraordinarily valuable to not only reproduce certain experimental results, but also to allow for a deeper understanding of the underlying processes. The two methods are the saddle point strong field approximation (SFA) and the SCTS (Semi-Classical Two-Step) model. The saddle point SFA is good at modeling the dynamics in the classical forbidden region (tunnel), but ignores most of the dynamics after tunneling. In contrast, the SCTS model is trajectory-based and is very useful for modeling the electron after it has left the classical forbidden region. The author of this thesis emphasizes that the explanations given in this chapter are written from an experimentalist's point of view and are not a theoretical review.

5.1. Saddle Point Strong Field Approximation - Method

Strong Field Approximation (SFA) is a commonly used method to calculate electron momentum distributions (see Ref. [46] for a review, see Refs. [22, 60, 61] for general ideas and see Ref. [62] for examples using two-color fields). The following short introduction aims at conveying the general idea of SFA. Despite the many correct predictions regarding non-adiabatic tunneling it is important to note that SFA suffers also many shortcomings. The gauge-invariance of SFA and the fact that SFA models the shape of the potential well incorrectly are a prominent examples (see e.g. Refs. [22, 46, 63, 64]). The structure and the content of chapter 5.1 are based on a talk by Dieter Bauer [65]. A more detailed and rigorous treatment is found in Ref. [64].

SFA allows for an approximation of the electron momentum spectrum $|M(\vec{p})|^2$ upon ionization by a given electric field $\vec{E}(t)$ (with the corresponding vector potential $\vec{A}(t)$). The Keldysh matrix element $M(\vec{p})$ can be expressed by [1, 66]:

$$M(\vec{p}) = -i \int_{-\infty}^{\infty} \langle \vec{p} + \vec{A}(t) | \vec{r} \cdot \vec{E}(t) | \Psi_0 \rangle \exp\left(-i \cdot S_0(\vec{p},t)\right) \mathrm{d}t \tag{10}$$

where $\vec{r}$ is the position coordinate and $|\Psi_0\rangle$ is the initial state of the electron. The action is defined by[42]:

$$S_0(\vec{p},t) = \int_t^{\infty} \left[\frac{1}{2} \vec{v}^2(\vec{p},t') + I_p \right] \mathrm{d}t' \tag{11}$$

where I_p is the ionization potential and the time-dependent velocity is given by:

$$\vec{v}(t) = \vec{p} + \vec{A}(t) \tag{12}$$

For $I_p/\omega \gg 1$ it is a good approximation to assume that all contributions with a non-constant action cancel out [61, 65]. This leads to the representation using saddle points in which the Keldysh matrix element can be written as (see Ref. [60]):

$$M(\vec{p}) = -i \sum_{\alpha} \sqrt{\frac{2 \cdot \pi}{i S_0''(\vec{p},t_{s_\alpha})}} \langle \vec{p} + \vec{A}(t_{s_\alpha}) | \vec{r} \cdot \vec{E}(t_{s_\alpha}) | \Psi_0 \rangle \exp\left(-S_0(\vec{p},t_{s_\alpha})\right) \tag{13}$$

where S_0'' is the second temporal partial derivative of the action. The sum of all α means that for a given $\vec{p}$ the signals of all contributing starting times t_{s_α} have to be summed up. The starting times t_{s_α} are complex values and can be obtained by solving $\partial S_0|_{t_{s_\alpha}} = 0$. Using Eqs.

[42] see e.g. Ref. [61]. Ref. [61] cites Refs. [66–68]

11 and 12 this leads to:

$$\left[\vec{p}+\vec{A}(t_{s_\alpha})\right]^2 = -2\cdot I_p \tag{14}$$

In addition, the exponential part dominates the expression shown in Eq. 13. Neglecting the preexponential factor still allows for the calculation of the electron momentum spectrum with "exponential accuracy" [65] for a single starting time t_{s_α}:

$$\begin{aligned}|M(\vec{p})|^2 &= |\exp\left(-i\cdot S_0\left(\vec{p},t_{s_\alpha}\right)\right)|^2 \\ &= \exp\left(-i\cdot\Re(S_0\left(\vec{p},t_{s_\alpha}\right)) - i^2\cdot\Im(S_0\left(\vec{p},t_{s_\alpha}\right))\right) \\ &\qquad \cdot\exp\left(i\cdot\Re(S_0\left(\vec{p},t_{s_\alpha}\right)) - i^2\cdot\Im(S_0\left(\vec{p},t_{s_\alpha}\right))\right) \\ &= \exp\left(2\cdot\Im(S_0\left(\vec{p},t_{s_\alpha}\right))\right)\end{aligned} \tag{15}$$

If interference of different starting times is ignored the electron momentum spectrum can be written as the incoherent sum of all starting times:

$$|M(\vec{p})|^2 = \sum_\alpha \exp\left(2\cdot\Im(S_0\left(\vec{p},t_{s_\alpha}\right))\right) \tag{16}$$

The result shows that the probability of liberating an electron in saddle point SFA depends on the imaginary part of the action evaluated at the complex starting time t_{s_α}. After the electron has left the classical forbidden region all times are real valued. In conclusion, the ionization probability depends only on the action under the tunnel barrier.

Hence, for every point in final momentum space $\vec{p}$ the following approach can be used to obtain the ionization probability in saddle point SFA:

- find all saddle points by solving Eq. 14 (leads to all t_{s_α} (complex values))
- calculate the action at all saddle points using Eq. 11
- calculate the intensity $|M(\vec{p})|^2$ using Eq. 16

5.2. Saddle Point Strong Field Approximation - Examples

The approach[43] that is described in chapter 5.1 is used in chapter 8. Employing the same numerical implementation of the saddle point SFA, in the following some examples are shown to illustrate the strength of saddle point SFA[44].

To this end the scaling factor α is introduced. α defines the ionization potential $I_p = \alpha \cdot 0.5811$ a.u., the angular frequency $\omega = \alpha \cdot 0.05841$ a.u. and a circularly polarized electric field with the amplitude $E_{780} = \alpha \cdot 0.05$ a.u. Based on these quantities the saddle point SFA calculation is performed for circularly polarized light. The results are shown in Fig. 5.1 for the scaling factors $\alpha = 0.1$, $\alpha = 1$ and $\alpha = 4$. The corresponding Keldysh-parameters are then given by $\gamma = 1.26 \cdot \sqrt{\alpha}$. Thus, the Keldysh-parameter can be varied by the scaling factor α while the condition $I_p/\omega \gg 1$, which is a prerequisite in saddle point SFA, remains valid.

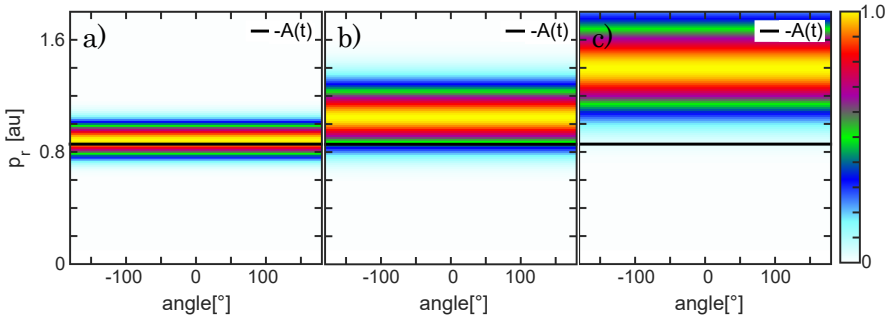


Figure 5.1: The simulated electron momentum distribution obtained from saddle point SFA. $p_r = \sqrt{p_y^2 + p_z^2}$ is the radial momentum in the plane of polarization and the angle is defined by atan2(p_z, p_y). The ionization potential $I_p = \alpha \cdot 0.5811$ a.u., the angular frequency $\omega = \alpha \cdot 0.05841$ a.u. and the electric field $E_{780} = \alpha \cdot 0.05$ a.u. are used for the scaling factor $\alpha = 0.1$ in (a), $\alpha = 1$ in (b) and $\alpha = 4$ in (c). The black line shows the negative vector potential which is independent of α. The color code shows the intensity in momentum space divided by the radial electron momentum p_r to take the volume element of the cylindrical coordinate system into account. This makes sure that the coordinate of the brightest pixel corresponds to the coordinate of the brightest pixel in Cartesian coordinates.

The black line in Fig. 5.1(a) shows the negative vector potential. It can be observed that for $\alpha = 0.1$ the most probable radial electron momenta almost coincide with the negative vector potential. The vector potential remains unchanged in Fig. 5.1(b) and 5.1(c) because the vector potential is independent of α. However, it can be observed that the most probable radial momentum increases with increasing α. Since the final momentum in saddle point SFA is the sum of the initial momentum and the negative vector potential this finding illustrates that there is almost no offset of the initial momentum distribution for very small

[43] The numerical implementation of the saddle point SFA calculation has been developed by Nicolas Eicke and Manfred Lein, made available to our group as part of the project described in chapter 8 and has been used by the author of this thesis to generate the results shown in chapter 5.1.

[44] For circularly polarized light there exists an analytic expression for the ionization probability in saddle point SFA which is not used here [65, 69].

Keldysh-parameters (Fig. 5.1(a)). For increasing Keldysh-parameters (Fig. 5.1(b) and Fig. 5.1(c)) the initial momentum offset increases [69]. The broadening of the width is discussed in Refs. [70, 71].

Adding the second harmonic to the driving field an interesting scenario emerges. The ionization potential is still given by $I_p = \alpha \cdot 0.5811\,\text{a.u.}$ and a counter-rotating two-color field is used. The fundamental at an angular frequency $\omega_{780} = \alpha \cdot 0.05841\,\text{a.u.}$ (second harmonic at an angular frequency $\omega_{390} = \alpha \cdot 2 \cdot 0.05841\,\text{a.u.}$) is circularly polarized with $E_{780} = \alpha \cdot 0.04\,\text{a.u.}$ ($E_{390} = \alpha \cdot 0.02\,\text{a.u.}$). For this field ratio the effective angular velocity (see chapter A.8) of the laser electric field is zero at the maximum of the electric field. As a result it is clear from symmetry that there cannot be any offset of the initial momentum distribution. This is illustrated by Fig. 5.2 by varying the scaling factor α similarly as it has been done for Fig. 5.1. It is seen that the most probable radial momentum in Fig. 5.2 only weakly depends on the scaling factor α. In chapter 8 the reason for the scaling of the results shown in Fig. 5.1 and Fig. 5.2 as a function of α are explained by performing single-color and two-color experiments.

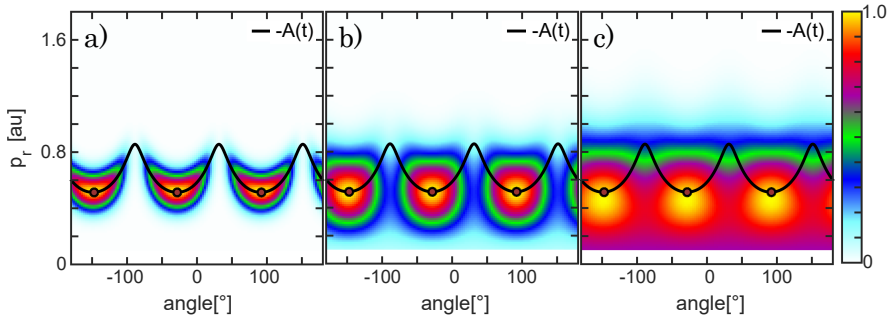


Figure 5.2: The simulated electron momentum distribution obtained from saddle point SFA is shown for a two-color field in analogy to Fig. 5.1. The ionization potential is $I_p = \alpha \cdot 0.5811\,\text{a.u.}$, the angular frequency of the fundamental is $\omega = \alpha \cdot 0.05841\,\text{a.u.}$ and the electric field amplitudes are $E_{780} = \alpha \cdot 0.04\,\text{a.u.}$ and $E_{390} = \alpha \cdot 0.02\,\text{a.u.}$ The scaling factor α is $\alpha = 0.1$ in (a), $\alpha = 1$ in (b) and $\alpha = 4$ in (c). The black line shows the negative vector potential which is independent of α. The red points indicates the minimal negative vector potential which belongs to the maxima of the combined electric field in counter-rotating two-color fields. The white area for $p_r < 0.1\,\text{a.u.}$ in (b) and (c) is an artifact of the numerical implementation. The color code shows the intensity in momentum space divided by the radial electron momentum p_r to take the volume element of the cylindrical coordinate system into account. This makes sure that the coordinate of the brightest pixel corresponds to the coordinate of the brightest pixel in Cartesian coordinates.

5.3. Semi-Classical Two-Step Model

Strong field ionization can be approximated as a tunneling event with subsequent classical propagation of the liberated electron. Repeated random sampling allows for the generation of an electron momentum distribution. This is the basic idea of classical trajectory Monte Carlo (CTMC) simulations. In 2016, Shvetsov-Shilovski et al. introduced a semi-classical two-step model (SCTS) assigning a semi-classical phase to each calculated trajectory[45]. They reached good agreement with exact numerical solutions of the time-dependent Schrödinger equation [38]. For the simulations the ionization rate ω_{rate} from Eq. 5 is used. Usually several million trajectories are calculated. For the calculation, candidates for the initial conditions (sets of the initial momentum at the tunnel exit $v_\perp$ and the instance of tunneling t_0) are randomly chosen. For the SCTS calculation, the probability that a trajectory is calculated using this set of initial conditions is proportional to $\sqrt{\omega_{\text{rate}}}$. For the final spectra this weight is also considered and allows for improved convergence of the simulation. [38] The tunnel exit position[46] is given by [73, 74]:

$$\vec{r_0} = -\frac{I_p + \sqrt{I_p^2 - 4 \cdot |E(t_0)|}}{2 \cdot |E(t_0)|^2} \vec{E}(t_0) \tag{17}$$

After tunneling the electrons are driven by the combined force of the Coulomb potential $V(r) = 1/r$ and the time-dependent laser electric field $E(t)$ (where r is the distance of the electron to the ion). After the end of the laser pulse, the asymptotic semi-classical phase and the asymptotic final momentum are calculated using analytic Coulomb mapping for Kepler hyperbola (see Eq. 29 and Eq. 40 from Ref. [38]). For each trajectory the bin (that corresponds to the final momentum of the trajectory that is considered) of the histogram $H(p_x,p_y,p_z)$ is increased by the complex number $\exp(i \cdot \phi_f)$. $H(p_x,p_y,p_z)$ has the same binning as the three-dimensional final momentum space $P(p_x,p_y,p_z)$. This is done for all trajectories that are to be considered. Then, the final intensity for each bin in the histogram representing final momentum space is calculated by:

$$P(p_x,p_y,p_z) = |H(p_x,p_y,p_z)|^2 \tag{18}$$

This allows for the interference of semi-classical trajectories and neatly compensates for the

[45] Already in 2014, Li et al. have introduced a semi-classical model incorporating the phase ("Quantum trajectory Monte Carlo" (QTMC), see Ref. [36, 72]). In contrast to the QTMC model, the influence of the Coulomb potential on the evolution of the electron's phase is calculated more accurately in the SCTS model (see discussion of Eq. 22 in Ref. [38]).

[46] The formula for $\vec{r_0}$ is only valid for $I_p^2 \geq 4 \cdot |E(t_0)|$

weight of $\sqrt{\omega_{\text{rate}}}$. The procedure is applicable for any three-dimensional time-dependent driving field $\vec{E}(t)$. The method is demonstrated using a circularly polarized driving field[47].

Using a circularly polarized driving field at 780 nm with a peak electric field of 0.05 a.u. the ionization of helium ($I_p = 24.5874$ eV) is simulated. The yz-plane is the plane of polarization. Here, and if not stated otherwise throughout this thesis, a 12 cycle laser field is used (total duration of 12 cycles, sine-square envelope, like in Fig. 7.5(d)). 50 million trajectories were calculated in the examples shown in chapter 5.3. Using a grid in final three-dimensional momentum space from -1.5 a.u. to 1.5 a.u. in all dimensions and a bin size of 0.015 a.u. the final momentum distribution shown in Fig. 5.3 is obtained. Fig. 5.3 shows a two-dimensional projection of three-dimensional momentum space. The momentum component in the light propagation direction is not shown. For Fig. 5.3 the semi-classical phase is ignored. This model is referred to as the classical two-step model (CTS) throughout this thesis[48].

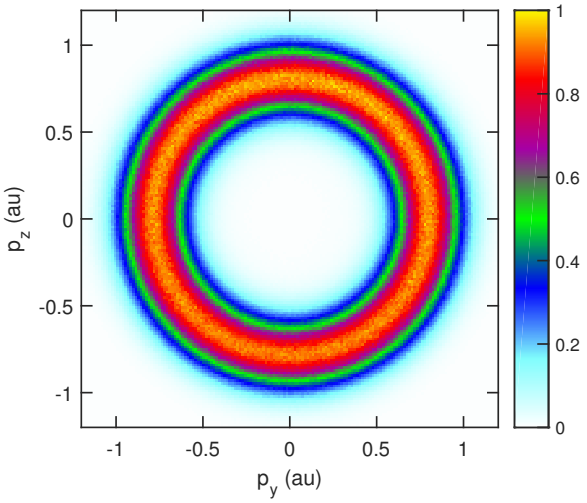


Figure 5.3: Simulated electron momentum distribution for the ionization of helium by a circularly polarized driving field at 780 nm with a peak electric field of 0.05 a.u. using the CTS model.

Not ignoring the semi-classical phase, yields the result shown in Fig. 5.4. It is obvious that the simulated results are inaccurate. The reason is that the bin size chosen is too big to account for the rapidly changing semi-classical phase. Since the binning is done using a Cartesian grid, the artifacts are stronger along the diagonal of Fig. 5.4.

[47] The SCTS calculations that are presented in this thesis were done using an implemented version of the procedure described above which was modified by the author of this thesis. The used software version is based on a software version which has been implemented by Maksim Kunitski.

[48] The classical two-step model (CTS) is the same as the SCTS model but ignores the semi-classical phase. For the CTS model, only the final momentum for each trajectory is considered. For each trajectory the bin in the histogram $P(p_x,p_y,p_z)$ that corresponds to the final momentum is identified and increased by the value of 1. For the CTS model the histogram $H(p_x,p_y,p_z)$ is not relevant.

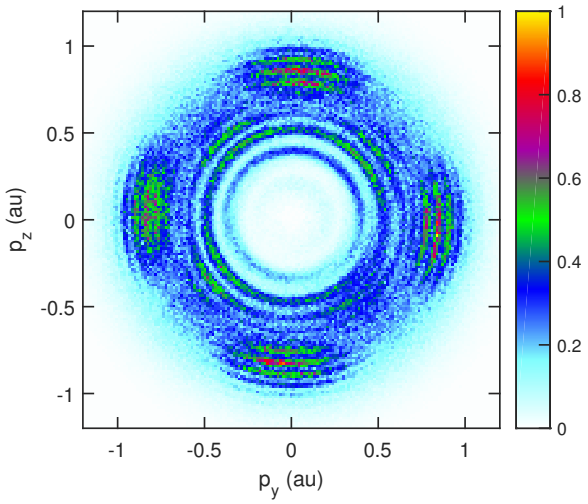


Figure 5.4: Simulated electron momentum distribution for the ionization of helium by a circularly polarized driving field at 780 nm with a peak electric field of 0.05 a.u. using the SCTS model. The bin size chosen is too big to produce physically meaningful results.

How to overcome this problem? Decreasing the bin size and increasing the total number of trajectories solves the convergence issue.[49] One possibility to improve convergence is described in the remainder of this subchapter[50]. For each final electron energy, the average of the semi-classical phases of all trajectories can be calculated. The result is shown in Fig. 5.5.

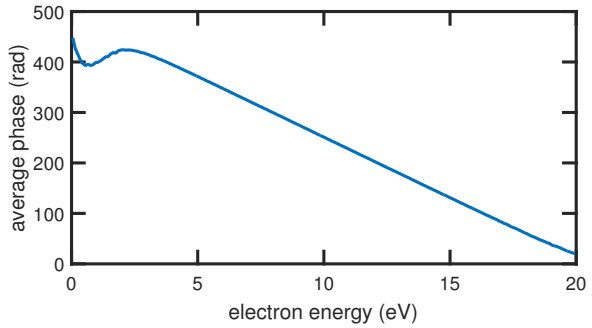


Figure 5.5: Average of the semi-classical phase as a function of the final electron energy in the SCTS calculation.

In the present case, the dependence of the semi-classical phase on the electron energy E can be approximated by:

$$\phi_{\mathrm{SCTS}}(E) = -E \cdot 24.09 \frac{\mathrm{rad}}{\mathrm{eV}} \tag{19}$$

[49] For example, for Fig. 7.6(c) 500 million trajectories were calculated and a bin size of only 0.005 a.u. is used. Convergence tests (e.g. varying the bin size and the total number of trajectories) were used to make sure that the results shown in Fig. 7.6(c) converged.

[50] To the best of my knowledge this method is not discussed in the literature.

Subtracting the phase $\phi_{\mathrm{SCTS}}(E)$ and filling $\exp(i \cdot (\phi_f - \phi_{\mathrm{SCTS}}(E)))$ as weight into the histogram $H(p_x,p_y,p_z)$ does not change the relative phase of two trajectories with the same final momentum, but reduces the gradient of the phase in momentum space. This improves the convergence and is referred to as "phase compression" in this thesis. The result is shown in Fig. 5.6.

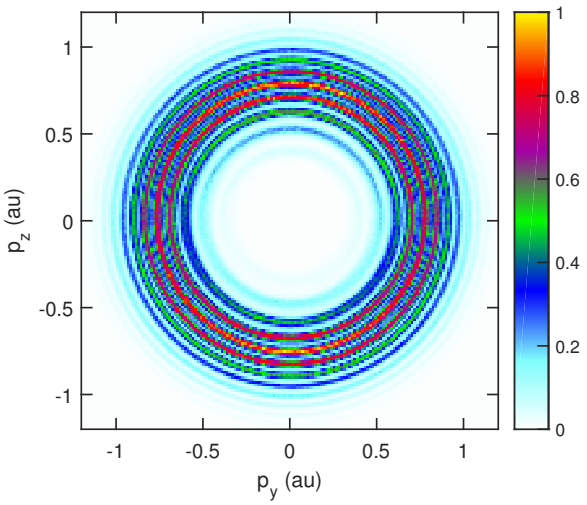


Figure 5.6: Simulated electron momentum distribution for the ionization of helium by a circularly polarized driving field at 780 nm with a peak electric field of 0.05 a.u. using the SCTS model. The "phase compression" method has been used (see text).

The remaining artifacts vanish if the bin size of $H(p_x,p_y,p_z)$ is reduced to 0.0075 a.u. The result is shown in Fig. 5.7 and for the visualization the binning of $P(p_x,p_y,p_z)$ is chosen as for Fig. 5.6.

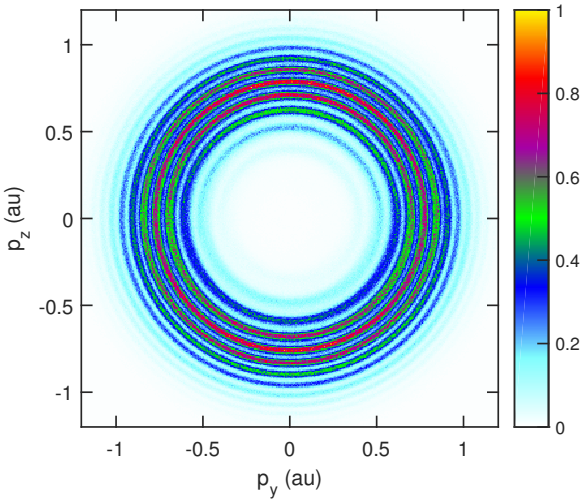


Figure 5.7: Shows the same as Fig. 5.6 but using a bin size of 0.0075 a.u. for $H(p_x,p_y,p_z)$. The result is rebinned to a histogram $P(p_x,p_y,p_z)$ with a resolution of 0.05 a.u. The distribution shown is a projection of the histogram $P(p_x,p_y,p_z)$. The plane of polarization ($p_y p_z$-plane) is shown.

The rings in final momentum are spaced by the photon energy. Hence, the SCTS calculation succeeds in reproducing the quantization of energy as an interference of trajectories.

5.3.1. Semi-Classical Trajectories

Another important strength of the SCTS calculations is that individual trajectories can be identified. Fig. 5.8 shows a typical trajectory in position space for the field parameters which were used for Fig. 5.7.

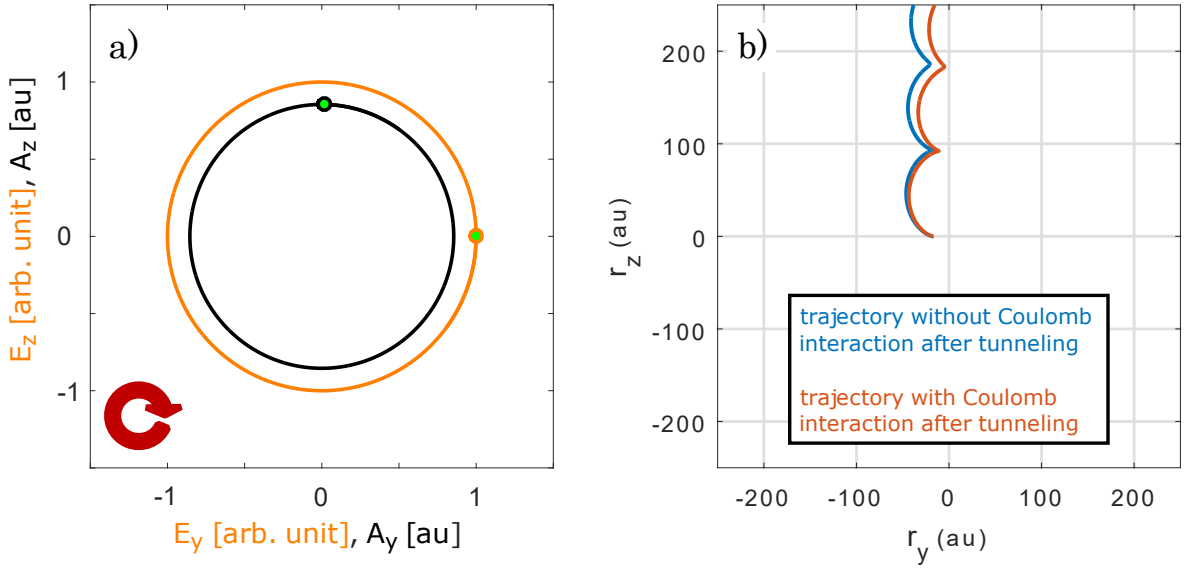


Figure 5.8: (a) shows the electric field as Lissajous curve (orange line) and the corresponding negative vector potential (black line). The green circle indicates the time at which the tunneling process occurs. The single-color intensitiy and helicitiy is illustrated by a red arrow. (b) shows the resulting trajectory in position space which starts at the tunnel exit that points to the opposite direction compared to the electric field at the instance of tunneling. For the blue (red) line the Coulomb potential after tunneling is ignored (taken into account).

Fig. 5.8(a) shows the electric field and the corresponding vector potential. Fig. 5.8(b) shows a typical trajectory ignoring the Coulomb potential of the parent ion after tunneling as a blue line. Taking the Coulomb potential of the parent ion after tunneling into account slightly affects the trajectory resulting in the red line.

Of course, more complicated driving fields can also be used. Fig. 5.9 shows a counter-rotating two-color (CRTC) field. The CRTC field is a superposition of one circularly polarized driving field at 780 nm and one circularly polarized driving field at 390 nm. Both circularly polarized single-color fields have opposite helicities.

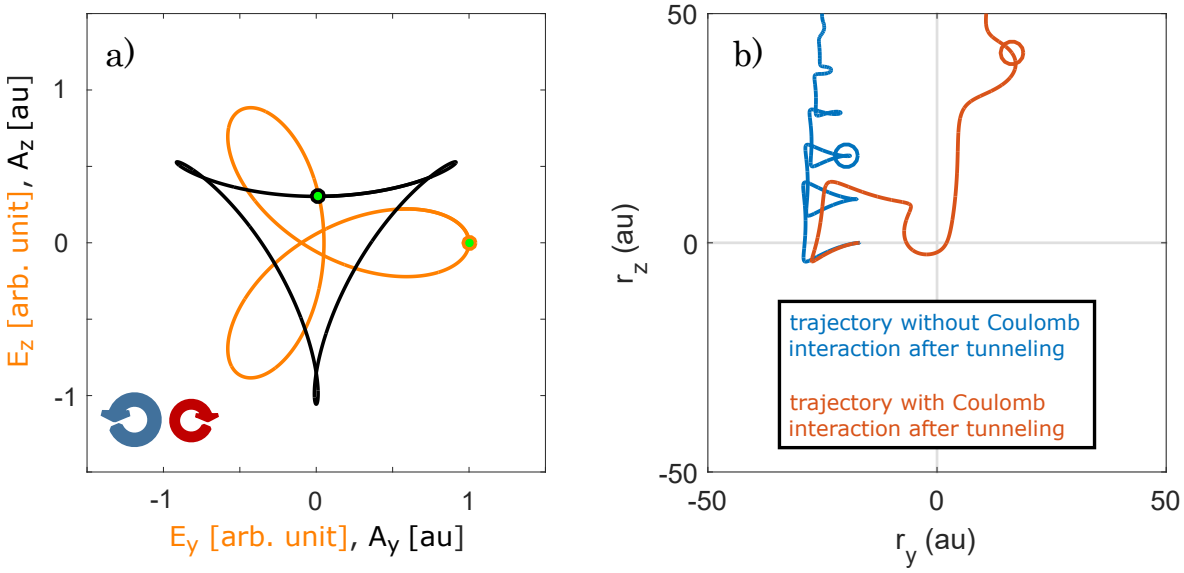


Figure 5.9: Shows the same as Fig. 5.8 but using a CRTC field instead of a circularly polarized field. The single-color intensities and helicities are illustrated by colored arrows. The closed circles in (b) indicate identical times after tunneling.

It is evident, that the electron revisits its parent ion after tunneling which can be considered as a recollision. Recolliding electrons are at the very heart of chapter 6 which discusses experimental findings by Eckart et al. [23].

6. Non-Sequential Double Ionization

Chapter 6 is based on the peer-reviewed publication[51] by Eckart et al. [23] and focuses on the experimental results, specific methods and issues regarding the project which led to the publication. The experimental idea for this project was theoretically proposed in 2016 by Chaloupka and Hickstein [76] simultaneously with the completion of our interferometric two-color setup. We decided to conduct the corresponding experiment because we realized that our setup is ideal for this project, since all relevant parameters can be precisely and automatically controlled.

The scientific idea of this project is based on the following question: can an electron that has been liberated by a strong counter-rotating two-color (CRTC) field recollide with its parent ion? For circularly polarized light recollisions do not occur, while for linear light

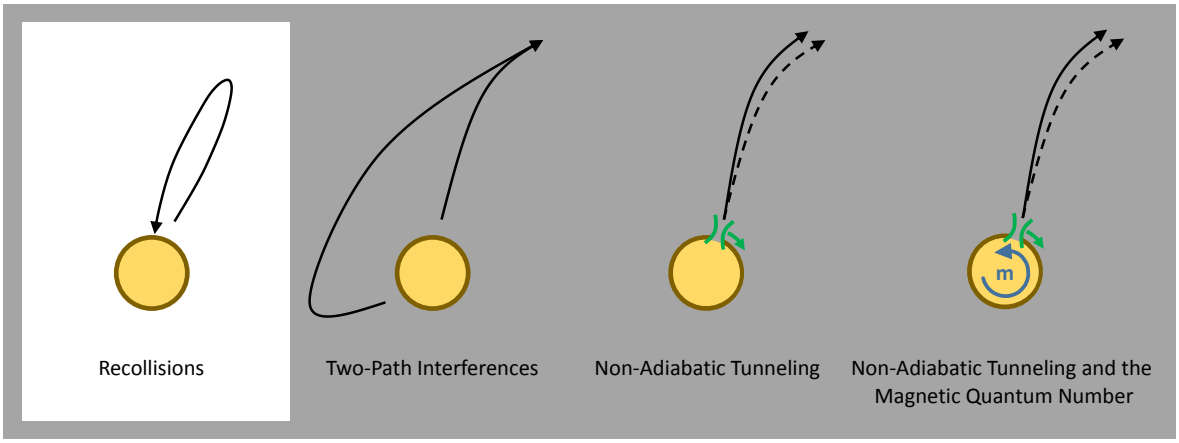


Figure 6.1: Illustration of the key scientific questions of this thesis. Chapter 6 focuses on recollisions in two-color laser fields.

they are likely. The experimental strategy which is applied to answer this question is to use CRTC fields and vary the field ratio of the two single-color laser fields (one laser pulse at a central wavelength of 390 nm and the other at a central wavelength of 780 nm) while keeping the peak electric field constant[52]. A constant peak electric field leads to identical tunneling dynamics, identical positions of the tunnel exit and identical initial momentum distribution at the exit of the tunnel for all field geometries[53]. However, the temporal evolution of the

[51] This work is very similar to the work by Mancuso et al. [75] that was published in Phys. Rev. Lett. the same day.

[52] Tunneling occurs in a good approximation only at the peak electric field because the tunnel probability increases exponentially with the electric field (see Eq. 5).

[53] This is only valid for adiabatic tunneling. In the experimental regime that is accessible using our setup tunneling occurs non-adiabatically (see chapter 8). However, the non-adiabaticity of the process is not necessary to understand the general idea and it will turn out that the adiabatic model using classical trajectories (QTMC) qualitatively agrees with the experimental observation (see Fig. 6.6(a) and Fig. 6.11).

laser electric field after tunneling can be modified by changing the two-color field ratio. This allows for the steering of the electron wave packet upon ionization using the combined two-color field.

Basic question for this project: Is it possible to steer an electron using two-color fields such that the tunneled electron can reencounter its parent singly charged argon ion and how much energy does the electron possess at the time of the recollision?
Experimental idea: If the recolliding electron has enough energy to produce an excited state in the singly charged argon ion this ion will have an increased probability for double ionization. The ratio of the double to single ionization is an experimental quantity that is easy to measure and allows one to determine whether high energy electrons re-encounter their parent ions.
Experimental beauty: The two-color field ratio is a very well defined control parameter which can be easily and reproducibly manipulated using the fully automated two-color interferometric setup.

6.1. State of the Art: Non-Sequential Double Ionization

Single ionization of noble gas (xenon) atoms by strong field ionization using optical fields was already observed in 1966 [32]. The measured ionization rates scaled as predicted [1]. In 1982 double ionization by strong fields was experimentally observed for the first time using noble gas atoms (krypton) [77] and in 1992, it was found by Fittinghoff et al. that the double ionization rate does not scale as expected (Eq. 2 in [78]). Surprisingly, the double ionization rate was underestimated by the theory that considered the emission of the first and the second electron to be independent of each other (sequential double ionization). This scaling manifests itself as the famous "knee-structure" which emerges when the double ionization rate is plotted as a function of the laser intensity (see Fig. 1 in Ref. [79]). Because the increase in the ionization rate was observed only for double ionization, but absent for single ionization, it was concluded that electron-electron interaction is relevant for double ionization. This double ionization mechanism in which both electrons cannot be described independently was termed non-sequential double ionization (NSDI). Since then NSDI has also been of high interest because it is a "smoking gun" of electron-electron interaction and has led to the development of the simple man's model (three-step model) by Corkum [44] (see chapter 3.2.1). The three-step model provides a simple picture of non-sequential double ionization: The first electron, which is liberated by tunneling, is driven by the laser's electric field and recollides with its parent ion. If the recolliding electron has enough energy it can transfer energy to its parent ion during the recollision, leading to electron impact ionization. If the recolliding electron does not have enough energy for electron impact ionization, but has enough energy to populate the first excited state of the ion, then double ionization can occur by "recollision with subsequent electric field (tunnel) ionization" (RESI). The relevance of RESI for double ionization has been shown by Feuerstein et al. [80]. In RESI the recollisional excited singly charged ion is ionized by the laser field which occurs most likely in one of the subsequent maxima of the electric field. As a result a doubly charged ion is produced. An important difference to electron impact ionization is that in RESI the two electrons are emitted at different times, because in RESI the second electron has to "wait" for the laser field to liberate it. Another important detail of RESI is that the cross section for impact ionization depends on the energy of the recolliding electron (see Fig. 3 in Ref. [81]). Non-sequential double ionization is also of great interest because the electron-electron correlation can be accessed performing kinematically complete experiments by measuring correlations of the two emitted electrons in momentum space. Examples for experiments studying electron-electron correlation are

found in Refs. [82–89].

Historically, an important reason to study recolliding electrons is that the energy of a recolliding electron can also be emitted as a photon. The photon energy can be much higher than the photonenergy of the driving field but must be a whole multiple of it. The related process is termed high harmonic generation (HHG, see Ref. [90–92] for reviews). The maximum photon energy in a classical picture is $I_p + 3.17\,U_p$. This so called "cut-off law" was observed experimentally by Krause et al. [93] and can be explained by the three-step model [44]. An alternative model providing a fully quantum mechanical description of HHG is the "Lewenstein model" [94]. However, the three-step model already provides an intuitive explanation why non-sequential double ionization cannot be observed for circularly polarized light [95]. The reason is that for circularly polarized light the electron is driven away from its parent ion and cannot recollide. However, if one aims at producing circularly polarized high harmonics it is clear from symmetry that this is impossible using linearly polarized light.

Eichmann, Becker and others proposed using tailored two-color fields[54] for HHG allowing for the production of circularly polarized high harmonics [96–98]. Those ideas led to the experimental work of Fleischer et al. showing that the ellipticity of high harmonics can be controlled using two-color fields [99]. A subset of the class of tailored two-color fields is the class of co- and counter- rotating two-color fields where both colors are circularly polarized, the helicities are identical or opposite and one color is the second harmonic of the other. Using such fields, Mancuso and others showed the first electron momentum distributions for the single ionization of noble gas atoms (argon) in 2015 (in particular, see Fig. 3 in Ref. [100]). The data was measured using a velocity map imaging spectrometer[55] which only records a two-dimensional projection of three-dimensional momentum space. The missing momentum component was reconstructed using a tomographic reconstruction. In 2016 Chaloupka and Hickstein suggested studying non-sequential double ionization in counter-rotating two-color fields [76] by using the relative intensity of the fundamental and its second harmonic as a control parameter for two-color circularly polarized fields (see Fig. 2 in Ref. [76]). Depending on the field ratio the occurrence of electron impact ionization was examined as a function of the two-color field ratio by analysing the double ionization yield of helium. A very similar experiment using argon and RESI as double ionization mechanism was carried out by Eckart et al. and Mancuso et al. simultaneously, but independently [23, 75].

[54] "Tailored two-color fields" means that the ellipticity, the main axis of the ellipse, the intensity of both colors and the relative phase of the two single-color laser pulses are viewed as paramaters to tailor the most suitable combined electric field for the respective objective.

[55] A relevant limitation of velocity map imaging spectrometers is that there is no information available whether the detected electron belongs to an event in which a singly or a doubly charged ion has been produced.

6.2. Single Ionization of Argon in Counter-Rotating Two-Color Fields

Before the experiment was conducted the argon jet was collimated to $40 \pm 10\,\mu m$ which is shorter than the Rayleigh length of the laser beam (about $150\,\mu m$) in order to minimize volume averaging (see chapter A.1). The geometry of the COLTRIMS setup is as described in chapter 4.1.3 with ($E_{\text{spectrometer}} = 11.2\,\text{V}\,\text{cm}^{-1}$ and $B_{\text{spectrometer}} = 8.3\,\text{G}$). The inlet pressure of the gas nozzle was set to $1.3\,\text{bar} \pm 0.1\,\text{bar}$.

COLTRIMS can measure electrons and ions in coincidence. This allows for the production of separate electron momentum distributions for single and double ionization of argon. In a first step the condition on the ionic side is omitted and the electron momentum distributions for different field ratios $R_{\text{twocolor}} = E_{390\,\text{nm}}/E_{780\,\text{nm}}$ are presented in Fig. 6.2. $E_{390\,\text{nm}}$ ($E_{780\,\text{nm}}$) is the peak electric field of the circularly polarized laser pulse with the central wavelength of 390 nm (780 nm). The helicities of the two laser pulses are opposite to each other. The combined intensity, which is explained later in this chapter, is held approximately constant for all cases shown in Fig. 6.2.

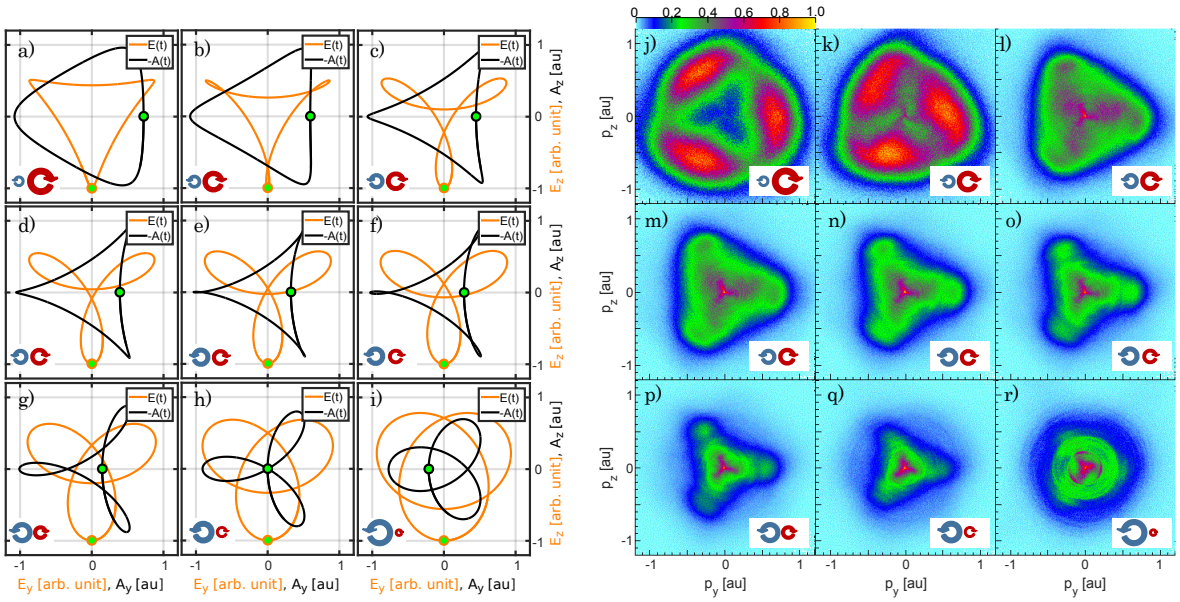


Figure 6.2: (a-i) show the combined two-color field $E(t)$ as Lissajous curves (orange lines) and the corresponding negative vector potentials $-A(t)$ are depicted as black lines. The green dot indicates the phase corresponding to a maximum of $|E(t)|$ which corresponds to a minimum of $|-A(t)|$. (j-r) show the associated electron momentum distributions which were measured without condition on the ion but are completely dominated by single ionization of argon. The two-color field ratio $R_{\text{twocolor}} = E_{390\,\text{nm}}/E_{780\,\text{nm}}$ increases from (a) to (i). The single-color intensities and helicities are illustrated by colored arrows in the panels. All single-color intensities which were used can be found in Tab. 6.2. In general, the relative phase of the two single-color laser pulses in the experiment (j-r) is not known. As a result the rotation of the Lissajous curves in (a-i) does not match the experiment (see Fig. 6.6 for three examples where the rotation angles of the Lissajous curves were matched with the experiment).

The distribution shown in Fig. 6.2(j) is similar to the commonly known "donut" -like distribution which is observed in the tunneling regime for ionization by a single-color circularly polarized field. The weak electric field of the second harmonic leads to a modulation of the ionization probability which results in the observed threefold symmetry. Further, the shape of the negative vector potential and the combined electric field are as illustrated in Fig. 6.2(a). As the two-color field ratio $R_{\mathrm{twocolor}} = E_{390\,\mathrm{nm}}/E_{780\,\mathrm{nm}}$ increases (from Fig. 6.2(a) to (i)), the absolute value of the negative vector potential at the phase corresponding to the maximum of the absolute value of the combined electric field first decreases, crosses zero (see Fig. 6.2(h)) and finally increases again. The zero crossing occurs at $R_{\mathrm{twocolor}} = 2$. At this ratio the rotational direction of the vector potential at the minimum of $|-A(t)|$ changes its sign. The sign change of the rotational direction of the combined two-color field at the maximum value of the absolute value of the combined electric field already occurs at $R_{\mathrm{twocolor}} = 0.5$ which is due to the appearance of loops in the Lissajous curves (see Fig. 6.2(b)). Those sign changes are not coincidence, but necessary because for $R_{\mathrm{twocolor}} = 0$ ($R_{\mathrm{twocolor}} \to \infty$) the laser electric field is a single-color field rotating clockwise (counter-clockwise) in the plane of polarization (plane defined as in Fig. 6.2). Moreover, a very prominent peak at zero momentum appears in Fig. 6.2(l)-(r). This is because most electrons escape at the maximum of $|E(t)|$ and the value $|-A(t)|$ is small (marked as green dots in Fig. 6.2(a-i)). $|-A(t)|$ is a good measure for the final electron momentum, not taking Coulomb interaction after tunneling into account. If the absolute value of the negative vector potential is large (Fig. 6.2(a) and (b)) the long-range atomic potential can be ignored. If the electron is slow the attractive atomic potential cannot be ignored and leads to a significant reduction of the electron's momentum (and can also result in recapture) resulting in the peak at zero momentum (see chapter 7.3 for details).

6.3. Non-Sequential Double Ionization - Experimental Protocol

In order to perform an experiment with precisely known conditions the following methodology was used. All electron momentum distributions in Fig. 6.2 were measured in a single measurement in which the neutral density filters were adjusted using the motorized translations stages and the configuration was modified every 30 minutes. After 4.5 hours one scan (consisting of nine configurations, see Tab. 6.1) was complete. After each scan both filters were set to maximal attenuation for 5 minutes before the next scan was started. The measurement was stopped after 25 hours. For this measurement the nm-delay stage was not moved. The data in Fig. 6.2 shows the data of the first four scans (see Fig. 6.3).

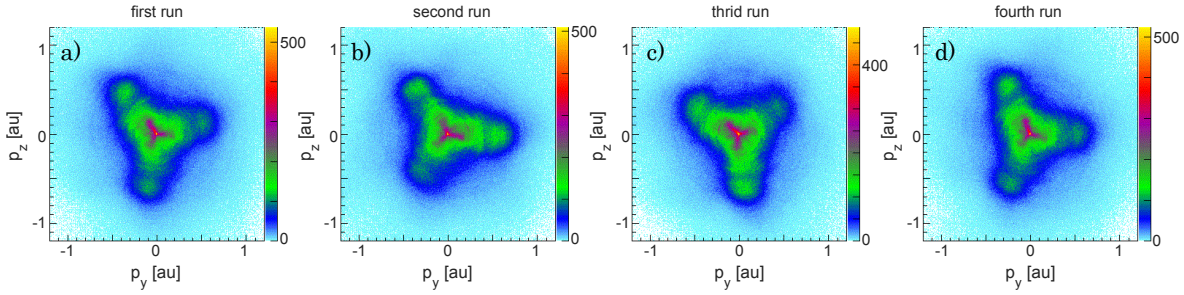


Figure 6.3: Electron momentum spectra generated by strong field ionization using a CRTC field with an average power of 18 ± 1 mW (54 ± 1 mW) at a wavelength of 780 nm (390 nm). The data in each panel was collected for 30 minutes. The counts are color coded. There is no condition on the ion and the experimental parameters are identical in all cases. (a) shows the data set that was measured first. (b) shows the second run which was performed 4.5 hours later. (c) and (d) were measured 9 hours and 13.5 hours later than (a). The rotation of the threefold electron momentum distribution is due to drifts of the relative phase. This indicates that those drifts are not relevant on a time scale of 30 minutes but cannot be ignored for timescales of several hours.

The drifts of the relative phase measuring one configuration for 30 minutes were ignored. Before the electron momentum spectra were added up to the result shown in Fig. 6.2 the relative phase for each configuration was adjusted manually to yield the most symmetric result.

Fig. 6.4 shows the position of the translation stage that is used to attenuate the laser pulse at 390 nm $x_{\mathrm{ND390}nm}$ as a function of the eventcounter. The positions $x_{\mathrm{ND390}nm}$ of the translation stage are as in Tab. 6.1 ($x_{\mathrm{ND780}nm}$ is the position of translation stage that is used to attenuate the laser pulse at 780 nm and is always adjusted accordingly).

To illustrate the high reproducibility of the filter positions, Fig. 6.5 shows the electron rate as a function of time for the first 12 hours. The data acquisition is paused during the movement of the stages which takes about 30 s. The low rate at about 17000 s and 33500 s corresponds to the dark count rate (at this time no strong field ionization occurs because both filters were set to maximum attenuation as a reference).

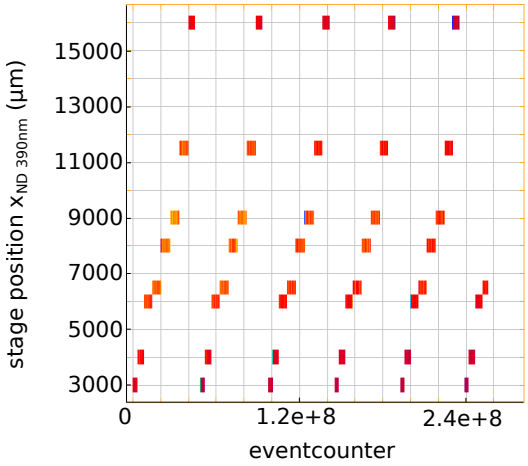


Figure 6.4: The position $x_{\mathrm{ND390}nm}$ of the translation stage that is used to attenuate the laser pulse at a central wavelength of 390 nm is plotted vs. the eventcounter (which is in a good approximation linear to the absolute measurement time). The stage position is adjusted every 30 minutes. The colored areas indicate counts and the white area indidicates no counts.

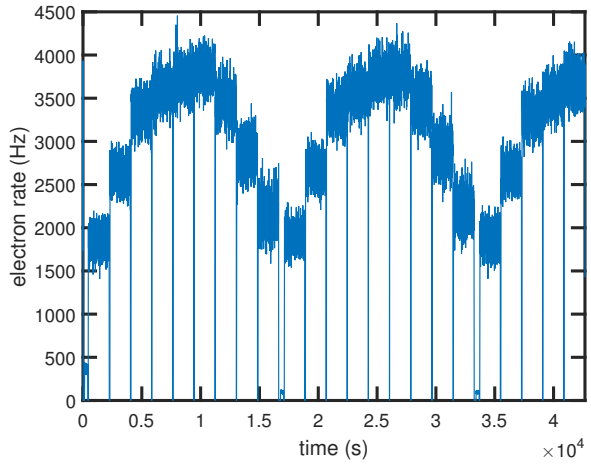


Figure 6.5: The electron rate is shown as a function of time. The vertical lines appear every 30 minutes because the data acquisition is paused during the movement of stages. The scan started with the highest two-color field ratio $R_{\mathrm{twocolor}} = E_{390\,\mathrm{nm}}/E_{780\,\mathrm{nm}}$ and proceeded in the order of Tab. 6.1 to lower values of R_{twocolor}.

It is important to point out that the electron rate increases exponentially with the intensity of the laser which means that the differences in electron rate, which differ by a factor of up to two, correspond to much smaller differences in intensity (see Tab. 6.2 for the calibrated intensities). This is a shortcoming of the performed experiment but at the end of chapter 6.4 it will be explained why this does not adversely affect the conclusions.

To be able to perform an automated scan changing the field ratio of the two-color field the neutral density filters have to be calibrated beforehand. This was done several days before the measurement for Fig. 6.6 by using a power meter[56] to determine the average power

[56]The used power meter is the "FieldMate" in combination with the air-cooled thermopile sensor "PM10" (both from Coherent Inc.).

in front of the vacuum chamber for the desired filter positions. The exact in situ intensity calibration was performed after the main experiment. During the measurement the sum of the average powers was held constant, which results in variation of the combined intensity. The measured average powers which were measured in front of the vacuum chamber are listed in Tab. 6.1.

Table 6.1: Data of the measurement that was used to calibrate the neutral density filters. $x_{\mathrm{ND780}nm}$ ($x_{\mathrm{ND390}nm}$) is the position of the translation stage that moves the neutral density filter that attenuate the laser pulse at 780 nm (390 nm). $P_{780\,nm}$ ($P_{390\,nm}$) is the average power that was measured with a power meter in front of the vacuum chamber for the single-color beam at a central wavelength of 780 nm (390 nm). The uncertainty of the power measurement using the optical power meter is about 1 mW, but is ignored for the calibration of the neutral density filters.

$x_{\mathrm{ND780}nm}$ (µm)	$x_{\mathrm{ND390}nm}$ (µm)	$P_{780\,nm}$ (mW)	$P_{390\,nm}$ (mW)
25000	5590	5.5 ± 1	57.5 ± 1
15800	6590	14.5 ± 1	49.5 ± 1
11300	7590	23.5 ± 1	44.5 ± 1
8800	8400	30.0 ± 1	33.0 ± 1
7900	9000	32.5 ± 1	30.5 ± 1
6700	10000	36.8 ± 1	26.2 ± 1
5900	11000	40.4 ± 1	22.8 ± 1
4100	14000	49.3 ± 1	14.2 ± 1
3100	18000	56.5 ± 1	7.4 ± 1

Just before the main experiment was conducted the average power was $P_{780\,nm} = 28.9\,\mathrm{mW}$ at $x_{\mathrm{ND780}nm} = 6700\,\mu\mathrm{m}$ and ($P_{390\,nm} = 31.5\,\mathrm{mW}$ at $x_{\mathrm{ND390}nm} = 10\,000\,\mu\mathrm{m}$). This is different to the measurement which was done several days before for the calibration of the filters. Since the alignment was not changed and the laser oscillator was not restarted, this difference is very likely due to an increase of the duration of the laser pulses. To best account for this the resulting scaling factors ($\frac{28.9\,\mathrm{mW}}{26.2\,\mathrm{mW}} = 1.1$ for 780 nm and $\frac{31.5\,\mathrm{mW}}{36.8\,\mathrm{mW}} = 0.86$ for 390 nm) were used to calculate the intensities of the single-color pulses that are shown in Tab. 6.2. The conversion of average power to in situ intensity was performed as described in chapter 4.1.5. The necessary intensity calibration-measurements were done directly after the measurement for Fig. 6.6 to minimize the relevance of drifts regarding the laser parameters. The resulting laser field parameters for the data shown in Fig. 6.2 are presented in Tab. 6.2. The measurement was conducted using the fully automated interferometric two-color setup. The conversion factor used to calculate the intensity from the average power is $0.044 \times 10^{14}\,\mathrm{W/cm^2}$ per mW for the fundamental laser pulse and $0.034 \times 10^{14}\,\mathrm{W/cm^2}$ per mW for the laser pulse at the second harmonic frequency.

The systematic uncertainties for the values shown in Tab. 6.2 which are due to the method of the intensity calibration are typically about 10% for the fundamental and 20% for the

Table 6.2: Overview of the single-color intensities I_{780nm} and I_{390nm} and the corresponding two-color ratios $R_{\mathrm{twocolor}} = E_{390\,\mathrm{nm}}/E_{780\,\mathrm{nm}} = \sqrt{I_{390\,\mathrm{nm}}/I_{780\,\mathrm{nm}}}$. The combined intensities are $I_{\mathrm{combined}} = \left(\sqrt{I_{780\,\mathrm{nm}}} + \sqrt{I_{390\,\mathrm{nm}}}\right)^2$ which are used for the data shown in Fig. 6.2. The uncertainty of the power measurement using the optical power meter is about 1 mW which corresponds to less than $0.05 \times 10^{14}\,\mathrm{W/cm^2}$ for the fundamental and the second harmonic. The indicated uncertainties ignores drifts of the laser system. The systematic uncertainties of the single-color intensities are discussed in chapter 4.1.5 and are typically about 10% for the fundamental and 20% for the second harmonic.

$I_{780\,\mathrm{nm}}(10^{14}\,\mathrm{W/cm^2})$	$I_{390\,\mathrm{nm}}(10^{14}\,\mathrm{W/cm^2})$	$E_{390\,\mathrm{nm}}/E_{780\,\mathrm{nm}}$	$I_{\mathrm{combined}}(10^{14}\,\mathrm{W/cm^2})$
0.2 ± 0.05	2.3 ± 0.05	3.5 ± 0.47	3.8 ± 0.23
0.5 ± 0.05	2.0 ± 0.05	2.0 ± 0.10	4.5 ± 0.17
0.8 ± 0.05	1.8 ± 0.05	1.5 ± 0.05	5.0 ± 0.15
1.0 ± 0.05	1.3 ± 0.05	1.1 ± 0.04	4.7 ± 0.14
1.1 ± 0.05	1.2 ± 0.05	1.1 ± 0.03	4.7 ± 0.14
1.3 ± 0.05	1.1 ± 0.05	0.9 ± 0.03	4.6 ± 0.14
1.4 ± 0.05	0.9 ± 0.05	0.8 ± 0.03	4.6 ± 0.14
1.7 ± 0.05	0.6 ± 0.05	0.6 ± 0.03	4.2 ± 0.16
1.9 ± 0.05	0.3 ± 0.05	0.4 ± 0.03	3.8 ± 0.19

second harmonic (see chapter 4.1.5 for details). It is important to notice that the relative intensities for the single-colors are known with the power meter's accuracy. However, this does not allow one to determine the exact value of the two-color field ratio $R_{\mathrm{twocolor}} = E_{390\,\mathrm{nm}}/E_{780\,\mathrm{nm}} = \sqrt{I_{390\,\mathrm{nm}}/I_{780\,\mathrm{nm}}}$ experimentally with high precision for two reasons. First, the laser systems output power is not perfectly stable during the measurement. Second, because the relative uncertainty for R_{twocolor} depends on the systematic uncertainties of the single-color intensities and is approximately 11% (see A.7).

The field geometries that are visualized in Fig. 6.2 are based on the results shown in Tab. 6.2. These results set the stage for the investigation of inelastic recollisions using counter-rotating two-color fields.

6.4. Controlling Inelastic Recollisions using Counter-Rotating Two-Color Fields

An electron that inelastically recollides with its parent ion can transfer energy to the ion. As discussed in chapter 6.1, the inelastic recollision can lead to ionization or excitation of the ion. The cross-section for these processes is dependent upon on the energy of the impinging electron (see Fig. 3 in Ref. [81]). Excitation is only possible if at least 17.14 eV are transferred (first relevant excited state of Ar^+ is at 17.14 eV [81]). Subsequent ionization of the excited singly charged argon ion Ar^{+*} is very likely because the remaining ionization potential is only about 10 eV (instead of $I_p^+ = 27.6\,\text{eV}$). This is lower than the ionization potential for the single ionization of argon $I_p^+ = 15.76\,\text{eV}$.

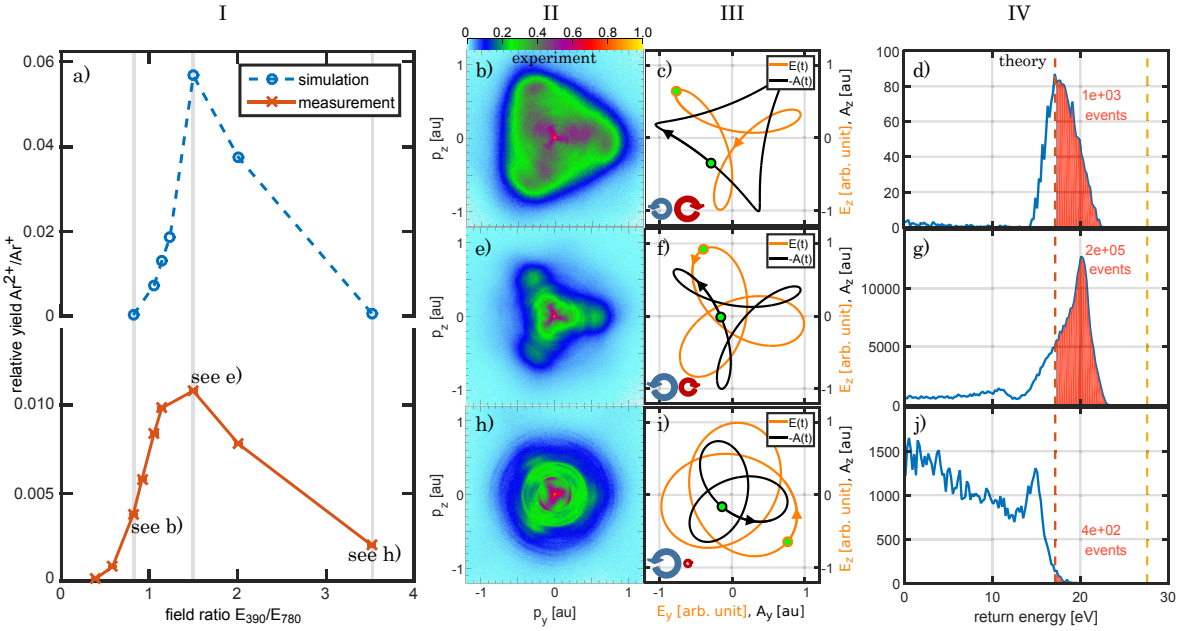


Figure 6.6: "The measured and simulated relative yield of double to single ionization is shown in column I. In column II measured electron momentum distributions are shown for the field ratios E_{390}/E_{780} of (b) 0.8:1, (e) 1.5:1 and (h) 3.5:1 and a maximum combined intensity of $5.0 \times 10^{14}\,\text{W/cm}^2$. In column III the corresponding combined electric fields $E_{y/z}$ (arb. units) as well as the vector potentials $A_{y/z}$ (atomic units) are depicted for the same ratios E_{390}/E_{780} (c) 0.8:1, (f) 1.5:1 and (i) 3.5:1. One maximum of the combined electric field is marked with a green dot. The helicities and the temporal development of the electric fields and the vector potentials are indicated with arrows. In IV the corresponding simulated energy distribution of the returning electrons is shown which has been calculated also for the ratios E_{390}/E_{780} (d) 0.8:1, (g) 1.5:1 and (j) 3.5:1 using CTMC. The energy needed for double ionization (27.6 eV) and the relevant excitation energy (17.14 eV) are marked with a dashed orange and a red line, respectively. The number of recollision events is normalized to 10^6 single ionization events in IV. All events exceeding 17.14 eV are integrated which is visualized as the red shaded area. This integral corresponds to the number of returning electrons having enough energy to excite Ar^+ and strongly depends on the field ratio E_{390}/E_{780}." (Figure and caption are taken from Eckart et al. [23].)

The red data points in Fig. 6.6(a) show the measured relative yield of doubly to singly charged ions Ar^{2+}/Ar^{+} as a function of the two-color ratio $R_{\mathrm{twocolor}} = E_{390\,\mathrm{nm}}/E_{780\,\mathrm{nm}}$ for the experimental conditions presented in Fig. 6.2. For two-color fields that are dominated by a single color (low and high values of $E_{390\,\mathrm{nm}}/E_{780\,\mathrm{nm}}$) almost no double ionization is observed. This indicates that there are almost no recolliding electrons with sufficient energy ($\geq 17.14\,\mathrm{eV}$). At the same time it is shown that the peak electric fields that were used are too low to sequentially double ionize argon. Changing the two-color field ratio, but keeping the peak electric field approximately constant will not change the probability for sequential double ionization. Considering only the peak electric field, also the tunneling distance and the tunneling probability remain unchanged. The only part that changes is the trajectory of the liberated electron. This trajectory can be very different in a two-color field compared to the single-color scenario. Any increase of the relative yield of doubly to singly charged ions Ar^{2+}/Ar^{+} will reveal that the electron reencounters its parent ions on its trajectory and possesses more than $17.14\,\mathrm{eV}$ at that time. In Fig. 6.6(a) it is evident that the maximum relative yield of doubly to singly charged ions Ar^{2+}/Ar^{+} is reached for $R_{\mathrm{twocolor}} = E_{390\,\mathrm{nm}}/E_{780\,\mathrm{nm}} = 1.5$. However, it should be noted that the absolute value of the obtained relative yield is difficult to determine (see chapter A.5.1 for details). Fig. 6.6(b),(c),(e),(f),(h),(i) are similar to Fig. 6.2(l),(c),(p),(g),(r),(i) but in Fig. 6.6(c),(f),(i) the relative phase (rotation of the Lissajous curves) of the two-color field has been matched with the experimental data as far as possible. The rotation angle in Fig. 6.6 (i) is determined by comparing the electron momentum distribution with the numerical result[57] from solving the time-dependent Schrödinger-equation (TDSE). Unfortunately, for the field ratio of $E_{390}/E_{780} = 0.8$ in Fig. 12 of [101] there is no corresponding panel, but upon request Xiao-Min Tong provided the corresponding data in numerical form. This allowed us to perform the necessary comparison and determine the rotation angle in Fig. 6.6(c) as well. We were not able to find a corresponding TDSE data set for the field ratio of $E_{390}/E_{780} = 1.5$. Therefore, a CTMC calculations was performed[58] and we used the electrons with an absolute momentum of about 0.6 a.u. to determine the rotation angle of the combined laser electric field. An alternative approach to determine the rotation angle for two-color fields with two-color ratios close to $E_{390}/E_{780} = 1.5$ makes use of the low energy structure (see chapter 7.3).

To verify our model that is used to explain the experimental observation we used a classical trajectory Monte Carlo (CTMC) simulation. To this end we calculated classical trajectories

[57] The result of solving the TDSE is shown in Fig. 12(c) of [101].
[58] The CTMC calculation was carried out by Martin Richter (see [36] for details).

that are governed by the force of the Coulomb potential ($V = -1/r$, where r is the distance of the electron to the ion) and the instantaneous combined laser electric field. At the exit of the tunnel, a two-dimensional Gaussian initial momentum distribution perpendicular to the tunneling direction and zero initial momentum in the tunneling direction is used to start a trajectory which is calculated in the presence of the Coulombic potential and the combined laser electric field. The probability for a given trajectory to occur is proportional to the tunneling rate. Details regarding the classical trajector Monte Carlo simulation are found in Ref. [36]. For each two-color field scenario from Tab. 6.2 in total 10^6 trajectories were calculated. All trajectories on which the electron comes closer than 5 a.u. are defined as recollision trajectories and the kinetic energy of the recollding electron at the closest approach to its parent ions is considered as the recollision energy. This procedure leads to the distributions shown in Fig. 6.6(d), (g) and (j). It is found that out of 10^6 single ionized electrons $2 \cdot 10^5$ electrons have enough energy to potentially excite Ar^+ for the two-color ratio of $E_{390}/E_{780} = 1.5$. For the ratios of $E_{390}/E_{780} = 0.8$ $(E_{390}/E_{780} = 3.5)$ siginificantly less electrons fulfill this criterion. In a last step for each two-color field ratio the histogram showing the return energy (Fig. 6.6(d), (g) and (j)) is weighted with the cross-section for electron impact excitation [81] and finally integrated. As a result, an estimate for non-sequential double-ionization by electron impact excitation is obtained for each experimentally used field geometry. The result is shown in Fig. 6.6(a) and shows qualitative agreement with the experiment.

Finally, the presented results confirm the prediction by Chaloupka and Hickstein (see Fig. 2 in Ref. [76]) and agree with the experimental findings of Mancuso et al. [75, 76].

6.4.1. Intensity Dependence of Non-Sequential Double Ionization

Having investigated the influence of the two-color ratio on the recollision dynamics; in a next step the intensity dependence of the recollisions dynamics in a two-color field will be examined. The dependence is similar to the well-known "knee"-like structure that appears for linearly polarized light (see chapter 6.1). For this measurement campaign the two-color field ratio was held constant at $R_{\mathrm{twocolor}} = 1.23$ and the intensity was slowly increased. The driving pressure of the gas inlet had been adjusted accordingly (1.4 bar to approximately 0.01 bar) to make sure that the event rate on the MCP of the electron side was always below 3000 Hz. Afterwards, the same was done for linearly polarized light. For this measurement the gas jet was not collimated in order to achieve a higher count rate which was important for low intensities[59]. The result is shown in Fig. 6.7. The error bars show the standard deviation of the statistical errors.

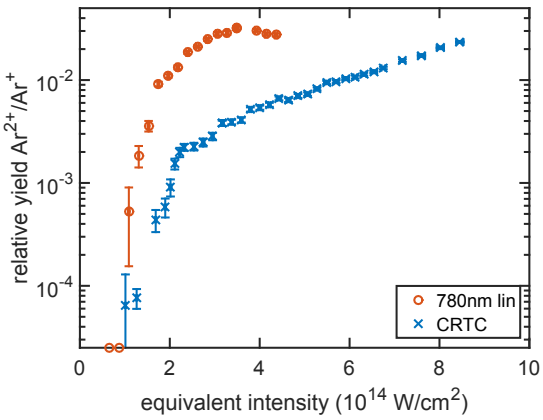


Figure 6.7: "Relative yield of double ionization is shown as a function of intensity in the focus for linear polarization at 780 nm and for a CRTC field with $E_{390}/E_{780} = 1.23$ which is close to the maximum in Fig. 6.6 (a) [remark - the number of the referenced figure has been adapted]. For the CRTC field a similar 'knee'-like shape is observed as it is commonly known for linear polarization. The two first points for linear polarization on the ordinate indicate that no double ionization events were measured within a reasonable amount of time." (Figure and caption are taken from Eckart et al. [23].)

The shape of the curve for linearly polarized light and the relative yield $\mathrm{Ar}^{2+}/\mathrm{Ar}^{1+}$ are consistent with the results of Walker et al. [79]. However, the decrease of the relative yield $\mathrm{Ar}^{2+}/\mathrm{Ar}^{1+}$ for very high intensities in Fig. 6.7 was not expected and could be explained by the position dependent detection efficiency of the MCP stack, because higher intensities lead to a larger focal volume and a larger spot on the MCP (see Fig. A.27(b)). For the settings with high laser intensity of this measurement campaign the decrease in the driving pressure

[59] Because the focal volume was changed by not collimating the jet for the measurements regarding Fig. 6.7 the focal intensity was calibrated separately for these jet setting. The conversion factor used to calculate the intensity from the average power is $0.047 \times 10^{14}\,\mathrm{W/cm^2}$ per mW for the fundamental laser pulse and $0.029 \times 10^{14}\,\mathrm{W/cm^2}$ per mW for the laser pulse at the second harmonic frequency.

of our supersonic expansion led to a slightly different velocity of the jet and thus to shifts of the spot on the ion MCP-stack in y-direction (jet-direction). This shift had to be taken into account as the gates for the doubly charged ion gates were adjusted. The time to take a data point in Fig. 6.7 varied from 2 minutes for the highest intensity of the single-color data set to 20 hours for the lowest intensity of the single-color data set[60].

Finally, Fig. 6.7 allows for the investigation of the problem that the combined intensity was not constant during the measurement in which the two-color field ratio was varied. As presented in Tab. 6.2 the combined intensities vary from $3.8 \times 10^{14}\,\mathrm{W/cm^2}$ to $5.0 \times 10^{14}\,\mathrm{W/cm^2}$. The relative yield $\mathrm{Ar}^{2+}/\mathrm{Ar}^{1+}$ is 0.7 % (0.5 %) for $5.1 \times 10^{14}\,\mathrm{W/cm^2}$ ($3.8 \times 10^{14}\,\mathrm{W/cm^2}$). Hence, the variations that are due to the varied intensity in Fig. 6.6 are expected to be on the order of $\frac{0.7-0.5}{0.7} = 29\%$. The observed differences in Fig. 6.6 are significantly larger showing that the conclusions that are drawn in chapter 6.2 are not affected by the problem that the combined intensity is not constant.

[60] Not a single Ar^{2+} ion was detected within 20 hours for the lowest intensity of the single-color data. This illustrates that the Ar^{2+} rate can be measured free of any background.

6.5. Electron Momentum Distributions for Non-Sequential Double Ionization of Argon

The coincidence detection of electrons and argon ions allows for the investigation of the electron momentum distribution for single ionization, double ionization and without any conditions on the ion.

For the measurement in chapter 6.5 the gas jet was collimated to $40 \pm 10\,\mu m$ (the same configuration as for Fig. 6.6)[61]. The relative phase of the two single-color laser pulses was adjusted by moving the delay stage in 108 steps over a distance of 600 nm. At each position, data was taken for 3 minutes. After the end of one scan the scan started over from the beginning.[62]

Fig. 6.8(a) shows the combined electric field[63]. Fig. 6.8(b)- (d) show the electron momentum distribution for different condition on the ion for the conicidence detection.

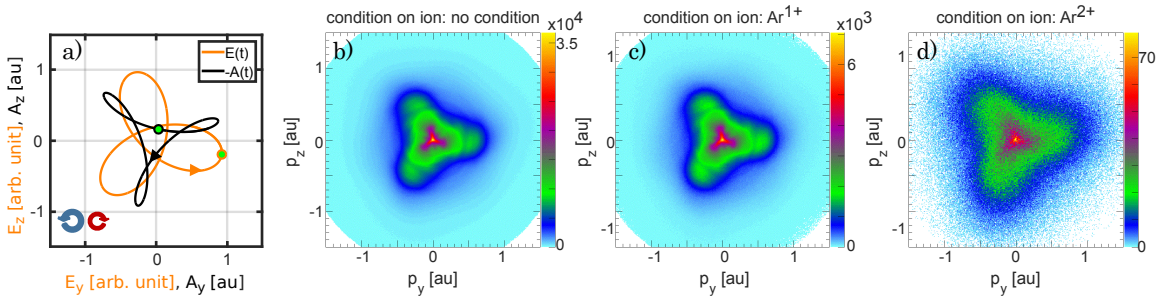


Figure 6.8: Based on the same data set as Fig. 6.11. (a) shows the combined electric field. (b) shows the electron momentum distribution without condition on the ion. (c) [(d)] shows the electron momentum distribution that was measured in coincidence with singly [doubly] charged argon ions.

[61] For this measurement the same calibration measurement as for the measurement regarding Fig. 6.6 was used because the focal volume was assumed to be identical since the jet was collimated in the same way. The conversion factor used to calculate the intensity from the average power is again $0.044 \times 10^{14}\,W/cm^2$ per mW for the fundamental laser pulse and $0.034 \times 10^{14}\,W/cm^2$ per mW for the laser pulse at the second harmonic frequency. Changes of the laser pulse duration are ignored but lead to potential systematic errors regarding the intensity calibration for the measurement Fig. 6.11 is based on.

[62] Changes of the relative phase of the two single-color laser pulses due to thermal effects in the interferometric setup lead to rotations of the combined electric field in the plane of polarization. The resulting electron momentum distribution also rotates. However, the thermal drifts are unpredictable and detection inefficiencies lead to unwanted artifacts in the final electron momentum distribution after correction of the thermal phase drifts. Moving the delay stage actively allows one to control the rotation of the electron momentum distribution which minimized artifacts that are due to detector inefficiencies.

[63] The relative phase of the two single-color laser pulses was found by comparisons with the CTMC calculations (see discussion of Fig. 6.6).

6.5.1. Non-Sequential Double Ionization: The First Electron

What can be learned from the electron momentum distributions shown in Fig. 6.8? One observation is the rotation of the low energy structure (momenta smaller than 0.3 au). This is most likely because the Coulombic attraction is much stronger if a doubly charged argon ion is left behind than in the case of single ionization (see also dashed white line in Fig. 6.11). However, if one now steps back and looks at the overall situation there is an interesting opportunity. The directly measured electron momentum distribution for non-sequential double ionization of argon $Y_{\text{deteced elec Ar}^{2+}}$ does not distinguish between the first and the second electron:

$$Y_{\text{deteced elec Ar}^{2+}} = 0.5 \cdot \left(Y_{\text{1st elec Ar}^{2+}} + Y_{\text{2nd elec Ar}^{2+}}\right) \tag{20}$$

where $Y_{\text{1st elec Ar}^{2+}}$ ($Y_{\text{1st elec Ar}^{2+}}$) is electron momentum distribution for the first (second) electron in the case of non-sequential double ionization of argon.

The electron momentum distribution that was measured in coincidence with Ar^{2+} is the sum of two distributions that are multiplied with the factor 0.5 because from two electrons only one is detected for each event. It is unknown whether the first or the second electron is detected. This is because the temporal resolution of the detector is about 1 ns and the differences in the release times of the electrons is on the femtosecond timescale. Also in final momentum space there cannot be any preference of one electron over the other (in contrast to the experiment shown in chapter 9) since the relative phase of the two single-color laser pulses is varied during the measurement.

It can be assumed that the electron momentum distribution of the second electron in non-sequential double ionization $Y_{\text{2nd elec Ar}^{2+}}$ has the same shape as the electron from single ionization $Y_{\text{1st elec Ar}^{1+}}$ because in both cases the electron is liberated by the laser electric field[64]. After normalizing these two distributions to the same integral this leads to:

$$Y^{\text{norm}}_{\text{1st elec Ar}^{1+}} \approx Y^{\text{norm}}_{\text{2nd elec Ar}^{2+}} \tag{21}$$

This assumption allows for the calculation of the normalized electron momentum distribution of the first electron in the case of non-sequential double ionization of argon by

$$Y^{\text{norm}}_{\text{1st elec Ar}^{2+}} \approx 2 \cdot Y^{\text{norm}}_{\text{detected elec Ar}^{2+}} - Y^{\text{norm}}_{\text{detected elec Ar}^{1+}} \tag{22}$$

[64] The differences that are ignored are the charge of the ion, the binding energy of the electron prior to ionization, non-adiabatic effects and multi-electron effects.

where $Y^{\text{norm}}_{\text{detected elec Ar}^{2+}}$ ($Y^{\text{norm}}_{\text{detected elec Ar}^{1+}}$) is the detected electron momentum distribution for double (single) ionization of argon which has been normalized such that the integral is one. This assumes[65] that double ionization can only occur non-sequentially via RESI for the given laser electric fields (see chapter 6.4). The results of this approach are shown in Fig. 6.9.[66] The electron momentum distributions for single and double ionization are shown in Fig. 6.9(a) and (b). The inferred electron momentum distribution of the first electron is shown in Fig. 6.9(c) and 6.9(d). It can be seen that the first electron has a triangular shape and has the same shape as the vector potential. This underlines the interpretation that the final momentum of the scattered, first electron is determined by the vector potential at the time of the recollision. Further, this finding indicates that recollisions occur at all times and are not restricted to single times within an optical cycle.

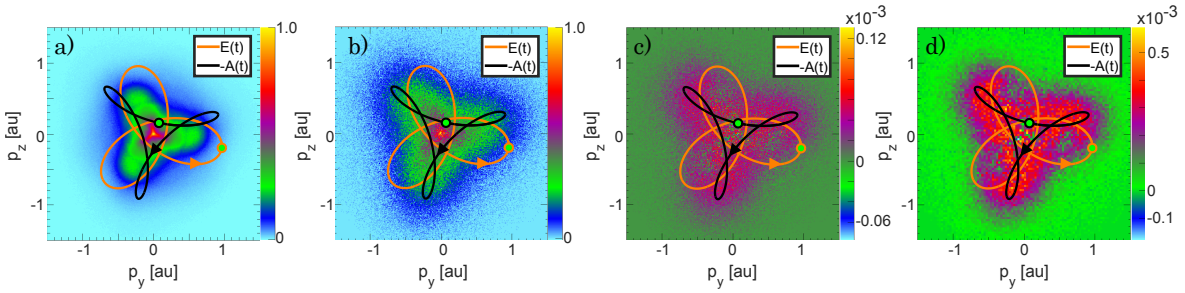


Figure 6.9: (a) [(b)] show the normalized electron momentum distribution $Y^{\text{norm}}_{\text{detected elec Ar}^{1+}}$ [$Y^{\text{norm}}_{\text{detected elec Ar}^{2+}}$] for single [double] ionization. The data shown in (a) [(b)] is based on the same data as Fig. 6.8(c) [Fig. 6.8(d)] but here the data has been corrected for false electron-ion coincidences and normalized to the maximum of one afterwards. (c) shows the calculated electron momentum distribution of the first electron assuming that it can be calculated using $Y^{\text{norm}}_{\text{1st elec Ar}^{2+}} \approx 2 \cdot Y^{\text{norm}}_{\text{detected elec Ar}^{2+}} - Y^{\text{norm}}_{\text{detected elec Ar}^{1+}}$. (d) shows the same as (c) using coarse binning. The vector potential and the combined electric field are shown as in Fig. 6.8 to guide the eye.

Fig. 6.10 is based on the same data as Fig. 6.9 but uses cylindrical coordinates. p_x is the momentum in the light propagation direction and $p_r = \sqrt{p_y^2 + p_z^2}$ is the radial momentum in the polarization plane. The electron momentum distribution of the inferred first electron in Fig. 6.9(c) and 6.9(d) is very different to the distribution shown in Fig. 6.9(a) that shows the electron for the single ionization of argon and is assumed to be equivalent to the second electron from non-sequential double ionization. The first electron appears like a sum of spheres that have their origins at the negative vector potential. The radius of the sphere in momentum space is about 0.3 a.u. which corresponds to an energy of about 1.2 eV that could be interpreted as the energy the rescattering electron keeps after the inelastic rescattering process.

[65] This assumption can be justified because the expected recollision energies are significantly below the second ionization threshold (see Fig. 6.6(d), (g) and (j)).

[66] The data shown in Fig. 6.9 is corrected for false electron-ion coincidences (see chapter A.5.2).

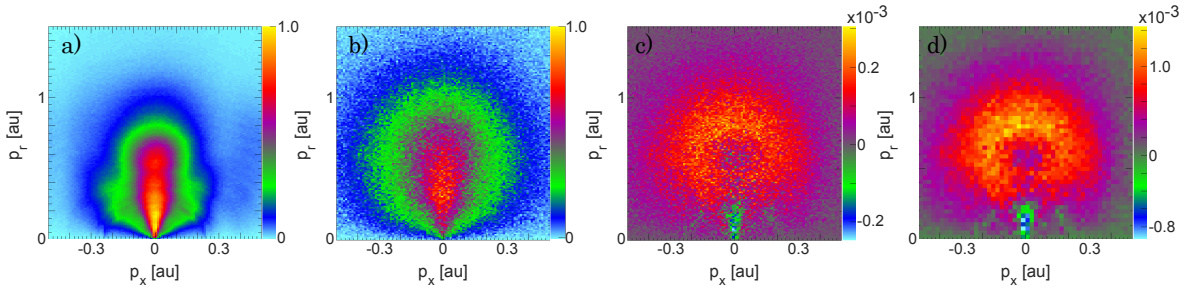


Figure 6.10: (a), (b) are based on the same data as Fig. 6.9 but a different perspective is chosen. p_x is aligned along the light propagation direction and $p_r = \sqrt{p_y^2 + p_z^2}$ is the radial momentum in the polarization plane. (a), (b) show the normalized electron momentum distribution for single (a) and double (b) ionization. (c) shows the calculated electron momentum distribution of the first electron assuming that it can be calculated using $Y^{\text{norm}}_{\text{1st elec Ar}^{2+}} \approx 2 \cdot Y^{\text{norm}}_{\text{detected elec Ar}^{2+}} - Y^{\text{norm}}_{\text{detected elec Ar}^{1+}}$. (d) shows the same as (c) using coarse binning.

6.5.2. Tomographic Reconstruction of the Second Electron

So far it has been shown that double ionization in CRTC field can be non-sequential and the second electron escapes from an intermediate excited state of Ar^+. Since the recolliding (first) electron enables the emission of the second electron the correlation of the two emitted electron is an interesting aspect (see chapter 6.1). There are two prerequisites to study the correlation of the first and the second electron in non-sequential double ionization using CRTC fields. One needs information about the momenta of both electrons and ideally it is known which of the two electrons was liberated first.

In general, direct detection of two electrons suffers two shortcomings. First, the detection efficiency is low[67]. Second, it is difficult to prove that the electronic signal belonging to the second detected electron is not affected by the first detected electron. Nevertheless, the direct detection of two electrons can be accomplished (see. e.g. Ref. [103]).

However, our spectrometer geometry combined with the (high) mass of argon leads to a loss of momentum resolution for two momentum components. Only the momentum component along the time-of-flight direction of the argon ions can be resolved with sufficient resolution[68].

Detection of one electron in coincidence with a double charged argon ion provides the three-dimensional momentum of this electron $\vec{p}^{\text{electron}}$ and the time-of-flight component of the ion (p_z^{ion}). Because the momentum of the impinging photons can be neglected momentum conservation allows for the calculation of the momentum component of the undetected

[67] The detection efficiency is energy-dependent and typically about 0.65 to 0.82 [102].

[68] For the spectrometer settings which are used in this experiment the resolution for doubly charged argon is 0.2 a.u. in time-of-flight direction and 7 a.u. perpendicular to that direction. In the jet-direction the sum of the momenta of ion and electron is not a sharp peak but broad due to finite momentum distribution of the jet in that direction.

electron in the time-of-flight direction

$$p_z^{\text{calc}} = -p_z^{\text{electron}} - p_z^{\text{ion}}. \tag{23}$$

Luckily, the z-direction lies in the plane of polarization and the 9 dimensional momentum distribution (3 particles with 3 momentum components) rotates in the plane of polarization as the relative phase of the two single-color laser pulses φ is varied. Thus, a tomographic reconstruction[69] allows for the reconstruction of information about the missing electron momentum component in the plane of polarization.

At this point it is important to distinguish between momentum information for single events (single laser shots) and knowledge about electron momentum distributions which are integrated over several laser shots. Ideally, for each and every event, 9 momentum components for 3 particles would be known. Above, it has been shown that for each laser shot we know $\vec{p}^{\text{electron}}$, p_z^{calc} and φ.

Restricting the considered events to any subset in the phase corrected momentum space of the detected electron $p^{\text{electron_phase_corrected}}$ leads to a distribution $T(p_z^{\text{calc}},\varphi)$ which is called "sinogram". The distribution $T(p_z^{\text{calc}},\varphi)$ shows projections of the undetected electron in momentum space from different angles in the plane of polarization. Since for the reconstruction of the momentum distribution of the undetected electron several laser shots are needed it is obvious that the information about single events is lost during the tomographic reconstruction.

In the appendix A.5.3 single ionization is used to benchmark the method of tomographic reconstruction by comparing the directly measured electron momentum distribution with the tomographically reconstructed electron momentum distribution.

Electron-Electron Correlation

In a next step a tomographic reconstruction is applied to the experimental data.[70] The idea is to impose a condition in final phase corrected momentum space on the measured electron and tomographically reconstruct the corresponding undetected electron. To this end we need to identify a region in momentum space that is dominated by either the first (rescattered) electron or the second electron that escapes from an excited state of Ar^+. Fig. 6.11(a) and

[69] The tomographic reconstruction has been inspired by Mancuso et al. who have used the tomographic reconstruction for the generation of three-dimensional momentum spectra for single ionization upon ionization by circularly polarized two-color fields using data from a velocity map imaging spectrometer (VMI) [100].

[70] See also Fig. A.33 which illustrates the basic idea using single ionization.

6.11(b) show the electron momentum distributions for single and double ionization (same as in Fig. 6.9). Calculating the normalized differences of those two distributions leads to the distribution shown in Fig. 6.11(c).

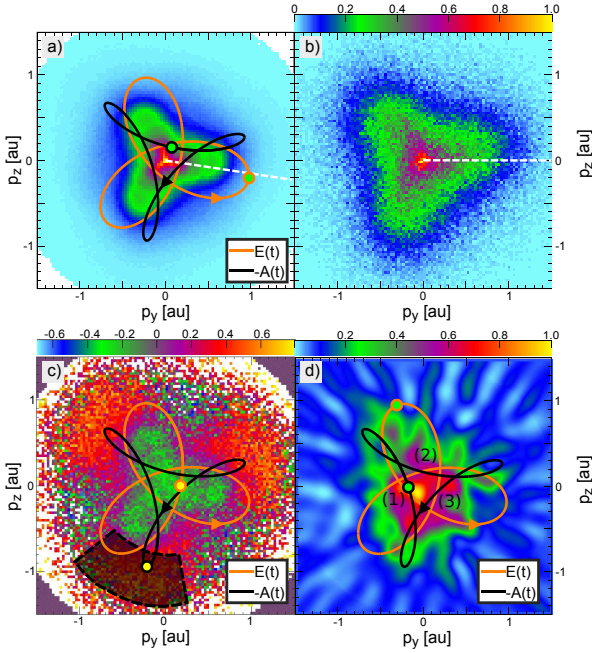


Figure 6.11: "Measured electron momentum distributions for single (a) and double (b) ionization for a ratio of $E_{390}/E_{780} = 1.42$ and a combined intensity of $4.5 \times 10^{14}\,\mathrm{W/cm^2}$. The corresponding vector potential is shown in black and the phase that belongs to the maximum combined field is indicated by a green dot. The dashed white line serves as guide to the eye regarding the rotation of the low energy structure (purple structure at momenta smaller than 0.3 au). (c) shows the normalized difference $\frac{A-B}{A+B}$ where A (B) is the number of counts in the corresponding bins normalized to the sum of all counts for double (single) ionization. In (d) the tomographically reconstructed electron momentum distribution is shown for the condition that the first electron has been detected in the shaded area in (c). Electrons in this area have recollisonally excited the ion at the time of the pulse which is indicated by the yellow dot in c). d) shows the momenta of the corresponding excited electron set free later in the pulse. The labels 1, 2, 3 the first (1) second (2) or third (3) maximum of the field following the recollision and correspond to time delays of 433, 1300, 2167 attoseconds after recollision." (Figure and caption are taken from Eckart et al. [23].)

It can clearly be seen that for higher radial momenta there is a yellow reddish area that is dominated by electrons from double ionization. Restricting all measured events to a subset where the detected electron is in the shaded region[71] and performing a tomographic reconstruction, the distribution shown in Fig. 6.11(d) is obtained[72].

This is a spectacular result because it underlines the non-sequential nature of the observed double ionization mechanism. If the first electron is ionized at the time indicated as a green

[71] The advantage to applying the condition to the first (rescattered) electron is that this elegantly excludes sequential double ionization. Both electrons in sequential double ionization are expected to have a similar electron momentum distribution that is similar to the distribution of the second electron in non-sequential double ionization.

[72] The parameters for the tomographic reconstruction are as for Fig. A.33. A low-pass filter (parameter 0.09) is used and the projection data is deconvolved using the distribution shown in Fig. A.29. This assumes that the doubly charged ion is affected in the same way as the singly charged ion by the oscillating mirror. This is not exact but the best approximation available.

dot in Fig. 6.11(a) the recollsion can occur approximately 1.3 fs later (which is a possible scenario according to the CTMC simulation). At the recollision time, the electron can transfer part of its kinetic energy to the ion and is subsequently driven by the laser's electric field. Thus, the final momentum of the rescattered electron is expected to be close to the vector potential at the recollision time which is indicated by a yellow dot in Fig. 6.11(c) and points directly to the yellow reddish area. After the recollision an excited state in Ar^+ can be easily ionized in the next maximum of the laser electric field which is indicated by a green dot in Fig. 6.11(d). The tomographically reconstructed electron momentum distribution shows a maximum very close to the vector potential that corresponds to this time which is only 433 as after the recollision time and 1733 as after the first electron has been liberated. Further details about the tomographic reconstruction are found in the appendix A.5.4.

6.6. Three-Dimensionality of the Measured Momentum Distribution

During the discussion of the electron momentum distribution of the first electron it was already clear that the measured data is three-dimensional and that there are interesting opportunities to investigate the full three-dimensional electron momentum distribution. In order to provide a short preview of the next chapter, that will deal with three-dimensional electron momentum distributions, here, several slices of the three-dimensional electron momentum distributions for the single ionization of argon are presented. The slices are shown in Fig. 6.12. For small values of the momentum in the light propagation direction p_x a very localized distribution at zero momentum is found. In chapter 7.3 it will be shown that this is due to Coulomb interaction after the end of the laser pulse. The blobs at a radial momentum of 0.5-0.6 a.u. look very similar to the elastically scattered electron described in [101]. The sharp structures in (b)-(d) might be related to ATI rings or sub-cycle interference which are discussed in detail in chapter 7.5.

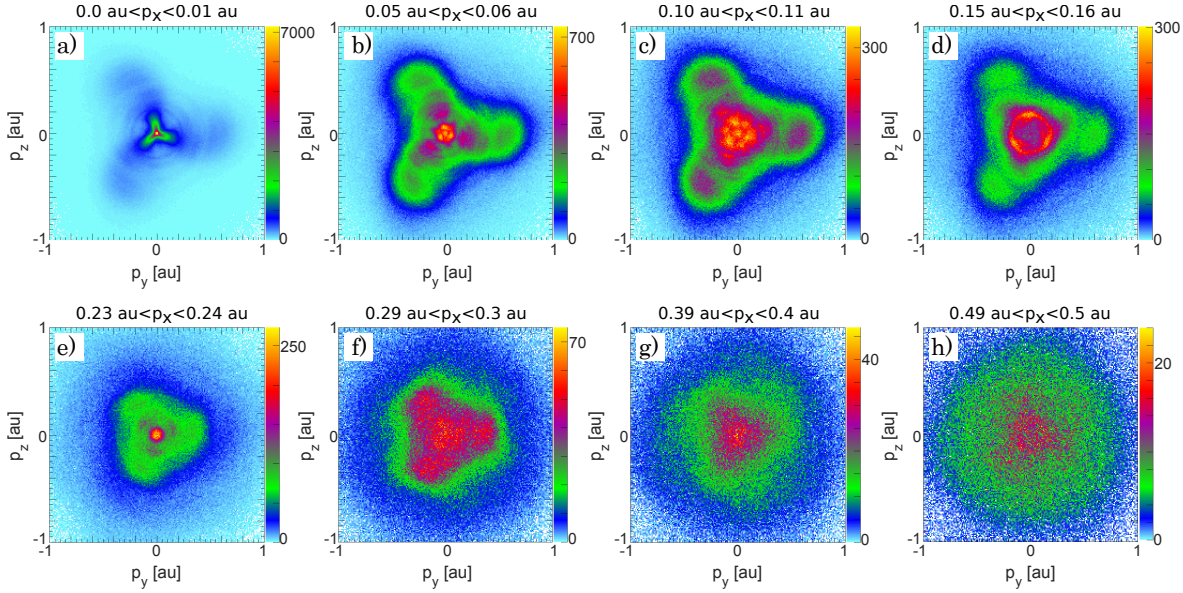


Figure 6.12: Two-dimensional slices of the three-dimensional electron momentum distribution without any condition on the ion. The slices show subsets of Fig. 6.8(b) and illustrate that the electron momentum distribution shows a rich structure in three dimensions. (a) exhibits strong Coulomb focusing leading to the concentration of intensity at zero kinetic energy. (b)-(d) show very sharp structures.

In conclusion, non-sequential double ionization can be understood by treating the electron as a point-like particle. In the following chapter it will be shown that a liberated electron is more than a point-like particle and its quantum nature gives rise to (unexpected) structures, that are due to interference in the final three-dimensional momentum space.

7. Three-Dimensional Electron Momentum Distributions

Chapter 7 is based on the peer-reviewed publication by Eckart et al. [24], focuses on the experimental results leading to the publication[73] and presents additional experimental results. After a very careful examination of the measured electron momentum distribution upon strong field single ionization of helium by a CRTC (counter-rotating two-color) field a surprising result was obtained: an unexpected intensity modulation along the light propagation direction (p_x) in momentum space. However, the modulation was only present in a small region in the plane of polarization ($p_y p_z$-plane). This intensity modulation is a two-path interference and is a result of two different "birth-times" of the electron within a single cycle of the driving electric field. Therefore, the observed interference is a sub-cycle interference.

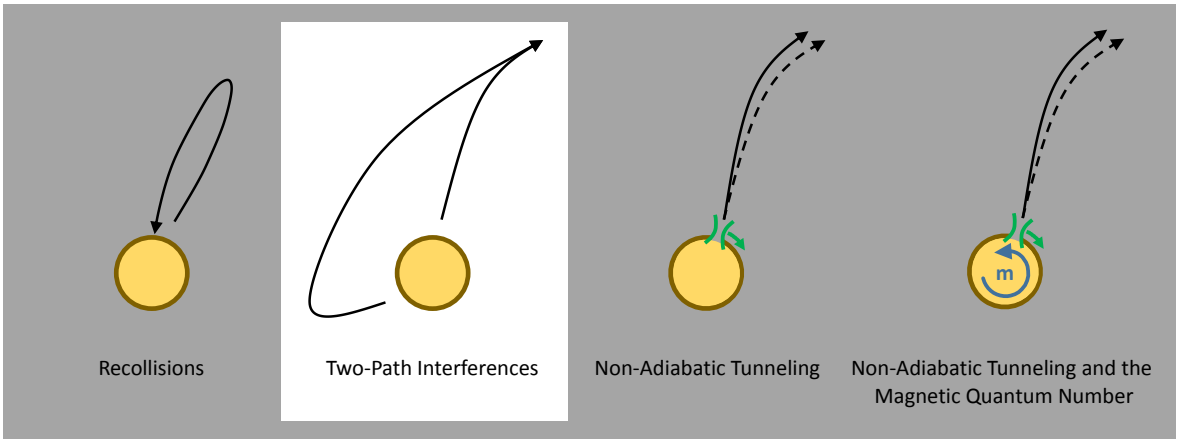


Figure 7.1: Illustration of the key scientific questions of this thesis. Chapter 7 focuses on interference in two-color laser fields.

Basic question for this project: Is it possible for an electron in a CRTC field to be liberated at two different times such that two-path interference appears? Or in other words: can an electron that has been liberated by a single cycle strong CRTC field interfere with itself?
Experimental procedure: The three-dimensional electron momentum distributions upon the ionization of helium by a CRTC field were measured.
Methodological beauty: A semi-classical two-step (SCTS) simulation reproduces the experimentally observed interference and allows one to trace the trajectories of all electrons that contribute to the interference pattern.

[73] The results that were finally published, ended up being very different from the initial experimental idea for this project. Originally, the experimental idea was to measure the (three-dimensional) final momentum distribution upon strong field ionization of helium and neon. The goal was to find differences in the final momentum distribution comparing the two different targets. The expectations were based on the fact that the liberated electron in helium stems from an s-orbital, whereas the liberated electron in neon stems from a p-orbital. In all cases CRTC fields with a threefold symmetry were used. The results are not spectacular, since they show almost no difference comparing the data of helium and neon. The unpublished results using neon as gas target are discussed in chapter 7.7.

7.1. State of the Art: Sub-Cycle Interferences

Three-dimensional electron momentum distributions upon strong field ionization are routinely measured using COLTRIMS reaction microscopes or velocity map imaging. A very prominent feature of the electron momentum distributions obtained, are spheres of equal kinetic energy. This discretization in energy is called above-threshold ionization (ATI) [33, 34]. The energy spacing corresponds to the photon energy and can be interpreted as additionally absorbed photons. Alternatively, ATI can be viewed as an interference pattern that emerges due to the oscillation of the ionizing electric field which acts as a grating in time for a multi-cycle laser pulse and leads to a spacing in time of the electrons' "birth-times" that is defined by the oscillation period of the photon (see also chapter 5.3).

In contrast to this inter-cycle interference, there is sub-cycle interference[74] which occurs if the "birth-times" contributing to the interference are separated in time by less than an optical cycle [104, 105]. However, sub-cycle interference does not appear under all conditions. For circularly polarized light sub-cycle interference cannot be observed, because for every angle in final momentum space in the plane of polarization there is only one "birth-time" within a single-cycle laser field. Two-color fields have been suggested as promising candidates to investigate sub-cycle interference which might provide insight related to the atomic or molecular potential, ultrafast electron dynamics and electron-electron correlations [106–110]. In previous experiments sub-cycle interference was studied using orthogonal polarized two-color fields, because for those waveforms there are two "birth-times" within a single cycle that have the same vector potential [111–113]. In those experiments the visibility of sub-cycle interferences depended on the relative phases of the two colors of the driving field. Using sub-cycle interference, it was shown by Xie et al. [114] that sub-cycle interference can be used to retrieve information about the valence-electron cloud in atoms. Han et. al showed experimentally using sub-cycle interference that the phase of the electronic wave packet changes under the tunnel barrier [115].

[74] "Sub-cycle interference" is also known as "intra-cycle interference".

7.2. Single Ionization of Helium in Counter-Rotating Two-Color Fields

The experiment was performed using a mixed gas jet containing helium and neon atoms. Data was recorded for two different CRTC fields having different two-color field ratios and different peak electric fields. The result for helium is shown in Fig. 7.2.

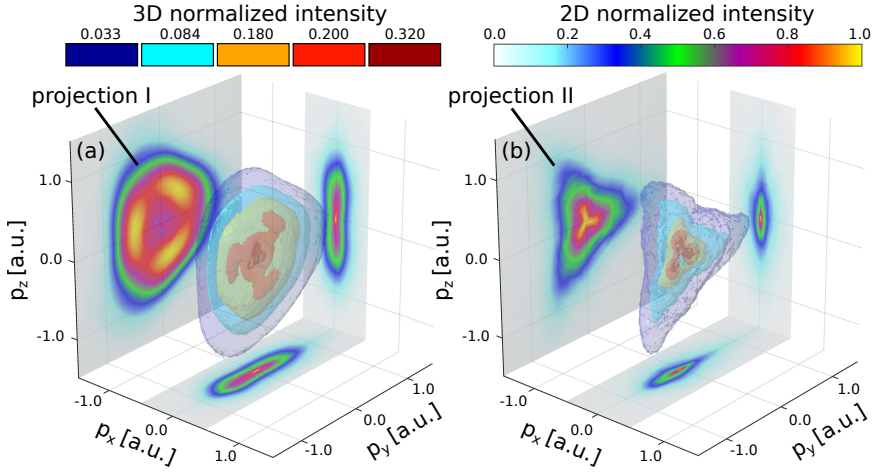


Figure 7.2: "Three-dimensional (3D) electron momentum distributions from ionization of helium by counterrotating two-color fields are shown. The 3D momentum distributions are visualized by combining five semitransparent isosurfaces encoding the intensity of the 3D histogram by color. The $p_y p_z$-plane is the polarization plane. The 2D histograms show projections. a) The field ratio of the two colors and their combined intensity are $E_{390}/E_{780} = 0.84$ and $I = 8.14 \times 10^{14}\,\mathrm{W/cm^2}$. Note the pronounced (red) inner low energy structure in the 3D distribution which is almost invisible in projection I. b) shows the same as (a) but for $E_{390}/E_{780} = 1.20$ and $I = 6.75 \times 10^{14}\,\mathrm{W/cm^2}$." (Figure and caption are taken from Eckart et al. [24].)

It is evident that projection I and projection II in Fig. 7.2 are very different. Projection I belongs to a two-color field ratio of $E_{390}/E_{780} = 0.84$ and still looks similar to the "donut"-like distribution which is observed in the tunneling regime for ionization by a single-color circularly polarized field. Projection II belongs to a two-color field ratio of $E_{390}/E_{780} = 1.20$ and is very different to the "donut" -like distribution. This dependence is already known from the single ionization of argon (see Fig. 6.2). Surprisingly, the two three-dimensional (3D) electron momentum distributions presented in Fig. 7.2 are similar and are both dominated by the low energy electrons at zero momentum.[75] Slices for a given momentum in the light propagation direction p_x from the data shown in Fig. 7.2(a) and 7.2(b) are depicted in Fig. 7.3 and Fig. 7.4. As expected for the tunneling rate it is clearly seen that the overall counts reduce with increasing $|p_x|$. Moreover, also here the low energy structure is seen for small values of $|p_x|$. What is the origin of the low energy structure and what can it be used for? The answers to those two questions are given in chapter 7.3.

[75] The absolute rotation of the electron momentum distribution in the plane of polarization should be neglected for the comparison because the rotation only reflects the relative phase of the two single-color laser pulses (see also chapter 6.5).

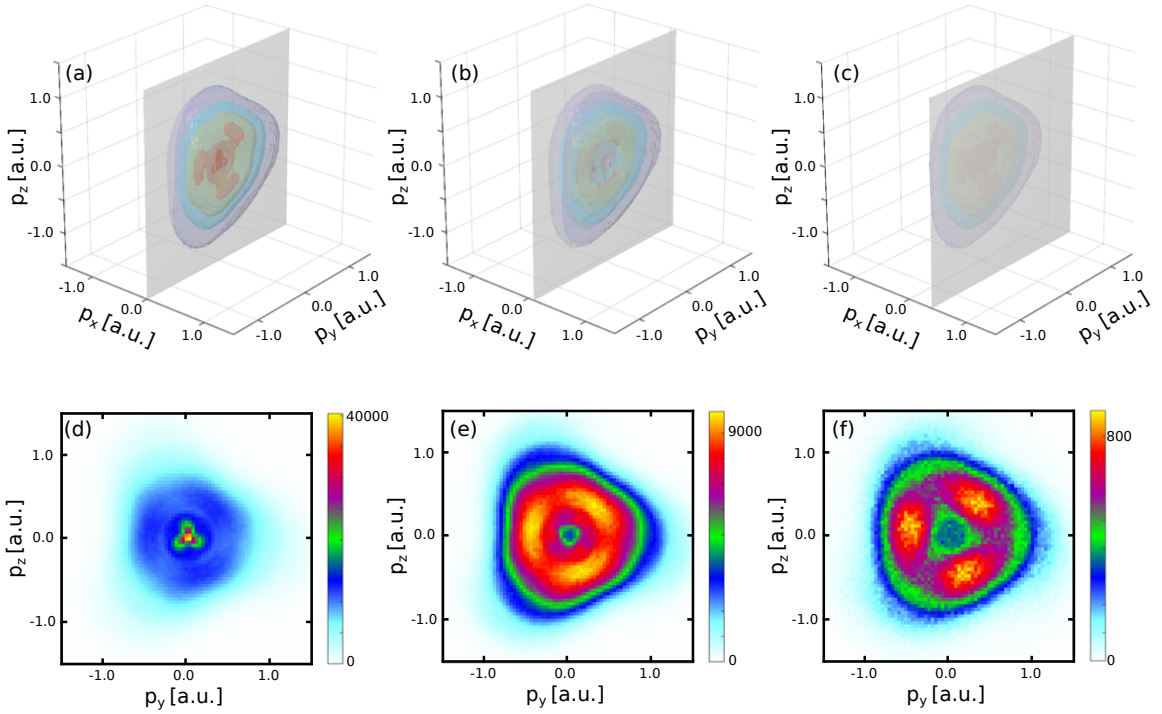


Figure 7.3: The data shown is the same as in Fig. 7.2(a). (a) illustrates a slice imposing the condition $|p_x| < 0.02$ a.u. and (d) shows the resulting two-dimensional momentum distribution. For (b) [(c)] the corresponding condition is 0.09 a.u.$< p_x <$0.11 a.u. [0.39 a.u.$< p_x <$0.41 a.u.] and the related electron momentum distribution is presented in (e) [(f)]. The color scales in (d)-(f) show counts.

The details used to obtain the results shown in Fig. 7.2 are as follows:

- The experiment was performed using an uncollimated supersonic gas jet containing helium and neon atoms. The corresponding gas bottle contained 15 times more helium atoms than neon atoms because this was the approximated difference in ionization rate (see Eq. 5). The driving pressure of the mixed gas jet was 1.2 ± 0.1 bar.

- The nm-delay stage was moved in steps of 5 nm over a distance of 600 nm within 110 minutes for the measurements for Fig. 7.2 and after one scan was complete the scan restarted from the beginning. The data shown in Fig. 7.2(a) was collected within 115 hours. The count rate of helium (neon) was on average 140 Hz (138 Hz).

- The changes in relative phase of the two-colors that are due to the displacement of the nm-delay stage and slow drifts of the relative phase were compensated for[76] (see chapter A.2 and chapter 6.3).

- The data shown in Fig. 7.2(b) was collected within 25 hours. The count rate of helium

[76] Helium has been used to determine the slow phase drifts for the offline phase compensation and the phase of the electron has been corrected for independently of the detected ion.

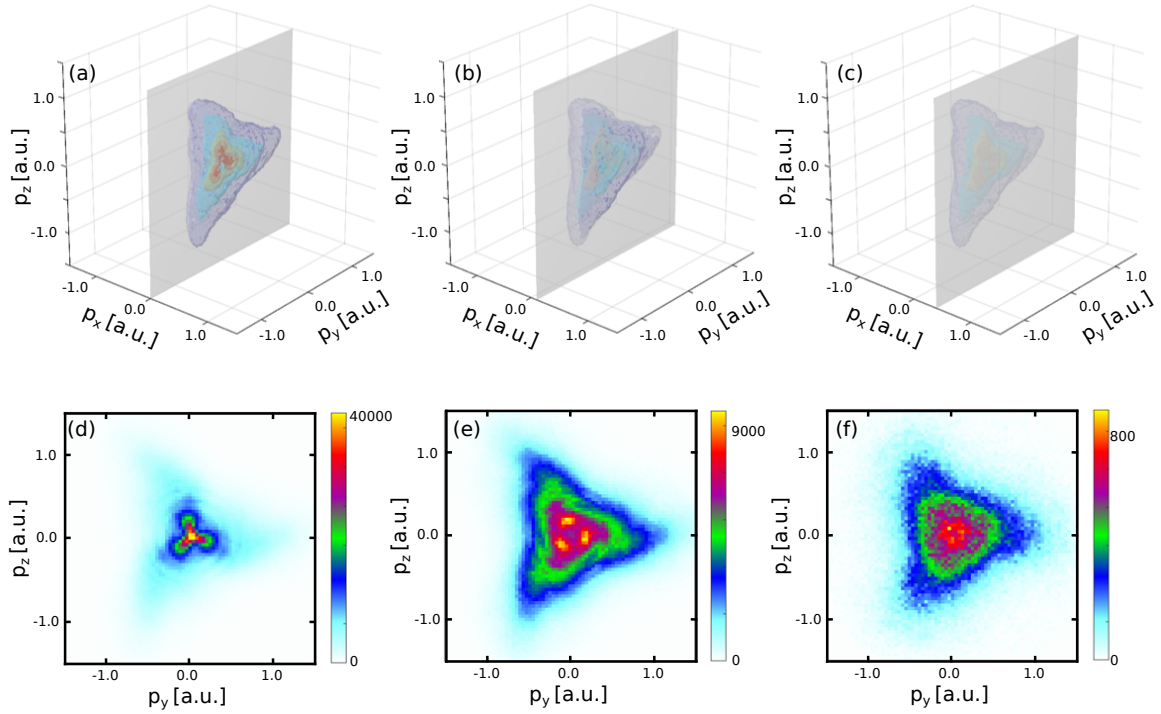


Figure 7.4: The data shown is the same as in Fig. 7.2(b). (a) illustrates a slice imposing the condition $|p_x| < 0.02$ a.u. and (d) shows the resulting two-dimensional momentum distribution. For (b) [(c)] the corresponding condition is 0.09 a.u.$< p_x <$0.11 a.u. [0.39 a.u.$< p_x <$0.41 a.u.] and the related electron momentum distribution is presented in (e) [(f)]. The color scales in (d)-(f) show counts.

(neon) was on average 93 Hz (115 Hz). The fact that the ratio of the helium count rate divided by the neon count rate is smaller for the measurement from Fig. 7.2(b) than it is the case for the measurement from Fig. 7.2(b) is due to the intensity difference.[77]

- The electron momentum distributions shown in this chapter were symmetrized by taking the original data and rotating the measured electron momentum distribution in the plane of polarization by 120° and 240° and finally summing up the original and the two rotated distributions. It is important to notice that each of the three distributions looks almost as symmetric as the final distribution. This is not surprising since all detector inefficiencies and polarization imperfections have already been distributed to the three lobes by performing the offline compensation of the relative phase (see chapter A.2).

- The electron momentum distribution shown was measured in coincidence with helium ions. For the analysis of the measurement which Fig. 7.2(a) is based on, all events were omitted that have a mismatch of electron and ion momentum in the time-of-flight direction that is greater than 0.275 a.u. (0.375 a.u.) for helium (neon). For the

[77] The ionization rate of helium is more sensitive to changes in intensity than the rate of neon due to the higher ionization potential of helium (see Eq. 5).

measurement that led to Fig. 7.2(b) the same was done for all events with a mismatch larger than 0.2 a.u. (0.4 a.u.) for helium (neon). An analysis following the procedure described in chapter A.5.2 shows that the ratio of false electron-ion coincidences in the electron momentum distribution presented is approximately 10%.

- The information about the ion momenta in time-of-flight direction and a look-up-table were used to compensate for distortions of the electron momenta due to imperfections in the spectrometer fields (similar to the procedure described in Ref. [55]). In all cases in which helium and neon are compared the same corrections are applied to the electron momenta.

7.3. Low Energy Electrons

The low energy structure known from Fig. 7.4 (d) is shown again in Fig. 7.5(a). Fig. 7.5(b) shows a solution of the time-dependent Schrödinger-equation[78] (TDSE). Experiment and theory show excellent agreement. Fortunately, for the solution of the TDSE the combined electric field is known. Using the solution of the TDSE as reference the combined electric field can be shown together with the experimental data as an orange line in Fig. 7.5(a).

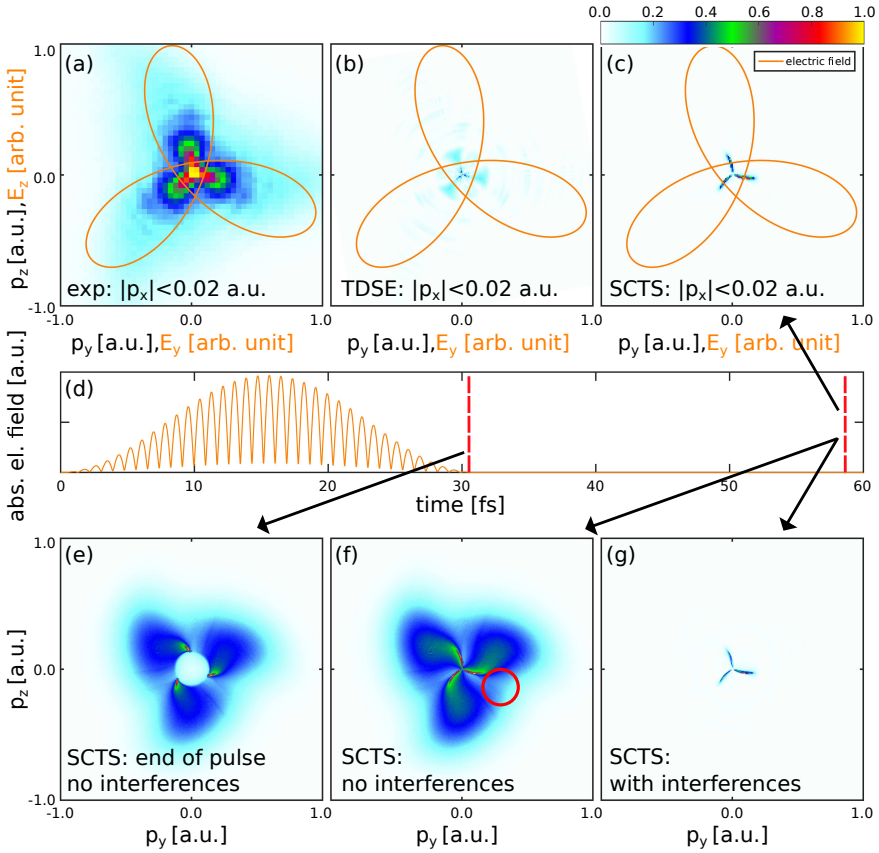


Figure 7.5: "Comparison of the experiment (a), a solution of the TDSE (b) and the SCTS result (c) for small momenta in the light propagation direction $|p_x| < 0.02$ a.u. shows a very good agreement. The temporal evolution of the laser field magnitude used in the SCTS model is shown in (d). (e) shows the electron momentum distribution from the SCTS immediately after the end of the laser pulse (without interferences and only electrons with positive total energy are shown). In (f) the same electrons are presented for asymptotically large time. It can be graphically seen that the Coulomb potential slows down the electrons after the laser pulse is over. This is the reason for the pronounced low energy structure in CRTC fields. (g) is the same as (f) but includes interferences. The red circle in (f) guides the eye to the overlapping region of two neighboring lobes. The momentum component which is not shown (p_x) is projected out in (e), (f), (g)." (Figure and caption are taken from Eckart et al. [24].)

This is a first important result because it shows that the low energy structure can be used to infer the relative phase of the two single-color laser pulses. In a next step the semi-classical two-step simulation (SCTS, see chapter 5.3) is used to reveal the origin of the low energy structure. Fig. 7.5(c) shows the result of the SCTS simulation (for small momenta in the

[78] The numerical TDSE simulation has been carried out by Igor Ivanov and Anatoli Kheifets.

light propagation direction $|p_x| < 0.02\,\text{a.u.}$). It is seen that the orientation of the low energy structure is consistent with the result from solving the TDSE in Fig. 7.5(b). This validates the SCTS model. Since the SCTS model is trajectory-based the momenta and positions of all electrons can be traced as a function of time which allows one to gain insight.

Fig. 7.5(d) shows the absolute value of the combined electric field as a function of time. The end of the laser pulse with a sine-square envelope is marked by a red dashed line at about 31 fs. Fig. 7.5(e) shows the electron momentum distribution without interference (CTS model, see chapter 5.3) at the end of the laser pulse. Here, only electrons with positive total energy (sum of kinetic and potential energy) are shown. The white circle indicates that electrons within that circle end up as bound, excited electrons[79]. The radius of the circle is about 0.13 a.u. which allows one to calculate the corresponding kinetic energy of an electron at the edge of the white circle (in the plane of polarization) to be 0.008 a.u. (0.2 eV). Therefore, it is known that such an electron has to be closer than 130 a.u. to its parent ion in position space for an 1/r-potential at the end of the laser pulse. Fig. 7.5(f) shows the electron momentum distribution for an asymptotically large time which is calculated by analytic Coulomb mapping (see Ref. [38]). Also in Fig. 7.5(f) only electrons with positive total energy are shown. The empty circle at zero momentum is filled up with electrons that had absolute momenta bigger than 0.13 a.u. at the end of the laser pulse.

Thus the low energy structure is a consequence of Coulomb focusing (see Ref. [117]) and contains electrons that were liberated from the atom at times when the vector potential was non-zero. Including interference (SCTS model, see chapter 5.3) Fig. 7.5(g) is obtained and the low-energy electrons are even more prominent. However, this result should be taken with care since the particle number is not conserved in the SCTS model[80].

[79] This process is known as frustrated tunnel ionization in the literature [116].

[80] The fact that the particle number is not conserved in the SCTS model can be made plausible employing the following argument. Assuming only two possible instances of ionization and destructive interference leads to a final electron momentum distribution which is empty. In contrast, without interference the particle number is expected to be conserved.

7.4. Interference in the Plane of Polarization

For the sake of completeness a slice for non-zero momentum in the light propagation direction at $p_x = 0.25 \pm 0.02$ a.u. will be investigated. Fig. 7.6 shows the corresponding subsets of the three-dimensional momentum distribution in analogy to Fig. 7.5(a), 7.5(b) and 7.5(c). It is found that the ATI structures are blurred due to volume averaging in the experiment. With the exception of this prominent difference the TDSE agrees with the experimental data. The interference structures in the SCTS model agree with those of the solution of the TDSE but the SCTS model misses a weak threefold structure at low energies. More importantly, the intensity envelope appears to be rotated for the data from the SCTS model with respect to the TDSE and the experiment. This rotation is indicated by a black dashed line in Fig. 7.6(a), 7.6(b) and 7.6(c) and might be related to a non-adiabatic offset of the initial momentum distribution that is not included in the SCTS model (see chapter 8). Future experiments could vary the wavelength of the driving fields to study the influence of non-adiabaticity.

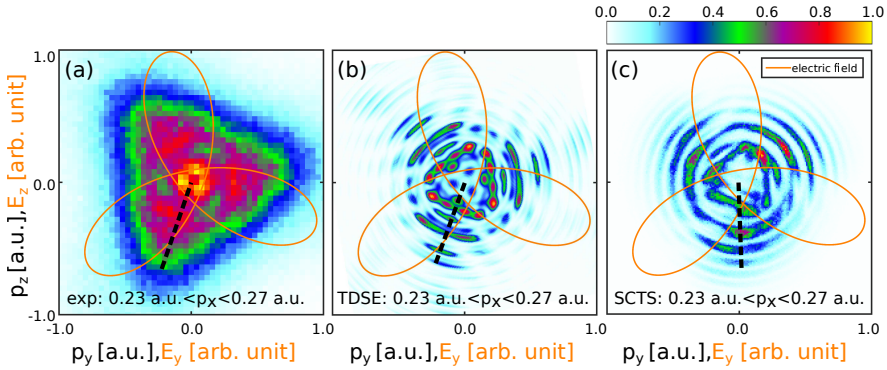


Figure 7.6: Electron momentum distribution in analogy to Fig. 7.5(a), 7.5(b) and 7.5(c) for the condition $p_x = 0.25 \pm 0.02$ a.u. The black dashed line guides the eye to see the orientation of the intensity envelope of the electron momentum distributions. It can be seen that the intensity envelope for the experimental data (a) and the result from solving the TDSE (b) agree. (c) shows the result from the SCTS model which appears to have a different rotation angle of the intensity envelope compared to (a) and (b). The interference structures agree (see text). The experimental distribution in (a) is blurred due to volume averaging. The TDSE simulation has been carried out by Igor Ivanov and Anatoli Kheifets. They provided the three-dimensional electron momentum distribution in numerical form.

The next chapter deals with a yet unobserved feature in three-dimensional momentum space which is due to the overlap of two neighboring lobes (see also the red circle in Fig. 7.5(f)). This feature emerges because the release times of electrons from two neighboring lobes are different and this double slit in time gives rise to interference.

7.5. Sub-cycle Interference along the Light Propagation Direction

Fig. 7.7(a) shows the electron momentum distribution that is labeled projection I in Fig. 7.2(a). Fig. 7.7(b)-(d) show subsets of Fig. 7.2(a) restricting the momentum in the plane of polarization ($p_y p_z$-plane) as indicated in the panels and showing the corresponding electron momentum distribution along the light propagation direction p_x.

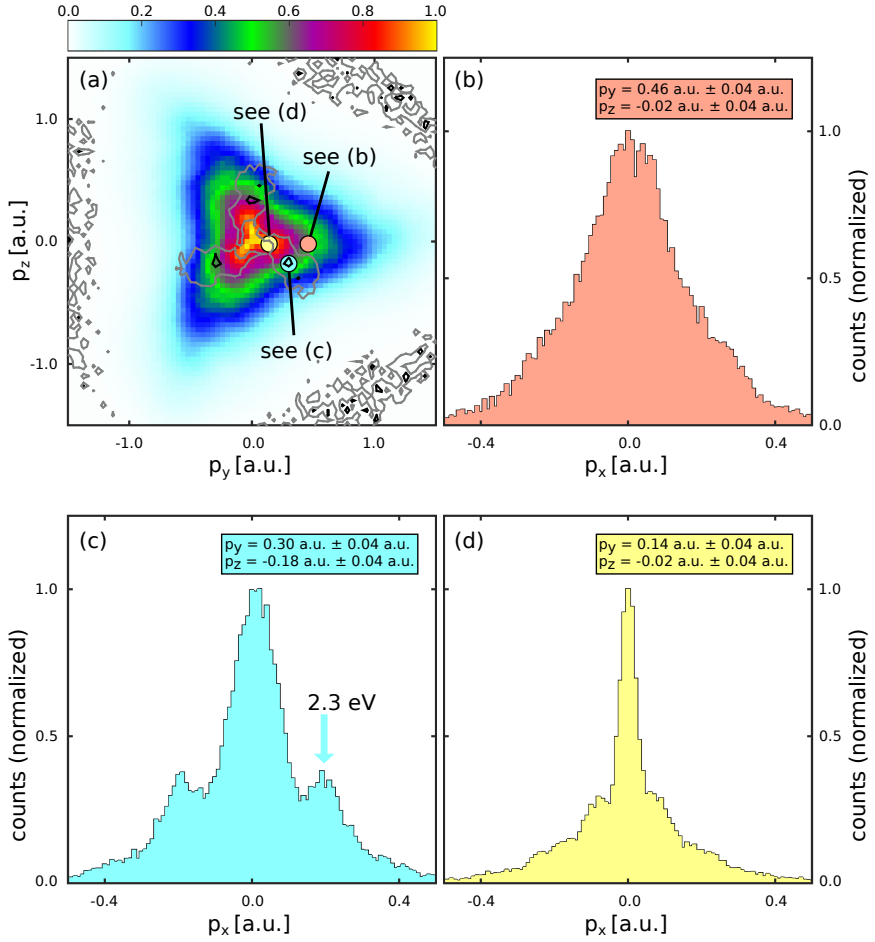


Figure 7.7: "The momentum distribution in the light propagation direction is investigated for various selected momenta in the plane of polarization. (a) shows projection II from Fig. 7.2 [remark - the number of the referenced figure has been adapted]. The dots in the polarization plane in (a) indicate the used condition for panel (b), (c), (d) that show the momentum (p_x) in the light propagation direction. (b) shows a Gaussian-like distribution (as for circularly polarized light), (c) shows sub-cycle interference (fringes) and (d) shows the cusp-like initial momentum distribution (as for linear light). The side-peaks of the sub-cycle interference in (c) correspond to an electron energy of 2.3 eV. The fringe visibility is indicated by contour lines in (a). Gray contour lines indicate 50 % fringe visibility compared to the black contour line." (Figure and caption are taken from Eckart et al. [24].)

For Fig. 7.7(b) the electron momentum is restricted to the peak of one lobe in the $p_y p_z$-plane. The distribution in p_x is a Gaussian distribution as it is expected from the tunneling rate (see Eq. 5) and commonly observed for circularly polarized light (see e.g. Refs. [25, 118]). For Fig. 7.7(c) the selected region in the plane of polarization is at the edge of one lobe in

the direction of the neighboring lobe. The corresponding momentum distribution along p_x shows a modulation which is typical for a two-path interference. However, the underlying distribution appears to be a Gaussian distribution. Fig. 7.7(d) shows a very sharp distribution centered at zero momentum that is due to Coulomb focusing and known for linearly polarized light (see e.g. Refs. [36, 119]).

7.5.1. Sub-cycle Interference: Fringe Visibility

The fringes in p_x-direction that are seen in Fig. 7.7(c) are a surprise since the vector potential is two-dimensional and lies in the $p_y p_z$-plane. In a first step to unravel the origin of this feature the fringe-visibility is analyzed for every bin in the plane of polarization ($p_y p_z$-plane). The procedure that is employed is illustrated using the distributions from Fig. 7.7(b)-(d). The blue line in Fig. 7.8(a) shows the same data as Fig. 7.7(b) after normalizing the integral to one. The red dashed line in Fig. 7.8(a) shows a fit of a Gaussian function to the blue line. The yellow line results subtracting the fit from the measured data. The yellow line is called the "non-gaussian residual". Summing up the absolute values of all entries in the "non-gaussian residual" results in a scalar value for the non-gaussian fraction $\alpha_{\text{remainder}}$ that is between zero and one. $\alpha_{\text{remainder}}$ would be zero if the original distribution (blue line) is a Gaussian distribution. In the next step the "non-gaussian residual" (yellow line) is Fourier transformed and the result is shown in Fig. 7.8(b) as a blue line. It is seen that the week modulation in Fig. 7.8(a) is reflected by a clear peak in Fig. 7.8(b) at about 3.2 oscillations per a.u. (the peak is determined by fitting a Gaussian distribution in Fourier-space, see red dashed line in Fig. 7.8(b)). The same procedure is applied to the data from Fig. 7.7(c) [(d)] and presented in Fig. 7.8(c) and (d) [(e) and (f)].

Inspecting those three examples it is evident that the value $\alpha_{\text{remainder}}$ is not sufficient to quantify the fringe visibility if there are high modulation frequencies and strong Coulomb focusing (see Fig. 7.8(e)). Therefore the fringe visibility will be quantified as the product of $\alpha_{\text{remainder}}$ and the amplitude corresponding to a modulation frequency of 4 oscillations per a.u. This value $\beta_{\text{amplitude}}$ can be read off from the blue lines in Fig. 7.8(b), (d), (f). Using this definition the fringe visibility is 0.00742 for Fig. 7.8(a), 0.02784 for Fig. 7.8(c) and 0.00736 for Fig. 7.8(e). This is consistent with the perception that the blue line in Fig. 7.8(c) shows fringes while in Fig. 7.8(a) and (e) they are not visible without the subtraction of the Gaussian distribution.

Of course the fringe visibility can be determined for every combination of p_y and p_z analyzing the corresponding distribution along the light propagation direction. To this end projection II from Fig. 7.2 is shown in Fig. 7.9(a) together with the combined electric field and the negative vector potential. The non-gaussian fraction $\alpha_{\text{remainder}}$ is presented in Fig. 7.9(b). It is clearly seen that the cusp-like distribution that emerges for the low energy structure due to Coulomb focusing is non-gaussian. Interestingly there exists a lightblue region that is almost perfectly gaussian. Just between those lightblue regions in Fig. 7.9(b) the

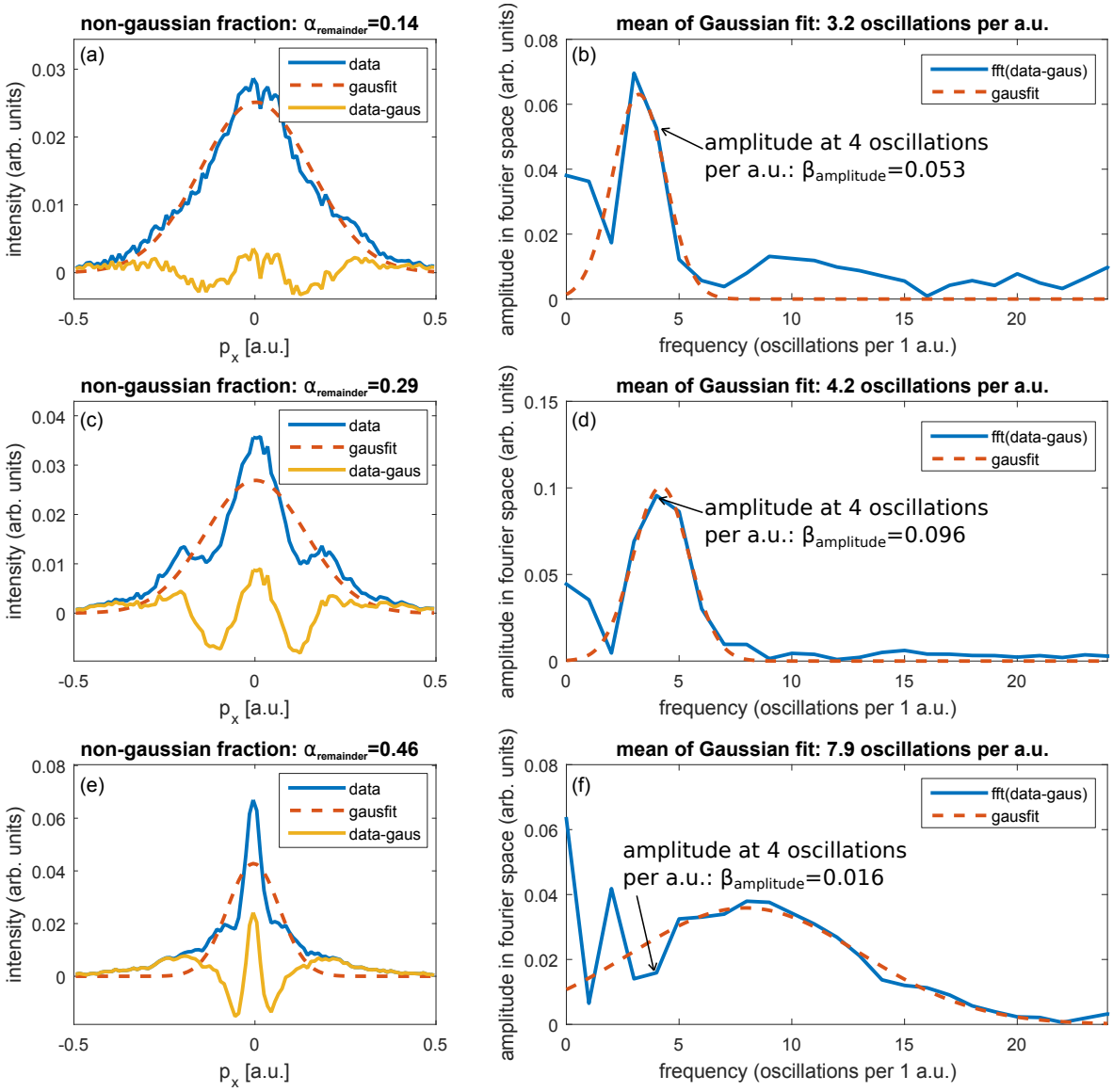


Figure 7.8: (a) shows the data from Fig. 7.7(b) as blue line and a fit of a Gaussian function to it (dashed red line). The yellow line shows the "non-gaussian residual" which is the subtraction of fit and data. The non-gaussian fraction $\alpha_{\text{remainder}}$ (see text) is quantified in the title of the panel. (b) shows the Fourier transform of the yellow line from (a) and a gaussian fit (excluding zero frequency) to the shown data is plotted as a red dashed line. The mean of the gaussian fit is indicated in the title of the panel. The value $\beta_{\text{amplitude}}$ (corresponding to the amplitude at 4 oscillations per a.u. of the Fourier transformed data) is also indicated in the panel. $\alpha_{\text{remainder}}$ and $\beta_{\text{amplitude}}$ are used to quantify the fringe visibility (see text and Fig. 7.9). (c), (d) and (e), (f) show the same as (a), (b) for the data from Fig. 7.7(c) and Fig. 7.7(d).

fringe visibility is highest which can be clearly seen in Fig. 7.9(c) that finally shows the fringe visibility. The data from Fig. 7.9(c) is shown as contour lines in Fig. 7.7(a) and it is seen that the condition for Fig. 7.7(b) was chosen to coincide with the maximal fringe visibility.

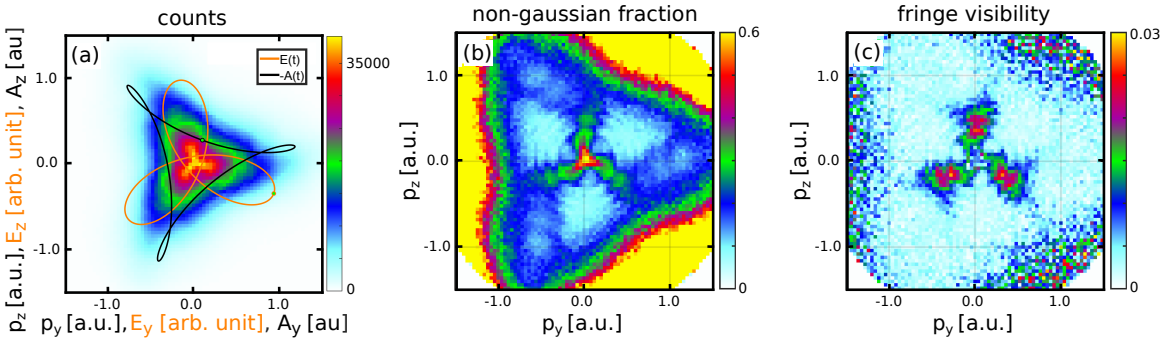


Figure 7.9: (a) shows the same data as projection II from Fig. 7.2. Additionally the combined electric field E(t) and the negative vector potential -A(t) are shown. (b) shows the non-gaussian fraction of the distribution in the light propagation direction p_x and (c) the fringe visibility for every combination of p_y and p_z (see text).

Also for the data belonging to Fig. 7.2(a) the fringe visibility can be calculated. The analogue results are presented in Fig. 7.10. It is evident that the fringe visibility is very low. Later on it will be clear that this is because the overlap of the three lobes is much weaker. However, one important question remains: where does the modulation along the p_x direction come from?

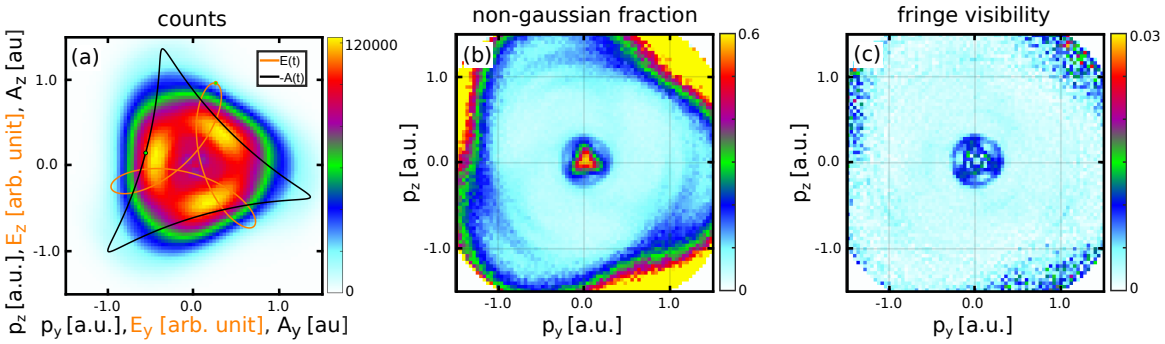


Figure 7.10: (a) shows the same data as projection I from Fig. 7.2. Additionally the combined electric field E(t) and the negative vector potential -A(t) are shown. Here no solution of the TDSE was available to benchmark the orientation of the combined electric field. Therefore the orientation of the combined electric field is a guess based on the position of the three lobes in the electron momentum distribution that was obtained using the SCTS simulation (not shown). (b) shows the non-gaussian fraction of the distribution in the light propagation direction p_x and (c) the fringe visibility for every combination of p_y and p_z (see text).

The SCTS simulation can be used to reveal the origin of the low energy structure. Fig. 7.11(a) and (c) show subsets of the final electron momentum distribution in cylindrical coordinates restricting the electron energy to $2.3 \pm 0.1\,\mathrm{eV}$. The condition that has been imposed on the electron energy makes sure all remaining modulations are not due to ATI fringes. In Fig. 7.11(a) the ionization-phase is restricted to one lobe of the three lobes (the ionization time is not restricted to a single cycle). For Fig. 7.11(c) the ionization time is restricted to one full single cycle.

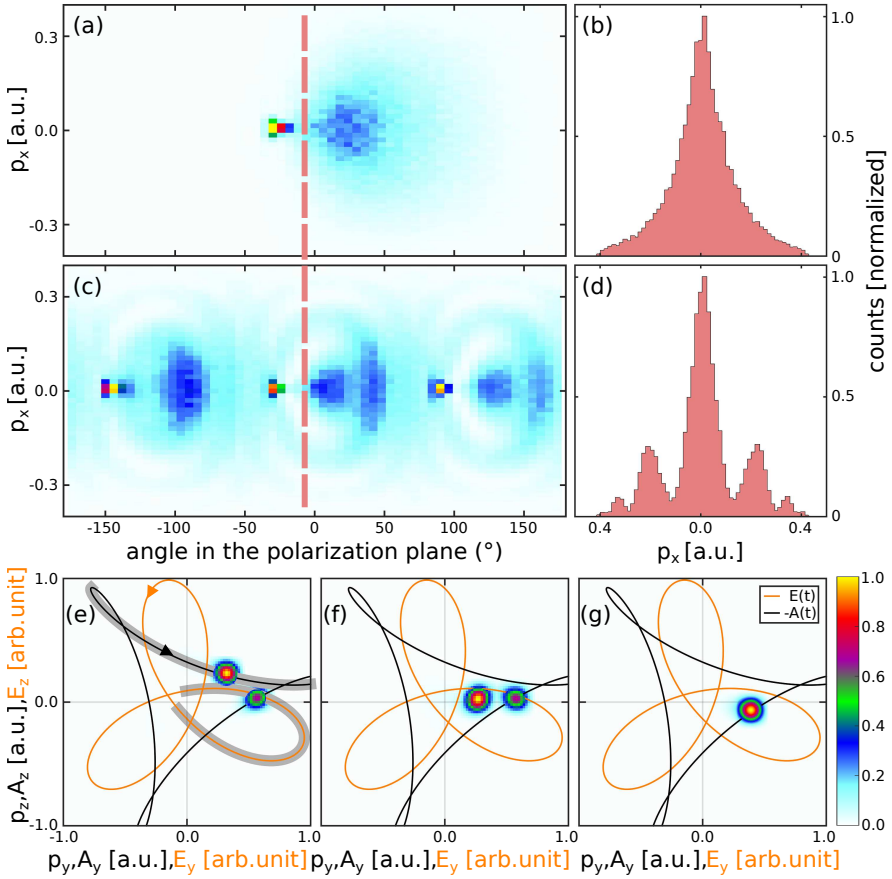


Figure 7.11: "The origin of the sub-cycle interferences is investigated using the semi-classical SCTS simulation. Only electrons with an energy of $2.3 \pm 0.1\,\mathrm{eV}$ are selected. The resulting subset is presented as 2D momentum distributions in (a), (c) for ionization within one lobe of the combined electric field (indicated as gray shaded phases of the electric field and the vector potential in (e)) and a full single cycle of the combined electric field respectively. Panels (b), (d) show subsets from (a), (b) selecting the angle in the polarization plane to be $-6 \pm 6°$. Manifestly panel (d) shows modulations which panel (b) does not show. This indicates that the observed modulations are indeed sub-cycle interferences. Tracing back all electrons by showing their negative vector potential (panel (e)) reveals their corresponding "birth-times". Those times/phases are seen as dots on the vector potential in panel (e). Panel (f) shows the sum of the negative vector potential at the instant of ionization and the initial momentum of the electrons just after tunneling. Panel (g) shows the final momentum. The data shown in (e), (f), (g) has been convoluted with a Gaussian distribution to facilitate visibility. The arrows in (e) indicate the time evolution of the electric field and the negative vector potential." (Figure and caption are taken from Eckart et al. [24].)

Since only in Fig. 7.11(c) interference appears it is proven that there is sub-cycle interference. Restricting Fig. 7.11(a) and (c) to small range for the angle in the plane of polarization Fig. 7.11(b) and 7.11(d) are obtained. The agreement of the distribution seen in Fig. 7.11(d) with the experiment allows for the conclusion that the experimentally observed fringes are indeed due to sub-cycle interference. Finally, the SCTS model can be used to investigate the initial conditions at the exit of the tunnel for all trajectories that contribute to Fig. 7.11(d). The final electron momentum is the sum of the negative vector potential, the initial momentum at the exit of the tunnel and the Coulomb interaction of the electron with its parent ion

after tunneling. For all trajectories that contribute to Fig. 7.11(d) the negative vector potentials at the "birth-time" are depicted in Fig. 7.11(e). Fig. 7.11(f) shows the sum of the negative vector potential and the initial momentum at the exit of the tunnel. It is evident that the two distributions do not coincide. A necessary prerequisite for interference is overlap in final momentum space. The overlap is reached by taking the initial momentum and the Coulomb interaction of the electron with its parent ion into account. The corresponding final electron momentum distribution is shown in Fig. 7.11(g). As expected all which-way-information is lost and interference is possible.

7.6. Conclusion: Sub-cycle Interference

Sub-cycle interference in momentum space along the light propagation direction has been observed. The quantitative semi-classical simulations show that the initial momentum at the exit of the tunnel and the Coulomb potential after tunneling are both relevant. This kind of sub-cycle interference might be useful to probe the phase of electron wave packets emerging from (chiral) molecules. Since the final momentum is due to the laser electric field, the initial momentum distribution and the Coulomb interaction it can be expected that the phase of the electronic wave packet is also sensitive to all three contributions. In particular, the phase the electron wave packet accumulates under the barrier might depend on the electron's emission direction[81]. The two possible "birth-times" that are illustrated by the negative vector potential in Fig. 7.11(e) belong to the two electric fields indicated by red dots in Fig. 7.12. The tunnel exit positions are anti-parallel to the laser electric field at the time of ionization. Thus, the relative angle of the tunnel exit positions in the plane of polarization is 136° in Fig. 7.12. This might allow a generalized approach similar to the work of Zhang et al. [114] in order to investigate the valence-electron cloud of molecules. CRTC fields allow

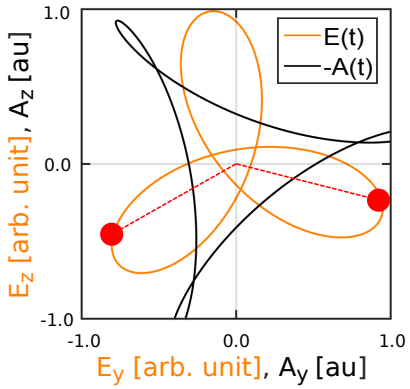


Figure 7.12: The electric fields corresponding to the two relevant "birth-times' from Fig. 7.11(e) are marked with red dots. The relative angle of the two electric field vectors is 136°.

for the observation of interference in an isolated region in momentum space and the low energy structure allows for a precise measurement of the orientation of the two-color electric field in situ (see chapter 7.3). Another advantage of the presented scheme is its robustness with respect to volume averaging. The sub-cycle interference remains visible although ATI peaks are already blurred (see Fig. 7.6 also chapter A.1).

[81] The orientation of the molecules can be determined by Coulomb explosion imaging [120]. To observe sub-cycle interference in the same measurement a pump-probe scheme might be used. The two-color pump-pulse could lead to single ionization and a circularly single-color probe-pulse with high vector potential could be used for Coulomb explosion imaging. In this scheme the electron liberated by the probe-pulse would not overlay with the electrons that are liberated by the pump-pulse (see also chapter 9).

7.7. Comparing the Ionization of Helium and Neon

The electron momentum distributions that are shown above were measured in coincidence with helium ions. However, for the experiment a mixed gas target was used containing helium and neon (see beginning of chapter 7). The electron momentum distributions measured in coincidence with neon can also be analyzed. The result is shown in Fig. 7.13 in analogy to Fig. 7.2.

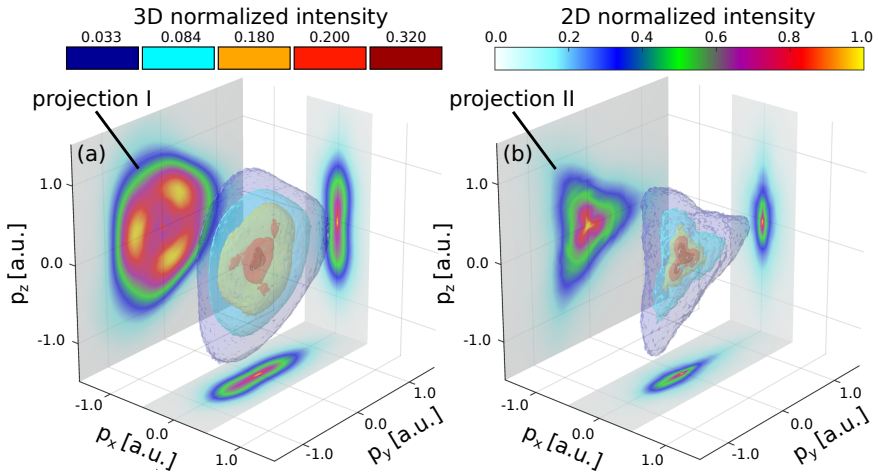


Figure 7.13: Electron momentum distribution measured in coincidence with neon ions. Everything else is as in Fig. 7.2.

Surprisingly the results for neon are very similar to those of helium. To quantify the differences the normalized difference of projection I of Fig. 7.2 and projection I of Fig. 7.13 is shown in Fig. 7.14(c). The differences for absolute momenta smaller than 1 a.u. are only on the order of 0.05 (red area in Fig. 7.14(c)). For larger radial momenta the differences are up to 0.3 (blue area in Fig. 7.14(c)). Interestingly the three red lobes in Fig. 7.14(c) are pointing to the minima of the original distributions (Fig. 7.14(a) and 7.14(b)). At closer inspection this reflects the smeared out peaks of the electron momentum distribution for helium (the yellow area is more localized in Fig. 7.14(b) than in Fig. 7.14(a)). This is unexpected since the ionization potential of helium is higher than that of neon. Thus strong field ionization is expected to be more sensitive to the amplitude of the laser electric field for helium. However, the relevance of systematic errors cannot be excluded. A possible systematic error arises because momentum conservation links the momentum of the electron to a position on the ion detector (for helium a change in electron momentum by 1 a.u. in position direction leads to an ion displacement of about 1.5 mm for the given spectrometer settings). A detector inefficiencies on the ion detector may produce a “shadow” in the electron momentum distribution

that is measured in coincidence with an ion. The rotation of the electron momentum distribution in the plane of polarization and the subsequent offline phase compensation partially compensates for this systematic error but it cannot be proven that this systematic error is irrelevant.

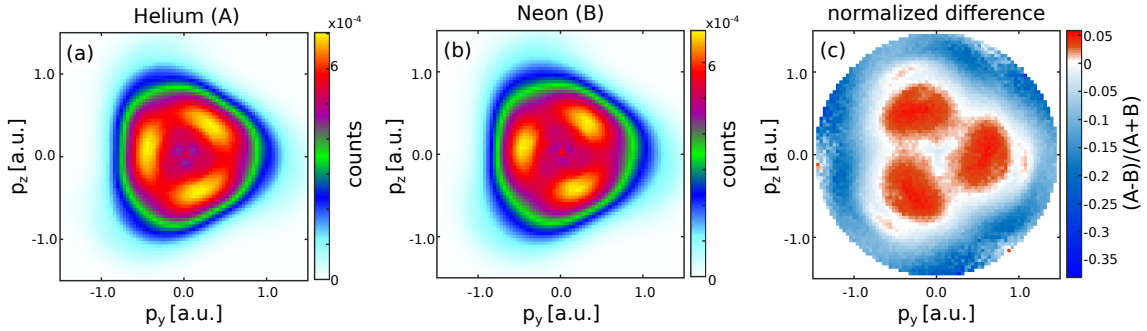


Figure 7.14: (a) shows the same data as projection I from Fig. 7.2 and (b) shows the same data as projection I from Fig. 7.13. The data in (a) [(b)] was normalized to a sum of one and is called A [B]. (c) shows the normalized difference (A-B)/(A+B).

Having realized that the differences of helium and neon are very small the differences can be calculated and visualized in three-dimensional momentum space. To this end the distributions in Fig. 7.2(a) and Fig. 7.13(a) are both normalized to a sum of one and subtracted from each other. The result is shown in Fig. 7.15. The differences that are seen in the projections to the $p_x p_z$- and the $p_x p_y$-plane show stripes with a modulation of about 0.25 a.u. perpendicular to the p_x-direction. Since this is the direction that is not affected by the offline phase compensation it is very likely that those structures are systematic errors due to local inefficiencies of the ion detector (see above).

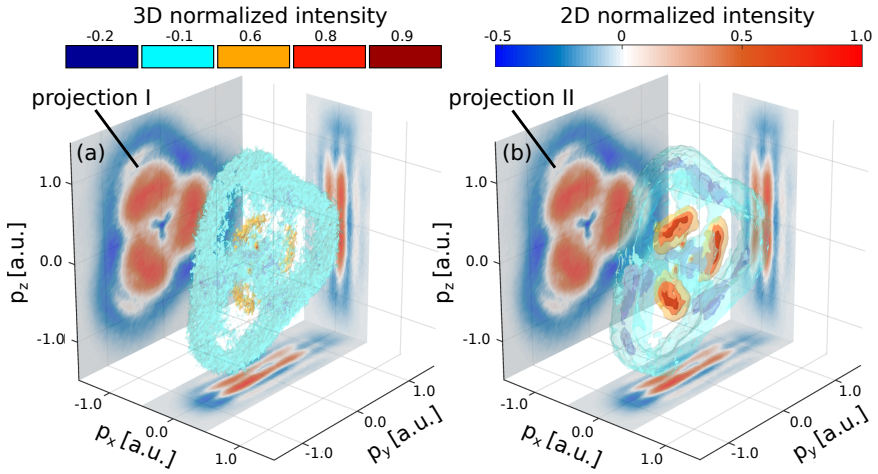


Figure 7.15: (a) shows the data from Fig. 7.2(a) minus the data from Fig. 7.13(a). (b) shows the same as (a) after the result was convoluted with a 3x3x3 matrix containing ones to reduce high frequency noise.

Quantitatively a change in position on the ion detector of 1 mm corresponds to a change in momentum of about 1.5 a.u. for a singly charged helium ion and the given spectrometer settings. The mesh (see chapter 4.1.3 and Ref. [36]) in front of the ion detector has a lattice spacing of 250 µm. The mesh might modulate the detection efficiency of helium on a length scale of 250 µm. This corresponds to a length scale in momentum space of about $\frac{250\,\mu m}{1\,mm} \cdot 1.5\,a.u. = 0.375\,a.u.$ Assuming that the mesh mainly affects helium ions (because neon is heavier) a detection inefficiency that is caused by the mesh in front of the ion detector is a possible explanation for the experimentally observed stripes perpendicular to the p_x-direction in Fig. 7.15.

Having analyzed the differences of helium and neon for the field parameters related to Fig. 7.13(a) the same can be done for the data set that belongs to Fig. 7.13(b). The results are shown in Fig. 7.16 and Fig. 7.17.

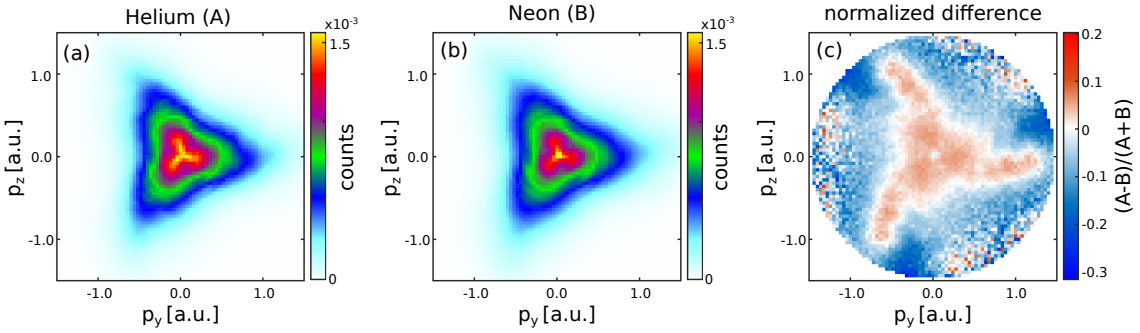


Figure 7.16: (a) shows the same data as projection II from Fig. 7.2 and (b) shows the same data as projection II from Fig. 7.13. The data in (a) [(b)] was normalized to the sum of one and is called A [B]. (c) shows the normalized difference (A-B)/(A+B).

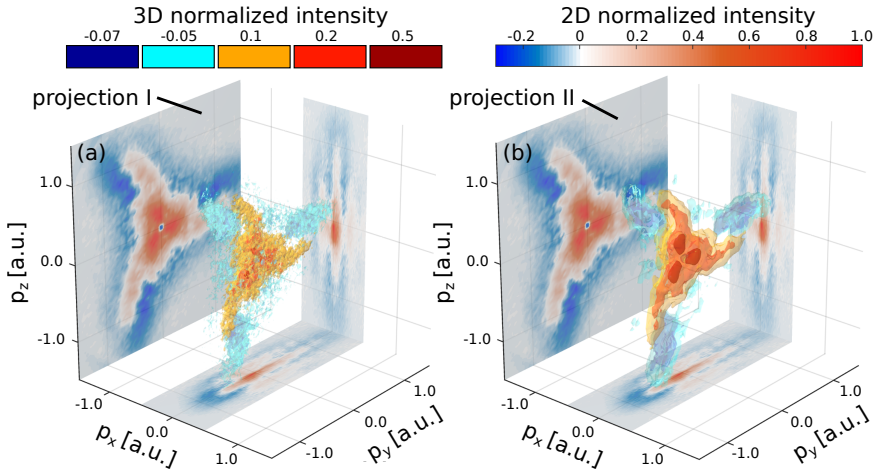


Figure 7.17: (a) shows Fig. 7.2(b) minus Fig. 7.13(b). (b) shows the same as (a) after the result was convoluted with a 3x3x3 matrix containing ones to reduce high frequency noise.

The differences seen in Fig. 7.16 and Fig. 7.17 are also minute. Nevertheless the shape and position of the red area coincides with the section of momentum space that has a high non-gaussian fraction (see Fig. 7.9). This motivates to investigate the sub-cycle interference also for neon but the comparison of Fig. 7.18 and Fig. 7.8 yields that the differences for the fringe visibility are insignificant.

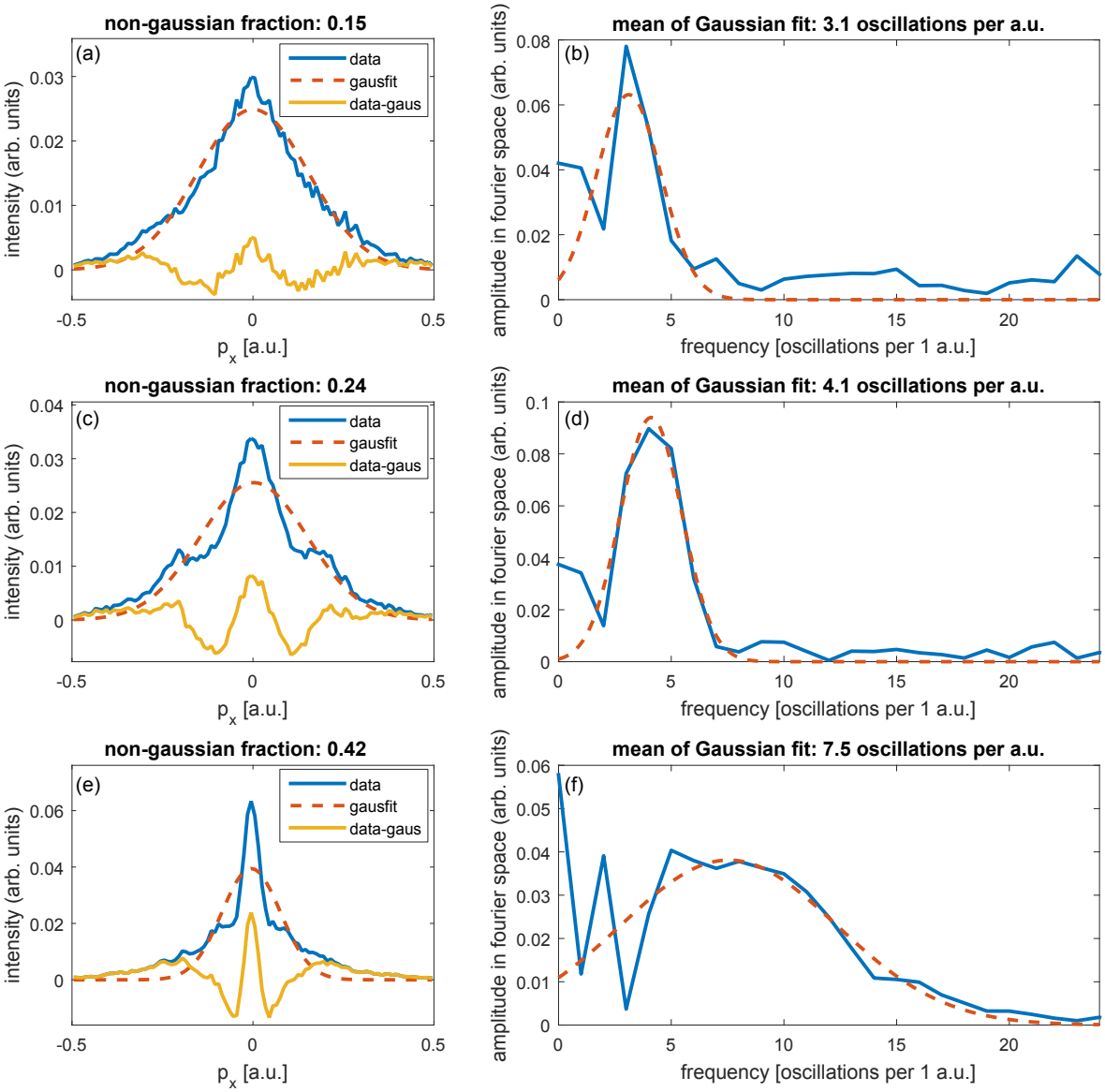


Figure 7.18: Everything is shown as in Fig. 7.8 but here the electrons are detected in coincidence with neon instead of helium. Interestingly also from the perspective of sub-cycle interference there are hardly any differences comparing the electron momentum distributions of helium and neon.

Finally, the differences seen in Fig. 7.17(b) can be interpreted as a rotation of the electron momentum distribution in the plane of polarization of helium relative to neon. From this

perspective the electron momentum distribution for neon is rotated counter-clockwise[82] with respect to that of helium. The following chapter provides a detailed analysis of the electron emission angles in the plane of polarization from helium and neon.

[82] Arguing along the line of Ref. [12] one could state that neon is ionized at "early" attoclock angles whereas helium is ionized at "late" attoclock angles (see e.g. Ref. [8]).

7.7.1. 2D Maps of the Electron's Angle in Momentum Space

Here another method to investigate three-dimensional electron momentum distributions is presented.

Fig. 7.19 shows the same data as Fig. 7.2(b) in cylindrical coordinates (i.e. showing only a two-dimensional projection on the momentum in the light propagation direction p_x and the radial momentum in the plane of polarization p_r). The strong Coulomb focusing for small values of p_r can clearly be seen.

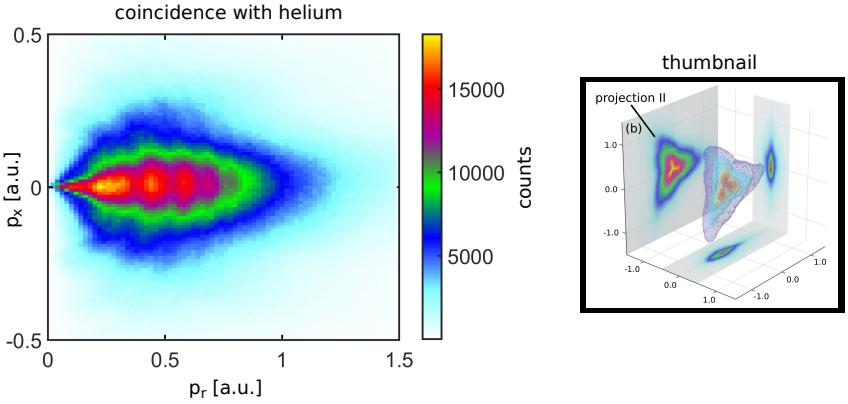


Figure 7.19: The data from Fig. 7.2(b) is shown in cylindrical coordinates with $p_r = \sqrt{p_y^2 + p_z^2}$ projecting out the angle in the plane of polarization. Fig. 7.2(b) is shown as thumbnail on the right.

Selecting the combination $p_x = 0.025 \pm 0.005$ a.u. and $p_r = 0.25 \pm 0.01$ a.u. allows one to plot the coordinate that is not shown in Fig. 7.19 which is the angle in the plane of polarization $\varphi = \text{atan2}(p_z, p_y)$ which leads to the distribution shown in Fig. 7.20(a). A Fourier transformation of this distribution leads to Fig. 7.20(b). From the amplitudes in Fourier space it is evident that the zero-frequency component and the frequency belonging to the threefold symmetry dominate the distribution. The phase in Fourier space of the component belonging to the threefold symmetry is -119°. Taking only the complex amplitudes belonging to the threefold symmetry performing an inverse Fourier transformation and scaling the minimum and the maximum to match Fig. 7.20(a) leads to the distribution in Fig. 7.20(c). This proves that the phase of the threefold structure in Fig. 7.20(a) is faithfully represented by the corresponding Fourier components.

Having reduced the rotation of the threefold structure of the angular distribution along φ to a simple scalar value opens up a new perspective on 3D momentum space. The extracted phase can be shown for every combination of p_x and p_r in a two-dimensional map.[83] The

[83] For the shown examples the phase is shifted using the definition $\Delta\text{phase} = \text{phasefromFFT} + 115°$ to avoid jumps from $-180°$ to 180° and vice versa.

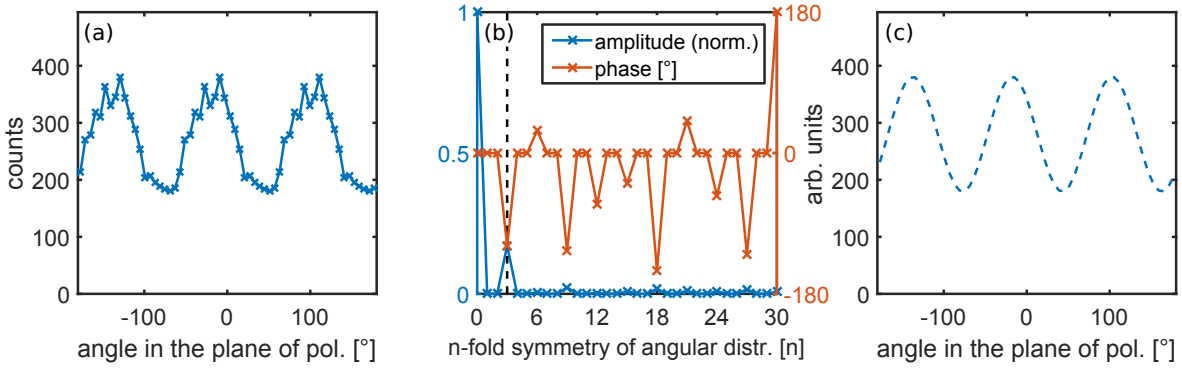


Figure 7.20: In (a) the angular distribution along the angle in the plane of polarization $\varphi = \mathrm{atan2}(p_z, p_y)$ is depicted for the condition $p_x = 0.025 \pm 0.005$ a.u. and $p_r = 0.25 \pm 0.01$ a.u. and (b) shows the Fourier transformation of this distribution. The frequency component in Fourier space that belongs to a threefold symmetry is marked with a vertical dashed black line and it is evident that the corresponding amplitude shows a clear peak. The phase that belongs to the three fold symmetry can be read of to be -119°and provides a scalar value that indicates the position of the peaks of the threefold structure in (a). To illustrate this a Fourier back-transformation of the Fourier components belonging to the threefold symmetry is done and the result is shown in (c) which is scaled such that the minimum and maximum coincide with the extrema of the distribution in (a).

resulting "phase-maps" are two-dimensional representations of the emission angle in the plane of polarization and a phase difference of 360°corresponds to a rotation of the threefold structure in the plane of polarization by 120°. This emission angle is the most important observable in attoclock experiments (see e.g. Refs. [8, 121, 122]).

The panel from Fig. 7.19 is shown again in Fig. 7.21 together with the corresponding phase map. So far only the phase of the threefold symmetry in Fourier space was used. Further, the amplitude of the threefold symmetry can also be analyzed. In Fig. 7.21(c) the color saturation is set to be proportional to the this amplitude leading to a "weighted phase map". This representation emphasizes features that correspond to high statistics in the original distribution.

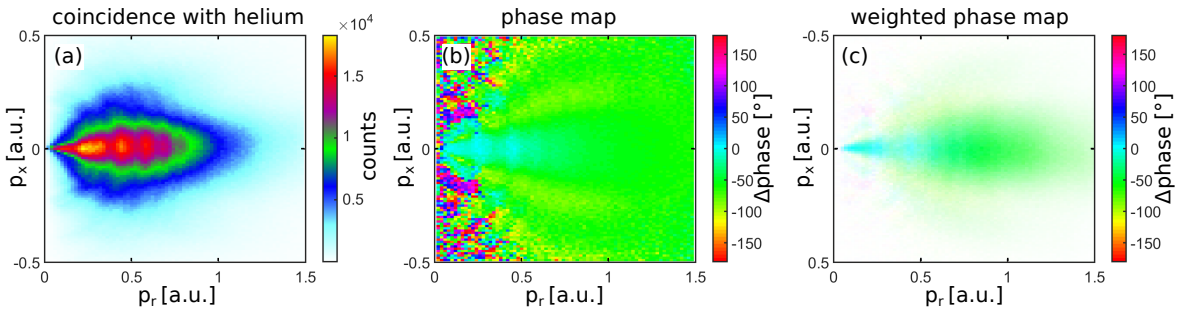


Figure 7.21: (a) shows the same as Fig. 7.19. (b) shows the "phase map" that encodes for each combination of p_x and p_r the rotational angle of the threefold structure in the plane of polarization (see text). (c) shows the same phases as (b) but here the color saturation reflects the modulation depth of the threefold structure (see Fig. 7.22).

The amplitudes used for weighting the color saturation are shown in Fig. 7.22 as an "amplitude map" to illustrate that the amplitudes follow the general trend of the overall counts from

Fig. 7.21(a) but are not identical. In particular, the "amplitude map" shows that for very high and very small momenta the threefold structure has a high visibility (compared to momenta at about 0.4 a.u.).

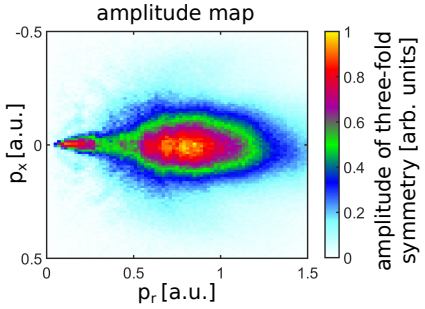


Figure 7.22: Shows the amplitude in Fourier space corresponding to a threefold symmetry (see black dashed line in Fig. 7.20(b)) for every combination of p_x and p_r.

Upon examination of the phase map shown in Fig. 7.21(b) it is found that at low p_r and non-zero p_x the extracted phases are very noisy because in this region of momentum space there is no intensity. Moreover, the entire phase map is dominated by phases that correspond to the green color. At close inspection very weak structures in blue and yellow can be seen. In order to make the differences visible the range of the color coded phases is restricted. The resulting "zoomed phase map" is presented in Fig. 7.23 revealing a very pronounced structure for small p_x that varies from purple (0°) via blue (−20°) to green (−60°) with increasing p_r. From values of around $|p_x| \approx 0.12$ a.u. and $p_r \approx 0.25$ a.u. to $|p_x| \approx 0.27$ a.u. and $p_r \approx 1.0$ a.u. a yellow arm (−80°) is visible. At small radial momenta $p_r < 0.2$ a.u. a purple fan-like structure is visible and at $|p_x| \approx 0.2$ a.u. and $p_r \approx 0.35$ a.u. a purple dot represents similar phases of about 0°. The reason for such highly structured phase maps is not clear. However, it appears to be straightforward that the low energy structure ends up at different rotational angles than the rest of the electron momentum distribution (see chapter 7.3). Moreover, one could imagine two other classes of electrons contributing to the final momentum distribution. The first class are electrons that are mainly guided by the laser electric field after tunneling and are only slighlty affected by the atomic potential (direct electrons). A second class are elastically[84] scattered electrons. The direct electrons are expected to end up at the negative vector potential belonging to the maximum of the laser electric field which is about 0.3 a.u. Thus the blue/purple feature might be related to direct electrons. Elastically scattered electrons that keep their energy during a recollision but loose the information about the direction of the electrons' momentum during recollision are

[84] Inelastically scattered electrons are not expected here because the energy of the recolliding electrons is too low (see chapter 6) to lead to relevant electron impact excitation cross-sections (see [81]).

expected to end up at higher radial momenta p_r and should be broad in p_x (see chapter 6). Consequently, the green feature might be related to the class of elastically scattered electrons. The remaining unexplained feature in Fig. 7.23 is the yellow curved one. Knowing that there are only two classes of electrons one could imagine that this feature shows interference of those two classes of electrons. A similarly shaped feature has been observed by Huismans et al. [123] for linearly polarized light and was attributed to interference of direct and indirect electrons (holography). However, all these conclusions are highly speculative and there are also other explanations possible.[85]

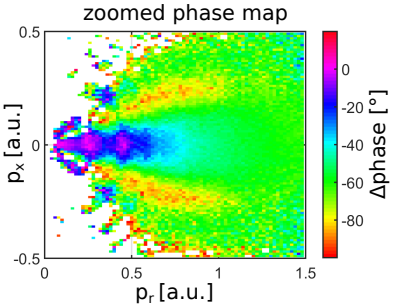


Figure 7.23: Shows the same as Fig. 7.21(b) but here the range of phases that are displayed is restricted to make smaller differences visible. A rich structure is revealed.

The analogue phase maps can also be created for electrons that were measured in coincidence with neon (see Fig. 7.24) and a comparison with the results from helium shows that the differences are small (see Fig. 7.25). Inspecting Fig. 7.25(b) the differences in Δphases are up to $\pm 10°$ and depend on p_r and p_x. A phase difference of 10° corresponds to a rotation angle in the plane of polarization of $(10/3)°$. This angle is equivalent to a time delay of 24 as in the attoclock framework.[86]

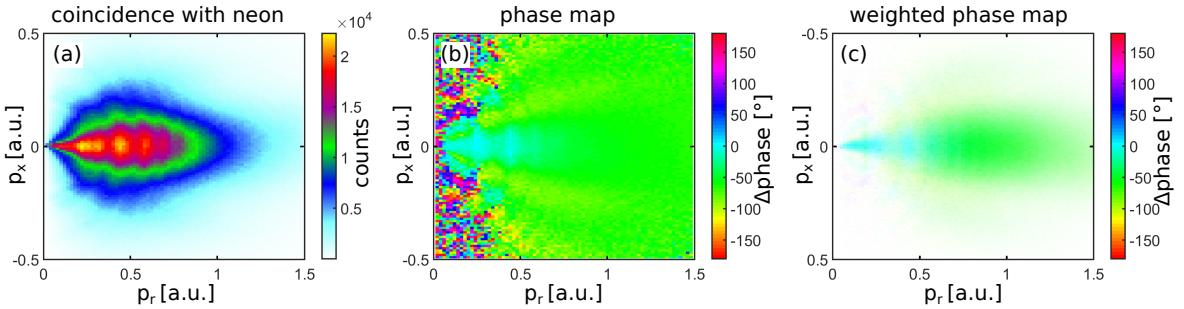


Figure 7.24: Shows the same as Fig. 7.21 but measuring electrons from neon instead of helium.

[85] For example one could imagine that the yellow arms emerge because there is less intensity in the class of electrons that belong to the green feature and in this region of momentum phase the "background" dominated the signal (but the author of this thesis considers this to be unlikely).

[86] A full rotation of 360° in the plane of polarization corresponds to a full cycle of the fundamental wavelength of 780 nm that takes 2.6 fs.

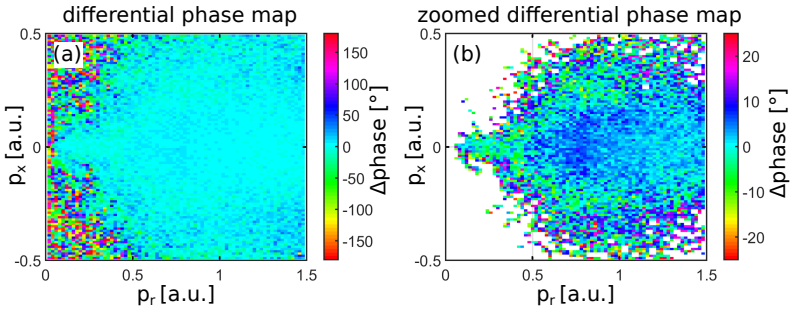


Figure 7.25: The difference of the phases from Fig. 7.21(b) and Fig. 7.24(b) are illustrated without (a) and with a restriction on the range of the differences of Δphases. In (b) differences of up to $\pm 10°$ are evident for $p_r \approx 0.8$ a.u. and the sign depends on p_x.

More phase maps are presented in chapter A.6 dealing with the results shown in Fig. 6.11(a), Fig. 7.2(a) and Fig. 7.13(a).

7.7.2. Conclusion: Comparing the Ionization of Helium and Neon

In conclusion, the differences in the electron momentum distributions comparing helium and neon are small for the given field parameters. The observed differences in the light propagation direction p_x and in the radial direction p_r appear to be biased by the detection efficiency of the ions since momentum conservation links the electron's momentum and the position on the ion detector. However, those systematic errors are expected to be small comparing the angle in the plane of polarization and the differences in this direction are on the order of $\pm 10°$ for the laser parameters belonging to the measurement of Fig. 7.2(b). A significant improvement of this measurement could be achieved using a warm gas target with a temperature such that the ions' momenta are big enough to make sure a large area on the ion detector is hit by the ions. Thus, the ions will have a big randomly oriented offset momentum (which corresponds to a certain velocity). Upon ionization the liberated electron will also posses this offset velocity and effectively this will reduce the momentum resolution for the electron in the experiment. Fortunately, the electron momentum resolution reduces only slightly because the time-of-flight of the electrons is on the order of 70 ns and the time-of-flight of the ions is on the order of 2500 ns.

8. Non-Adiabatic Tunneling: Offsets of the Initial Momentum Distribution

Chapter 8 is based on the peer-reviewed publication by Eckart et al. [25] and provides additional details. Applying a very strong static external electric field to an atom leads to adiabatic tunneling. Starting with a spherical symmetric atom it is clear from symmetry that all directions perpendicular to the direction of the external electric field are indistinguishable. In this case symmetry dictates that the electron wave packet exiting the tunnel must be rotationally symmetric with respect to the tunneling direction.
Using a time-dependent instead of a static driving field, the tunnel exit position changes with time. The resulting movement of the tunnel exit position can break the rotational symmetry around the tunneling direction. This enables to ask a central question of this chapter: if one could take a snapshot of the electron momentum distribution at the exit of the tunnel, would it be possible to infer the direction of rotation of the driving electric field?

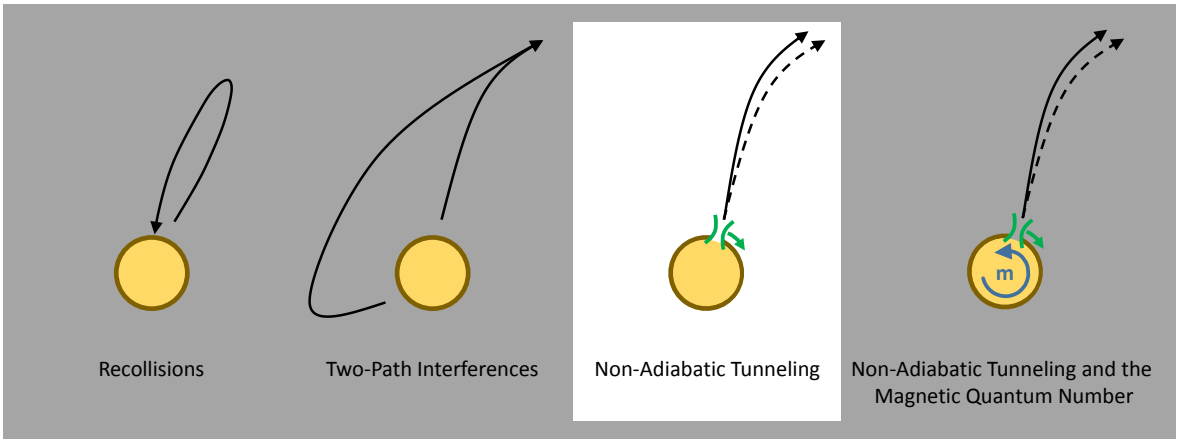


Figure 8.1: Illustration of the key scientific questions of this thesis. In chapter 8 the tunneling dynamics in the regime of non-adiabatic tunneling are investigated experimentally. The green arrows indicate the direction of the temporal evolution of the tunnel exit position.

The experimental strategy to answer this question is to use circularly polarized two-color fields. The laser field at 780 nm is very strong compared to the field at 390 nm and the helicity of the laser field at 390 nm can be used as control parameter and allows one to tune the angular velocity of the tunnel exit.

Basic question for this project: How is the momentum distribution of an electron wave packet affected if it tunnels through a potential barrier that evolves with time?

Important prerequisite: The final momentum $\vec{p}_f$ can be written as the sum of three terms: $\vec{p}_f = \vec{p}_i - \vec{A}(t_0) + \Delta\vec{p}_c$. Here $\vec{p}_i$ is the initial momentum, $-\vec{A}(t_0)$ is the negative vector potential at the instance of ionization and $\Delta\vec{p}_c$ is the momentum change that is due to Coulomb interaction after tunneling. Neglecting Coulomb interaction after tunneling, the initial momentum can be expressed by subtracting the negative vector potential from the measured final momentum. The relation $\vec{p}_i = \vec{p}_f - (-\vec{A}(t_0))$ is illustrated by Fig. 8.2 showing that a non-zero value for the initial momentum pointing along the derivative of the tunnel exit position for circularly polarized lights increases the final momentum because in this case $\vec{p}_i$ (red arrows in Fig. 8.2) is parallel to $-\vec{A}(t_0)$.

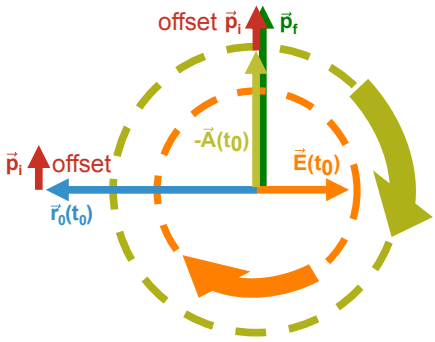


Figure 8.2: Schematic illustration of the geometry at the instance of tunneling t_0: the vector of the laser electric field $\vec{E}(t_0)$, the vector of the tunnel exit $\vec{r}_0(t_0)$, the non-adiabatic momentum offset (red arrows), the negative vector potential $-\vec{A}(t_0)$, a non-zero value for the initial momentum $\vec{p}_i$ at the tunnel exit and the final momentum neglecting Coulomb interaction after tunneling $\vec{p}_f$ are shown. The figure and its caption are based on Fig. 4(c) from Eckart et al. [25].

Experimental idea: Analyze offsets of the final electron momentum distribution depending on the effective angular frequency. The use of co- and counter-rotating two-color fields allows one to vary the effective angular frequency[87] but to keep the values of the extrema of the negative vector potentials identical[88]. See Fig. 8.3(a) and 8.3(b) for the combined electric fields and vector potentials illustrating the changes in effective angular frequency. Fig. 8.3(c) and 8.3(d) show the corresponding measured electron momentum distributions.

[87] The effective angular frequency is defined as $\omega_{\text{eff}} = \frac{\mathrm{d}\,\mathrm{atan}\left(\frac{E_z}{E_y}\right)}{\mathrm{d}t}$ (comp. Eq. 64 and see chapter A.8 for details).

[88] It is a property of circularly polarized two-color fields that the values for the minimum and the maximum of the negative vector potential are independent of the relative helicity of the two single-color laser pulses (see Fig. 8.5(a) and Fig. 8.5(b)).

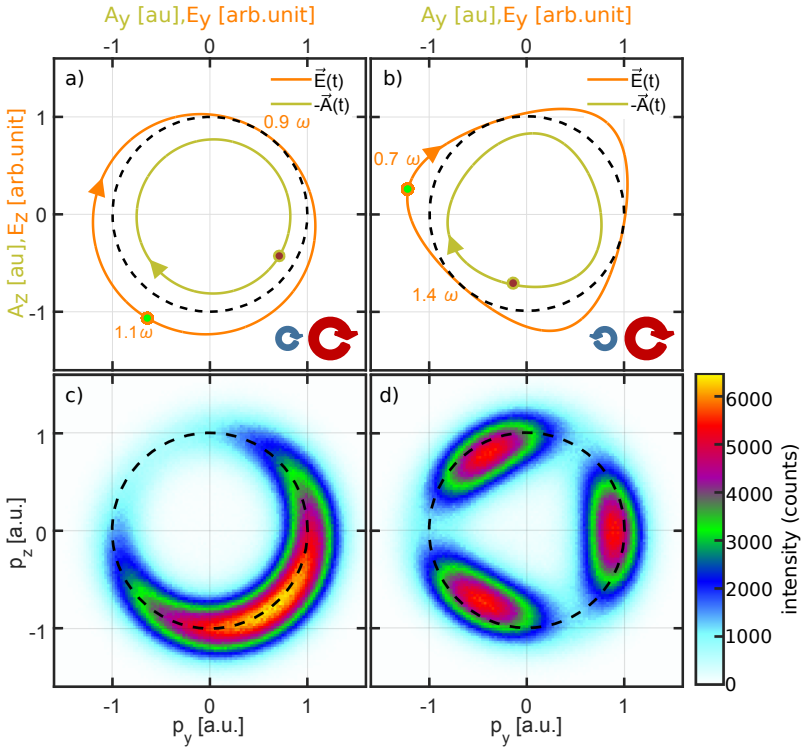


Figure 8.3: "Two-color field composed of a strong fundamental ($E_{780} = 0.046$ a.u.) and a weaker second harmonic ($E_{390} = 0.005$ a.u.) field. Both wavelengths are circularly polarized and co-rotating (a) and (c) or counter-rotating (b) and (d). Depending on the helicity of the second harmonic the derivative of the electric field can be modified (phase of highest field is shown as a dot). The angular velocity of the laser electric field for the co-rotating case is $\omega_{\text{eff}} = 1.1\,\omega$ ($\omega_{\text{eff}} = 0.9\,\omega$) and $\omega_{\text{eff}} = 0.7\,\omega$ ($\omega_{\text{eff}} = 1.4\,\omega$) for the counter-rotating case at the maximal (minimal) electric field. (c) and (d) show the corresponding experimental electron momentum distributions for single ionization of Ar. The black dashed circle guides the eye and has the same radius in all panels. The arrows indicate the temporal evolution of the laser electric field $\vec{E}(t)$ and the negative vector potential $-\vec{A}(t)$." (Figure and caption are taken from Eckart et al. [25]. A more detailed discussion of the figure is provided in chapter 8.2 and the origin of the values for the electric field's amplitude is explained in chapter 8.2.)

Experimental beauty: The only experimental parameter that is adjusted is the direction of rotation of the circularly polarized laser field at 390 nm leading to two distinct scenarios: one for co- and one for counter-rotating two-color fields. It can be shown that Coulomb interaction and thus the value of $\Delta\vec{p}_c$ is very similar for both scenarios. Thus, independent of the intensity calibration, any offset in final momentum $\Delta\vec{p}_f$ reflects an offset in initial momentum $\Delta\vec{p}_i$ leading to the relation $\Delta\vec{p}_i = \Delta\vec{p}_f$.

8.1. State of the Art: Non-Adiabatic Tunneling and the Initial Momentum Distribution

Non-adiabatic tunneling is called "non-adiabatic" because the expectation value of the electron's energy at the tunnel exit can be higher than the electron's energy in the initial state [21, 22]. This implies that the electron must have gained energy during tunneling. This is why the tunneling process is called "non-adiabatic". The gained energy modifies the shape of the initial momentum distribution leading to higher radial momenta in the plane of polarization for circularly polarized light (e.g. see Fig. 2 from Ref. [47]). Non-adiabatic tunneling occurs for Keldysh-parameters that are close to $\gamma \approx 1$. A central research question regarding non-adiabatic tunneling is how the tunnel exit position and the initial momentum distribution depend on the parameters of the driving field and the initial state.

Unfortunately, the momentum distribution at the exit of the tunnel cannot be measured experimentally because there is no experimental way to place a detector directly at the exit of the tunnel. In theory there are different approaches to infer the initial momentum distribution at the exit of the tunnel. In the following two very different approaches are presented.

One approach by Xu et al. is described in Ref. [124] and uses that the "local momentum" at any position can be extracted numerically using a "virtual detector" [125, 126]. In Ref. [124] the tunnel exit position is defined as the position where the kinetic energy is zero and it is shown that the "local momentum" (also called "flow momentum") at the tunnel exit can be non-zero. This directly implies that the local momentum is a quantum mechanical quantity without classical correspondence because classically zero kinetic energy and non-zero momentum are incompatible. However, it is an interesting result of Xu et al. that they have succeeded to show that the value of the "local momentum" depends on the wavelength of the driving field and the shape of the wave function close to the tunnel exit position.

In the second theoretic approach presented here the time-dependent Schrödinger-equation (TDSE) is solved on a grid in position space but the virtual detector is placed far away from the center of the atomic potential. It can be shown that the obtained electron momentum distribution is consistent with solving the TDSE on a grid in position space and calculating the Fourier transform after projecting out bound electronic states [127]. This result validates the "virtual detector"-method. Ni et al. [10, 74, 128] have built on this insight and introduced the method of classical backpropagation: First, the TDSE is solved on a grid in

position space and the wave function of the ground state is subtracted. The obtained complex valued wave function contains all necessairy information[89] that is needed to propagate classical trajectories backwards in time. The advantage of classical backpropagation is that there are no assumptions needed regarding the dynamics in the classical forbidden region. However, using this framework one needs to define when the backpropagation has to stop or in other words when it has reached the tunnel exit. Ni et al. name two possible criteria: One is to check for the velocity in the direction of the laser electric field to become zero ("momentum condition"). Another condition is the position condition that stops the backpropagation if the distance of the electron to the center of the potential is smaller or equal compared to the analytically known tunnel exit position ("position condition"). Ni et al. favor the momentum condition because the position conditions depends on the chosen model for the tunnel exit position (e.g. see Tab. 1 in Ref. [74]). An interesting result[90] is that the backpropagation-method and PPT-theory both predict that there is an offset[91] of the initial momentum distribution perpendicular to the tunneling direction [40, 69, 74, 129].

In order to test existing theoretic predictions, experiments have to be performed. Naturally, only experimentally accessible quantities can be compared with theory. As mentioned above, the initial momentum at the tunnel exit is not accessible by placing a detector close to the tunnel exit. Using a COLTRIMS reaction microscope the central experimental observables are the final momenta of all fragments and the corresponding ionization rates. Hence, from an experimental perspective, the ionization process is a black box and the edge of the box is reached when the laser pulse is gone and the electron is so far away that the atomic potential can be neglected. Afterwards, the electron is described as a freely propagating particle and possesses its final momentum. If one now assumes that all interaction after tunneling is classical then one can express the final momentum $\vec{p}_f$ as the sum $\vec{p}_f = \vec{p}_i - \vec{A}(t_0) + \Delta\vec{p}_c$ (see beginning of chapter 8).

Some recent achievements studying non-adiabatic tunneling that are related to the findings presented chapter 8 are:

- In 2005, Ivanov et al. [22] pointed out that in the framework of saddle point SFA an

[89] The phase-space density at every position is determined by the square of the absolute value of the wave function at this position and the momentum is encoded in the gradient of the phase at every point in position space (see paragraph above Eq. 1 in Ref. [10] for details).

[90] Another interesting result of the backpropagation method is related to the ongoing debate regarding the existence of tunneling delays (compare Eckle et al. [8]). Ni et al. argue that the work of Teeny et al. [11] and Camus et al. [12], who have claimed to have measured non-zero tunneling delays, allow for an alternative interpretation: using the momentum condition the tunneling delay is zero in both cases. Another aspect is the polarization of the initial state that can change the most probable "birth-time" of the electron (see the discussion of the work by Liu et al. [13] in chapter 9.1).

[91] The experimental access to this offset was realized by Eckart et al. [25] and is the central topic of chapter 8.

increase of initial momentum is equivalent to an increase of the ionization potential (discussion of Eq. 18 from Ref. [22]). To the best of the author's knowledge this prediction was experimentally untested until the work of Eckart et al. (see Fig. 4 of Ref. [25] or Fig. 8.10).

- In 2012, Pfeiffer et al. [130] compared experimental results with classical trajectory simulations to show that the width of the initial momentum distribution in the tunneling direction for non-adiabatic tunneling is non-zero (see also Ref. [131]).
- In 2014, Geng et al. [132] used different theoretic approaches including solving the three-dimensional Schrödinger equation, Coulomb corrected strong field approximation [68] and a trajectory based classical simulation to show that the final radial momentum in the plane of polarization p_r for circularly polarized light depends on the non-adiabaticity of the tunneling process. As a consequence, the use of adiabatic theory to calibrate the intensity in the non-adiabatic regime leads to systematic errors (see also Ref. [70]). In 2015, Geng et al. [108] employed orthogonal polarized two-color (OTC) fields to perform a similar theoretic study concluding that non-adiabatic effects alter the ionization rate (see also Ref. [21]) and lead to non-zero initial velocities at the tunnel exit.
- In 2015, Klaiber et al. [47, 48] proposed to model non-adiabatic tunneling as a two-step process (see also Ref. [133]). In a first step a few-photon absorption excites the electron to a virtual intermediate state. In a second step adiabatic tunneling occurs from that virtual state (see chapter 3.4).
- In 2016, Hofmann et al. [71] analyzed the width of the electron momentum distribution along the light propagation direction $\sigma_{\text{light prop}}$. $\sigma_{\text{light prop}}$ was measured experimentally as a function of the peak electric field showing that $\sigma_{\text{light prop}}$ can be used to determine the value of the peak electric field and thus be used to calibrate the laser intensity in experiments (see also Refs. [118, 134]).
- In 2017, Liu et al. [135] measured how the width of the electron momentum distribution along the light propagation direction $\sigma_{\text{light prop}}$ scales with the most probable radial momentum in the plane of polarization $p_r^{\max}$ for ionization by circularly polarized light. The result can be used as a benchmark that is free of any assumptions regarding the laser intensity to test the validity of adiabatic and non-adiabatic theories describing strong field ionization. Using a classical model including the magnetic quantum number (see also chapter 9) of the initial state they concluded that $p_r^{\max}$ and $\sigma_{\text{light prop}}$

both depend on the magnetic quantum number of the initial state and the long-range Coulomb potential.

From this list the most important limitation of experimental studies regarding non-adiabatic tunneling becomes obvious: it is very difficult to separate observable non-adiabatic effects from systematic uncertainties regarding the calibration of laser parameters (in particular the laser intensity). Futhermore, there is no mechanistic picture that explains the origin of non-adiabatic offsets in momentum space at the exit of the tunnel so far. For (almost) circularly polarized light both shortcomings are overcome by the work of Eckart et al. [25].

8.2. Single Ionization of Argon in Counter- and Co-Rotating Two-Color Fields

The insight that the effective angular frequency[92] ω_{eff} at the extrema of the absolute value of the combined electric field in CRTC fields can be modified by the two-color field ratio has already been evident[93] in Fig. 6.2.

Extending the parameter space by including co-rotating two-color (CoRTC) fields in addition to counter-rotating two-color (CRTC) fields the effective angular frequency at the extrema of the combined electric field depends not only on the two-color field ratio but can also be different for CoRTC and CRTC fields.[94]

Hence, a two-color experiment has been conducted searching for a footprint of ω_{eff} in final momentum space comparing CRTC and CoRTC fields with the same two-color field ratio.[95] The advantage comparing CoRTC with CRTC fields is that the intensities of the two individual single-color laser pulses can remain unchanged during the entire experiment.

Before the measurement has been conducted, the gas jet has been collimated to $40 \pm 10\,\mu\text{m}$ along the laser propagation direction in the laser focus (Rayleigh length of about $150 \pm 10\,\mu\text{m}$) to minimize the effect of focal averaging (see chapter A.1) and the inlet pressure of the gas nozzle was set to $1.25\,\text{bar} \pm 0.1\,\text{bar}$. Homogeneous electric and magnetic fields of $E_{\text{spectrometer}} = 18.0\,\text{V}\,\text{cm}^{-1}$ and $B_{\text{spectrometer}} = 10.4\,\text{G}$ guided electrons and ions in the spectrometer towards the detectors (see chapter 4.1.3). The three-dimensional electron momentum distributions from single ionization of argon presented in this chapter have not been measured in coincidence with argon ions (to increase statistics). The coincidence detection has only been used as a cross check to estimate the ratio of false electrons (which is here below 10% (for the methodology see chapter A.5.2)).

The result of the two-color measurement using an average power of $89 \pm 4\,\text{mW}$ ($2.3 \pm 1\,\text{mW}$) for the femtosecond laser pulse at a wavelength of 780 nm (390 nm) is shown in Fig. 8.3(c) and 8.3(d). The total measurement time was 5 hours. The relative phase of the two single-color laser pulses was adjusted every 4 minutes at 40 equidistant positions over a range of 389 nm. For each step of the relative phase data for the co-rotating scenario has

[92] $\omega_{\text{eff}} = \frac{\text{d}\,\text{atan}\left(\frac{E_z}{E_y}\right)}{\text{d}t}$

[93] In particular, in Fig. 6.2(b) in which the effective angular frequency is close to zero.

[94] To this end Fig. A.46 and chapter A.8 provide a rigorous analysis of the effective angular frequency in circularly polarized two-color fields.

[95] However, at first it was not clear how to analyze the measured data to access the initial momentum distribution. By coincidence, Kilian Fehre was analyzing data from the ionization of molecules by circularly polarized light using the normalization as in Fig. 8.10(d). This led to the first observation of the unexpected curved feature (see black solid line in Fig. 8.10(d) which is called the "banana"-like distribution) and triggered the search for its origin. The break through of this search was that saddle point SFA (which was known to the author of this thesis from a talk by Dieter Bauer [65]) succeeded to reproduce the "banana"-like distribution.

been collected for 2 minutes and data for the counter-rotating scenario has been collected for 2 minutes afterwards. (In fact, the helicity was inverted every 2 minutes throughout the measurement). After one scan of the relative phase was completed the scan started from the beginning. The changes due to the automated scan and drifts of the relative phase of the two single-color laser pulses were compensated offline as described in chapter A.2. Fig. 8.4(a) and 8.4(b) show the same data as Fig. 8.3 visualizing the data in three dimensions as routinely done in chapter 7.

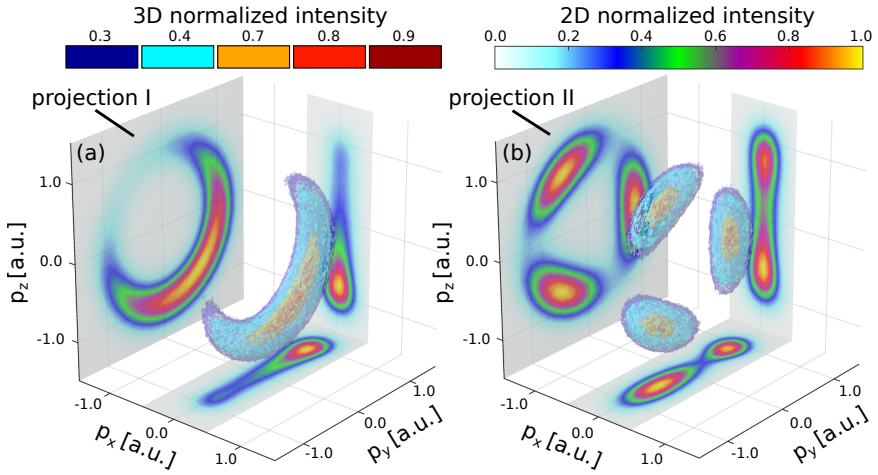


Figure 8.4: Three-dimensional (3D) electron momentum distributions upon the ionization of argon by co-rotating (a) and counter-rotating (b) two-color fields show the same data as in Fig. 8.3(c) and 8.3(d). The 3D momentum distributions are visualized by combining five semitransparent isosurfaces encoding the intensity of the 3D histogram by color as routinely done for chapter 7. The $p_y p_z$-plane is the polarization plane. The 2D histograms show projections.

Fig. 8.4(a) shows a clear single peak in three-dimensional momentum space reflecting the onefold symmetry of the corresponding CoRTC field (see Fig. 8.3(a)). Since (non-adiabatic) tunneling[96] is a highly nonlinear process almost all electrons are "born" close to the peak of the combined electric field which is marked by a green dot in Fig. 8.3(a). The corresponding negative vector potential is marked with a red dot and indicates the region in final momentum space where most electron are driven by the combined electric field (comp Fig. 8.3(c)). Fig. 8.4(b) shows three peaks in three-dimensional momentum space reflecting the threefold symmetry of the corresponding CRTC field (see Fig. 8.3(b)). Also here one peak of the combined electric field is marked by a green dot in Fig. 8.3(b). The corresponding

[96] Fig. 8.4(a) contains $14.1 \cdot 10^6$ counts and Fig. 8.4(b) contains $14.5 \cdot 10^6$ counts. This shows that the ionization rate is slightly increased for the counter-rotating scenario. This is in line with the observation by Mancuso et al. [136] that ionization is preferred in counter-rotating two-color fields compared to co-rotating two-color fields. This is an interesting result for itself, since for adiabatic tunneling there cannot be any difference for counter- and co-rotating fields regarding the tunneling probability after integrating over one optical cycle. Mancuso et al. attribute the difference to the circumstance that the conservation of angular momentum suppresses the population of intermediate states for CoRTC fields.

negative vector potential is marked with a red dot. Most electrons are observed in the region in momentum space which is marked with a red dot on the corresponding negative vector potential (comp. Fig. 8.3(b) and 8.3(d)).

8.2.1. Direct Access to Non-Adiabatic Offsets

Fig. 8.5(a) and 8.5(b) show the negative vector potential from Fig. 8.3(a) and 8.5(b) in cylindrical coordinates. It can be seen that the extrema of the absolute value of the negative vector potential $|-\vec{A}(t)|$ as a function of the angle in the plane of polarization in Fig. 8.5(a) and 8.5(b) have the same value. The aim is to compare electrons that are born at the minimum[97] of $|-\vec{A}(t)|$. The value of $|-\vec{A}(t)|$ is identical for CoRTC and CRTC fields but the effective angular frequency is $\omega_{\text{eff}} = 0.9\,\omega$ for the CoRTC field and $\omega_{\text{eff}} = 0.7\,\omega$ for the CRTC field. What is the impact of the difference in ω_{eff} on the radial momentum?

In order to provide the experimental answer to this question, the data shown in Fig. 8.4 is restricted to a small slice along the light propagation direction $|p_x| = 0.15 \pm 0.05$ a.u. to minimize the influence of the atomic potential after tunneling (see e.g. chapter 7.3). The two resulting subsets are presented in Fig. 8.5(c) and 8.5(d) after normalizing every column individually. The intensity prior to normalization is shown as contour lines (see caption of Fig. 8.5 for details). The intensity for the contours and the intensity in the normalized histograms in cylindrical coordinates show the counts divided by the radial electron momentum p_r to take the volume element into account. This makes sure that the coordinate of the brightest pixel in Fig. 8.5(c) and 8.5(d) corresponds to the coordinate of the brightest pixel in Cartesian coordinates.

[97] One could also compare electrons that are "born" at the maximum of $|-\vec{A}(t)|$. The disadvantage of this option is that for the CRTC field the electrons in final momentum space that belong to the maximum of $|-\vec{A}(t)|$ are very close to the electrons that belong to the minimum of $|-\vec{A}(t)|$. Most electrons are born at the maximum of $|E(t)|$. At this instance in time $|-\vec{A}(t)|$ is minimal for CRTC fields. Hence, the region in momentum space belonging to the minimum of $|-\vec{A}(t)|$ is very populated and close to the region belonging to the maximum of $|-\vec{A}(t)|$. Therefore, in the region in momentum space belonging to the maximum of $|-\vec{A}(t)|$ it is likely to find electrons that actually belong to the minimum of $|-\vec{A}(t)|$ but have a high initial momentum at the tunnel exit. For CoRTC field this problem is less critical because maximum and minimum of $|-\vec{A}(t)|$ belong to electrons that are further apart in final momentum space.

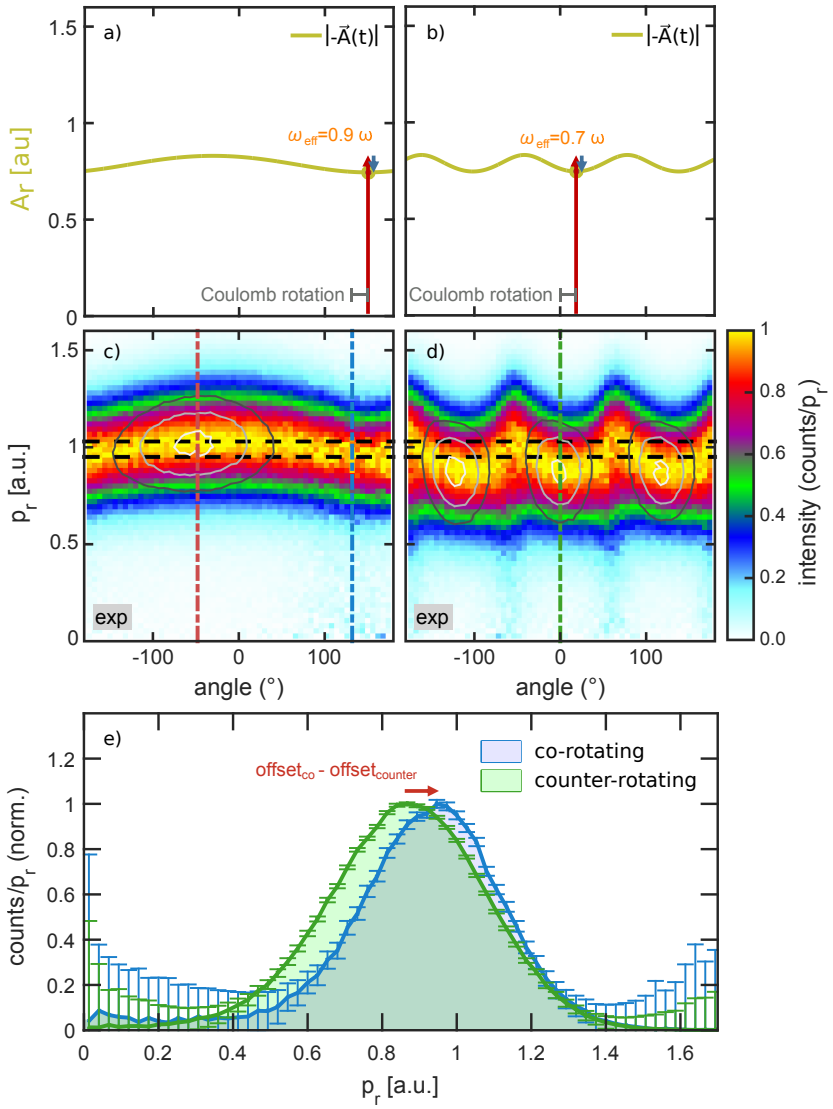


Figure 8.5: "The golden line in (a) and (b) shows the negative vector potentials from Fig. 8.3 [remark - the number of the referenced figure has been adapted] in cylindrical coordinates. The minimal vector potential is identical in (a) and (b) and marked with a long red and a short blue arrow that indicate the two driving fields that have anti-parallel vector potentials at this time. The effective angular frequency is not equal at this instance ($\omega_{\text{eff}} = 0.9\,\omega$ in (a) and $\omega_{\text{eff}} = 0.7\,\omega$ in (b)). (c)-(e) show the data from Fig. 8.3 [remark - the number of the referenced figure has been adapted] in cylindrical coordinates where p_x is the momentum component parallel to the light propagation and $p_r = \sqrt{p_y^2 + p_z^2}$ (subset of data with $|p_x| = 0.15 \pm 0.05$ a.u.). The data in (c) and (d) has been normalized columnwise. The most probable radial momentum $p_r^{peak}(\varphi)$ is angle-dependent. The minimal and the maximal p_r^{peak} in (c) are marked as black dashed lines and guide the eye in (c) and (d). (e) shows subsets of (c) and (d) restricting the angle to $132 \pm 10°$ in (c) and $0 \pm 10°$ in (d). The angular gates are indicated by blue and green vertical lines, which are shifted with respect to the corresponding vector potential due to the Coulomb rotation (obtained from the CTS model). Contour lines indicate the intensity in (c) and (d) prior to normalization of each angle individually. The dark gray, light gray and white lines indicate 45%, 70% and 95% of maximal intensity." (Figure and caption are taken from Eckart et al. [25].)

For every φ in Fig. 8.5(c) and Fig. 8.5(d) the most probable radial momentum p_r^{peak} can be determined. It is evident that the minimal value of p_r^{peak} is lower for Fig. 8.5(d) than for Fig. 8.5(c). In the following it will be shown that this is due to an non-adiabatic offset of the

initial momentum at the tunnel exit.

To further analyze this finding the angle in the plane of polarization can be used to restrict the "birth-times" of the electrons.[98] In Fig. 8.5(e) electrons stemming from the minimum of $|-\vec{A}(t)|$ are shown and it is clearly seen that the electrons from the CRTC field have lower radial momenta than the electrons from the CoRTC field. The difference is highlighted by a red arrow and is on the order of 0.1 a.u.

To demonstrate that this difference is really due to a difference in non-adiabatic offsets of the initial momentum distribution and not due to Coulomb interaction after tunneling two complementary theoretic models are used. The first model is saddle point strong field approximation (SFA) which incorporates non-adiabatic offsets but neglects all Coulomb interaction after tunneling. The second model is a classical two step (CTS) simulation which is an adiabatic theory (see chapter 5). Fig. 8.6(a) and 8.6(b) [8.6(c) and 8.6(d)] show the results from SFA [CTS] for the co- and the counter-rotating scenario, respectively.

[98] It is shown in chapter 8.2.2 that Coulomb interaction after tunneling slightly changes the angle in the plane of polarization. The corresponding angular offset is indicated in Fig. 8.5(a) and 8.5(b).

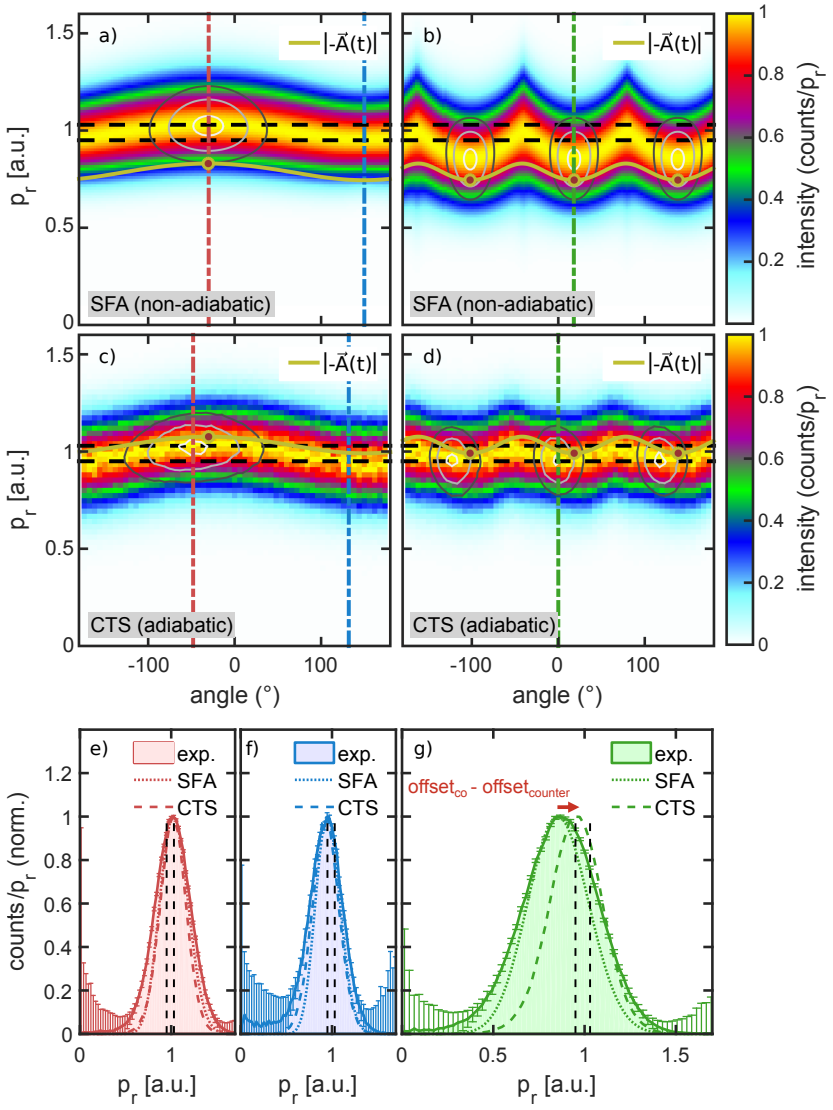


Figure 8.6: "Theoretical modeling of the experimental data shown in Fig. 8.5 [remark - the number of the referenced figure has been adapted]. The left column shows co-rotating fields, the right column counter-rotating fields. The black dashed lines from Fig. 8.6(c) [remark - the number of the referenced figure has been adapted] serve as references in all panels. (a) and (b) show the (non-adiabatic) SFA result neglecting intracycle interference. (c) and (d) show the result from the (adiabatic) CTS model. The intensity has been chosen for SFA ($E_{780} = 0.046$ a.u. and $E_{390} = 0.005$ a.u.) and CTS ($E_{780} = 0.060$ a.u. and $E_{390} = 0.005$ a.u.) independently such that (a) and (c) match Fig. 8.5(c) [remark - the number of the referenced figure has been adapted]. (e) and (f) show subsets of (a) ((c) and Fig. 8.5(c) [remark - the number of the referenced figure has been adapted]) restricting the angle to $-30 \pm 10°$ and $150 \pm 10°$ ($-48 \pm 10°$ and $132 \pm 10°$). (g) shows subsets of (b) ((d) and 8.5(d) [remark - the number of the referenced figure has been adapted]) restricting the angle to $18 \pm 10°$ ($0 \pm 10°$). The corresponding angular gates are indicated by colored vertical lines. The golden lines in (a)-(d) show the negative vector potentials. Contour lines in (a)-(d) indicate the intensity prior to normalization as in Fig. 8.5 [remark - the number of the referenced figure has been adapted]. All data shown is restricted to $|p_x| = 0.15 \pm 0.05$ a.u." (Figure and caption are taken from Eckart et al. [25].)

The field parameters[99] were adjusted by matching Fig. 8.6(a) and 8.6(c) to the experimental result (Fig. 8.5(c)) for the SFA and the CTS calculation independently (see Fig. 8.6(e) and

[99] The field parameters are $E_{780} = 0.046$ a.u. and $E_{390} = 0.005$ a.u. for the SFA model and $E_{780} = 0.060$ a.u. and $E_{390} = 0.005$ a.u. for the CTS model. For Fig. 8.3 and Fig. 8.5(a) and 8.5(b) the field parameters using the calibration that belongs to the model based on SFA are used.

8.6(f)). The presentation, the normalization and the lines to guide the eye are as in Fig. 8.5. The vertical lines[100] indicate the conditions on the angles in the final momentum space that are chosen to select electrons that are "born" at the extrema of $|-\vec{A}(t)|$. In Fig. 8.6(g) it is clearly seen that the experiment is reproduced by the model based on SFA while the CTS model fails to model the experiment. In other words, the adiabatic model with Coulomb interaction (CTS) fails to explain the experimental observation and the non-adiabatic model that neglects all Coulombic interaction after tunneling (SFA) correctly models the experimental outcome.

[100]The maximum of the contours in Fig. 8.6(c) and 8.6(d) is observed for an angle in the plane of polarization that differs from the angle that belongs to the extremum of $|-\vec{A}(t)|$ (the green, blue and red vertical dashed lines are shifted in angle for the CTS model compared to the SFA model). This shift of 18° is due to Coulomb interaction after tunneling and is used to determine the relative phase of the two single-color laser pulses for Fig. 8.3(a), 8.3(b), 8.5(a) and 8.5(b). See also chapter 8.2.2.

8.2.2. Analysis of Coulomb Interaction after Tunneling

To quantitatively analyze the changes that are due to the Coulombic interaction after tunneling the CTS model can be used. Each trajectory is simulated with and without taking the Coulomb potential into account after the electron has left the tunnel. The resulting two values for the radial momentum in the plane of polarization are $p_r^{\text{with Coulomb}}$ and $p_r^{\text{without Coulomb}}$. The difference of those two momenta is calculated for every trajectory and filled into a histogram as a function of the angle of the negative vector potential at the instance of ionization t_0 in Fig. 8.7. The colored vertical lines depict minima/maxima of $|-\vec{A}(t)|$ and the relevant ionization times are marked with arrows. It is clearly seen that the Coulomb interaction after tunneling at the relevant "birth-times" (which are indicated by arrows in Fig. 8.7(a) and 8.7(b)) is very similar for the co- and the counter-rotating scenario.

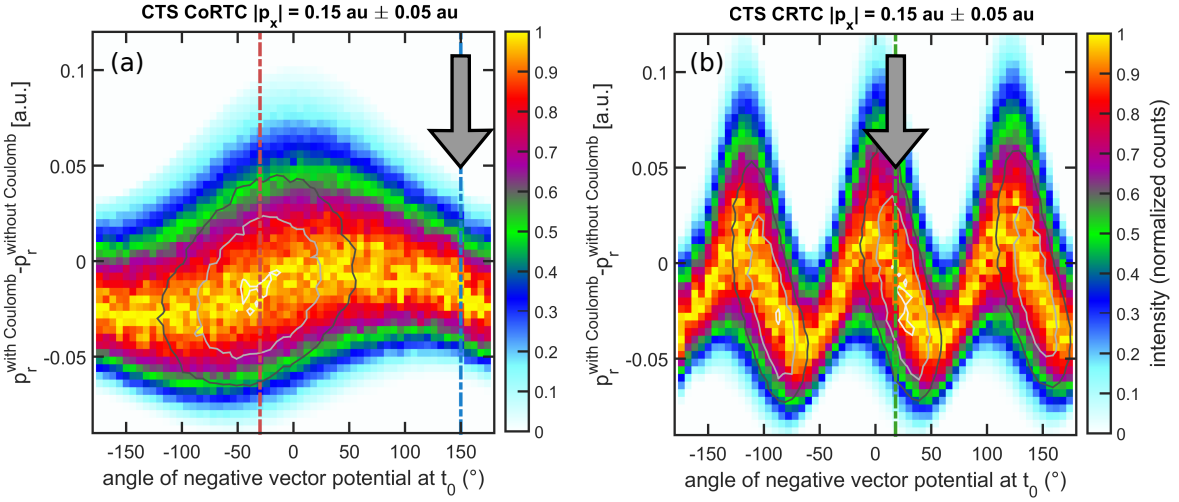


Figure 8.7: Deviations in radial momenta in the plane of polarization are shown as function of the angle of the negative vector potential in the plane of polarization for a subset of data with $|p_x| = 0.15 \pm 0.05$ a.u. for the CoRTC (a) and the CRTC (b) scenario. The deviations are calculated for each trajectory independently and filled into the shown histograms. The colored vertical lines indicate extrema of $|-\vec{A}(t)|$ and the relevant ionization times are marked with arrows. The contours are defined as in Fig. 8.6. The figure has been part of the answer to the referees regarding the publication Eckart et al. [25]. Labels and layout have been adapted.

Fig. 8.8 shows the change of the angle in the plane of polarization in electron momentum space in analogy to Fig. 8.7. Also here, each trajectory is simulated with and without taking the Coulomb potential into account after the electron has left the tunnel. The two values for the angle in momentum space in the plane of polarization are $angle^{\text{with Coulomb}}$ and $angle^{\text{without Coulomb}}$. For each trajectory, the difference of those two angles is filled into the histogram as a function of the angle of the negative vector potential at the instance of ionization t_0 in Fig. 8.7. Fig. 8.8 reveals that the offset angle depends on the electron's "birth-time" and varies between 11° and 18°. However, for the relevant "birth-time" (which

is marked with a gray arrow in Fig. 8.8) the offset angle is 18°. Further, it is clearly seen that the Coulomb interaction at the indicated times is very similar for the co- and the counter-rotating scenario and leads to rotation angles on the order of 18°. Originally, the offset angle of 18° has been determined comparing Fig. 8.6(a) and 8.6(c) [Fig. 8.6(b) and 8.6(d)] for the CoRTC [CRTC] field. Thus, the offset angle of 18° is already considered in the analysis leading to Fig. 8.5(e) and 8.6(g).

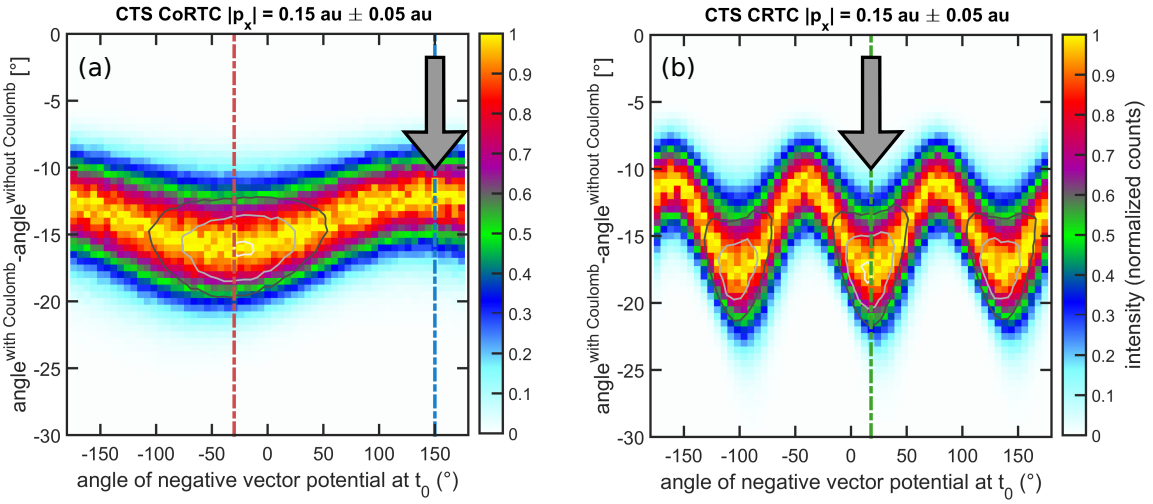


Figure 8.8: In analogy to Fig. 8.7 the deviations in the angle of the final momentum in the plane of polarization as a function of the angle of the negative vector potential in the plane of polarization are shown (see text for details and Fig. 8.7 for further descriptions).

8.3. Non-Adiabatic Offsets upon Ionization by a Single-Color Field

The fact that saddle point SFA correctly models the non-adiabatic offsets motivates to have a look at the definition of the action S_0 that lies at the heart of the method. Using Eq. 11 and Eq. 12 from chapter 5.1 the action can be written as[101]

$$S_0(\vec{p},t) = \int_t^\infty \left[\frac{1}{2}\left(\vec{p}+\vec{A}(t)\right)^2 + I_p\right] \mathrm{d}t' \tag{24}$$

where $\vec{p}$ is the final electron momentum. Since the driving field is zero along the light propagation direction S_0 can be rewritten as [25]:

$$S_0(\vec{p},t) = \int_t^\infty \left[\frac{1}{2}\begin{pmatrix} 0 \\ p_y + A_y(t) \\ p_z + A_z(t) \end{pmatrix}^2 + I_p + \frac{1}{2}p_x^2\right] \mathrm{d}t' \tag{25}$$

This is a surprising result because it indicates an equivalence of I_p and $\frac{1}{2}p_x^2$ (see also Ref. [22]). From chapter 3 it is known that I_p changes the Keldysh-parameter and therefore also the non-adiabaticity of the ionization process. Hence, saddle point SFA predicts that the non-adiabatic offsets in the plane of polarization depend on the momentum in the light propagation direction p_x.

This prediction is tested experimentally by analyzing the three-dimensional momentum distribution upon the single ionization of argon by a circularly polarized femtosecond single color laser field at 780 nm. For this measurement, everything is as for the measurement Fig. 8.3 is based on. The difference is that only the fundamental frequency is used with an average power of 90.5 ± 3.5 mW and of course no offline compensation or variations of the relative phase of the two single-color laser pulses were needed (because only a single color was used). $1.5 \cdot 10^8$ events were recorded during a total measurement time of 40 hours. Fig. 8.9 shows the resulting electron momentum distribution in the plane of polarization which shows the expected "donut"-like distribution.

[101] see e.g. Ref. [61] or chapter 5

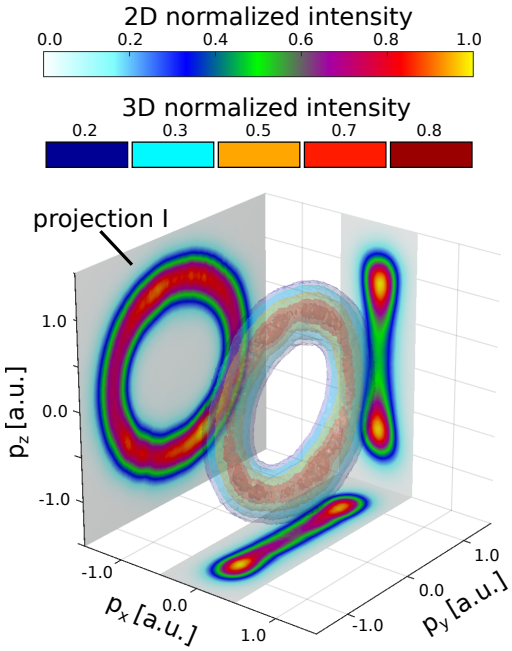


Figure 8.9: Three-dimensional (3D) electron momentum distribution upon the ionization of argon by a single color field at 780 nm. The 3D momentum distributions are visualized by combining five semitransparent isosurfaces encoding the intensity of the 3D histogram by color as routinely done in chapter 7. The $p_y p_z$-plane is the polarization plane. The 2D histograms show projections.

Fig. 8.10(a) shows projection I from Fig. 8.9. Fig. 8.10(b) shows the same data as Fig. 8.9 integrating over the angle in the plane of polarization. Normalizing every column of the histogram of Fig. 8.10(b) individually and restricting the range of p_r leads to the histogram shown in Fig. 8.10(d). A clear dependence of the radius in the plane of polarization $p_r = \sqrt{p_y^2 + p_z^2}$ on the momentum in the light propagation direction p_x is evident as a curved distribution ("banana"-like distribution) which is illustrated by the black line that guides the eye in Fig. 8.10(b) and 8.10(d).

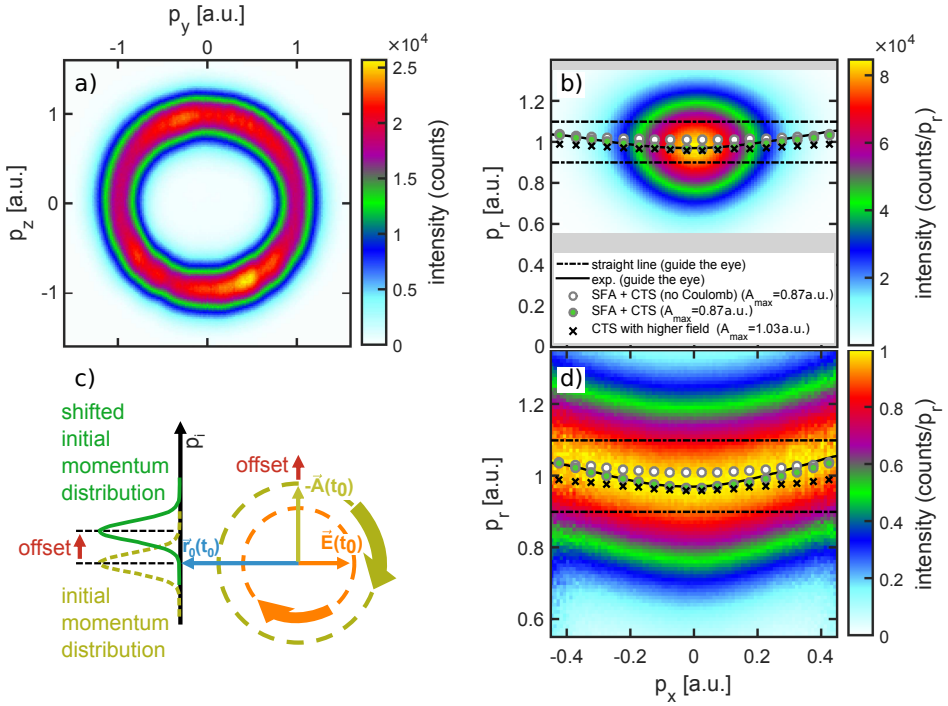


Figure 8.10: "Influence of the electron momentum p_x (along the laser propagation direction) on p_r (radial electron momentum in the plane of polarization). (a) experimental electron momentum distributions from single ionization of Ar by circularly polarized light at 780 nm. (b) shows the same data as (a) but in cylindrical coordinates. (c) illustrates the geometry at the instance of tunneling t_0: the direction of the laser electric field $E(t_0)$, the direction of the tunnel exit $r_0(t_0)$, the non-adiabatic offset (red arrow), the negative vector potential $-A(t_0)$ and the initial momentum (p_i) distribution at the tunnel exit. (d) shows the same as (b) after every column is normalized individually. The maximum of each column in (b) and (d) is indicated by the black solid line to guide the eye. The horizontal golden line shows the negative vector potential. The classical two-step (CTS) simulation with a peak vector potential of $A_{max} = 0.87$ a.u. including the initial momentum offset from SFA has been calculated without (white dots) and including Coulomb interaction (green dots) of the electron with the ion after tunneling. The black crosses show the CTS simulation for increased peak vector potential ($A_{max} = 1.03$ a.u.) and without initial momentum offset but with Coulomb interaction." (Figure and caption are taken from Eckart et al. [25].)

In a first attempt to understand the origin of the "banana"-like distribution the CTS model is used and the value for the peak vector potential is adjusted such that the most probable radial momentum agrees with the experiment for $p_x = 0$ a.u. The result of the CTS model is shown as black crosses in Fig. 8.10(b) and 8.10(d). It can be seen that the CTS model underestimates the curvature of the "banana" but apparently Coulomb interaction after tunneling produces about 50 % of the curvature of the experimentally observed "banana"-like distribution.

In a logical next step the offset of the initial momentum distribution at the exit of the tunnel can be extracted from saddle point SFA and used to offset the initial momentum distribution at the exit of the tunnel in the CTS model. The value for the peak vector potential has to be guessed and iteratively adjusted. For a value for the peak vector potential of $A_{max} = 0.87$ a.u.

the offset of the initial momentum distribution from saddle point SFA can be modeled[102] by $\Delta p_i(p_x) = 0.18164 + 0.12825 p_x^2 - 0.0091726 p_x^4$. The green dots indicate the most probable radial momentum predicted by this mixed model from SFA and CTS which almost perfectly coincide with the black line that guides the eye for the experimental data. In conclusion, the "banana"-like distribution is partly due to Coulomb interaction after tunneling and partly due to non-adiabatic offsets. This result is corroborated by switching off the Coulomb interaction after tunneling in the mixed model. The resulting white dots in Fig. 8.10(d) again underestimate the curvature of the "banana".

Fig. 8.10(c) provides an overview of the geometry of the offsets of the initial momentum distribution with respect to the electric field, the negative vector potential, the tunnel exit position and the definition of the direction of rotation of the electric field.

[102] The expression for p_i is represented as a Taylor-expansion to the 4th order. The choice of the fourth order has no physical meaning.

8.4. The Effective Keldysh-Parameter for Non-Adiabatic Offsets

Usually the Keldysh-parameter is defined by (see Ref. [1] and chapter 3):

$$\gamma = \frac{\omega}{E_0}\sqrt{2I_p} \tag{26}$$

Given the experimental observation of the "banana"-like distribution and knowing that SFA faithfully models non-adiabatic offsets the ionization potential I_p can be replaced with an effective ionization potential $I_p^{\text{eff}} = I_p + \frac{1}{2}p_x^2$ (see Eq. 25). Moreover, it has been shown experimentally in chapter 8.2 that the strength of the non-adiabatic offset scales with ω_{eff}.

Hence, the dependence of the non-adiabatic offset at the exit of the tunnel can be quantified by a single, newly introduced parameter which is the effective instantaneous Keldysh-parameter[103]

$$\gamma_{\text{eff}}(t) = \frac{\omega_{\text{eff}}(t)}{|E(t)|}\sqrt{2I_p^{\text{eff}}} \tag{27}$$

where $|E(t)|$ is amplitude of the instantaneous electric field at time t [25].

Having derived $\gamma_{\text{eff}}(t)$ as the figure of merit indicating the strength of the non-adiabatic offset one can ask the questions for the ideal two-color field ratio η to perform the experiment discussed in chapter 8.2. To this end Fig. A.47 from chapter A.8.1 provides the effective Keldysh-parameters at the extrema of the CoRTC and the CRTC field as a function of the relative intensity of the two single-color laser pulses. At first one might think that the ideal ratio is $\eta = 0.5$ because the effective Keldysh-Parameter is zero at the peak of the CRTC field. Interestingly, the effective Keldysh-parameter at the minimum of the CoRTC field vanishes as well for $\eta = 0.5$. Moreover, it is obvious that the assumption that the Coulomb interaction after tunneling is the same in the CoRTC and the CRTC case does only hold for $\eta \ll 1$ and $\eta \gg 1$. Another restriction is that for $\eta \gg 1$ there are two possible "birth-times" that have very similar vector potentials. Due to the initial momentum distributions there can be two pathways to the same final momentum. This gives rise to interference making the interpretation of the measured data more difficult (see e.g. Ref. [121]). In conclusion, η must be bigger than zero but as small as possible. $\eta = 0.1$ as chosen for the performed experiment appears to be an excellent choice.

[103] Barth and Smirnova [69, 129] write that the final momentum with the maximal ionization rate is given by $k_0 = A_0\sqrt{1+\gamma^2}\frac{1-\zeta_0}{1+\zeta_0}$ (see text below Eq. 5 in [69] for the definition of ζ_0 (which only depends on γ) and further details). If one replaces the Keldysh-parameter with the effective instantaneous Keldysh-parameter and subtracts the vector potential from the final momentum k_0 then the initial momentum at the exit of the tunnel can be calculated as a function of the vector potential, the ionization potential and the momentum in the light propagation direction.

8.5. Mechanistic Picture of Non-Adiabatic Tunneling

To illustrate that angular momentum is related to the non-adiabatic offset in saddle point SFA the SFA-trajectory in position space for circularly polarized light is calculated (see Fig. 8.11). The laser parameters are as for Fig. 8.10. The color code depicts the angular momentum L_x along the light propagation direction (corresponding to a classical movement in the plane of polarization) which has been obtained by calculating $\vec{L} = \Re(\vec{r} \times \vec{p})$. At the exit of the tunnel the value of $L_x = 1.8$ a.u. is obtained.

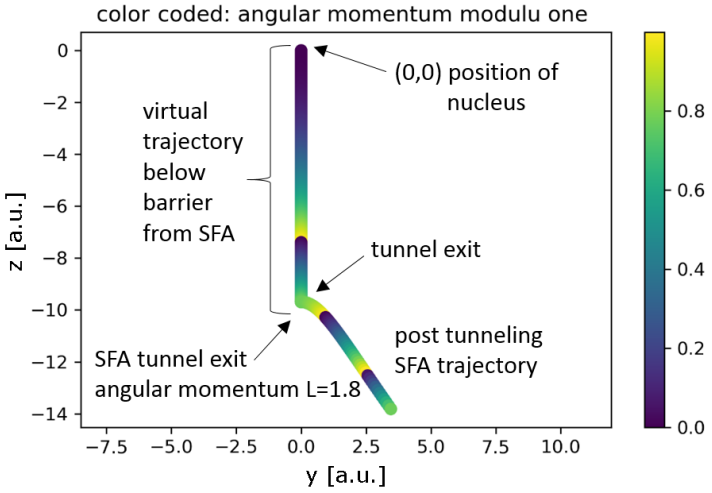


Figure 8.11: The real valued components of the position coordinates in the plane of polarization belonging to the saddle point SFA-trajectory that leads to the most probable final momentum. The color code shows the angular momentum $\vec{L} = \Re(\vec{r} \times \vec{p})$ modulo one. Here the value of $L_x = |\vec{L}|$ is equivalent to the energy of the electron (relative to the electron's energy in its ground state) in units of the photon energy. At the exit of the tunnel $L_x = 1.8$ is obtained. It is important to realize that the real part of the vertical momentum component in the tunnel (straigt section of the trajectory) is zero and the electron traverses the tunnel in zero real time. However, the imaginary component of time changes as the electron traverses the tunnel. The figure has been part of the answer to the referees regarding the publication by Eckart et al. [25]. Labels and layout have been adapted. The numerical implementation of the saddle point SFA calculation was realized by Nicolas Eicke and Manfred Lein. The SFA-trajectory representation of non-adiabatic tunneling was done by Nicolas Eicke upon suggestion by the author of this thesis and is based on ideas by Klaiber et al. [47, 48].

This result is the essence of this chapter and explains the mechanistic origin of the measured non-adiabatic offsets. As expected for non-adiabatic tunneling the electron's energy changes as it travels through the tunnel [22, 47, 48]. Since all energy the electron gains must come from the driving field the angular momentum in the plane of polarization must increase by one for every photon that is absorbed under the barrier. Assuming the conservation of angular momentum at the tunnel exit one can estimate the non-adiabatic offset of the initial momentum in the plane of polarization and perpendicular to the tunneling direction p_i by $L_x = |\vec{r}_0| \cdot p_i = m$ where $m = 1.8$ is the expectation value for the number of photons[104] that

[104]The photons that are absorbed lead to the population of virtual intermediate off-shell states (see Klaiber et al. [48]).

are absorbed under the tunnel barrier. Starting with an initial state that has a magnetic quantum number of zero allows one to assign m with the expectation value of the magnetic quantum number[105] of the virtually populated intermediate state (see also chapter 9). Assuming that the tunnel-exit position is known[106] to be approximately 10 a.u., the measurement of p_i allows one to infer the expectation value of the magnetic quantum number of the virtually populated intermediate state. Hence, the magnetic quantum numbers of virtually populated intermediate states are experimentally accessible.

For completeness, two further examples for SFA-trajectories are shown. In Fig. 8.12(a) the Keldysh-parameter has been set to $\gamma = 0.28$ using the scaling parameter $\alpha = 0.05$ (see chapter 5.2). The tunnel exit position is $r_0 = 11$ a.u. and $m = 0.15$ which leads to a value for the initial momentum offset of $p_i = 0.01$ a.u. which is almost zero as expected for $\gamma = 0.28$ which is close to adiabatic tunneling. Fig. 8.12(b) shows the same for $\alpha = 4$ leading to $m = 2.5$, $r_0 = 8$ a.u. and $p_i = 0.3$ a.u.

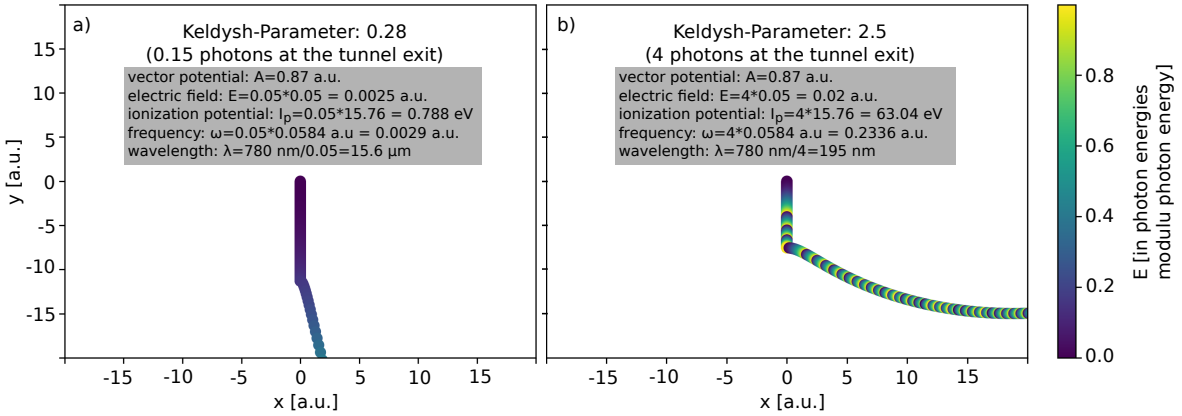


Figure 8.12: The real valued components of the position coordinates in the plane of polarization belonging to the saddle point SFA-trajectory that leads to the most probable final momentum. (a) [(b)] is calculated with $\alpha = 0.05$ [$\alpha = 4$] leading to a Keldysh-parameter of $\gamma = 0.28$ [$\gamma = 2.5$] (parameters and the definition of α are as in chapter 5.2). The color code shows the angular momentum L_x modulo one. At the exit of the tunnel $L_x = 0.15$ a.u. ($L_x = 4$) is obtained. In (a) the Keldysh-parameter is small. This means that the electric field is almost static. Hence, the photons' properties are not important for tunneling and almost no angular momentum is transferred. The gray boxes provide an overview of the relevant parameters. The numerical implementation of the saddle point SFA calculation has been realized by Nicolas Eicke and Manfred Lein and was used by the author of this thesis to obtain the results that are shown in the figure. The representation of non-adiabatic tunneling is related to ideas by Klaiber et al. [47, 48].

Fig. 8.13 (Fig. 8.14) presents the real component of the time (the electron's energy) as a function of the electron's radial position coordinate in the plane of polarization. Fig. 8.13

[105] The equivalence of the number of absorbed photons and the value of the magnetic quantum number was already described by Klaiber et al. [48] but to the best of the author's knowledge it was not suggested to use the conservation of angular momentum during tunneling to infer the initial momentum offset. However, in Ref. [48] another very interesting perspective has been presented regarding the spatial extend of the wave function: "After each photon absorption there is a changed wave function and, since the energy is higher, this wave function usually extends to larger distance. That is, as each photon is absorbed virtually, the atom 'swells' in extent."

[106] Various tunnel-exit positions are discussed in Ref. [74].

illustrates that tunneling occurs without changing the real component of time and that the tunnel exit position decreases for non-adiabatic tunneling compared to adiabatic tunneling. Fig. 8.14 underlines that almost adiabatic tunneling corresponds to almost horizontal transitions and non-adiabatic tunneling corresponds to diagonal transitions (see also Fig. 3.3).

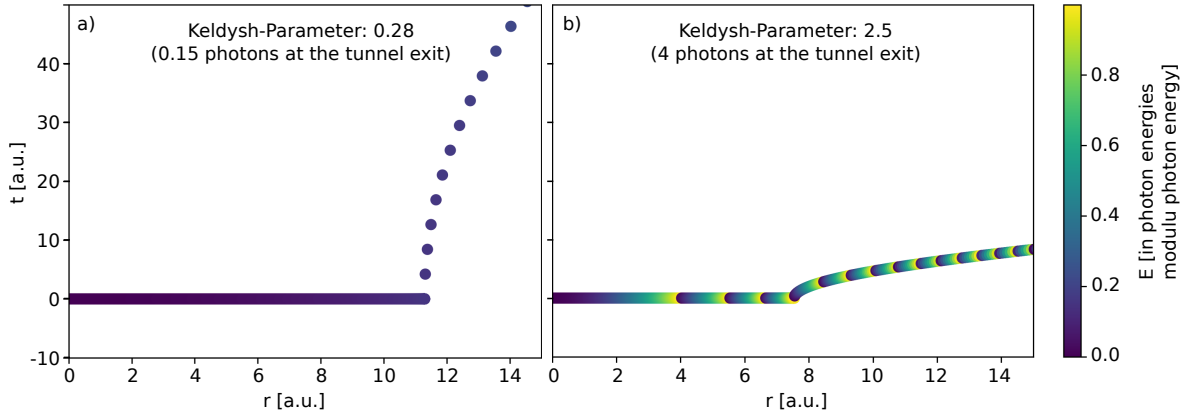


Figure 8.13: The real valued components of time and the radial position in the plane of polarization belonging to the saddle point SFA-trajectory that leads to the most probable final momentum. (a) [(b)] is calculated with $\alpha = 0.05$ [$\alpha = 4$] leading to a Keldysh-parameter of $\gamma = 0.28$ [$\gamma = 2.5$] (parameters and the definition of α are as in chapter 5.2). The color code shows the angular momentum $\vec{L} = \Re(\vec{r} \times \vec{p})$ modulo one (the value of $|\vec{L}| = L_x$ is equivalent to the energy of the electron (relative to the electron's energy in its ground state) in units of the photon energy). At the exit of the tunnel $L_x = 0.15$ a.u. ($L_x = 4$ a.u.) is obtained. The numerical implementation of the saddle point SFA calculation has been realized by Nicolas Eicke and Manfred Lein and was used by the author of this thesis to obtain the results that are shown in the figure. The representation of non-adiabatic tunneling is related to ideas by Klaiber et al. [47, 48].

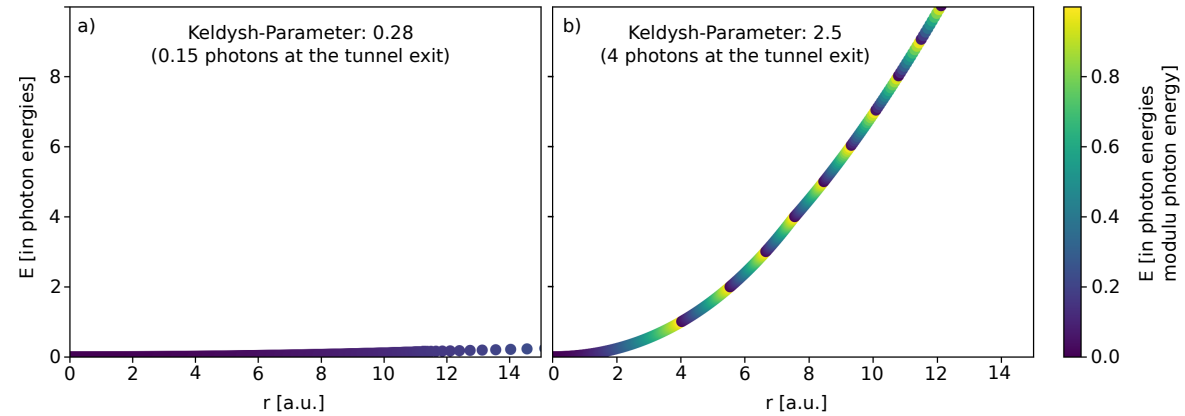


Figure 8.14: The electron energy (relative to the electron's energy in its ground state) and the real valued radial position in the plane of polarization belonging to the saddle point SFA-trajectory that leads to the most probable final momentum. (a) [(b)] is calculated with $\alpha = 0.05$ [$\alpha = 4$] leading to a Keldysh-parameter of $\gamma = 0.28$ [$\gamma = 2.5$] (parameters and the definition of α are as in chapter 5.2). The color code shows the angular momentum $\vec{L} = \Re(\vec{r} \times \vec{p})$ modulo one (the value of $|\vec{L}| = L_x$ is equivalent to the energy of the electron in units of the photon energy which makes the color coding redundant to the y-axis). At the exit of the tunnel $L_x = 0.15$ a.u. ($L_x = 4$ a.u.) is obtained. The numerical implementation of the saddle point SFA calculation has been realized by Nicolas Eicke and Manfred Lein and was used by the author of this thesis to obtain the results that are shown in the figure. The representation of non-adiabatic tunneling is related to ideas by Klaiber et al. [47, 48].

8.6. Conclusion: Non-Adiabatic Offsets

The dependence of the non-adiabatic offset at the exit of the tunnel can be quantified by a newly introduced parameter which is the effective instantaneous Keldysh-parameter γ_{eff} that depends on the ionization potential I_p, the amplitude of the instantaneous electric field $|\vec{E}(t)|$, the effective angular frequency ω_{eff} and the initial momentum in the light propagation direction p_x. Usually non-adiabatic tunneling is modeled by investigating the complex dynamics under the tunneling barrier [69]. However, the origin of the non-adiabatic offset upon the ionization by strong circularly polarized light has been illuminated presenting a mechanistic picture of non-adiabatic tunneling that is based on the conservation of angular momentum and links the initial momentum at the exit of the tunnel with the magnetic quantum number of virtually populated intermediate states.

Future theoretic studies could use the experimental results to benchmark theoretic models that include the influence of the Coulomb potential under the barrier and after the electronic wave packet has left the tunnel (see also [67, 104, 137]). In particular, a momentum along the tunneling direction, a "birth-time" of the electron that does not coincide with the time the electric field is at its maximum, a potential "tunneling time" and a modified tunnel exit position are possible candidates that might improve the agreement of theory and experiment (see chapter 9.12.1 and chapter 10.1). Finally, also experimental studies in which more than one electron is detected could be conducted. Such studies could aim at the investigation of electron-electron correlations for sequential double ionization in the non-adiabatic regime. Ideally, the interaction of two electrons in the classical forbidden region could be separated from classical Coulomb-repulsion.

9. Non-Adiabatic Tunneling: The Magnetic Quantum Number

Chapter 9, based on the peer-reviewed publication by Eckart et al. [26], provides additional experimental details and links the findings to the mechanistic picture of non-adiabatic tunneling presented in chapter 8.5.

It has been shown in chapter 8 that the temporal evolution of the driving field cannot be neglected for non-adiabatic tunneling; and the electron momentum distribution at the exit of the tunnel depends on the helicity of the driving field for almost circularly polarized light. In this chapter the role of the electron's initial state is investigated. Semi-classically, an electron with non-zero magnetic quantum number rotates around its ionic core and the sign of the magnetic quantum number m defines the direction of rotation which can be termed "ring current" [138]. Using circularly polarized light with defined helicity, the temporal evolution of the driving field allows for the separation of electrons into two classes: in their initial state, electrons can rotate in the same direction ($m = +1$) or in the opposite direction ($m = -1$) compared to the temporal evolution of the laser's electric field.

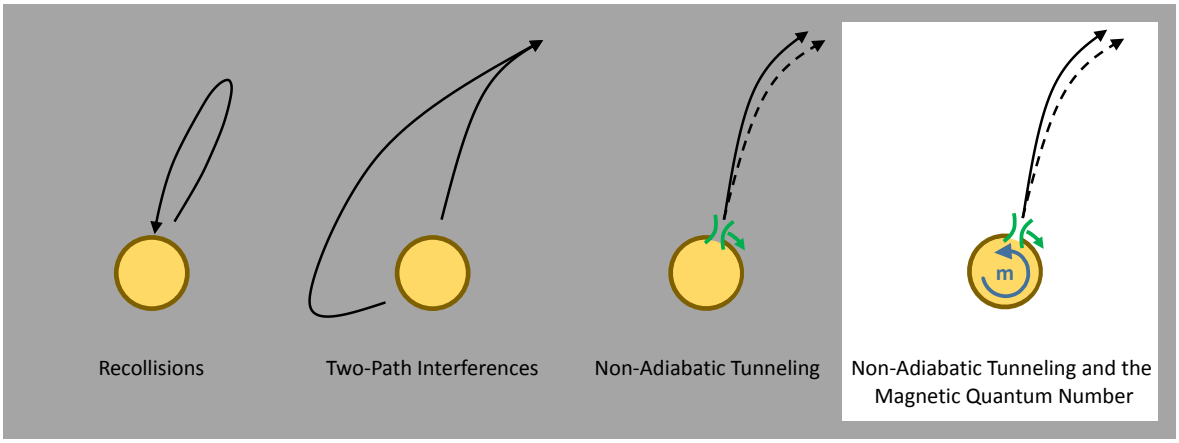


Figure 9.1: Illustration of the key scientific questions of this thesis. Chapter 9 focuses on the role of the initial state's magnetic quantum number for non-adiabatic tunneling.

Basic questions of this project: Is it more likely to ionize electrons with $m = -1$ or with $m = +1$? Is the value of m somehow encoded in the electron's final momentum distribution?

Experimental idea: Sequential double ionization is examined using a pump-probe-scheme. The circularly polarized pump-pulse leads to the ejection of one electron. The elliptically polarized probe-pulse leads to the ejection of the second electron. The polarization of the probe-pulse remains unchanged but the helicity of the pump-pulse is inverted leading to two different scenarios (see the two rows in Fig. 9.2). The experimental observation that the rate of sequential double ionization depends on the helicity of the pump proves that non-adiabatic

tunneling somehow[107] depends on m. The final momentum distribution of the electrons that are liberated by the probe-pulse allows one to infer that electrons with $m = -1$ are preferred for non-adiabatic tunnel ionization.

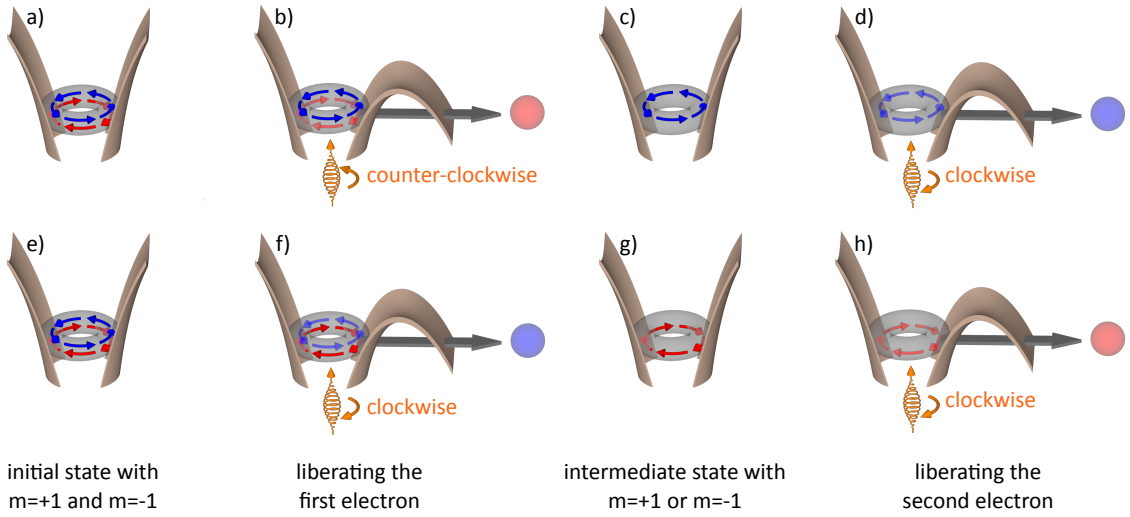


Figure 9.2: (a)-(d) schematically show sequential double ionization by two temporally separated laser pulses (pump-pulse in (b), probe-pulse in (d)). (e)-(h) show the same as (a)-(d) but with inverted helicity of the pump-pulse in (f). (c) and (g) show atoms possessing a defined ring current. The scheme presented here, shows the preparation and detection of ring currents in single atoms on sub-cycle timescales. The figure is taken from the publication by Eckart et al. [140] and the labels have been adapted.

Experimental beauty and the beauty of symmetry:

- The only control parameter that has to be changed is the helicity of the circularly polarized pump-pulse.[108]
- The coincidence detection of one electron and the doubly charged ion allows for the calculation of one momentum component of the undetected electron. The knowledge about momenta belonging to both ejected electrons and the very different vector potentials of pump and probe-pulse - which is due to the two-color scheme - allow one to distinguish electrons from the pump and the probe-pulse.
- The intermediate states shown in Fig. 9.2(c) and 9.2(g) are two degenerate states that only differ in the sign of their quantum phase (direction of rotation of the ring current).

[107] This was already proven in 2012 by Herath et al. [139].
[108] Circularly polarized and linearly polarized driving fields are the only two polarization settings that can be easily set experimentally (see chapter 4.1.5).

9.1. State of the Art: Non-Adiabatic Tunneling and the Magnetic Quantum Number

This subchapter is an extension to chapter 3 and chapter 8.1 which have already introduced non-adiabatic tunneling. Here, the missing literature that is relevant to the experimental findings of Eckart et al. [26] is presented.

Quantum numbers are commonly used to describe bound electrons. The energy and the shape of the orbital wave function are defined by the principal quantum number n, the orbital angular momentum quantum number l and the absolute value of the magnetic quantum number $|m|$. It is obvious that n, l and $|m|$ are invariant upon mirroring. However, the sign of m can change upon mirroring.

In argon there are two electrons with $m = -1$ and two electrons with $m = +1$ in the outermost orbital (3p orbital). Is it possible to selectively ionize an electron with a given sign of m on an attosecond timescale? Unfortunately, it is not possible to distinguish the two m-states in energy on an attosecond timescale. This is because of the uncertainty relation (23 fs minimal measurement time to resolve an energy difference of 177 meV corresponding to the spin-orbit splitting of argon). In contrast, there is non-adiabatic tunneling which is a non-resonant process, in which the electron is liberated from its parent ion on ultrafast timescales [8, 9]. The role of the magnetic quantum number in the regime of non-adiabatic tunneling has already been examined in the literature:

- Theoretic results presented in 2011 predicted that the ionization rate for negative[109] m is higher than for positive m for non-adiabatic tunneling[110] using circularly polarized light [69, 129].
- In 2012, Herath et al. showed experimentally that the sign of the magnetic quantum number is relevant for non-adiabatic tunneling. They used two subsequent circularly polarized femtosecond laser pulses and observed that the double ionization rate depends on the relative helicity of the two laser pulses. If both laser pulses have the same helicity the rate is lower than in the other case. This already implied that some information was stored in the ion after the first laser pulse has hit the atom. [139, 143] As discussed above, symmetry dictates that the information must be stored in the magnetic quantum of the hole of the singly charged ion.

[109] Negative m is defined such that the semi-classical motion of the bound electron is opposite to the temporal evolution of the laser electric field for circularly polarized light.

[110] Numerical simulations solving the time-dependent Schrödinger equation by Zhu et al. in Ref. [141] show that this preference inverts in the limit of adiabatic tunneling (see Fig. 2 in Ref. [141] and also see Ref. [142]).

- It has also been predicted that the electron energy and the electron momentum distribution depend on the sign of m such that the most probable electron energy is higher for $m = +1$ than for $m = -1$. [69, 129, 135, 144–146] Because the vector potentials are identical in both cases this difference can be attributed to differences of the initial momentum distribution at the tunnel exit. [69]
- A consequence of the m-dependent ionization probability is that the emitted electron can be spin-polarized. This is because the spin of the electron and the magnetic quantum number are not independent for the case of non-vanishing spin-orbit splitting. [147–150]
- A recent theoretic work by Liu et al. [13] predicts that for elliptically polarized light the most likely release time of the electron depends on the magnetic quantum number. Electrons that are counter-rotating with respect to the driving electric field are released up to about 60 as earlier than electrons that are co-rotating leading to differences in the angle in the plane of polarization in final momentum space of up to about 10°. The reason for this is a rearrangement of the electron density of the bound state that occurs on a sub-cycle time-scale and leads to a situation in which the orbitals of the co- and the counter-rotating electrons are differently deformed. The resulting polarized initial states for $m = -1$ and $m = +1$ are differently tilted with respect to the polarization ellipse of the driving electric field leading to the difference in the most probable release time.

Finally, all previous work indicated that strong field ionization is more than just ripping electrons away from the atom or molecule but is able to selectively liberate electrons from degenerate m-states on attosecond timescales. The first experimentally obtained electron momentum distributions and electron energy distributions that are resolved on the magnetic quantum number were presented by Eckart et al. [26].

9.2. Sequential Double Ionization of Argon using a Pump-Probe-Scheme

Before the experiment was started, the gas jet was collimated to about 10 µm along the laser propagation direction around the laser focus. The inlet pressure of the gas nozzle, the homogeneous electric and magnetic fields were as described in chapter 8.2. The electron momentum distributions are measured in coincidence with argon ions. Imposing the condition that the electron was detected in coincidence with Ar^{2+} (see also chapter 4.1.3 and chapter 6.5) results in three possible cases:

- Case 1: Both electrons are liberated by the pump-pulse.
- Case 2: Both electrons are liberated by the probe-pulse.
- Case 3: One electron is liberated by the pump-pulse and one electron is subsequently liberated by the probe-pulse.

For the current project only double ionization events that belong to case 3 are of interest. In order to exclude case 1 and case 2, four prerequisites can be identified:

- Prerequisite 1: A non-vanishing rate of Ar^{1+} due to the pump-pulse.
- Prerequisite 2: The rate of Ar^{2+} due to the pump-pulse alone must be zero.
- Prerequisite 3: A non-vanishing rate of Ar^{2+} which is due to atoms that were previously singly ionized by the pump-pulse.
- Prerequisite 4: The first and the second electron from case 3 must populate different regions in momentum space[111] because this will allow to exclude electrons from case 2 from the relevant final spectra[112].

[111] This is achieved by exploiting that the pump-pulse at a central wavelength of 390 nm and the probe-pulse at a central wavelength of 780 nm have different vector potentials.

[112] Alternatively, prerequisite 4 can be expressed as follows: "Electrons must not contribute to the relevant electron spectra if they are detected in coincidence with an Ar^{2+} ion, which has not been previously singly ionized by the pump-pulse."

9.3. Setting up the Pump-Pulse

Prerequisite 1 and 2 are easy to fulfil. To this end the probe-pulses are blocked, the pump-pulses' polarization is set to circular polarization (see chapter 4.1.5) and the intensity of the pump-pulses is increased as much as possible without observing double ionization. The average power in front of the vacuum chamber was measured with a power meter[113] to be 142 ± 6 mW and the rate on the electron detector was about 500 Hz. The process of single ionization by the pump-pulse is schematically depicted in Fig. 9.3(b) and 9.3(f). It is evident that the only difference between Fig. 9.3(b) and 9.3(f) is the helicity of the pump-pulse. Hence, the two scenarios are mirror symmetric and it is expected that the resulting ion (see Fig. 9.3(c) and 9.3(g)) and the measured electron momentum distributions are also mirror symmetric. The ions in the two scenarios must differ in the magnetic quantum number[114] of the electron hole.

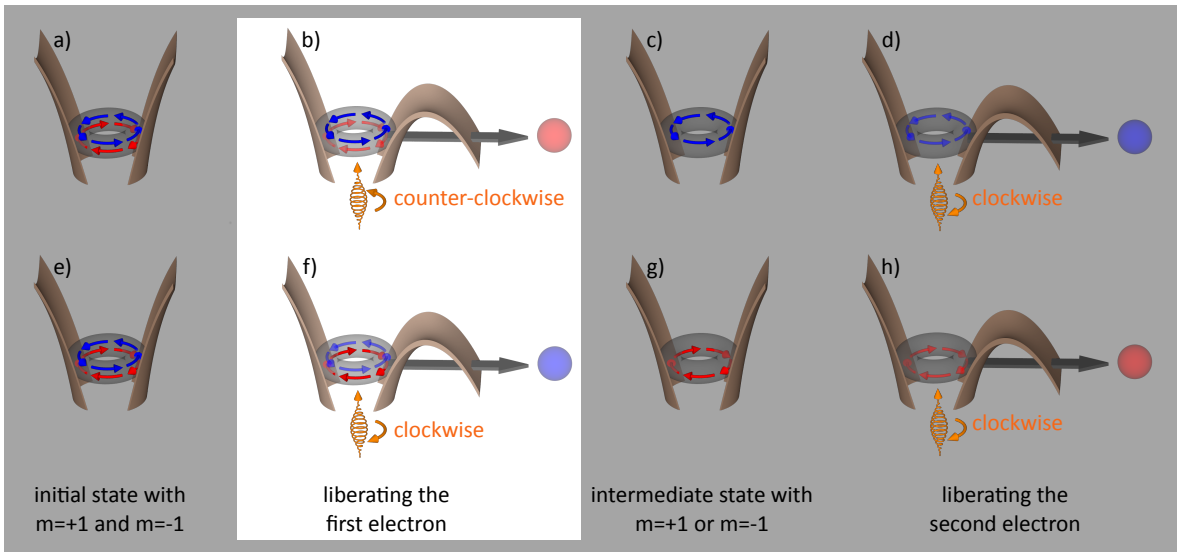


Figure 9.3: Shows the same as Fig. 9.2 highlighting the pump step. The figure is taken from the publication by Eckart et al. [140] and the labels have been adapted.

Fig. 9.4(a) [(d)] and 9.4(b) [(e)] show the same as Fig. 9.3(b) [(f)] and 9.3(c) [(g)]. The experimentally measured electron momentum distributions shown in Fig. 9.4(c) and 9.4(f) are almost identical. The data for this figure was measured within 3 hours and the helicity of the pump-pulse was inverted every 3 minutes using the automated two-color setup (see chapter 4.1.2). The observable "donut"-like distribution is expected for circularly polarized light and it is found that the number of counts only differs by about 0.5%. The peak intensity

[113] The used power meter is the "FieldMate" in combination with the air-cooled thermopile sensor "PM10" (both from Coherent Inc.).
[114] The principal quantum number and the orbital angular momentum quantum number do not change upon mirroring.

was calibrated by comparing the measured electron momentum distributions upon the single ionization of argon by the almost circularly polarized pump-pulses to TDSE calculations [26]. The peak electric field was found to be 0.055 a.u. which corresponds to an intensity of $2.1 \cdot 10^{14}\,\mathrm{W/cm^2}$.

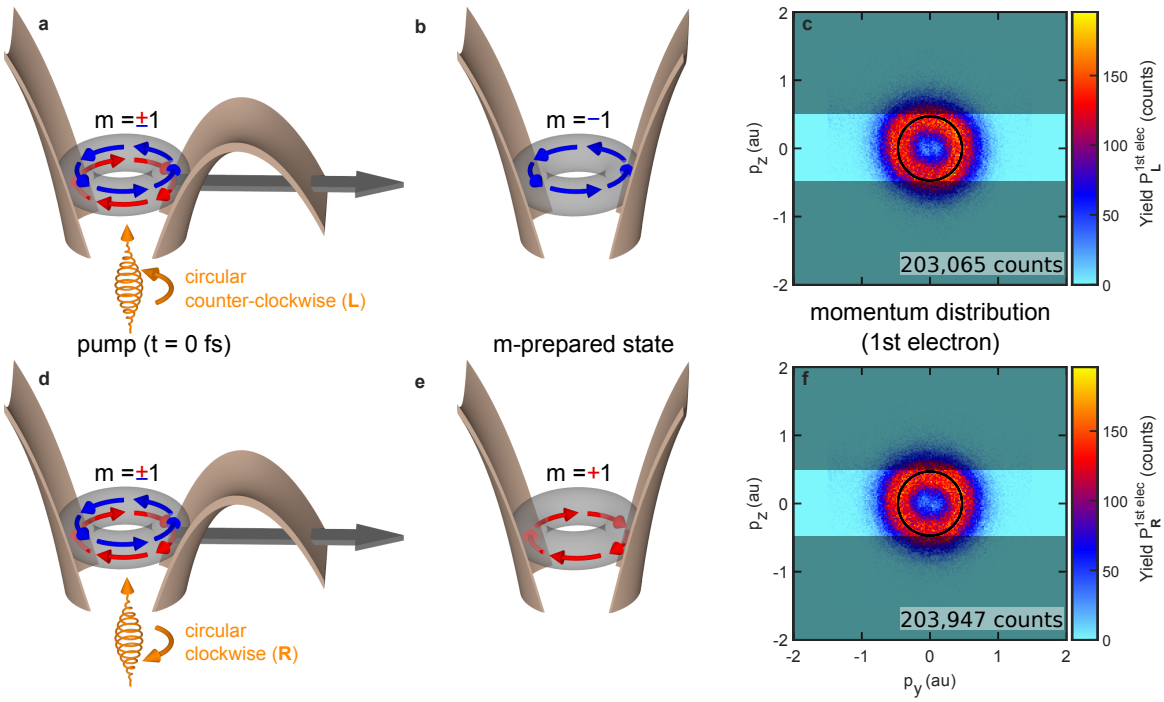


Figure 9.4: "Experimental preparation of ring currents by m-dependent tunnel-ionization. a, The circularly polarized laser pulse with an anticlockwise-rotating electric field liberates an electron by tunnel-ionization at $t = 0\,\mathrm{fs}$. Clockwise-rotating electrons ($m = +1$) are strongly preferred for ionization. b, Step a results in a persistent ring current in the remaining ion. d,e, The corresponding process for a circular clockwise-rotating electric field. The sign of m and direction of the ring current are inverted. c,f, Only the pump-pulse is used and the electron momentum distributions $P_{\mathrm{L}}^{1\mathrm{st\,elec}}$ and $P_{\mathrm{R}}^{1\mathrm{st\,elec}}$, showing electrons that are detected in coincidence with Ar^{1+} for equal acquisition times, are identical. The black lines show the negative vector potential of the pump-pulse. Most of the first electrons fulfil $|p_z| < 0.5\,\mathrm{a.u.}$ (indicated by the unshaded area), which will be utilized for distinguishing electrons from the pump and the probe-pulse. Note that the light propagation direction points out of the paper in c,f." (Figure is part of the final resubmitted manuscript. The content is the same as in Eckart et al. [26]. The caption is taken from Eckart et al. [26].)

Although circularly polarized light is desired, it is difficult to be sure that laser pulse at 390 nm is perfectly circularly polarized (see chapter 4.1.5). Hence, the ellipticity of the two possible pump-pulses that have opposite helicities need to be analyzed. To this end the number of liberated electrons is plotted as a function of the angle in momentum space in the plane of polarization. The two resulting data sets are fitted by ellipses with minor axis a and major axis b. Since the Keldysh-Parameter[115] is $\gamma = \frac{\sqrt{2I_p}}{E_{\mathrm{peak}}}\omega = 2.3 > 1$ and at least 5 photons have to be absorbed to overcome the ionization potential of argon, the ellipticity can

[115]The Keldysh-parameter is defined in Ref. [1] and explained in chapter 3.

be estimated[116] by $\varepsilon_{390\,\mathrm{nm}} = \left(\frac{a}{b}\right)^{\frac{1}{10}}$ (see chapter 3.1). It is found[118] that for both pump-pulse scenarios the value for the ellipticity is $\varepsilon_{390\,\mathrm{nm}} > 0.98$.

[116] For the described estimation of the ellipticity it is was concluded[117] that the pump-pulse is not saturating the single ionization of argon.

[118] The quantitative analysis of the ellipticities for the pump-pulse was carried out by Nikolai Schlott (see Fig. 4.12 in Ref. [55]).

9.4. Setting up the Probe-Pulse

Fig. 9.5 shows the overall experimental scheme and highlights the probe-step.

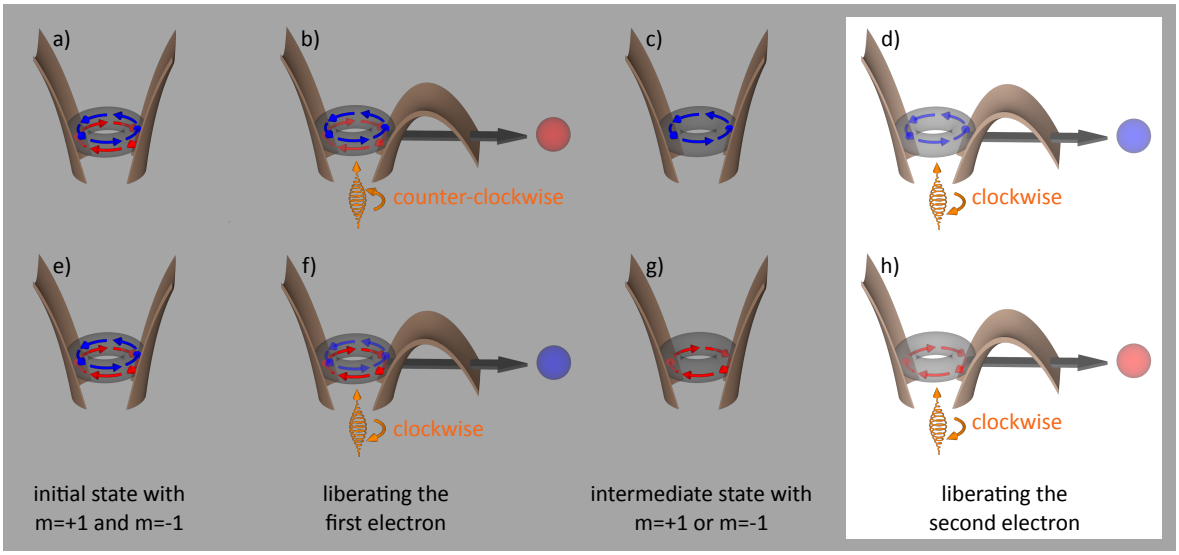


Figure 9.5: Shows the same as Fig. 9.2 highlighting the probe step. The figure is taken from the publication by Eckart et al. [140] and the labels have been adapted.

Prerequisite 3 ("A non-vanishing rate of Ar^{2+} which is due to atoms that were previously singly ionized by the pump-pulse.") is more difficult to achieve. To this end the pump-pulses have been blocked and the intensity of the elliptically[119] polarized probe-pulse is chosen as high as possible. The ellipticity $\varepsilon_{780\,\mathrm{nm}} = 0.61$ and the orientation of the main-axis of the ellipse $\alpha = 106 \pm 5°$ were measured with a linear polarizer in front of the vacuum chamber[120]. However, there are two upper limits regarding the intensity of the probe-pulse. First, the rate on the electron detector[121] should not exceed 50% of the laser's repetition rate (8 kHz). This limits the probability of having two ionization events for a single laser shot to be below 25%. Second, the double ionization probability of argon should not be saturated. Choosing the average power in front of the vacuum chamber to be 541 ± 9 mW leads to a rate on the electron detector of about 3500 Hz.

To make sure the double ionization probability is not saturated the intensity of the probe-pulse has to be calibrated. To this end helium is used to avoid the saturation of single ionization (helium has an ionization potential of 24.59 eV which is much larger than the ionization

[119] The reason why an elliptically polarized probe-pulse is used is explained in chapter 9.6.

[120] For the probe-pulse, the measurement of the ellipticity is not an in situ measurement and integrates over the entire duration of the laser pulse which is not ideal.

[121] This is the reason, why the gas jet is collimated to only 10 µm along the laser propagation direction in the laser focus. For longer interaction regions the ionization rate would be too high or one would have to decrease the intensity of the probe-pulse. Since 10 µm is also much smaller than the Rayleigh length of about 150 ± 10 µm it also minimizes the effect of focal averaging (see chapter A.1).

potential of argon which is 15.76 eV). Unfortunately, after the measurement using argon the laser system had to be restarted for technical reasons[122]. Probably, the pulse duration was different after the restart of the laser system. This conjecture is based on the comparison of the relative yield of doubly to singly charged ions Ar^{2+}/Ar^{+} before and after the restart of the laser system. In order to keep the ratio Ar^{2+}/Ar^{+} constant[123] an average power of only $I_{Ar} = 390\,\text{mW}$ had to be used (instead of 541 mW) for the probe-pulse. For the helium measurement $I_{He} = 440\,\text{mW}$ was used. The resulting electron momentum distribution is shown in Fig. 9.6(a). Fig. 9.6(b) indicates an angular gate that is used to restrict the "birth"-time of the electrons to the peak of the electric field. Fig. 9.6(c) shows that those electrons have a most probable electron energy of 23.2 eV. This value is compared to solutions of the TDSE in order to calibrate the intensity of the probe-pulse[124].

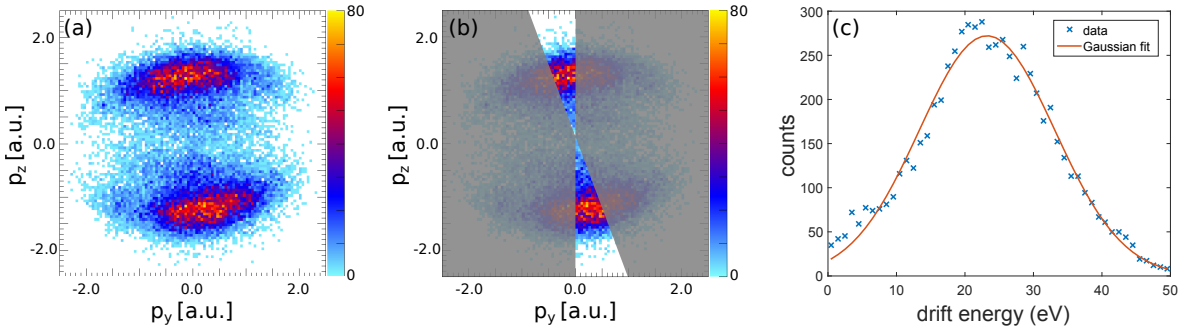


Figure 9.6: (a) shows the electron momentum distribution measured in coincidence with helium ions. (b) illustrates a condition on the angle in the plane of polarization. All electrons that do not have an angle between 90° and 110° or between -90° and -70° are excluded. The excluded region in momentum space is indicated by the gray shaded area. (c) shows the electron energy distribution of the electrons that are not excluded. A Gaussian fit (red line) is done. The mean of the Gaussian distribution is 23.2 eV. Comparing this value with solutions of the TDSE allows for the calibration of the laser intensity in the experiment.

Hence, the peak electric field for the helium measurement is known to be $E_{\text{He peak}} = 0.115\,\text{a.u.}$ and this allows for the calculation of the peak electric field of the probe-pulse for the measurement using argon to be:

$$E_{\text{Ar peak}} = E_{\text{He peak}} \cdot \sqrt{\frac{I_{\text{Ar}}}{I_{\text{He}}}} = 0.115\,\text{a.u.} \cdot \sqrt{\frac{390\,\text{mW}}{440\,\text{mW}}} = 0.11\,\text{a.u.} \tag{28}$$

[122] The restart of the laser system can lead to a different pulse duration. Assuming that the product of pulse duration and peak intensity is constant a decrease of the pulse duration by 20% leads to an increase in the peak intensity by 25%. Assuming that the ionization only occurs at the peak of the laser pulse, the peak intensity is much more important than the pulse duration or the average power of the laser pulse.

[123] The measured ratio Ar^{2+}/Ar^{+} was on the order of 20% but the absolute value is not accurately known. This is because the efficiency of the MCP stack decreases after many particles have hit the same spot. The rate of Ar^{+} is higher than the rate of Ar^{2+} and both ions hit different positions on the MCP stack. Hence, the detection efficiency of Ar^{+} is expected to be lower than the detection efficiency of Ar^{2+}.

[124] The TDSE calculations were done by the coworkers from the collaborating theory-groups regarding the project leading to Ref. [26]

Based on this intensity calibration it was concluded[125] that the probe-pulse is not saturating the double ionization of argon.

[125]This conclusion was drawn with the help of the coworkers from theory regarding the project that led to Ref. [26].

9.5. Setting up the Temporal Overlap and the Spatial Overlap of Pump and Probe-Pulse

Moreover, prerequisite 3 ("A non-vanishing rate of Ar^{2+} which is due to atoms that were previously singly ionized by the pump-pulse.") can only be fulfilled if the pump and the probe-pulse overlap spatially, because, otherwise, the probe-pulse will never ionize atoms that have already been singly ionized by the pump-pulse. In other words, the pump-pulses in Fig. 9.5(b) and 9.5(f) and the probe-pulses in 9.5(d) and 9.5(h) must be focused to the same spot. Since, the nm-delay stage allows for the variation of the temporal overlap without changing the spatial overlap, the spatial overlap is optimized first.

Four days before the measurement for Fig. 9.4, Fig. 9.10 and Fig. 9.11 was conducted the intensities of the pump-pulse and the probe-pulse were decreased. The blue crosses in Fig. 9.7 show the absolute yield of singly charged argon ions as a function of the position of the nm-delay stage[126]. The maximum is at 19 µm. After the manual delay stage (see chapter A.1) is moved by 20 µm the red open circles are measured. Low values of the nm-delay stage position correspond to long time-delays of pump-pulse and probe-pulse.

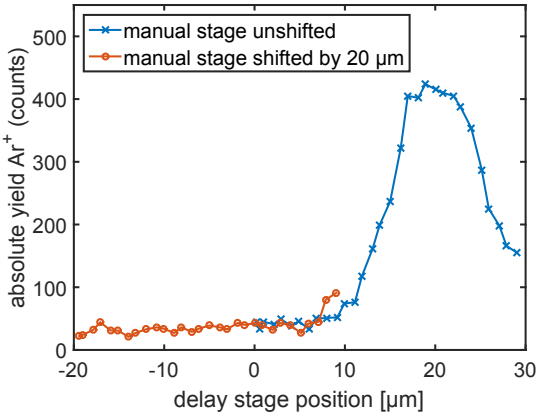


Figure 9.7: The absolute yield of singly charged argon ions is shown as a function of the delay of pump-pulse and probe-pulse. Since the nm-delay stage has a travel range of only 30 µm, the manual delay stage is moved by 20 µm for the measurement of the red open circles. Low values for the delay stage position indicate that the probe-pulse arrives later compared to the pump-pulse.

Directly before the measurement for Fig. 9.4, Fig. 9.10 and Fig. 9.11 was started the manual delay stage was set to its final position which was the same as for the measurement belonging to the red open circles in Fig. 9.7. Afterwards, the nm-delay stage was set to its minimal

[126] For the measurement regarding Fig. 9.7 different laser intensities (average power of 83.5 mW for 780 nm and 30 mW for 390 nm) were used than in the rest of the chapter. Also, the jet was collimated to 80 µm along the laser propagation direction which is different than in the rest of the chapter.

position ensuring maximal delay between pump-pulse and probe-pulse. A second cross-correlation for this setting of the manual delay stage is presented in Fig. 9.8. Fig. 9.8(a) shows the single ionization of argon as a function of the position of the nm-delay stage. The peak at 1 µm is due to a longer measurement time for this position.

Fig. 9.8(b) shows the double ionization of argon as a function of the position of the nm-delay stage. A clear dependence of the yield of Ar^{2+} as a function of the delay is seen. The relative yield Ar^{2+}/Ar^{+} shown in Fig. 9.8(c) shows the same dependence. The reason why the single ionization does not depend on the delay is that the single ionization of argon is saturated.

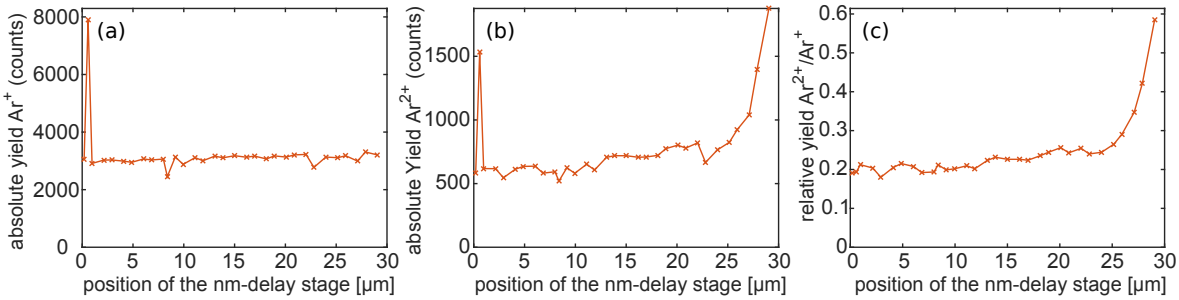


Figure 9.8: (a) [(b)] shows the single [double] ionization of argon and (c) shows the relative yield of double and single ionization Ar^{2+}/Ar^{+}. Due to saturation the single ionization does not depend on the position of the delay stage. Hence, the double ionization rate should be used to optimize the spatial overlap.

This is an important insight regarding the optimization of the spatial overlap because it indicates that it is impossible to use the single ionization rate for this optimization. The following procedure was used to adjust the spatial and the temporal overlap:

- Fig. 9.7 is measured and the overlap of pump-pulse and probe-pulse is determined to be at a delay stage position of 19 µm for the unshifted manual stage (see blue crosses in Fig. 9.7).
- The manual delay stage is shifted by 20 µm (see red circles in Fig. 9.7). This means that the nm-delay stage would have to move[127] to $r_{\text{overlapp}} = 20\,\mu\text{m} + 19\,\mu\text{m} = 39\,\mu\text{m}$ to reach a perfect overlap of the pump-pulse and the probe-pulse. The possible temporal delays are between 39 µm and 9 µm which corresponds to temporal delays[128] of between 260 fs and 60 fs.
- The neutral density filters are used to set the desired intensities for pump-pulse and probe-pulse.

[127] Due to the travel range of the nm-delay stage, which is limited to 30 µm, this is impossible.

[128] The speed of light is 3.33 fs per 1 µm. Any displacement of the delay stage by a distance Δx will change the distance the probe-pulse has to travel by $2\Delta x$.

- Afterwards, the manual delay stage and the neutral density filter were not touched anymore because they might have affected the spatial overlap.
- The nm-delay stage is set to $r_{\text{overlapp}} = 30\,\mu\text{m}$ (corresponds to a pump-probe delay of about 60 fs) which is as close to the overlap of pump-pulse and probe-pulse as possible.
- The pump-pulse is blocked and the focusing mirror in the chamber is minimally adjusted to ideally hit the collimated jet.
- The pump-pulse is unblocked and the rate of Ar^{2+} is used to optimize the spatial overlap of pump-pulse and probe-pulse by changing the pointing of the pump-pulse. This is done by slightly adjusting the mirror between the neutral density filter and the lambda-quarter wave plates in the arm of the pump-pulse ("TM4a" in Fig. 4.6).
- After this procedure was done the cross-correlation shown in Fig. 9.8 was conducted and afterwards the measurement leading to Fig. 9.4, Fig. 9.10 and Fig. 9.11 was started.[129]

In a next step, it is possible to test whether prerequisite 3 ("A non-vanishing rate of Ar^{2+} which is due to atoms that were previously singly ionized by the pump-pulse.") is fulfilled. Fig. 9.9(a) [(b)] shows the electron momentum distribution measured in coincidence with Ar^{2+} using only the pump-pulse [probe-pulse].

[129] During the measurement data was taken at two positions of the nm-delay stage. The positions were $r_{\text{overlapp}} = 4\,\mu\text{m}$ and $r_{\text{overlapp}} = 8\,\mu\text{m}$ corresponding to pump-probe delays of 233 fs and 207 fs. Separate analysis of the two positions showed no significant difference. To increase statistics both positions were combined and for simplicity the delay was written to be 200 fs in Ref. [26].

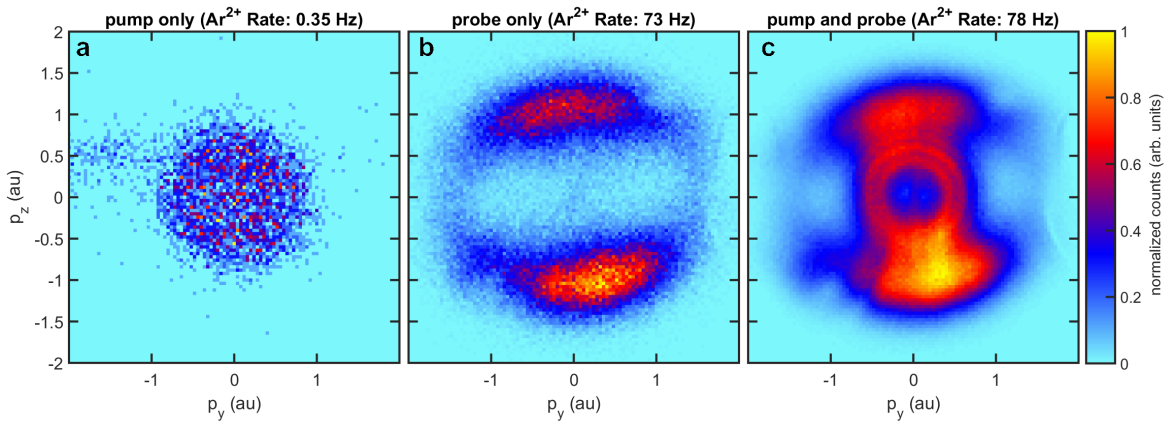


Figure 9.9: "Electron momentum distributions measured in coincidence with Ar^{2+}. a, Normalized electron momentum distribution in the plane of polarization recorded using only the pump-pulse. b is the same as a but only the probe-pulse was used and in c pump and probe-pulse were both used. It can be seen that only pump and probe-pulse together are able to produce electrons with $|p_z| < 0.5$ au efficiently. We have checked that electrons from the probe-pulse alone that would contribute to the final energy spectrum and fulfilling $|p_z_calc| < 0.5$ au are eliminated by the subtraction of random coincidences. Above each distribution the detection rate of Ar^{2+} is shown for the corresponding case which is negligible for the case where there is only the pump-pulse." (Figure is part of the final resubmitted manuscript. The figure and its caption are taken from the supplementary information of Eckart et al. [26].)

The double ionization rate that is produced by the pump-pulse is more than two orders of magnitude lower than the double ionization rate that is due to the probe-pulse. Inspection of Fig. 9.9(c) shows that using the pump-probe scheme leads to a very different electron momentum distribution. This distribution shows an additional, very prominent "donut"-like electron momentum distribution that is identical to the electron momentum distribution for the single ionization by the pump-pulse alone (see Fig. 9.4(c) and 9.4(f)).

This is a great result because it proves that a significant part of the electrons that are double ionized by the probe-pulse have already been singly ionized by the pump-pulse. Thus, prerequisite 3 is fulfilled.

9.6. Distinguish First and Second Electron

Prerequisite 4 ("The first and the second electron from case 3 must populate different regions in momentum space[130] because this will allow to exclude electrons from case 2 from the relevant final spectra.") is the last prerequisite that needs to be fulfilled in order to be able to execute the experimental scheme presented in Fig. 9.2 (see chapter 9.2 for the definition of case 2 and case 3). Although prerequisite 4 sounds complicated it can be easily fulfilled by using the power of coincidence-detection. The first electron that is detected is analyzed. Using the detected Ar^{2+} ion a momentum component in the time-of-flight direction of the undetected electron can be calculated using momentum conservation (see chapter 6.5.2). The inferred electron momentum component $|p_z_calc|$ can be used to generate a subset of the data shown in Fig. 9.9(c) that fulfills prerequisite 4. This is done by imposing the condition $|p_z_calc| < 0.5$ a.u. because electrons with $|p_z_calc| < 0.5$ a.u. cannot stem from events in which both electrons have been liberated by the probe-pulse (as seen in Fig. 9.9(b)).

Electrons that are detected in coincidence with an Ar^{2+} ion and fulfil $|p_z_calc| < 0.5$ a.u. can be divided into two sub-groups. Fig. 9.10(c) [(f)] shows those electron that were detected while pump-pulse and the probe-pulse had opposite [the same] helicity. The data[131] for Fig. 9.10 was measured within 35 hours and the helicity of the pump-pulse was inverted every 3 minutes using the automated two-color setup (see chapter 4.1.2). Comparing Fig. 9.10(c) and 9.10(f) two observation can be made:

- The yield for double ionization by the pump-probe scheme highly depends on the relative helicity of the pump and the probe-pulse and is about 16% higher for the scenario with opposite helicities (431,530 counts in Fig. 9.10(c) and 372,490 counts Fig. 9.10(f)).
- The radial momentum appears to be slightly different for the two scenarios. The black line in Fig. 9.10(c) and 9.10(f) shows the negative vector potential and is identical in both panels and therefore guides the eye to see the unobtrusive radial difference. From chapter 8 it is known that radial differences can be related to offsets of the initial momentum distributions.[132]

[130] This is achieved by exploiting that the pump-pulse at a central wavelength of 390 nm and the probe-pulse at a central wavelength of 780 nm have different vector potentials.

[131] For Fig. 9.10, random coincidences have already been subtracted (see chapter 9.7).

[132] This is in line with predictions by Ingo Barth and Olga Smirnova [69]. Using the parameters from the experiment the theoretic calculations were carried out by coworkers from the collaborating theory-groups regarding the project leading to Ref. [26]. The results for the theoretically calculated offsets of the initial momentum distributions are shown in Fig. 9.10(b) and 9.10(e). The calculated offset is $p = 0.$ a.u. [$p = 0.12$ a.u.] for the scenario in which both laser pulses have opposite [the same] helicities. The theoretic results are not discussed, but are mentioned for the sake of completeness.

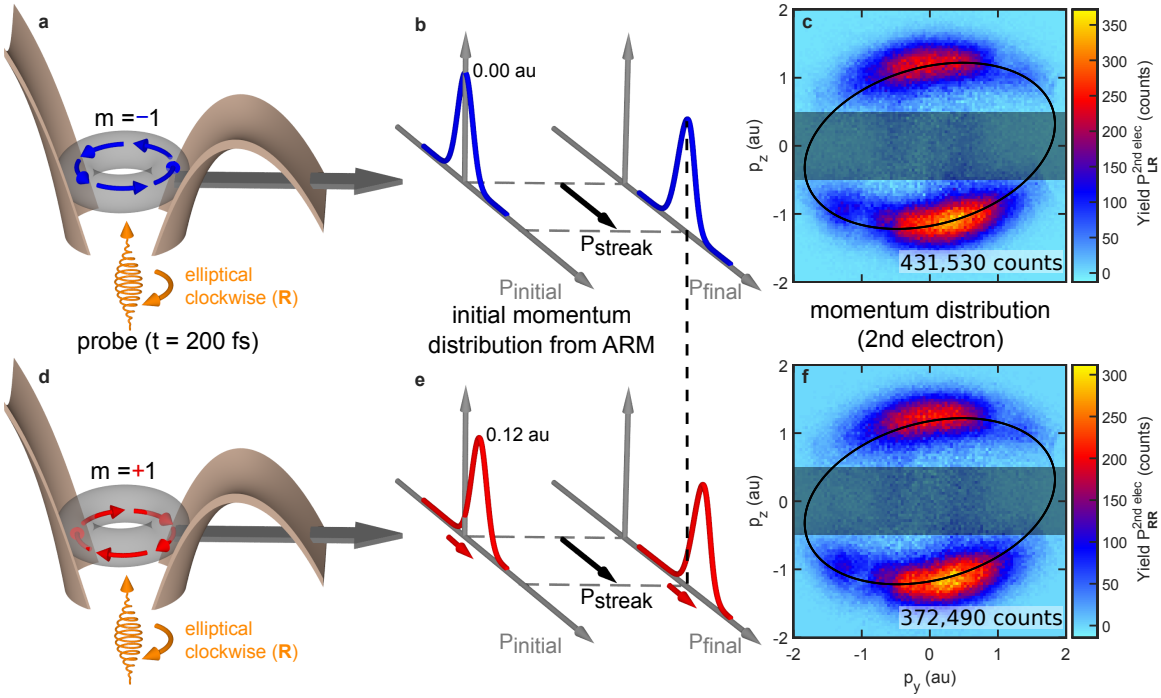


Figure 9.10: "Detection of ring currents by momentum-resolved m-dependent tunnel-ionization. a,d, At $t = 200$ fs, the elliptically polarized probe-pulse with a clockwise-rotating electric field hits the ion that has been created by the pump-pulse (see Fig. 9.4 [remark - the number of the referenced figure has been adapted]). c,f, The second electron's momentum distributions $P_{\mathrm{LR}}^{\mathrm{2nd\,elec}}$ and $P_{RR}^{\mathrm{2nd\,elec}}$ for equal acquisition times (the electron that is not measured is calculated from momentum conservation and the measured electron is shown in c, f only if the calculated electron fulfils $|p_{z_\mathrm{calc}}| < 0.5$ a.u.). The momenta agree with the negative vector potential of the field (black line).There are more events in $P_{\mathrm{LR}}^{\mathrm{2nd\,elec}}$ than in $P_{RR}^{\mathrm{2nd\,elec}}$, proving that the sign of the magnetic quantum number influences tunnel ionization. The angular and radial differences are discussed in Fig. 9.11 [remark - the number of the referenced figure has been adapted] and Supplementary Fig. 9.28 [remark - the number of the referenced figure has been adapted]. The electron's „initial" momentum distributions after tunnelling (dashed line in b, e) with $m = +1$ have a higher momentum (peak at $p = 0.12$ a.u.) than $m = -1$ (peak at $p = 0.00$ a.u.). These add to the drift momentum imparted by the laser pulse, leading to different final radial momenta (solid lines in b,e). The transverse offsets for distributions in b,e are estimated using ARM theory (see text). Note that the light propagation direction points out of the paper in c,f." (Figure is part of the final resubmitted manuscript. The content is the same as in Eckart et al. [26]. The caption is taken from Eckart et al. [26].)

However, the differences of Fig. 9.10(c) and 9.10(f) appear to be very small. The visibility of the difference is more obvious in Fig. 9.11 which shows the electron energy for all events that are within the angular gate indicated by the inset. The blue data in Fig. 9.11 $Y_{\mathrm{LR}}^{\mathrm{2nd\,elec}}$ is a subset of Fig. 9.10(c) and shows a lower most probable electron energy, but a higher total yield compared to the red data $Y_{\mathrm{RR}}^{\mathrm{2nd\,elec}}$ which is a subset of Fig. 9.10(f).

What is the physical meaning of the data shown in Fig. 9.11? It shows the energy spectra of the electrons which are emitted from two mirror symmetric m-prepared , singly charged states. However, $P_{\mathrm{LR}}^{\mathrm{2nd\,elec}}$, $P_{RR}^{\mathrm{2nd\,elec}}$, $Y_{\mathrm{LR}}^{\mathrm{2nd\,elec}}$ and $Y_{RR}^{\mathrm{2nd\,elec}}$ are quantities that are related to the experimental scheme. A more interesting result would be to infer separate energy dependent yields for the liberation of an electron with $m = -1$ and $m = +1$. Those yields are called $Y_{\mathrm{m=-1}}^{\mathrm{2nd\,elec}}$ and $Y_{\mathrm{m=+1}}^{\mathrm{2nd\,elec}}$. But how to extract those quantities from the measured data? To answer

this question the pump-probe scheme has to be analyzed in detail (see chapter 9.8). But before this is done an important experimental detail has to be investigated, namely “random coincidences”. Those “random coincidences” stem mainly from laser shots that not only doubly ionized one argon atom, but ionized an additionally atom or molecule.

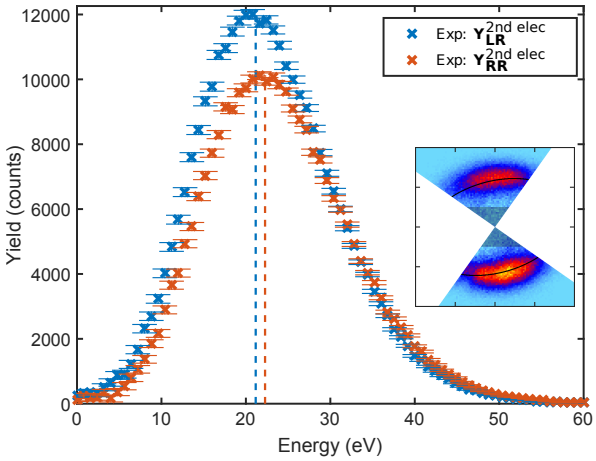


Figure 9.11: “Energy-resolved electron spectra showing ring current transport during tunnelling. a, Measured electron energy spectra for $Y_{\mathrm{LR}}^{2\mathrm{nd\,elec}}$ and $Y_{RR}^{2\mathrm{nd\,elec}}$. To reduce noise, the momentum window shown in the inset is applied to the experimental data; the same window is used to gate theoretical and numerical results. [...]” (The panel is part of a figure in the final resubmitted version. The content is the same as in Eckart et al. [26] but the layout has been adapted. Part of the caption is taken from Eckart et al. [26].)

9.7. Random Coincidences

The experimental quantities $Y_{\mathrm{LR}}^{\mathrm{2nd\,elec}}$, $Y_{\mathrm{RR}}^{\mathrm{2nd\,elec}}$, $P_{\mathrm{LR}}^{\mathrm{2nd\,elec}}$ and $P_{\mathrm{RR}}^{\mathrm{2nd\,elec}}$ have already been corrected for random coincidences. It is assumed that random coincidences create a background that has the same distribution as the electron momentum distribution that is detected without any condition regarding the detected ion. $P(\text{“random coincidences”})$ denotes the probability that an electron, which stems from random coincidences, is detected in coincidence with an Ar^{2+} ion and fulfills the condition $|p_{z_\mathrm{calc}}| < 0.5$ a.u. For the subtraction of the random coincidences it is assumed that $P(\text{“random coincidences”}) = 35\%$.

The subtraction of random coincidences leads to the results shown in Fig. 9.11. For comparison Fig. 9.12 shows the same results without subtracting random coincidences. It is evident that the yield for high energy electrons is not affected significantly. This confirms that the discussion in chapter 9.10, which is based on R_{highE} is not affected by the choice of $P(\text{“random coincidences”})$. The value of $P(\text{“random coincidences”}) = 35\%$ is estimated using the following procedure.

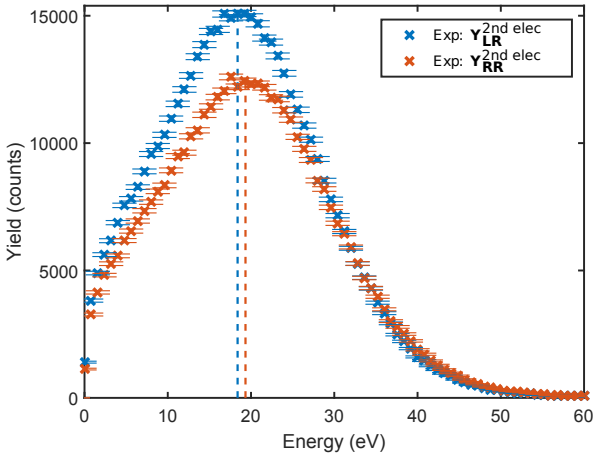


Figure 9.12: Shows the same results as Fig. 9.11 without subtracting random coincidences.

First, the momentum conservation for the single ionization of argon is investigated. Fig. 9.13 shows the sum of electron and ion momentum versus the difference of electron and ion momentum. About 71% of all events appear to fulfil momentum conservation, which is visible as a horizontal line (this is identified with “case A” in Tab. 9.1). There are two blurred maxima that are aligned vertically at zero difference momentum and a sum momentum of about plus or minus 1.5 a.u. Those two maxima correspond to 14% of the counts in Fig. 9.13 and it is interpreted that they belong to scenarios in which two Ar^{+} ions were produced.

Those two ions have release times with antiparallel negative vector potentials. Detecting the electron that does not belong to the detected ion leads to such observed blurred maxima. This is indicated as “case B” in Tab. 9.1. The rest of the counts in Fig. 9.13 belong to “case C”. Here, the detected electron stems from residual gas and not from argon at all.

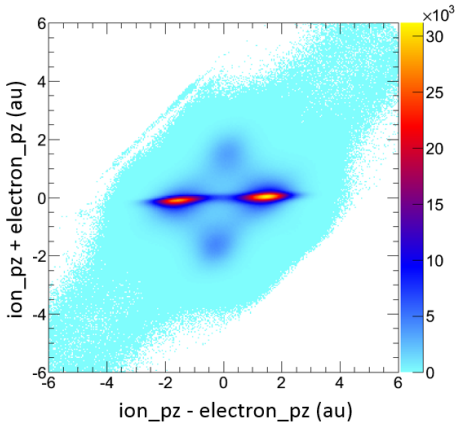


Figure 9.13: The sum of electron and ion momentum is shown versus the difference of electron and ion momentum. (The figure was part of the answer to the referees regarding the publication by Eckart et al. [26]. Labels and layout have been adapted.)

Table 9.1: Overview of the relevant ionization channels. The detected particles are highlighted. (The table is the same as in the answer to the referees regarding the publication by Eckart et al. [26]. Labels and layout have been adapted.)

channel	created ions	created electrons	probability	case A	case B	case C
1	**Ar^+**	**e^-**	p_1	100%		
2a	**Ar^+**, Ar^+	**e^-**, e^-	p_2	100%		
2b	**Ar^+**, Ar^+	e^-, **e^-**	p_2	50%	50%	
2c	Ar^+, **Ar^+**	**e^-**, e^-	p_2	50%	50%	
2d	Ar^+, **Ar^+**	e^-, **e^-**	p_2	100%		
3a	**Ar^+**, residual gas	**e^-**,e^-	p_3	100%		
3b	**Ar^+**, residual gas	e^-, **e^-**	p_3			100%
sum			100 %			

Using Tab. 9.1 allows for the calculation of the probabilities p_1, p_2 and p_3:

$$\begin{aligned} p_1 + 2 \cdot p_2 + 2 \cdot 0.5 \cdot p_2 + p_3 &= 0.71 \\ 2 \cdot 0.5 \cdot p_2 &= 0.14 \\ p_3 &= 0.15 \end{aligned} \tag{29}$$

Knowing that an Ar^+ ion has been detected, this allows for the following conclusions:

- $p_1 = 0.14$ denotes the probability that no additional gas atom has been ionized in the laser focus.
- $4 \cdot p_2 = 0.56$ denotes the probability that another Ar^+ ion has been ionized in the laser focus.
- $2 \cdot p_3 = 0.30$ denotes the probability that another additional gas atom has been ionized in the laser focus.

These conclusions are conditional probabilities and are also true if Ar^{2+} has been detected instead of Ar^{1+}. This allows for the creation of a table in analogy to Tab. 9.1 taking the liberation of one additional electron into account. Additionally, it is known that for the relevant final spectra one electron is liberated by the pump-pulse (indicated by e_1^-) and one electron is liberated by the probe-pulse (indicated by e_2^-). The result is shown in Tab. 9.2.

Table 9.2: Overview of the relevant ionization channels as described in the text. The detected particles are highlighted. The column "gates" indicates if the condition $|p_{z_calc}| < 0.5$ a.u. is expected to be fulfilled. (The table is the same as in the answer to the referees regarding the publication by Eckart et al. [26]. Labels and layout have been adapted.)

channel	created ions	created electrons	probability	gated	relevant probability
1a	**Ar^{2+}**	**e_1^-**, e_2^-	$\frac{1}{2} \cdot p_1$	no	0%
1b	**Ar^{2+}**	e_1^-, **e_2^-**	$\frac{1}{2} \cdot p_1$	yes	$q_1^{\text{good}} = \frac{1}{2} \cdot p_1$
2a	**Ar^{2+}**, Ar^+	**e_1^-**, e_2^-, e^-	$\frac{4}{3} \cdot p_2$	no	0%
2b	**Ar^{2+}**, Ar^+	e_1^-, **e_2^-**, e^-	$\frac{4}{3} \cdot p_2$	yes	$q_2^{\text{good}} = \frac{4}{3} \cdot p_2$
2c	**Ar^{2+}**, Ar^+	e_1^-, e_2^-, **e^-**	$\frac{4}{3} \cdot p_2$	maybe	$q_3^{\text{bad}} = \frac{1}{2} \cdot \frac{4}{3} \cdot p_2$
3a	**Ar^{2+}**, residual gas	**e_1^-**, e_2^-, e^-	$\frac{2}{3} \cdot p_3$	no	0%
3b	**Ar^{2+}**, residual gas	e_1^-, **e_2^-**, e^-	$\frac{2}{3} \cdot p_3$	yes	$q_4^{\text{good}} = \frac{2}{3} \cdot p_3$
3c	**Ar^{2+}**, residual gas	e_1^-, e_2^-, **e^-**	$\frac{2}{3} \cdot p_3$	maybe	$q_5^{\text{bad}} = \frac{2}{3} \cdot p_3$
sum			100%		55%

The column "relevant probabilities" in Tab. 9.2 are 0% if the condition $|p_{z_calc}| < 0.5$ a.u. is not expected to be fulfilled. For example in channel 1a the electron from the pump-pulse is detected. This event will not contribute to the spectra of interest (see chapter 9.6). For channel 2c the "relevant probability" is the "probability" weighted with the factor 0.5 because there are two possible emission directions for the electron that is liberated by the elliptically polarized probe-pulse. Hence, there is a 50% chance that the electron from the parasitic Ar^+ has a similar momentum as the electron e_2^- and therefore $|p_{z_calc}| < 0.5$ a.u.

is fulfilled in 50% of the events. The same arguments hold for channel 3c but here the factor 0.5 has been omitted[133]. This is because the probe-pulse is expected to liberate more than one electron from the residual gas for laser shots that double ionize argon. Finally, $P(\text{“random coincidences”})$ can be written as:

$$P(\text{“random coincidences”}) = \frac{q_3^{\text{bad}} + q_5^{\text{bad}}}{q_1^{\text{good}} + q_2^{\text{good}} + q_3^{\text{bad}} + q_4^{\text{good}} + q_5^{\text{bad}}} = 0.35 \qquad (30)$$

[133]Not omitting the factor 0.5 for channel 3c in Tab. 9.1 leads to a value of $P(\text{“random coincidences”}) = 0.29$.

9.8. Detailed Model of the Pump-Probe-Scheme

Fig. 9.14 highlights the two mirror-symmetric m-prepared states. There are two electrons with $m = -1$ and two electrons with $m = +1$ in the outermost orbital (3p orbital) of argon and only one electron is ejected by the pump-pulse. This means that Fig. 9.14 is a good schematic overview, but is an oversimplification.

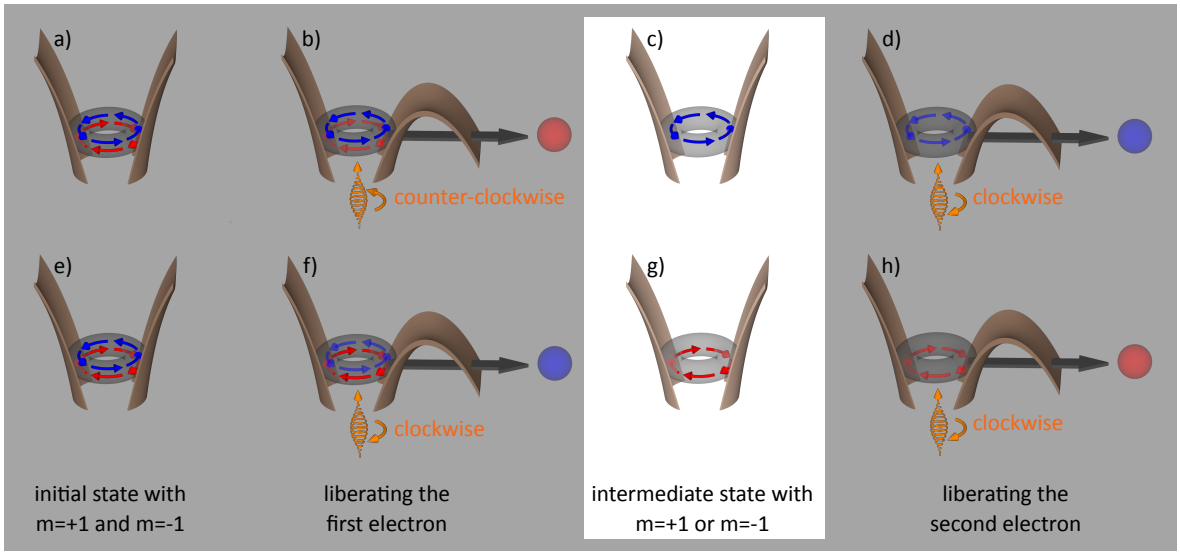


Figure 9.14: Shows the same as Fig. 9.2 highlighting the prepared ring currents in the singly charged ions. The figure is taken from the publication by Eckart et al. [140] and the labels have been adapted.

Fig. 9.15 provides an overview including all relevant ionization pathways. In Fig. 9.15(a) the initial state (with two $m = +1$ and two $m = -1$ electrons[134]), the two possible intermediate ionic states and the four possible final ionic states are illustrated as boxes containing up to four colored circles corresponding to the relevant electrons. Knowing that the pump-pulse and the probe-pulse both liberate one electron, the transition probabilities can be defined as is provided in the white boxes on the arrows connecting the atomic states[135]. In Fig. 9.15(a) the pump-pulse and the probe-pulse have opposite helicities. In Fig. 9.15(b) the pump-pulse and the probe-pulse have the same helicity and the resulting differences compared to Fig. 9.15(a) are marked in yellow.

[134] Electrons with $m = -1$ rotate counter-clockwise in the plane of polarization using the semi-classical picture. Since in all scenarios the probe-pulse's electric field rotates clockwise ("R") electrons with $m = -1$ are counter-rotating with respect to temporal evolution of the laser's electric field of the probe-pulse. $(1-a)$ denotes the probability to liberate an electron that is counter-rotating with respect to the pump-pulse ($m = +1$ in Fig. 9.15(a) and $m = -1$ in Fig. 9.15(b)).

[135] Which transitions are more likely will be examined in chapter 9.12. In Fig. 9.15 the transitions that are more likely are marked as bold arrows, but this does not change the analysis and is only intended to guide the reader.

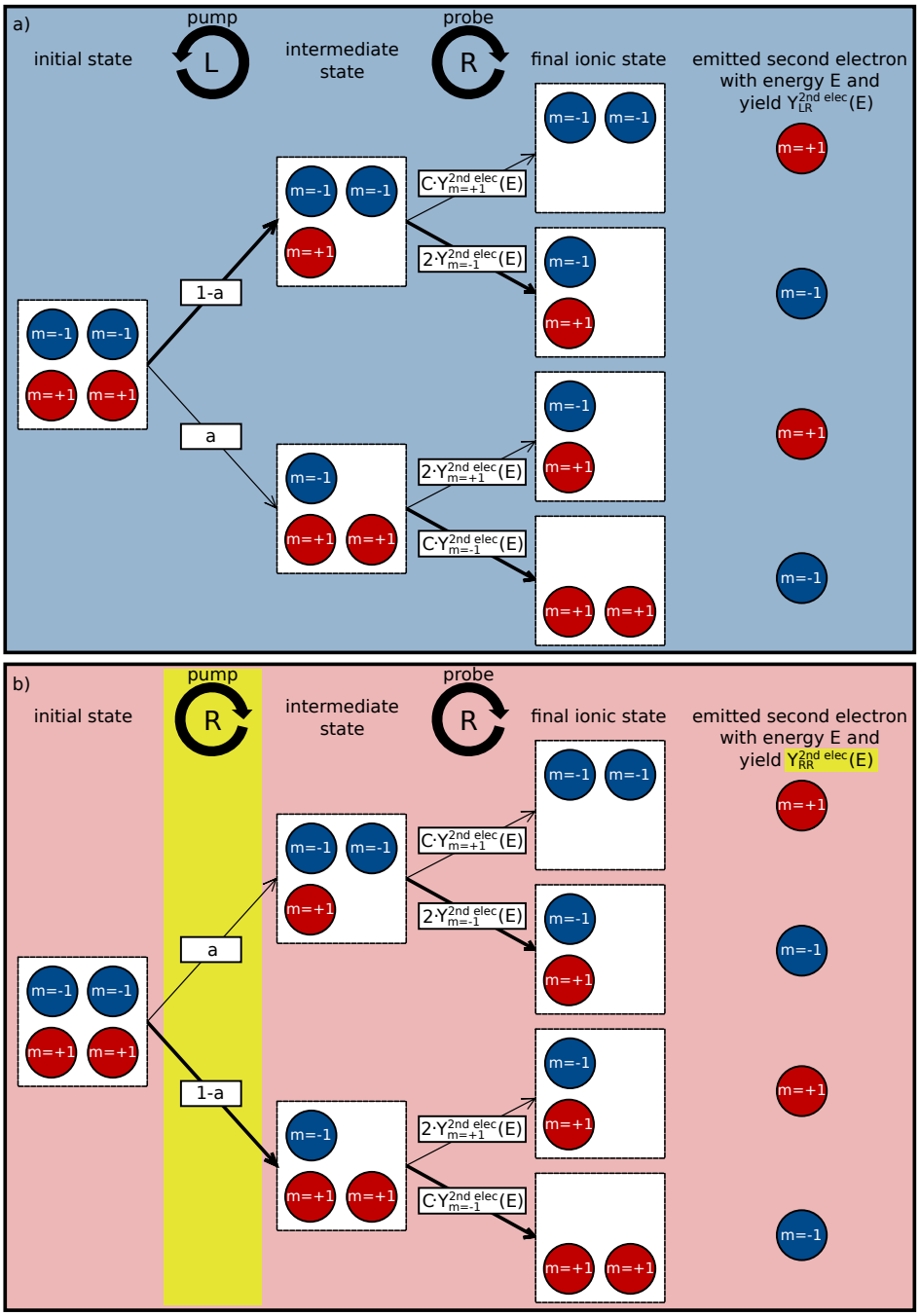


Figure 9.15: (a) shows an overview of all relevant pathways for the scenario in which the pump-pulse and the probe-pulse have opposite helicities. The pump-pulse liberates one electron. Here, the variable a (with $0 \leq a \leq 1$) indicates the probability of removing an electron with $m = -1$. The complementary probability $1 - a$ denotes the probability of removing an electron with $m = +1$. This leads to two possible intermediate states and the probabilities are shown on the arrows connecting the schematic representation of the initial state (with two $m = +1$ and two $m = -1$ electrons) and the intermediate state containing one electron hole. The probe-pulse can either eject an electron with $m = -1$ or $m = +1$ leading to four possible branches and therefore to four possible situations for the emission of the second electron (see text for details). The bold arrows indicate the pathways that will turn out to be preferred. (b) shows the same as (a) but for a pump-pulse with inverted helicity. Everything remains unchanged and only the probability a and $1 - a$ have to be exchanged. The differences with respect to (a) are highlighted.

The probability of liberating an electron with the final kinetic energy E and $m = -1$ [$m = +1$] is given by $Y^{\text{2nd elec}}_{\text{m}=-1}(E)$ [$Y^{\text{2nd elec}}_{\text{m}=+1}(E)$]. The two occurring prefactors are "2" and "C". The prefactor "2" accounts for the availability of two electrons for certain transitions. The prefactor C (with $C \geq 0$) allows one to include correlation effects[136] and is relevant for all transitions leading to a final state that is missing two electrons with the same magnetic quantum number. $C = 1$ would indicate that correlation effects can be neglected and $C = 0$ would describe a situation in which it is impossible to remove two electrons with the same magnetic quantum number.

Summing up all possible pathways in Fig. 9.15(a) leads to the electron yield $Y^{\text{2nd elec}}_{\text{LR}}(E)$ for an electron with final kinetic energy E:

$$\begin{aligned} Y^{\text{2nd elec}}_{\text{LR}}(E) = {} & (1-a)\cdot C \cdot Y^{\text{2nd elec}}_{\text{m}=+1}(E) \\ & + (1-a)\cdot 2 \cdot Y^{\text{2nd elec}}_{\text{m}=-1}(E) \\ & + a \cdot 2 \cdot Y^{\text{2nd elec}}_{\text{m}=+1}(E) \\ & + a \cdot C \cdot Y^{\text{2nd elec}}_{\text{m}=-1}(E) \end{aligned} \tag{31}$$

In comparison, summing up all pathways in Fig. 9.15(b) results in:

$$\begin{aligned} Y^{\text{2nd elec}}_{\text{RR}}(E) = {} & a \cdot C \cdot Y^{\text{2nd elec}}_{\text{m}=+1}(E) \\ & + a \cdot 2 \cdot Y^{\text{2nd elec}}_{\text{m}=-1}(E) \\ & + (1-a)\cdot 2 \cdot Y^{\text{2nd elec}}_{\text{m}=+1}(E) \\ & + (1-a)\cdot C \cdot Y^{\text{2nd elec}}_{\text{m}=-1}(E) \end{aligned} \tag{32}$$

The formal analysis is continued in chapter 9.10. In chapter 9.9 important aspects of non-adiabatic tunneling are qualitatively discussed and it will be shown that $0 \leq a < 0.5$.

[136] Removing two electrons with $m = +1$ or two electrons with $m = -1$ from the 3p-orbital of argon leads to an excited state (^{1}D state) of Ar^{2+}. Liberation of two electrons with unequal magnetic quantum number can either lead to Ar^{2+} in its ground state (^{3}P state) or in an excited state (^{1}D state). The ^{3}P state and the ^{1}D state differ in energy by about 1.74 eV. Different tunnel ionization rates are expected for final states that differ in energy (see Ref. [151] on p. 343f. and Ref. [26]).

9.9. Qualitative Results

At this stage of the analysis it is important to gain some insight regarding the qualitative results because it will help during the rest of the quantitative analysis.

The most probable energy is higher in $Y_{\mathrm{RR}}^{\mathrm{2nd\,elec}}(E)$ than it is in $Y_{\mathrm{LR}}^{\mathrm{2nd\,elec}}(E)$. Since the probe rotates clockwise in the plane of polarization in both cases this energy difference can be related to offsets of the initial momentum distribution (see also chapter 8) which is illustrated in Fig. 9.16.

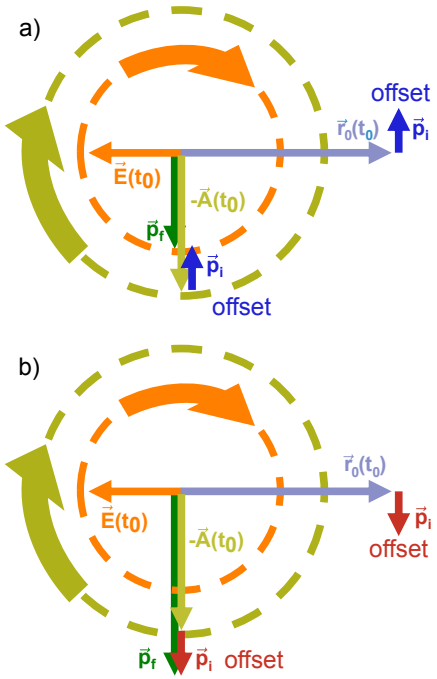


Figure 9.16: In analogy to Fig. 8.2 in (a) [(b)] a schematic illustration of the geometry at the instance of tunneling t_0 is shown for initial momentum offset related to negative [positive] values of the magnetic quantum number m. The vector of the laser electric field $\vec{E}(t_0)$, the vector of the tunnel exit $\vec{r}_0(t_0)$, the initial momentum offset, the negative vector potential $-\vec{A}(t_0)$, a non-zero value for the initial momentum $\vec{p}_i$ at the tunnel exit and the final momentum neglecting Coulomb interaction after tunneling $\vec{p}_f$ are shown in both panels. The figure and its caption are based on Fig. 4(c) from Eckart et al. [25].

Now, for a given tunnel exit position $\vec{r}_0$ the relation $L_x = |\vec{r}_0| \cdot p_i = m$ (see chapter 8.5) can be used. This implies that the value of m at the tunnel exit is lower for $Y_{\mathrm{LR}}^{\mathrm{2nd\,elec}}(E)$ than it is for $Y_{\mathrm{RR}}^{\mathrm{2nd\,elec}}(E)$. Knowing that there are only two possible initial states ($m = -1$ and $m = +1$) this allows for the conclusion that the majority of electrons contributing to $Y_{\mathrm{LR}}^{\mathrm{2nd\,elec}}(E)$ originates from electrons with $m = -1$. Further, the integral of $Y_{\mathrm{LR}}^{\mathrm{2nd\,elec}}(E)$ is larger than that of $Y_{\mathrm{LR}}^{\mathrm{2nd\,elec}}(E)$ which experimentally proves that it is more likely to liberate electrons with $m = -1$ than with $m = +1$ for a laser electric field that rotates clockwise.

Assuming that also for 390 nm electrons that are counter-rotating with respect to the temporal evolution of the laser's electric field are preferred to be liberated, it can be concluded that the pump-pulse prefers electrons with $m = +1$ [$m = -1$] in Fig. 9.15(a) [Fig. 9.15(b)] because the pump-pulse's electric field rotates counter-clockwise [clockwise] in this scenario. As a result the value of a is known to be $0 \leq a < 0.5$.

9.10. m-Dependent Electron Momentum Distributions

Is it possible to obtain the energy dependent yields for $Y^{\mathrm{2nd\,elec}}_{\mathrm{m=-1}}(E)$ and $Y^{\mathrm{2nd\,elec}}_{\mathrm{m=+1}}(E)$ from the measured data without input from theory? In order to gain this quantitative insight a formula that expresses $Y^{\mathrm{2nd\,elec}}_{\mathrm{m=-1}}(E)$ and $Y^{\mathrm{2nd\,elec}}_{\mathrm{m=+1}}(E)$ in dependence of measured quantities has to be derived.
Summing up $Y^{\mathrm{2nd\,elec}}_{\mathrm{LR}}(E)$ and $Y^{\mathrm{2nd\,elec}}_{\mathrm{RR}}(E)$ gives:

$$\begin{aligned} Y^{\mathrm{2nd\,elec}}_{\mathrm{LR}}(E) + Y^{\mathrm{2nd\,elec}}_{\mathrm{RR}}(E) &= C \cdot Y^{\mathrm{2nd\,elec}}_{\mathrm{m=+1}}(E) \\ &\quad + 2 \cdot Y^{\mathrm{2nd\,elec}}_{\mathrm{m=-1}}(E) \\ &\quad + 2 \cdot Y^{\mathrm{2nd\,elec}}_{\mathrm{m=+1}}(E) \\ &\quad + C \cdot Y^{\mathrm{2nd\,elec}}_{\mathrm{m=-1}}(E) \\ &= (C+2) \cdot \left(Y^{\mathrm{2nd\,elec}}_{\mathrm{m=+1}}(E) + Y^{\mathrm{2nd\,elec}}_{\mathrm{m=-1}}(E) \right) \end{aligned} \tag{33}$$

The difference of $Y^{\mathrm{2nd\,elec}}_{\mathrm{LR}}(E)$ and $Y^{\mathrm{2nd\,elec}}_{\mathrm{RR}}(E)$ is:

$$\begin{aligned} Y^{\mathrm{2nd\,elec}}_{\mathrm{LR}}(E) - Y^{\mathrm{2nd\,elec}}_{\mathrm{RR}}(E) &= (1-2\cdot a) \cdot C \cdot Y^{\mathrm{2nd\,elec}}_{\mathrm{m=+1}}(E) \\ &\quad + (1-2\cdot a) \cdot 2 \cdot Y^{\mathrm{2nd\,elec}}_{\mathrm{m=-1}}(E) \\ &\quad - (1-2\cdot a) \cdot 2 \cdot Y^{\mathrm{2nd\,elec}}_{\mathrm{m=+1}}(E) \\ &\quad - (1-2\cdot a) \cdot C \cdot Y^{\mathrm{2nd\,elec}}_{\mathrm{m=-1}}(E) \\ &= (C-2) \cdot (1-2\cdot a) \cdot \left(Y^{\mathrm{2nd\,elec}}_{\mathrm{m=+1}}(E) - Y^{\mathrm{2nd\,elec}}_{\mathrm{m=-1}}(E) \right) \end{aligned} \tag{34}$$

The energy dependent value for the normalized difference $N_d(E)$ is[137]:

$$\begin{aligned} N_d(E) &= \frac{Y^{\mathrm{2nd\,elec}}_{\mathrm{LR}}(E) - Y^{\mathrm{2nd\,elec}}_{\mathrm{RR}}(E)}{Y^{\mathrm{2nd\,elec}}_{\mathrm{LR}}(E) + Y^{\mathrm{2nd\,elec}}_{\mathrm{RR}}(E)} \\ &= \frac{(C-2)\cdot(1-2\cdot a)}{(C+2)} \cdot \frac{Y^{\mathrm{2nd\,elec}}_{\mathrm{m=+1}}(E) - Y^{\mathrm{2nd\,elec}}_{\mathrm{m=-1}}(E)}{Y^{\mathrm{2nd\,elec}}_{\mathrm{m=+1}}(E) + Y^{\mathrm{2nd\,elec}}_{\mathrm{m=-1}}(E)} \end{aligned} \tag{35}$$

$N_d(E)$ unambiguously defines the ratio of $Y^{\mathrm{2nd\,elec}}_{\mathrm{m=-1}}(E)$ and $Y^{\mathrm{2nd\,elec}}_{\mathrm{m=+1}}(E)$ based on the measured distributions $Y^{\mathrm{2nd\,elec}}_{\mathrm{LR}}(E)$ and $Y^{\mathrm{2nd\,elec}}_{\mathrm{RR}}(E)$. Assuming that the value of C is independent of the final kinetic energy of the second electron E, the sum of $Y^{\mathrm{2nd\,elec}}_{\mathrm{m=-1}}(E)$ and $Y^{\mathrm{2nd\,elec}}_{\mathrm{m=+1}}(E)$ is known using Eq. 33. Thus, the value of C only scales the absolute heights of $Y^{\mathrm{2nd\,elec}}_{\mathrm{m=-1}}(E)$ and

[137] It is assumed that $Y^{\mathrm{2nd\,elec}}_{\mathrm{m=-1}}(E) > 0$ and $Y^{\mathrm{2nd\,elec}}_{\mathrm{m=+1}}(E) > 0$ for all E.

$Y^{\text{2nd elec}}_{\text{m=+1}}(E)$. Hence, even without any knowledge about the value of C, the knowledge of the prefactor $S = \frac{(C-2)\cdot(1-2\cdot a)}{(C+2)}$ (see Eq. 35) already allows for the calculation of the normalized distributions:

$$Y^{\text{2nd elec}}_{\text{m=-1 norm.}}(E) = \frac{Y^{\text{2nd elec}}_{\text{m=-1}}(E)}{\max\limits_{E}\left(Y^{\text{2nd elec}}_{\text{m=-1}}(E)\right)}$$
$$Y^{\text{2nd elec}}_{\text{m=+1 norm.}}(E) = \frac{Y^{\text{2nd elec}}_{\text{m=+1}}(E)}{\max\limits_{E}\left(Y^{\text{2nd elec}}_{\text{m=-1}}(E)\right)} \tag{36}$$

If the pre-factor $S = \frac{(C-2)\cdot(1-2\cdot a)}{(C+2)}$ can be expressed as a function of experimentally accessible quantities this would allow one to calculate $Y^{\text{2nd elec}}_{\text{m=-1 norm.}}(E)$ and $Y^{\text{2nd elec}}_{\text{m=+1 norm.}}(E)$ without input from theory.

To this end, the ratio $R = \frac{Y^{\text{2nd elec}}_{\text{LR}}(E)}{Y^{\text{2nd elec}}_{\text{RR}}(E)}$ is presented in Fig. 9.17. The value for high energy electrons E_{high} is estimated to be $R_{\text{highE}} = 0.6 \pm 0.1$.

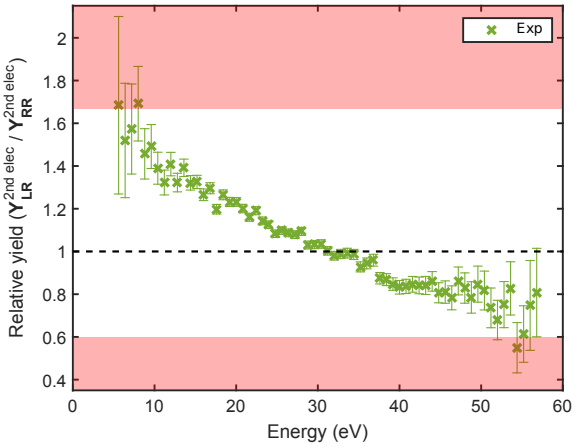


Figure 9.17: "[...] b, The ratio of ionization rates $\frac{Y^{\text{2nd elec}}_{\text{LR}}}{Y^{\text{2nd elec}}_{\text{LR}}}$ is found to be between 0.6 and 1.67. This asymptotic behaviour for low and high energies can be used to experimentally obtain $Y^{\text{2nd elec}}_{\text{m=-1}}$ and $Y^{\text{2nd elec}}_{\text{m=+1}}$ (see Methods [in this thesis this is explained in section 9.8 - author's note] for details). [...]" (The panel is part of a figure in the final resubmitted version. The content is the same as in Eckart et al. [26] but the layout has been adapted. Part of the caption is taken from Eckart et al. [26].)

For a high energy E_{high} the relation $Y^{\text{2nd elec}}_{\text{m=+1}}(E_{\text{high}}) \gg Y^{\text{2nd elec}}_{\text{m=-1}}(E_{\text{high}})$ holds. This is based on the assumption that the energy depend yields $Y^{\text{2nd elec}}_{\text{m=-1}}(E)$ and $Y^{\text{2nd elec}}_{\text{m=+1}}(E)$ are similar to Gaussian distributions and shifted with respect to each other. Thus, for high E_{high} Eq. 31

simplifies to:

$$\begin{aligned} Y_{\mathrm{LR}}^{\mathrm{2nd\,elec}}(E_{\mathrm{high}}) &= (1-a)\cdot C\cdot Y_{\mathrm{m=+1}}^{\mathrm{2nd\,elec}}(E_{\mathrm{high}}) \\ &\quad + a\cdot 2\cdot Y_{\mathrm{m=+1}}^{\mathrm{2nd\,elec}}(E_{\mathrm{high}}) \\ &= ((1-a)\cdot C + a\cdot 2)\cdot Y_{\mathrm{m=+1}}^{\mathrm{2nd\,elec}}(E_{\mathrm{high}}) \end{aligned} \tag{37}$$

and Eq. 32 simplifies to:

$$\begin{aligned} Y_{\mathrm{RR}}^{\mathrm{2nd\,elec}}(E_{\mathrm{high}}) &= a\cdot C\cdot Y_{\mathrm{m=+1}}^{\mathrm{2nd\,elec}}(E_{\mathrm{high}}) \\ &\quad + (1-a)\cdot 2\cdot Y_{\mathrm{m=+1}}^{\mathrm{2nd\,elec}}(E_{\mathrm{high}}) \\ &= (a\cdot C + (1-a)\cdot 2)\cdot Y_{\mathrm{m=+1}}^{\mathrm{2nd\,elec}}(E_{\mathrm{high}}) \end{aligned} \tag{38}$$

Eq. 37 and Eq. 38 allow one to express the ratio as:

$$\begin{aligned} R_{\mathrm{highE}} &= \frac{Y_{\mathrm{LR}}^{\mathrm{2nd\,elec}}(E_{\mathrm{high}})}{Y_{\mathrm{RR}}^{\mathrm{2nd\,elec}}(E_{\mathrm{high}})} \\ &= \frac{2\cdot a + (1-a)\cdot C}{2\cdot(1-a) + a\cdot C} \end{aligned} \tag{39}$$

Solving Eq. 39 for C leads to:

$$C = \frac{2\cdot a - 2\cdot(1-a)\cdot R_{\mathrm{highE}}}{(1+R_{\mathrm{highE}})\cdot a - 1} \tag{40}$$

Using Eq. 40, the scaling factor $S = \frac{(C-2)\cdot(1-2\cdot a)}{(C+2)}$ for $0 \leq a < 0.5$ (see chapter 9.9) and $R_{\mathrm{highE}} < 1$ can be written as:

$$\begin{aligned} S &= \frac{(C-2)\cdot(1-2\cdot a)}{(C+2)} = \frac{(\frac{2\cdot a-2\cdot(1-a)\cdot R_{\mathrm{highE}}}{(1+R_{\mathrm{highE}})\cdot a-1} - 2)\cdot(1-2\cdot a)}{(\frac{2\cdot a-2\cdot(1-a)\cdot R_{\mathrm{highE}}}{(1+R_{\mathrm{highE}})\cdot a-1} + 2)} \\ &= \frac{\left[2\cdot a - 2\cdot(1-a)\cdot R_{\mathrm{highE}} - 2\cdot((1+R_{\mathrm{highE}})\cdot a - 1)\right]\cdot(1-2\cdot a)}{2\cdot a - 2\cdot(1-a)\cdot R_{\mathrm{highE}} + 2\cdot((1+R_{\mathrm{highE}})\cdot a - 1)} \\ &= \frac{\left[2\cdot a - 2\cdot R_{\mathrm{highE}} + 2\cdot a\cdot R_{\mathrm{highE}} - ((1+R_{\mathrm{highE}})\cdot 2\cdot a - 2)\right]\cdot(1-2\cdot a)}{2\cdot a - 2\cdot R_{\mathrm{highE}} + 2\cdot a\cdot R_{\mathrm{highE}} + ((1+R_{\mathrm{highE}})\cdot 2\cdot a - 2)} \\ &= \frac{-2\cdot R_{\mathrm{highE}} + 4\cdot R_{\mathrm{highE}}\cdot a + 2 - 4\cdot a}{-2\cdot R_{\mathrm{highE}} + 4\cdot R_{\mathrm{highE}}\cdot a - 2 + 4\cdot a} = \frac{R_{\mathrm{highE}}-1}{R_{\mathrm{highE}}+1}\cdot\frac{4\cdot a-2}{4\cdot a-2} \\ &= \frac{R_{\mathrm{highE}}-1}{R_{\mathrm{highE}}+1} \end{aligned} \tag{41}$$

This is the desired result, because using Eq. 35 it allows one to write:

$$\frac{Y^{\text{2nd elec}}_{\text{m=+1}}(E) - Y^{\text{2nd elec}}_{\text{m=-1}}(E)}{Y^{\text{2nd elec}}_{\text{m=+1}}(E) + Y^{\text{2nd elec}}_{\text{m=-1}}(E)} = \frac{N_d(E)}{S} = N_d(E) \cdot \frac{R_{\text{highE}} + 1}{R_{\text{highE}} - 1} \tag{42}$$

Eq. 42 can also be written as:

$$\frac{Y^{\text{2nd elec}}_{\text{m=+1}}(E)}{Y^{\text{2nd elec}}_{\text{m=-1}}(E)} = \frac{1 + N_d(E) \cdot \frac{R_{\text{highE}}+1}{R_{\text{highE}}-1}}{1 - N_d(E) \cdot \frac{R_{\text{highE}}+1}{R_{\text{highE}}-1}} \tag{43}$$

Using Eq. 33 this can be transformed to:

$$\begin{aligned} Y^{\text{2nd elec}}_{\text{m=+1}}(E) &= Y^{\text{2nd elec}}_{\text{m=-1}}(E) \cdot \frac{1 + N_d(E) \cdot \frac{R_{\text{highE}}+1}{R_{\text{highE}}-1}}{1 - N_d(E) \cdot \frac{R_{\text{highE}}+1}{R_{\text{highE}}-1}} \\ &= \left(\frac{Y^{\text{2nd elec}}_{\text{LR}}(E) + Y^{\text{2nd elec}}_{\text{RR}}(E)}{C+2} - Y^{\text{2nd elec}}_{\text{m=+1}}(E) \right) \cdot \frac{1 + N_d(E) \cdot \frac{R_{\text{highE}}+1}{R_{\text{highE}}-1}}{1 - N_d(E) \cdot \frac{R_{\text{highE}}+1}{R_{\text{highE}}-1}} \end{aligned} \tag{44}$$

Eq. 44 can be written as:

$$\begin{aligned} Y^{\text{2nd elec}}_{\text{m=+1}}(E) \left(1 + \frac{1 + N_d(E) \cdot \frac{R_{\text{highE}}+1}{R_{\text{highE}}-1}}{1 - N_d(E) \cdot \frac{R_{\text{highE}}+1}{R_{\text{highE}}-1}} \right) &= \left(\frac{Y^{\text{2nd elec}}_{\text{LR}}(E) + Y^{\text{2nd elec}}_{\text{RR}}(E)}{C+2} \right) \\ &\quad \times \frac{1 + N_d(E) \cdot \frac{R_{\text{highE}}+1}{R_{\text{highE}}-1}}{1 - N_d(E) \cdot \frac{R_{\text{highE}}+1}{R_{\text{highE}}-1}} \end{aligned} \tag{45}$$

This can be simplified to:

$$\begin{aligned} Y^{\text{2nd elec}}_{\text{m=+1}}(E) \left(\frac{2}{1 - N_d(E) \cdot \frac{R_{\text{highE}}+1}{R_{\text{highE}}-1}} \right) &= \left(\frac{Y^{\text{2nd elec}}_{\text{LR}}(E) + Y^{\text{2nd elec}}_{\text{RR}}(E)}{C+2} \right) \\ &\quad \times \frac{1 + N_d(E) \cdot \frac{R_{\text{highE}}+1}{R_{\text{highE}}-1}}{1 - N_d(E) \cdot \frac{R_{\text{highE}}+1}{R_{\text{highE}}-1}} \end{aligned} \tag{46}$$

Solving for $Y^{\text{2nd elec}}_{\text{m=+1}}(E)$ yields:

$$Y^{\text{2nd elec}}_{\text{m=+1}}(E) = \frac{Y^{\text{2nd elec}}_{\text{LR}}(E) + Y^{\text{2nd elec}}_{\text{RR}}(E)}{2 \cdot C + 4} \cdot \left(1 + N_d(E) \cdot \frac{R_{\text{highE}} + 1}{R_{\text{highE}} - 1} \right) \tag{47}$$

An analogue expression can be derived for $Y^{\text{2nd elec}}_{\text{m=}-1}(E)$:

$$Y^{\text{2nd elec}}_{\text{m=}-1}(E) = \frac{Y^{\text{2nd elec}}_{\text{LR}}(E) + Y^{\text{2nd elec}}_{\text{RR}}(E)}{2 \cdot C + 4} \cdot \left(1 - N_d(E) \cdot \frac{R_{\text{highE}} + 1}{R_{\text{highE}} - 1}\right) \tag{48}$$

Eq. 47 and Eq. 48 are the final expression for the energy dependent yield for electrons from $m = -1$ and $m = +1$. All quantities except C are experimentally accessible quantities. The value of C is only a common normalization factor that does neither change the relative yield of $Y^{\text{2nd elec}}_{\text{m=}-1}(E)$ and $Y^{\text{2nd elec}}_{\text{m=}+1}(E)$ nor the shape of the distributions.

Interestingly, Eq. 47 and Eq. 48 do not depend on the value of a and it is possible to obtain $Y^{\text{2nd elec}}_{\text{m=}-1\,\text{norm.}}(E)$ and $Y^{\text{2nd elec}}_{\text{m=}+1\,\text{norm.}}(E)$ from the experiment without any input from theory. The result is shown in Fig. 9.18 and the difference of the yields of $Y^{\text{2nd elec}}_{\text{m=}-1\,\text{norm.}}(E)$ and $Y^{\text{2nd elec}}_{\text{m=}+1\,\text{norm.}}(E)$ is very pronounced.

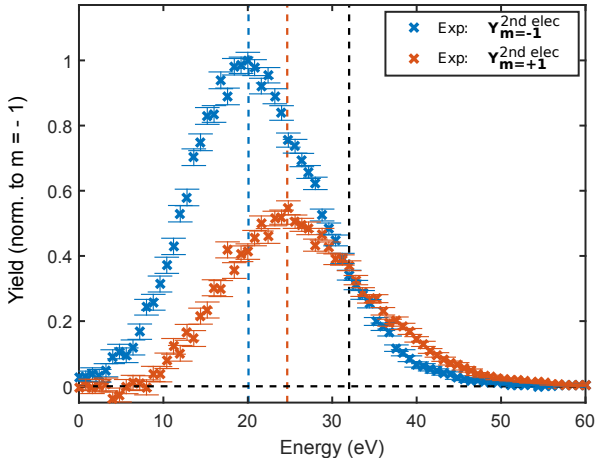


Figure 9.18: The energy-dependent yields $Y^{\text{2nd elec}}_{\text{m=}-1}$ and $Y^{\text{2nd elec}}_{\text{m=}+1}$ are calculated directly from the measured data using $R_{\text{highE}} = 0.6$ (which has been experimentally obtained using the data shown in Fig. 9.17). The error bars only show the standard deviation of the statistical errors. The maxima are indicated by the vertical coloured lines. (The panel is part of a figure in the final resubmitted version. The content is the same as in Eckart et al. [26] but the layout has been adapted and the data from theory has been removed.)

The ratio of the integrals over energy of $Y^{\text{2nd elec}}_{\text{m=}-1}$ and $Y^{\text{2nd elec}}_{\text{m=}+1}$ is:

$$\frac{\int Y^{\text{2nd elec}}_{\text{m=}-1}(E)dE}{\int Y^{\text{2nd elec}}_{\text{m=}+1}(E)dE} = 1.8 \tag{49}$$

This indicates that it is 1.8 times more likely to ionize an electron with $m = -1$ than an electron with $m = +1$ from a singly charged argon ion in its ground state by the probe-pulse. The peak energies are 20.1 eV for $Y^{\text{2nd elec}}_{\text{m=}-1}$ and 24.7 eV for $Y^{\text{2nd elec}}_{\text{m=}+1}$ and the ratio $\frac{Y^{\text{2nd elec}}_{\text{m=}-1}}{Y^{\text{2nd elec}}_{\text{m=}+1}}$ equals one at about 31.2 eV. The error bars that are shown in Fig. 9.18 represent the standard deviation of the statistical errors. The uncertainty of $R_{\text{highE}} = 0.6 \pm 0.1$ has not yet

been considered. Fig. 9.19 shows how different values of R_{highE} affect the calculated yields $Y^{\mathrm{2nd\,elec}}_{\mathrm{m=-1}}$ and $Y^{\mathrm{2nd\,elec}}_{\mathrm{m=+1}}$. The values $R_{\mathrm{highE}} = 0.5$ and $R_{\mathrm{highE}} = 0.7$ are used.

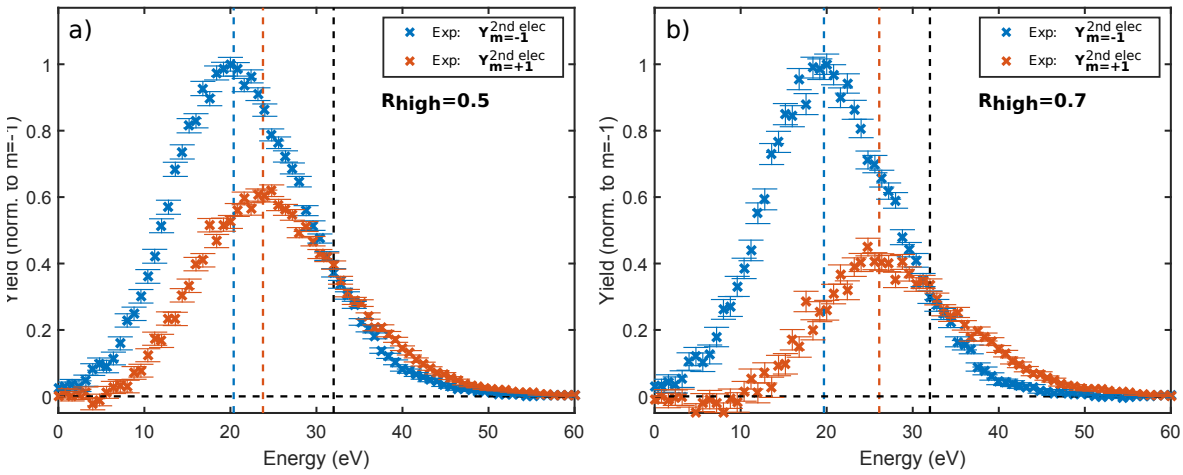


Figure 9.19: (a) [(b)] shows the same as Fig. 9.18 but using $R_{\mathrm{highE}} = 0.5$ [$R_{\mathrm{highE}} = 0.7$] instead of $R_{\mathrm{highE}} = 0.6$. (The figure was part of the answer to the referees regarding the publication by Eckart et al. [26]. Labels and layout have been adapted. Results from theory have been removed for clarity.)

The differences in the retrieved yields $Y^{\mathrm{2nd\,elec}}_{\mathrm{m=-1}}$ and $Y^{\mathrm{2nd\,elec}}_{\mathrm{m=+1}}$ increase with increasing R_{highE}. This is expected. Choosing $C = 1$ the value of $R = 0.5$ implies that $a = 0$. As discussed above $a = 0$ is equivalent to perfect preparation of the m-prepared state by the pump-pulse. In other words: For $a = 0$ the imperfect preparation by the pump-pulse can be neglected, leading to the results in Fig. 9.19(a). If the imperfection of preparation by the pump-pulse is compensated for, the difference of $Y^{\mathrm{2nd\,elec}}_{\mathrm{m=-1}}$ and $Y^{\mathrm{2nd\,elec}}_{\mathrm{m=+1}}$ increases (see Fig. 9.19(b)).

9.10.1. Comparison of the Results with Theory

The simplest theory that is used is the SCTS model introduced in chapter 5.3 which is extended by including an offset of the initial momentum distribution p_i at the tunnel exit perpendicular to the tunnel exit and in the plane of polarization. The offset momentum is calculated assuming momentum conservation during tunneling and thus $p_i = \frac{m \cdot \hbar}{r_0}$. This SCTS calculation was carried out by Maksim Kunitski and further details are described in see Ref. [26]. Fig. 9.20 shows the results for $Y^{\text{2nd elec}}_{\text{m=-1}}$ and $Y^{\text{2nd elec}}_{\text{m=+1}}$ after normalizing $Y^{\text{2nd elec}}_{\text{m=-1}}$ to a maximum of one and $Y^{\text{2nd elec}}_{\text{m=+1}}$ to the peak of the experimental data for $Y^{\text{2nd elec}}_{\text{m=+1}}$.

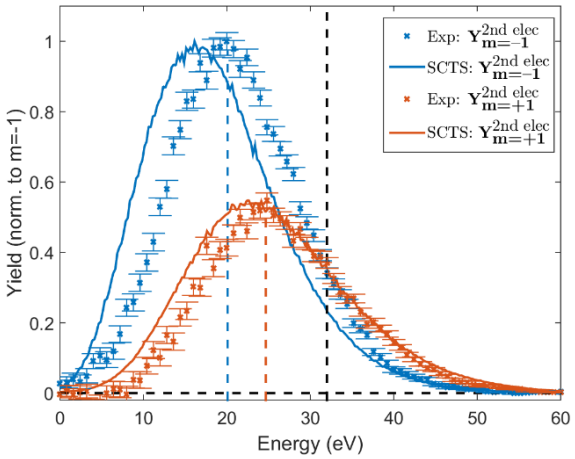


Figure 9.20: "Semiclassical simulation of the electron spectra. Comparison of the experimental results from Fig. 3c with SCTS calculations. The semiclassical simulations assume that the tunneling electron preserves the magnetic quantum number m during tunneling and hence has an initial transverse momentum $p_\perp = m\hbar/r$ at the tunnel exit r. The peaks of the classical distributions are normalized to experimental data. Error bars show the standard deviation of the statistical errors." (Figure is part of the final resubmitted manuscript. The figure and its caption are taken from the supplementary information of Eckart et al. [26].)

The results shown in Fig. 9.20 are calculated without the "phase compression" described in chapter 5.3. Anyway, the results are accurate: In chapter 8 it has been shown that for radial momenta on the order of 1 a.u. the Coulomb-interaction after tunneling is very weak and only leads to slight changes of the final momentum. Therefore, it is possible to conclude the following: if the initial momentum at the tunnel-exit is given by $p_i = \frac{m \cdot \hbar}{r_0}$ and assuming that the tunnel exit position is about $r_0 = 8$ a.u., then the difference in final momentum is $\Delta p_i = \Delta p_f = \frac{m_+ \cdot \hbar}{r_0} - \frac{m_- \cdot \hbar}{r_0} = \frac{1 \cdot \hbar}{8} - \frac{-1 \cdot \hbar}{8} = 0.25$ a.u. comparing electrons from $m = -1$ and $m = +1$.

This agrees very well with the results shown in Fig. 9.20 but it is seen that the experimental differences are a bit smaller than the semi-classical model predicts. Fig. 9.21 is based on the same numerical result as Fig. 9.20 but shows the differences in electron momentum

instead of electron energy. To this end in Fig. 9.21(a) the radial momentum $p_r = \sqrt{p_y^2 + p_z^2}$ is plotted as a function of the angle in the plane of polarization atan2(p_z, p_y). Fig. 9.21(b) depicts the same as Fig. 9.21(a) but showing the deviation of the radial momentum to the mean of the radial momentum belonging to electrons with $m = -1$ and $m = +1$ (for details, see supplementary information of Eckart et al. [26]).

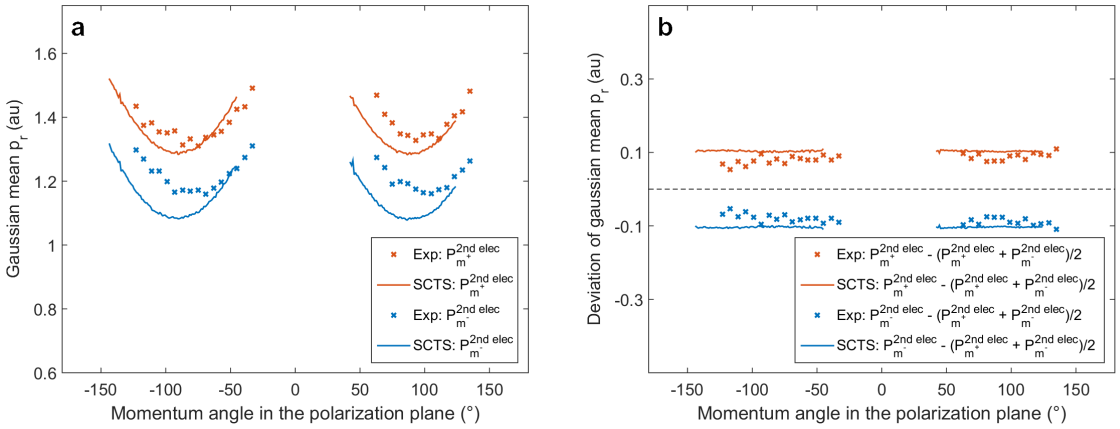


Figure 9.21: "Results of the semiclassical simulation. a, Mean momentum (obtained by fitting a Gaussian distribution and only shown if experimental statistics are sufficient) vs. the momentum angle in the plane of polarization for the experimental data compared to the same quantity from the semiclassical simulations for $m = +1$ (m^+) and $m = -1$ (m^-). b, The same as a but as deviation to the mean of the m^+ and m^-. Besides a good agreement it is found that the semiclassical simulation slightly overestimates the momentum difference in comparison to the experimental results. This overestimation has its roots in higher differences in the initial transverse momenta for $m = +1$ and $m = -1$ states which are assumed in the semiclassical simulations." (Figure is part of the final resubmitted manuscript. The figure and its caption are taken from the supplementary information of Eckart et al. [26].)

Are the differences of the results from the SCTS model and the experimental results due to systematic experimental errors or is the semi-classical model overestimating the differences in the initial momentum distributions for electrons with $m = -1$ and $m = +1$? The latter is true, as can be shown using two additional and more sophisticated theoretical approaches. One is solving the TDSE and the other is using analytical R-matrix theory (ARM). Both take the complex dynamics in the tunnel and Coulomb interaction fully into account (see Refs. [26, 152] for details). The corresponding results are shown in Fig. 9.22 together with the experiment. The peak energies of experiment and theory conform perfectly.

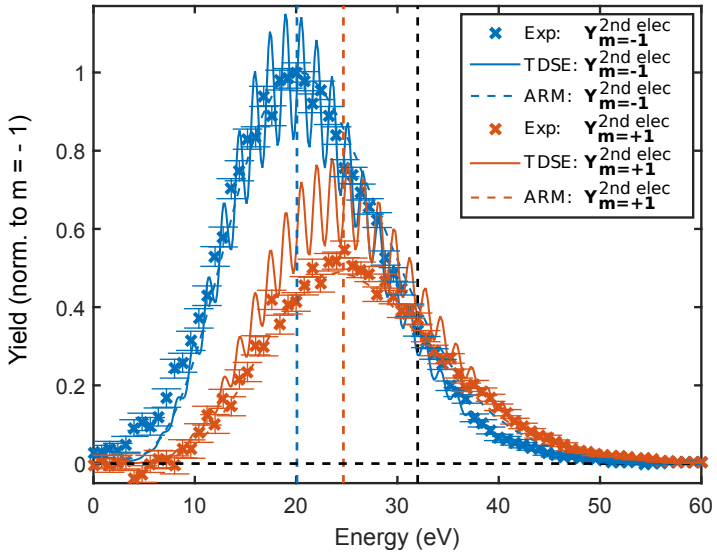


Figure 9.22: The experimentally obtained energy-dependent yields $Y^{\text{2nd elec}}_{\text{m=-1}}$ and $Y^{\text{2nd elec}}_{\text{m=+1}}$ are shown (squares) together with the results results from ARM theory (dashed lines) and numerical solutions of the time-dependent Schrödinger equation (solid lines). The error bars show the standard deviation of the statistical errors. The maxima of the experimental data are indicated by the vertical coloured lines. (The content is the same as in Eckart et al. [26]. The figure is part of the final resubmitted manuscript. The content of the caption is similar to the content of the corresponding caption in Ref. [26].)

From Fig. 9.10(b) and 9.10(e) it is known that the difference of the offsets of the initial momentum distributions using ARM is only $\Delta p_f = 0.12$ a.u. This means that the complex dynamics in the classical forbidden region are responsible for the fact that the difference of the offsets of the initial momentum distributions is not $\Delta p_f = 0.25$ a.u. (classical expectation) but only about $\Delta p_f = 0.12$ a.u.

Eventually, these findings can be evaluated using the concepts introduced in chapter 8. Starting with an angular momentum of $L_x = -1$ for the electron with $m = -1$ in its initial state and having an initial offset momentum of 0 a.u. at the exit of the tunnel, the missing angular momentum must have been absorbed from the driving laser field. Here, the driving laser field is not circularly but elliptically polarized. Nevertheless, this proves that at least one photon has been absorbed in the classical forbidden region for the electron with $m = -1$. Surprisingly, for the electron with $m = +1$ the angular momentum of the initial state and at the tunnel exit is very similar. Hence, for $m = +1$ no minimal number of photons that are absorbed under the tunnel barrier can be estimated.

9.11. Temporal Evolution of the Electron-Hole

Another aspect that should be considered is if the magnetic quantum number of the created electron hole in singly charged argon is a conserved quantity.

In fact, the magnetic quantum number m is not conserved and only the total angular momentum J is conserved. Upon the creation of a spin-up electron hole with $m = +1$ the total angular momentum can only be $J = \frac{3}{2}$. In contrast, a spin-down electron hole with $m = +1$ has to be described as a superposition of two states having different angular momenta ($J = \frac{3}{2}$ and $J = \frac{1}{2}$). In other words, the electron hole is described as a superposition of the originally created spin-down electron hole with $m = +1$ and a spin-up electron hole with $m = 0$. The energy difference $\Delta E_{\mathrm{SO}} = 177\,\mathrm{meV}$ of these two states is given by spin-orbit splitting and leads to an oscillation of the electron hole between $m = +1$ and $m = 0$ giving rise to electron hole dynamics[138] in the singly charged ion [153, 154]. The oscillatory period is $T = \frac{\Delta E_{\mathrm{SO}}}{\hbar} = 23.3\,\mathrm{fs}$. The analogue arguments hold for the creation of an $m = -1$ electron hole.

At first this appears to render the tree diagram presented in Fig. 9.15 useless and since the entire data analysis is based on this diagram this would be very disquieting. However, there are two reasons why the data analysis is correct as it is. First, the laser pulses used in the experiment are at least 40 fs long. Hence, the temporal oscillations average out. What remains is a partially refilled electron hole. This is schematically shown in Fig. 9.23.

[138] Ref. [153] contains a link to a film that illustrates the electron hole dynamics.

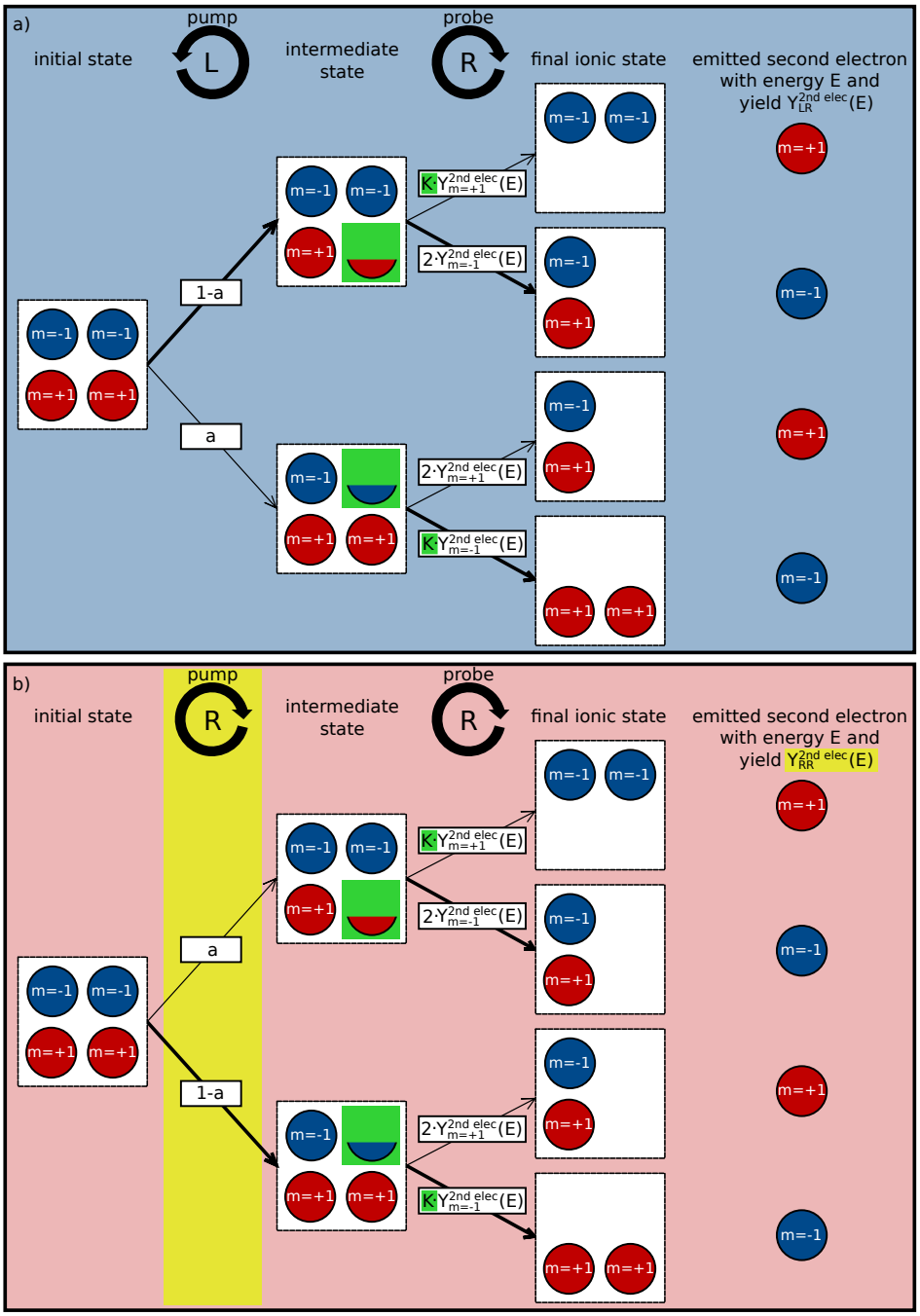


Figure 9.23: Shows an overview of all relevant pathways including "refilling of the electron hole". The differences with respect to Fig. 9.15 are highlighted in blue. The prefactor $K = Q \cdot C$ combines the prefactor for correlation effects C (see chapter 9.10) and the prefactor for "refilling of the electron hole" Q.

In Fig. 9.23 it can be seen that "refilling of the electron hole" simply increases the probability of removing two electrons with the same magnetic quantum number. The prefactor Q is used to model this amplification. In chapter 9.10 the prefactor C has been introduced to account for correlation effects that reduce the probability of removing two electrons with the same magnetic quantum number. Fig. 9.23 illustrates that the prefactors Q and C can be combined

to a single prefactor $K = Q \cdot C$.

During the analysis no assumptions about C were made. Replacing C with K in Eq. 47 and Eq. 48 is enough to prove that none of the experimental findings regarding $Y^{\text{2nd elec}}_{\text{m=-1}}$ and $Y^{\text{2nd elec}}_{\text{m=+1}}$ are affected.

Furthermore, it can be shown that the value of the prefactor for the quantitative description of the "refilling of the electron hole" is $Q = 1 + \frac{2}{9}$ (see Eckart et al. [26]). And although this does not change the experimental results for $Y^{\text{2nd elec}}_{\text{m=-1}}$ and $Y^{\text{2nd elec}}_{\text{m=+1}}$, it allows one to determine the value for C combing the experimentally obtained value $R_{\text{high}} = 0.6$ (see chapter discussion of Fig. 9.17) and the value of a. a models the m-selectivity of the pump-step and is known from the solutions of the TDSE to be $a_{\text{th}} = 0.12$ (see Eckart et al. [26]). Using Eq. 40 and replacing C with $K = Q \cdot C$ and a with $a_{\text{th}} = 0.12$ yields:

$$K = \frac{2 \cdot a_{\text{th}} - 2 \cdot (1 - a_{\text{th}}) \cdot R_{\text{highE}}}{(1 + R_{\text{highE}}) \cdot a_{\text{th}} - 1} = 1.01 \pm 0.17 \tag{50}$$

As a consequence, the value for the correlation effects can be determined to be $C = 0.83 \pm 0.14$. This is an interesting physical insight because correlation effects are generally difficult to quantify in theory which is because solving the TDSE for more than one active electron is numerically expensive.

It can be concluded that although the magnetic quantum number m is not conserved, this does not alter any conclusion drawn so far. In future experiments the temporal evolution of the electron hole on a fs-timescale could be further investigated[139].

[139] See Refs. [155, 156] for two related publications using a pump-probe scheme with pulse durations below 10 fs in their experiments.

9.12. m-Dependent Electron Momentum Distributions

So far only the electron energy distributions $Y^{\text{2nd elec}}_{\text{m=-1}}$ and $Y^{\text{2nd elec}}_{\text{m=+1}}$ have been discussed. The same procedure can be carried out for the full electron momentum distributions. These are defined as $P^{\text{2nd elec}}_{\text{m=-1}}$ and $P^{\text{2nd elec}}_{\text{m=+1}}$ and can be obtained in complete analogy and are also experimental results that are independent of theoretical calculations.

Fig. 9.24 shows $P^{\text{2nd elec}}_{\text{m=-1}}$ and $P^{\text{2nd elec}}_{\text{m=+1}}$ together with the negative vector potential of the probe-pulse. The radial differences are very prominent. A closer inspection shows that there are also small angular differences.

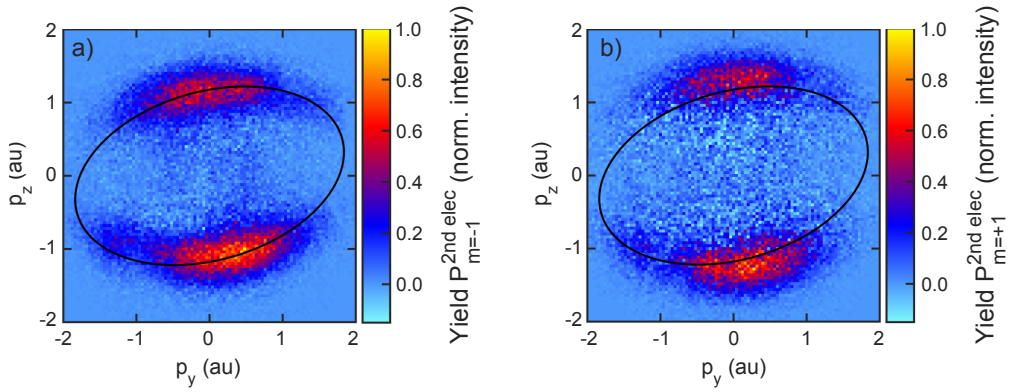


Figure 9.24: The experimentally obtained electron momentum distributions for the ionization of an electron with $m = -1$ [$m = +1$] from a singly charged argon ion is shown in (a) [(b)]. The results are based on the data shown in Fig. 9.10. The black solid line shows the negative vector potential of the probe-pulse.

To make those angular differences visible the difference of Fig. 9.24(a) and Fig. 9.24(b) is investigated. Eq. 34 proves that the difference $Y^{\text{2nd elec}}_{\text{m=-1}} - Y^{\text{2nd elec}}_{\text{m=+1}}$ is proportional to the difference $Y^{\text{2nd elec}}_{\text{LR}} - Y^{\text{2nd elec}}_{\text{RR}}$. Because the normalization of $Y^{\text{2nd elec}}_{\text{m=-1}}$ and $Y^{\text{2nd elec}}_{\text{m=+1}}$ depends on the prefactor C, in Fig. 9.25 the difference $Y^{\text{2nd elec}}_{\text{LR}} - Y^{\text{2nd elec}}_{\text{RR}}$ is depicted together with the negative vector potential of the probe-pulse and straight black lines to guide the eye. In order to draw the contour lines the data shown has been convoluted with a two-dimensional Gaussian distribution with a standard deviation of 0.01 a.u.

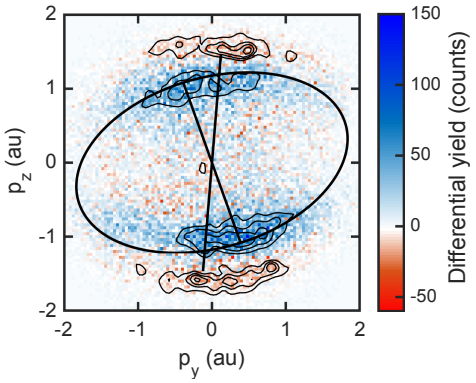


Figure 9.25: The electron momentum distribution shown is proportional to $Y^{\text{2nd elec}}_{\text{m}=-1}$ and $Y^{\text{2nd elec}}_{\text{m}=+1}$. The negative vector potential and straight black lines are shown to guide the eye. (The figure was part of the initial draft regarding the publication by Eckart et al. [26]. Labels and layout have been adapted.)

What is the origin of the angular differences which can be seen in Fig. 9.25? The answer will be given in chapter 9.12.1.

9.12.1. Comparison with Theory and m-Dependent Release Time of the Electron

In a first attempt, the angular differences that are visible in Fig. 9.25 are compared to the data from the SCTS calculation[140] which incorporates Coulomb interaction after tunneling. Fig. 9.26 is based on the same calculation as Fig. 9.20. Also here, the radial differences are visible as expected. The overall rotation of the electron momentum distribution in the plane of polarization is different from the overall rotation found in the experiment. This could be due to an inaccurate determination of the tilt of the polarization ellipse in the experiment. Moreover, the interplay of Coulomb interaction after tunneling and the non-adiabatic offsets of the initial momentum distribution at the tunnel exit might affect the overall rotation of the electron momentum distribution in the plane of polarization.

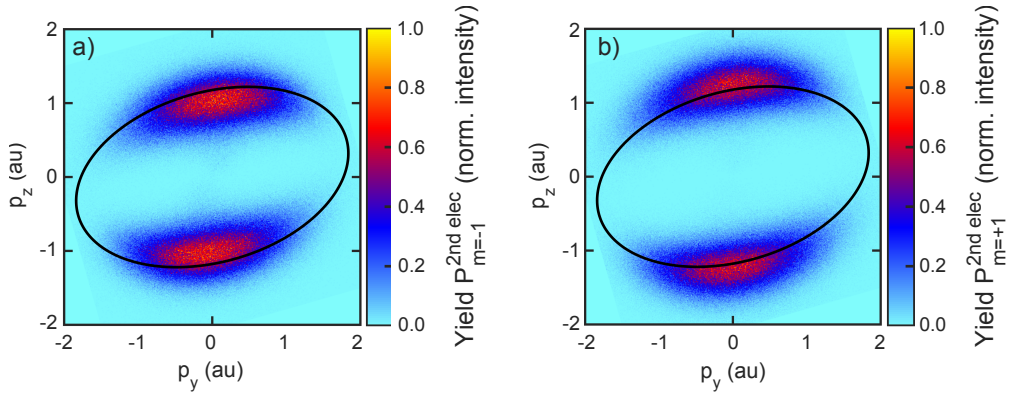


Figure 9.26: The data from the SCTS calculation for the ionization of an electron with $m = -1$ [$m = +1$] from a singly charged argon ion is shown in (a) [(b)]. The black solid line depicts the negative vector potential of the probe-pulse.

In analogy to Fig. 9.25 the difference of Fig. 9.26(a) and Fig. 9.26(b) is depicted[141] in Fig. 9.27. The angular differences are very prominent compared to the experiment. The result from the SCTS calculation shows that $Y^{\text{2nd elec}}_{\text{m=-1}}$ is rotated clockwise with respect to $Y^{\text{2nd elec}}_{\text{m=+1}}$ and the experiment shows the opposite.

[140] This SCTS calculation was carried out by Maksim Kunitski and further details are described in see Ref. [26].

[141] The distribution shown in Fig. 9.26(a) is normalized to the sum of 1.8 and the distribution from Fig. 9.26(b) is normalized to the sum of one and subtracted. The normalization accounts for the different ionization probabilities for $m = -1$ and $m = +1$ which is known from the experiment (see Eq. 49).

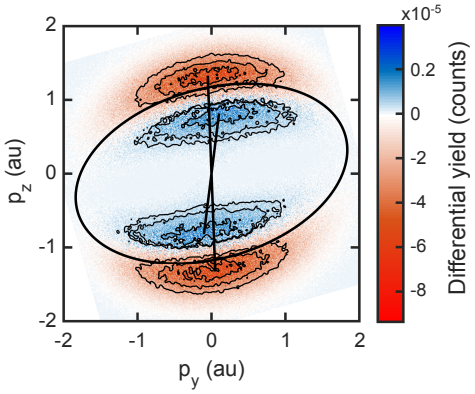


Figure 9.27: In analogy to Fig. 9.25 the corresponding differential electron momentum distribution is shown which is based on the SCTS calculation. The negative vector potential, the straight black lines and the contours are shown to guide the eye.

This is a surprising result. Interestingly, the more sophisticated theoretical approach show good agreement with the experimental results. The results from the TDSE and ARM are shown in Fig. 9.28 together with the experiment.

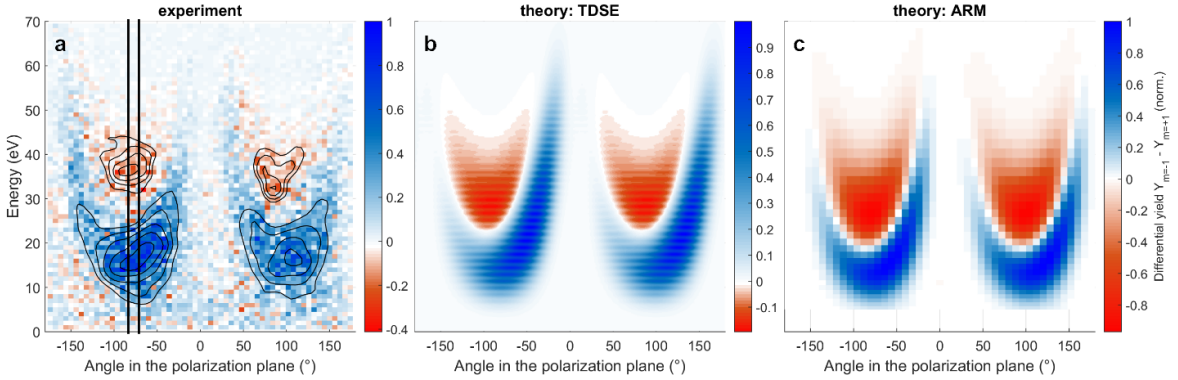


Figure 9.28: "Differences of the m-prepared state's electron momentum distributions. Differential electron momentum distributions $P^{\text{2nd elec}}_{m=-1} - P^{\text{2nd elec}}_{m=+1}$ for experiment in a, numerical simulation of the time-dependent Schrödinger equation in b and analytical R-matrix theory (ARM) in c. The differences in the second electron's momenta (created by the probe-pulse which is identical in all cases) are caused by the helicity of the pump-pulse (which has created the ring current with defined sign in the singly charged ion). The radial differences divide the momentum distribution into a negative region and a positive region. The angular differences (marked with black vertical lines in a) are due to different 'initial' momentum distributions of the electrons tunneling from states $m = -1$ (blue area) and $m = +1$ (red area). Black lines in a show contours to guide the eye." (Figure is part of the final resubmitted manuscript. The figure and its caption are taken from the supplementary information of Eckart et al. [26].)

Recently, Kunlong et al. [13] have theoretically shown that the observed angular differences are due to the differences in the polarization of the initial states with $m = -1$ and $m = +1$. The different alignment of the polarized orbitals, with respect to the long axis of the polarization ellipse of the driving laser field, leads to different "most probable release times" for electrons with $m = -1$ and $m = +1$. For similar laser parameters as in the current experiment, Kunlong et al. [13] conclude that electrons with $m = -1$ are "born" several tens of

attoseconds earlier than electrons with $m = +1$.

In conclusion, the angular differences shown in Fig. 9.25, which were obtained from experimental data, show a fingerprint of the different release times of electrons with $m = -1$ and $m = +1$.

9.13. Conclusion: The Magnetic Quantum Number

The transport of angular momentum from the initial state to the tunnel exit through the classical forbidden region was investigated experimentally for the first time.The experiment presented here provides the first experimentally obtained electron momentum distributions and electron energy spectra that are resolved on the magnetic quantum number of the bound electronic state. It is found that the most probable energy is higher for the ionization of electrons with $m = +1$ than is the case for electrons with $m = -1$ (confirming theoretic predictions [69, 129, 135, 144–146]). This insight allows for the first experimental confirmation that the ionization of electrons that are counter-rotating ($m = -1$) with respect to the driving electric field are preferred for non-adiabatic tunnel-ionization.

The lower ionization rate of electrons with $m = +1$ can be qualitatively explained describing non-adiabatic tunneling as a two-step process (see chapter 8). The first step is a multi-photon absorption to a virtual intermediate state. In the second step adiabatic tunneling occurs from that intermediate state. Assuming that about one photon is absorbed under the barrier (see Fig. 4 of Ref. [48]); this leads to zero offset momentum for the initial state with $m = -1$ and non-zero offset momentum for the initial state with $m = +1$. Since adiabatic tunneling is less probable for high initial momentum components perpendicular to the tunnel exit (see Eq. 5), it can be qualitatively understood why counter-rotating electrons ($m = -1$) are preferred for non-adiabatic tunneling.

The angular difference in the differential electron momentum distribution, comparing electrons from $m = -1$ and $m = +1$, is a feature that cannot be explained using the SCTS model. Thus, the angular difference is a fingerprint of different release times for electrons from $m = -1$ and $m = +1$. This experimental observation is in accordance with recent theoretic results [13].

In the future, a similar experiment could be carried out using circularly polarized driving fields and a mixed gas target of argon and helium[142]. This way the number of photons that are absorbed in the classical forbidden region could be experimentally retrieved because for circularly polarized light the angular momentum at the exit of the tunnel and the electron energy are linked unambiguously. Since the electrons in helium have magnetic quantum numbers of zero, the corresponding electron momentum distribution for the single ionization of helium could be used as a reference.

Moreover, the intensity dependence of m-selective ionization could be further investigated.

[142]The ionization potential of helium is similar to the ionization potential of singly charged argon.

Illchen et al. [157] concluded that for low light intensities ($10^{12}\,\mathrm{W/cm^2}$) co-rotating electrons can be preferred for ionization. They have investigated four-photon ionization by a near-infrared pulse from an excited $He^+(3p)$ state. The near-infrared pulse temporally overlapped with an extreme-ultraviolet pulse that created the excited $He^+(3p)$. This implies that there could be at least one crossover[143] from the preference of co- to counter-rotating electrons as a function of the laser intensity in strong field ionization[144].

[143] Also see the theoretical work by Bauer et al. Ref. [142]: They have investigated the ionization probability of excited hydrogen as a function of the light intensity at a central wavelength of 800 nm. They found that co-rotating (counter-rotating) electrons are preferred for ionization for peak intensities below (above) $10^{13}\,\mathrm{W/cm^2}$.

[144] Also see the discussion about the generation of spin-polarized electrons in the regime of weak electric fields and the regime of single-photon ionization in the introduction of the theoretical work by Ayuso et al. [158]. The spin of the electron is linked to the magnetic quantum number of the electron in the case of non-vanishing spin-orbit splitting (see chapter 9.11 or e.g. Ref. [149]).

10. Evidence for Non-Adiabatic Over-The-Barrier Ionization

This chapter builds on the findings of chapter 8 and chapter 9. The data that is analyzed in this chapter is based on the same measurement that led to the peer-reviewed publication by Eckart et al. [25]. However, the conclusions that are presented in this chapter are new and are only possible because the data has been analyzed from a new perspective. In chapter 8 and chapter 9 the angular movement of the tunnel exit position was considered. Is there also a fingerprint in the electron momentum distribution that is due to the radial movement of the tunnel exit position?

Basic idea: Besides the momentum offset perpendicular to the tunneling direction, there could be a momentum offset along the tunneling direction. Is it possible to also access this momentum offset experimentally?
Basic experimental method: Using the data from chapter 8 and analyzing the data in the direction that is orthogonal to the direction that has already been analyzed. Fig. 10.1 illustrates that an initial momentum offset perpendicular to the tunneling direction leads to a rotation of the final momentum vector[145] in the plane of polarization.

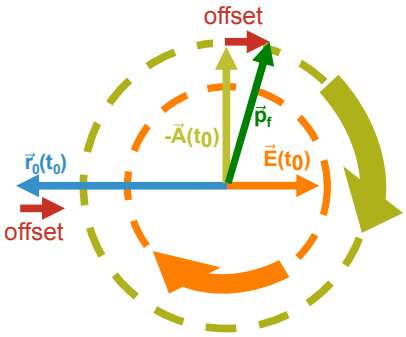


Figure 10.1: In analogy to Fig. 8.2 the geometry at the instance of tunneling t_0 is illustrated for an initial momentum offset that points antiparallel to the tunneling direction: the vector of the laser electric field $\vec{E}(t_0)$, the vector of the tunnel exit $\vec{r}_0(t_0)$, a non-adiabatic momentum offset (red arrow), the negative vector potential $-\vec{A}(t_0)$, a non-zero value for the initial momentum ($\vec{p}_i$) at the tunnel exit and the final momentum neglecting Coulomb interaction after tunneling $\vec{p}_f$ are shown. The figure and its caption are based on Fig. 4(c) from Eckart et al. [25].

Conceptual challenge: Tunneling and a non-zero initial momentum distribution appear to be contradictive to each other (see chapter 8.1).

[145] Neglecting Coulomb interaction, a small offset of the initial momentum antiparallel to the tunneling direction cannot be distinguished from a positive tunneling delay.

10.1. Non-Zero Initial Momentum in the Tunneling Direction

For convenience, the three-dimensional data, that has already been presented in Fig. 8.3, is shown again in Fig. 10.2. The field parameters are found in the caption of Fig. 10.2 and the details about the experiment that was carried out to obtain the shown data are found in chapter 8.

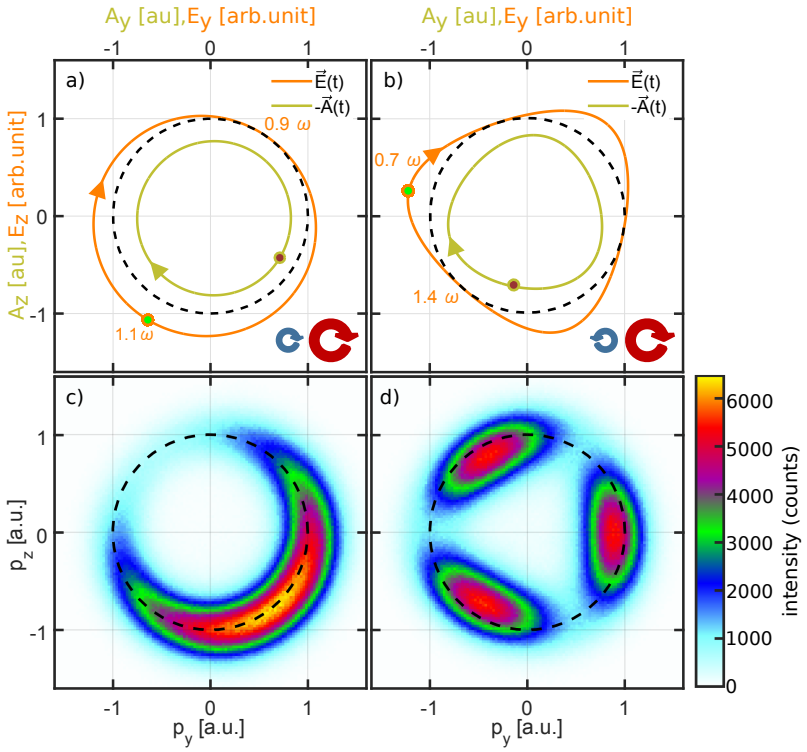


Figure 10.2: "Two-color field composed of a strong fundamental ($E_{780} = 0.046$ a.u.) and a weaker second harmonic ($E_{390} = 0.005$ a.u.) field. Both wavelengths are circularly polarized and co-rotating (a) and (c) or counter-rotating (b) and (d). Depending on the helicity of the second harmonic the derivative of the electric field can be modified (phase of highest field is shown as a dot). The angular velocity of the laser electric field for the co-rotating case is $\omega_{\text{eff}} = 1.1\,\omega$ ($\omega_{\text{eff}} = 0.9\,\omega$) and $\omega_{\text{eff}} = 0.7\,\omega$ ($\omega_{\text{eff}} = 1.4\,\omega$) for the counter-rotating case at the maximal (minimal) electric field. (c) and (d) show the corresponding experimental electron momentum distributions for single ionization of Ar. The black dashed circle guides the eye and has the same radius in all panels. The arrows indicate the temporal evolution of the laser electric field $\vec{E}(t)$ and the negative vector potential $-\vec{A}(t)$." (Figure and caption are taken from Eckart et al. [25]. The figure is the same as Fig. 8.3 and further details about the experiment are found in chapter 8.)

A subset of the experimental data from Fig. 10.2(c) and 10.2(d) is shown in Fig. 10.3(a) and 10.3(b) in cylindrical coordinates[146]. For large values of p_r the angle[147] changes with p_r for the CRTC field (Fig. 10.3(b)).

[146] The same procedure as for Fig. 8.5(c) and 8.5(d) is used but every row is normalized individually instead of every column.

[147] The angle is defined such that an increase of the value for the angle corresponds to an anti-clockwise rotation in Fig. 10.1 and Fig. 10.2.

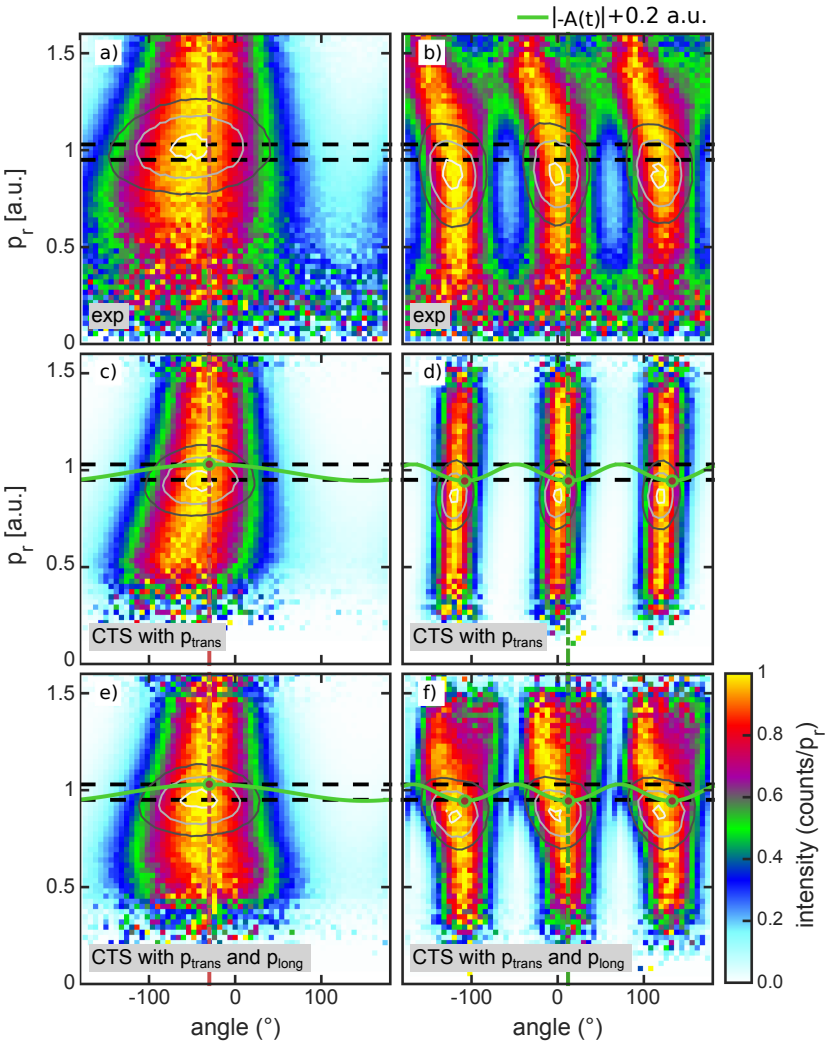


Figure 10.3: (a) and (b) show the same experimental data as Fig. 8.5(c) and 8.5(d) but here every row is normalized independently. It is seen in (b) that for high values of p_r the most probable angle decreases with increasing p_r. The simulation results using the CTS model and an additional momentum offset perpendicular to the tunnel exit of 0.2 a.u. produce the results shown in (c) and (d). The green line indicates the absolute value of the negative vector potential plus the additional momentum offset perpendicular to the tunnel exit of 0.2 a.u. (e) and (f) show the results of a CTS simulation in which an additional momentum offset in the direction of the tunnel exit is included that depends on the temporal derivative of the amplitude of the laser electric field (see Eq. 51 and text). All data shown is restricted to $|p_x| = 0.15 \pm 0.05$ a.u.

Applying the same procedure to the data from the CTS model (as for Fig. 8.6(c) and 8.6(d), but including a constant offset of the initial momentum perpendicular to the tunnel exit of 0.2 a.u.) results in Fig. 10.3(c) and 10.3(d). It is evident that the data from the CTS model shown in Fig. 10.3(c) and 10.3(d) does not agree with the experimental observations. Can this dependence be explained by an initial momentum offset along the tunneling direction? To this end the CTS model is extended and an initial momentum offset along the tunneling direction $\vec{p}_{\text{long}}$ at the exit of the tunnel is included which is proportional to the temporal

derivative of the amplitude of the laser electric field. $\vec{p}_{\text{long}}$ is chosen to be

$$\vec{p}_{\text{long}} = 130 \cdot \frac{\vec{r}_0(t)}{|\vec{r}_0(t)|} \cdot \frac{\mathrm{d}|\vec{E}(t)|}{\mathrm{d}t} \tag{51}$$

where $\vec{E}(t)$ is the instantaneous electric field at time t.

The results of the simulation using this extended model are shown in Fig. 10.3(e) and 10.3(f) reach much better agreement with the experimental results. It is evident from Eq. 51 that the sign of $\vec{p}_{\text{long}}$ is negative (positive) if the amplitude of the electric field decreases (increases) with time. Further, Fig. 10.1 illustrates that the final angle in the plane of polarization rotates clockwise (anti-clockwise) if $\vec{p}_{\text{long}}$ is negative (positive). Finally, a clockwise (anti-clockwise) rotation of the final angle in the plane of polarization decreases (increases) the value for the angle in the plane of polarization.

In conclusion, the decreased value for the angle in Fig. 10.3(b) is equivalent to negative values of $\vec{p}_{\text{long}}$ and the corresponding electron wave packets are expected to be released while the amplitude of the electric fields decreases (falling edge of the time-dependent electric field).

The CTS simulation can be used to test this conclusion for consistency. Fig. 10.4(a) shows the same as Fig. 10.3(d). Fig. 10.4(b) and 10.4(c) show subsets of 10.4(a) restricting the "birth-times" of the electrons to one rising and one falling edge of the combined electric field, respectively.

Fig. 10.4(d)-(f) show the same as Fig. 10.4(a)-(c) but adding $\vec{p}_{\text{long}}$ at the exit of the tunnel. The angle dependent feature in Fig. 10.4(d) at high values of p_r is due to electron wave packets that are released on the falling edge of the combined laser electric field. A similar feature exists for the rising edge which is bent to the opposite direction (see Fig. 10.4(e)). The reason why the wave packets emitted at the rising edge cannot be seen for high values of p_r is the interplay of Coulomb interaction and normalization. As discussed in chapter 8.2.2 the Coulomb effects for electrons that are born on the falling edge of the combined electric field lead to higher radial momenta p_r compared with the electrons that are released on the falling edge of the combined electric field (see Fig. 8.7). For the sake of the argument, at two different instances in time (t_1 on the rising and t_2 on the falling edge of $|E(t)|$) two wave electrons with zero initial momentum are released with the same absolute value of the negative vector potential $|-\vec{A}(t_1)| = |-\vec{A}(t_2)|$ and identical ionization rates. Due to Coulomb interaction after tunneling, the two final momenta are different $p_r(t_1) < p_r(t_2)$. In order to reach $p_r(t_1) = p_r(t_2)$, electrons emitted at t_1 would have to start with initial

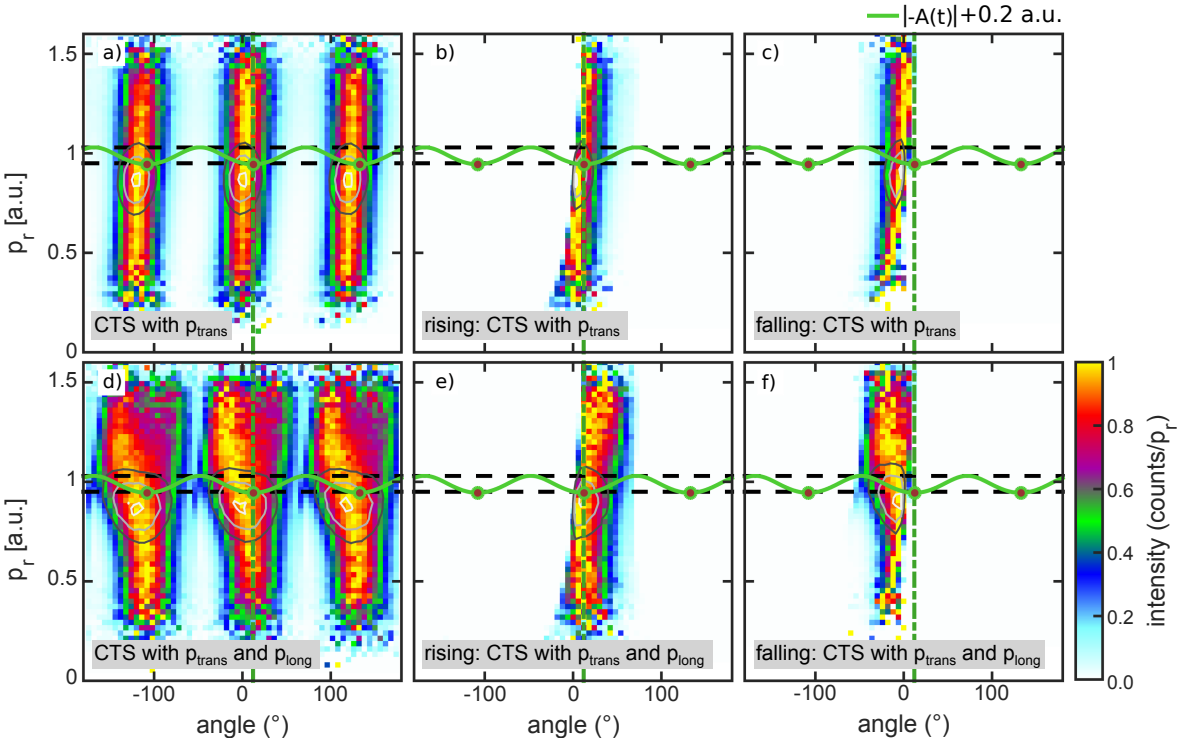


Figure 10.4: (a) shows the same as Fig. 10.3(d). (b) [(c)] shows subsets of (a) restricting the time of ionization to the rising [falling] edge of a single lobe of the two-color field. (d) shows the same as Fig. 10.3(f) and (e) and (f) show again subsets of (d) in analogy to (a)-(c). The additional momentum offset along the tunneling direction which is present for (d)-(f) leads to a significant change of the angle for high values of p_r. The signal at high values of p_r in (a) which is shifted towards lower angles is due to electrons that are liberated on the falling edge of $|\vec{E}(t)|$. All data shown is restricted to $|p_x| = 0.15 \pm 0.05$ a.u.

momentum perpendicular to the tunneling direction which reduces the tunneling rate (see chapter 3). Normalizing the intensity for every p_r individually as for Fig. 10.4(d) then leads to a situation in which at high values of p_r the visible distribution is dominated by electrons that are "born" on the falling edge of $|E(t)|$.

Fig. 10.5 shows the same as Fig. 10.4 but for the CoRTC field. It is evident that for the CoRTC field the changes due to $\vec{p}_{\text{long}}$ are seen at low values of p_r and are generally less pronounced. It is expected that the influence of $\vec{p}_{\text{long}}$ is weaker for the CoRTC field because the shape of the CoRTC field (see Fig. 8.3(a)) is very similar to circularly polarized light. Comparison of Fig. 10.5(c) and 10.5(f) shows almost no difference while comparison of Fig. 10.5(b) and 10.5(e) shows a small difference for low values of p_r.

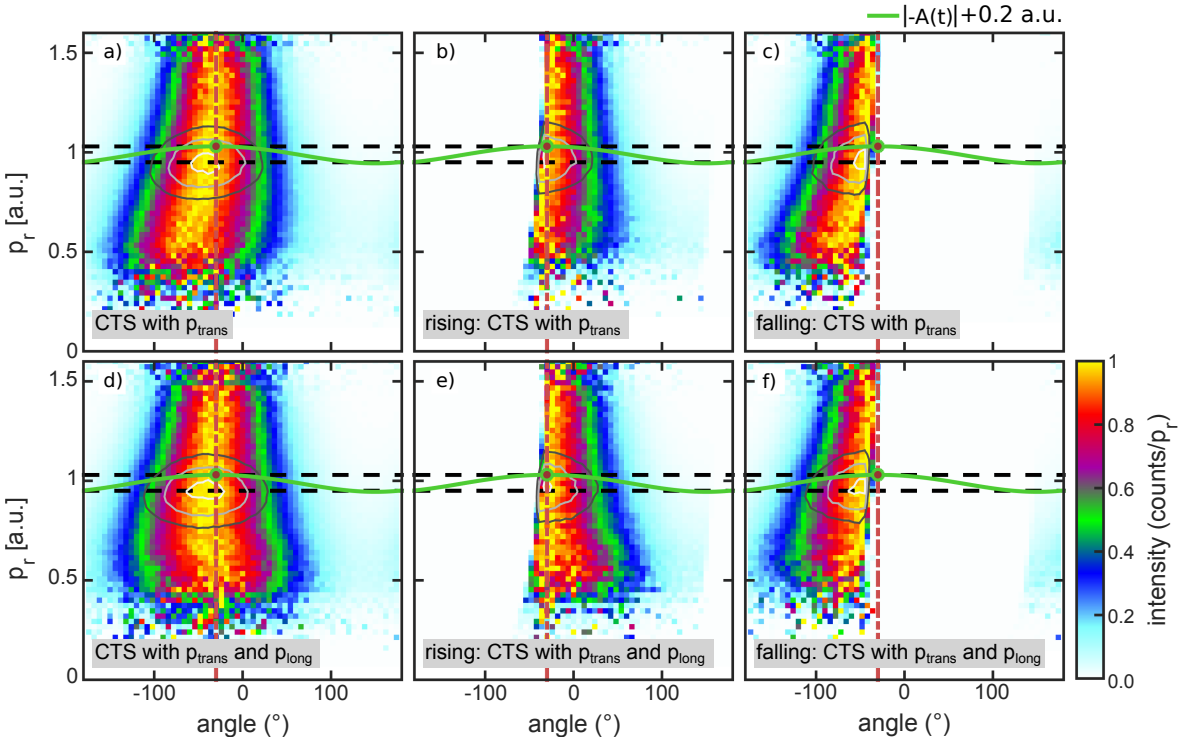


Figure 10.5: (a) shows the same as Fig. 10.3(c). (b) [(c)] shows subsets of (a) restricting the time of ionization to the rising [falling] edge of the two-color field. (d) shows the same as Fig. 10.3(e) and (e) and (f) show again subsets of (d) in analogy to (a)-(c). It is evident that the additional momentum offset along the tunneling direction which is present for (d)-(f) only leads to minute differences for small values of p_r. All data shown is restricted to $|p_x| = 0.15 \pm 0.05$ a.u.

Finally, Eq. 51 appears to be contradictive to the concept of tunneling. Usually, one would expect that the initial momentum along the tunneling direction at the tunnel exit is zero because otherwise this momentum component would have to be unsteady at the tunnel exit or the electron energy in the tunneling region would be positive. The latter could not be considered as tunneling but would qualify as an over-the-barrier ionization. Chapter 10.2 tries to speculate along this line.

10.2. Non-Adiabatic Over-The-Barrier Ionization

This sub-chapter is highly speculative and further theoretic modeling is needed to back up the preliminary conclusions that are drawn. As discussed in chapter 8.1 an initial momentum along the tunneling direction can be viewed to be contradictive to tunneling. A possible solution for the paradox observations presented in chapter 10.1 is that for high final radial momenta tunneling is not the most important ionization mechanism. Instead, a new ionization channel might be relevant which is called "non-adiabatic over-the-barrier ionization" (NAOBI). This chapter discusses experimental evidence for NAOBI. The mechanism discussed is closely related to ideas by Klaiber and Briggs (see Ref. [48]).

NAOBI is the same as non-adiabatic tunnel ionization that is described in the two-step picture by Klaiber et al. (see chapter 8.5) with the difference that the second step is not adiabatic tunneling but over-the-barrier ionization.

The newly introduced mechanistic model for non-adiabatic tunnel ionization (see chapter 8.5) can be used to infer the number of absorbed photons for a radial momentum of $p_r = 1.4\,\text{a.u.}$ The highest yield in Fig. 10.3(b) is found at a radial momentum of about $p_r = 0.9\,\text{a.u.}$ Hence, one can conclude that the momentum offset perpendicular to the tunneling direction[148] at the tunnel exit position is $\Delta p_r = 0.5\,\text{a.u.}$ in this case. Assuming the tunnel exit position to be at $r_0 = 10\,\text{a.u.}$ the magnetic quantum number of the virtually populated intermediate state is (see chapter 8.5):

$$m^{\text{virtual}} = r_0 \cdot \Delta p_r = 5 \tag{52}$$

Knowing that ionization from the initial state with $m^{\text{initial}} = -1$ is preferred for ionization (see chapter 9) and assuming a circularly polarized driving field, this directly provides the approximate number of virtually absorbed photons to be:

$$\Delta n^{\text{virtual}} = m^{\text{virtual}} - m^{\text{initial}} = 6 \tag{53}$$

The absorption of six photons at a wavelength of 780 nm corresponds to an energy of 9.54 eV. Thus, the virtually populated intermediate state has an ionization potential of only:

$$I_p^{\text{virtual}} = I_p - \Delta n^{\text{virtual}} \cdot 1.59\,\text{eV} = 15.76\,\text{eV} - 9.54\,\text{eV} = 6.22\,\text{eV} \tag{54}$$

[148] In subchapter 10.2 "tunneling direction" is used although there is not tunnel for NAOBI. Nonetheless, with "tunneling direction" the direction which is antiparallel to the instantaneous laser electric field will indicated.

The peak electric field is known to be 0.05 a.u. (see Fig. 10.3). Fig. 10.6 shows the atomic potential in the presence of the external electric field including the energy level of the virtual intermediate state at I_p^{virtual}. Obviously, the energy level of the virtual intermediate state,

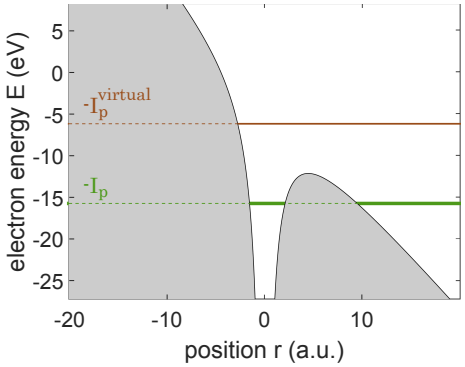


Figure 10.6: The black line shows a distorted Coulomb potential $V(r) = -1/r - F \cdot r$ in the presence of an electric field with $F = 0.05$ a.u. in analogy to Fig. 3.2(b). The classically forbidden region ($E(r) < V(r)$) is shaded in gray. The dashed green line indicates the ionization potential corresponding to the single ionization of argon of $I_p = 15.76\,\text{eV}$. The bold green line indicates the regions that are allowed for an electron with an energy of $E = -I_p$. The reddish brown line shows the same as the green line but for the ionization potential $I_p^{\text{virtual}} = 6.22\,\text{eV}$.

after the absorption of six photons, is high enough to allow the electron to leave the atomic potential by over-the-barrier ionization (OBI, see chapter 3.2). Using the criterion for OBI (Eq. 6) with I_p^{virtual} instead of I_p leads to the criterion:

$$I_p^{\text{virtual}} < \sqrt{4 \cdot E_{\text{OBI}}} \tag{55}$$

If the amplitude of the electric field is set to $E_{\text{OBI}} = 0.05$ a.u., it turns out that an ionization potential of $I_p^{\text{virtual}} < 12.17$ eV already qualifies for OBI. Thus, the absorption of three virtual photons already allows for OBI. Starting with an initial state of $m^{\text{initial}} = -1$ the absorption of three virtual photons leads to a virtual intermediate state with $m^{\text{virtual}} = 2$ and a non-adiabatic offset of the initial momentum distribution of about $\Delta p_r = m^{\text{virtual}}/r_0 \approx 0.2$. This would lead to a final radial momentum of about $p_r = (0.9 + 0.2)$ a.u. $= 1.1$ a.u.. This is in line with the radial momentum at which the bending of the vertical structures in Fig. 10.3(b) sets in.

However, one could argue that the tunnel exit position also depends on the number of absorbed photons and that for the measurement that is discussed a two-color field is used. For $E_{\text{OBI}} = 0.05$ a.u. the maximum of the barrier is found at a distance of $r_0 = \frac{1}{\sqrt{E_{\text{OBI}}}} = 4.5$ a.u. Choosing the tunnel exit to be at this position leads to a virtually populated intermediate state with $m^{\text{virtual}} = r_0 \cdot \Delta p_r = 2.25 \approx 2$ for $\Delta p_r = 0.5$ a.u. This leads to a number of virtually absorbed photons of $\Delta n^{\text{virtual}} = m^{\text{virtual}} - m^{\text{initial}} = 3$. And as described above, even $\Delta n^{\text{virtual}} =$

3 would allow for NAOBI. But this is still a very strong simplification because the kinetic energy $(\Delta p_r)^2/2$ of the electron at the tunnel exit is neglected. For a single-color field and the ionization from an initial state with $m^{\text{initial}} = -1$ the condition for NAOBI could be rewritten as:

$$I_p^{\text{virtual}} + E_{\text{kin}}^{\text{initial}} < \sqrt{4 \cdot E_{\text{OBI}}} \tag{56}$$

Here, the kinetic energy at the tunnel exit is $E_{\text{kin}}^{\text{initial}} = (\Delta p_r)^2/2 + (\Delta p_x)^2/2$ and p_x is the initial momentum in the light propagation direction which is set to zero for simplicity. Using

- $I_p^{\text{virtual}} = I_p - \Delta n^{\text{virtual}} \cdot E_{\text{photon}}$,
- $\Delta p_r = m^{\text{virtual}}/r_0$,
- $I_p = 15.76\,\text{eV}$ and
- $E_{\text{OBI}} = 0.05\,\text{a.u.}$

results in:

$$\Delta n^{\text{virtual}} \cdot E_{\text{photon}} - 0.5 \cdot \left(m^{\text{virtual}}/r_0\right)^2 - 3.59\,\text{eV} > 0 \tag{57}$$

Based on Eq. 57 the combinations allowed of $\Delta n^{\text{virtual}}$ and m^{virtual} are shown in Fig. 10.7 as a green area for $r_0 = 4.5\,\text{a.u.}$ In Fig. 10.7(a) the photon energy is $E_{\text{photon}} = 1.59\,\text{eV}$ (corresponds to a wavelength of 780 nm) and in Fig. 10.7(b) the photon energy is $E_{\text{photon}} = 3.18\,\text{eV}$ (corresponds to a wavelength of 390 nm).

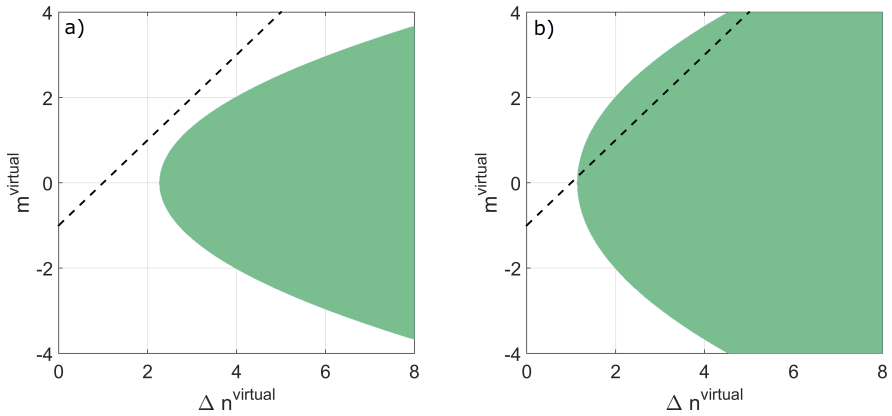


Figure 10.7: The green area shows the allowed combinations of $\Delta n^{\text{virtual}}$ and m^{virtual} for a driving field at 780 nm [390 nm] in (a) [(b)] (using Eq. 57 with $r_0 = 4.5\,\text{a.u.}$). The black dashed line indicates the condition $\Delta n^{\text{virtual}} = m^{\text{virtual}} - m^{\text{initial}} = m^{\text{virtual}} - 1$.

The black dashed line indicates the condition $\Delta n^{\text{virtual}} = m^{\text{virtual}} - m^{\text{initial}} = m^{\text{virtual}} - 1$ which applies to the ionization of an electron with $m^{\text{initial}} = -1$ in its initial state and circularly polarized driving fields. It is evident that for a single-color driving field at 780 nm both

conditions cannot be fulfilled at the same time but that there is an overlap of the two conditions for the driving field at 390 nm. Fig. 10.7 indicates that NAOBI is not possible in a single-color field at 780 nm, but is possible in a single-color field at 390 nm. Why is this the case? Eq. 57 relates the energy of the virtual intermediate state ($\Delta n^{\text{virtual}}$) and the magnetic quantum number of the virtual intermediate state (m^{virtual}). NAOBI is not allowed in a single-color field at 780 nm because the photons at 780 nm do not posses enough energy for a given amount of angular momentum.

The data shown in Fig. 10.3 was taken using a two-color field. Whether or not NAOBI is possible or not for the given field geometry is more difficult to determine. However, there is one important argument that should be considered: in circularly polarized counter-rotating two-color (CRTC) fields the absorption of an additional photon can reduce the value of m^{virtual}. In circularly polarized co-rotating two-color (CoRTC) fields this is not the case. Therefore, NAOBI might be preferred in CRTC fields compared to CoRTC fields or single-color fields.

Assuming that NAOBI is relevant for the experimental data shown in Fig. 10.3(b): can the model of NAOBI qualitatively explain why there is a sign change in Eq. 51 for the rising and the falling edge of the absolute value of the laser electric field? Eq. 51 was found empirically and the conclusion which was found in chapter 10.1 is:

- On the rising edge of the absolute value of the laser electric field, the initial momentum distribution appears to have an offset which is parallel to the tunneling direction.
- On the falling edge of the absolute value of the laser electric field, the initial momentum distribution appears to have an offset which is anti-parallel to the tunneling direction.

The different offsets of the initial momentum along the tunneling direction for the rising and the falling edge of the laser electric field might be understood classically: Fig. 10.8 illustrates the relevant degrees of freedom of a bound electron that escapes the distorted atomic potential from a virtual intermediate state that allows for OBI. Until the electron has reached the maximum of the potential (Fig. 10.8(b)) the electric field is relatively weak (Fig. 10.8(a)). During this time period the electron is accelerated in the direction that is anti-parallel to the tunneling direction. After the electron has passed the maximum of the potential the electric field is relatively strong (Fig. 10.8(c)) and during this time period the electron is accelerated in the tunneling direction. To conclude, one could imagine that the acceleration along the tunneling direction dominates if the absolute value of the laser electric field increases with time as the electron leaves its bound state. This is in line with Eq. 51.

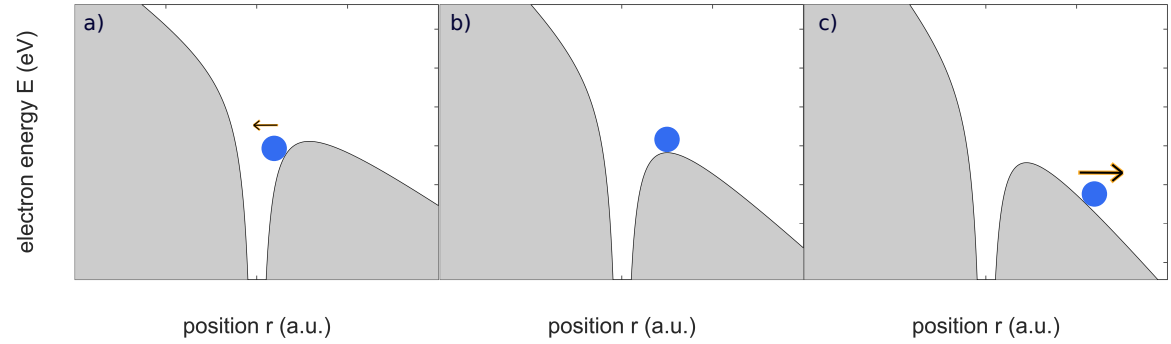


Figure 10.8: Illustrates the relevant degrees of freedom: the potentials shown in (a)-(c) are the sum of the Coulomb potential and the laser potential (see Fig. 10.6). The laser potential is low in (a), has a medium strength in (b) and is strong in (c) to illustrate an electric field that increases its absolute value with time. An electron starting to leave the atom is schematically shown in (a). Until the electron reaches the maximum of the potential in (b), it is accelerated to the left (illustrated by a small arrow). After the electron has passed the maximum of the potential (see (c)) it is strongly accelerated to the right (illustrated by a large arrow). As a result the electron is accelerated more strongly in the direction which is parallel to the direction the tunnel exit would point to for tunneling.

In full analogy to Fig. 10.8 the process of an electron that escapes its atomic potential by NAOBI is illustrated in Fig. 10.9 for the scenario of a laser field that decreases its strength with time.

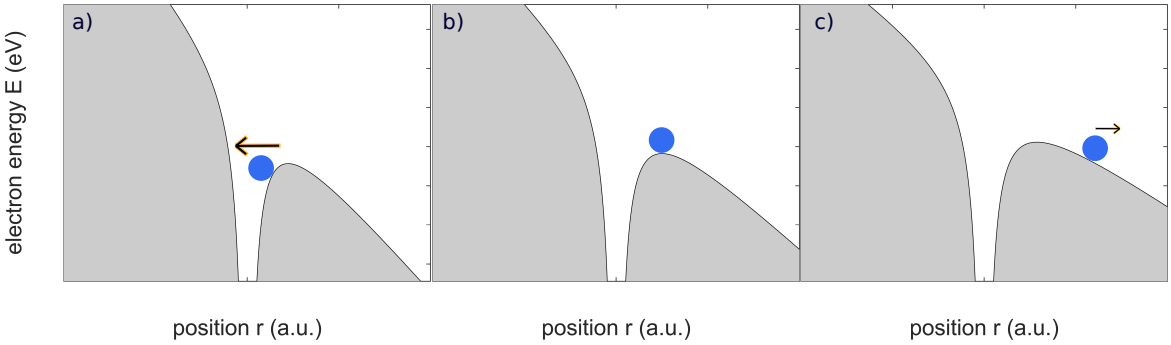


Figure 10.9: The same is shown as in Fig. 10.8 but here the absolute value of the electric field decreases with time. As a result the electron is accelerated more strongly in the direction which is anti-parallel to the direction the tunnel exit would point to for tunneling.

From Fig. 10.9 it appears to be plausible that the acceleration in the direction that is anti-parallel to the tunneling direction dominates. Also, this finding is in line with Eq. 51 which provides further evidence for the existence of the newly described ionization channel of NAOBI.

10.3. Conclusion: Initial Momentum in the Tunneling Direction

In conclusion, experimental evidence for an offset of the initial momentum distribution along the tunneling direction for high radial momenta p_r is presented[149]. Trying to use the two-step picture by Klaiber et al. (see chapter 8.5 and Ref. [48]) it is found that the energy of the virtual intermediate state is high enough for OBI. This gives rise to the development of the concept of NAOBI which succeeds in qualitatively explaining the experimental findings. In analogy to Fig. 3.3 the process of non-adiabatic over-the-barrier ionization can be visualized as shown in Fig. 10.10.

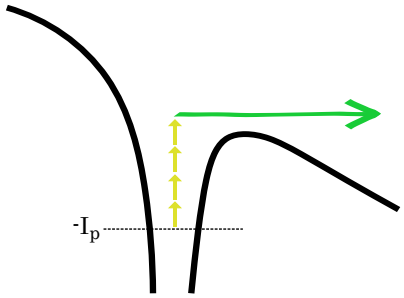


Figure 10.10: Schematic representation of non-adiabatic over-the-barrier ionization (NAOBI) which is shown in analogy to Fig. 3.3. Starting from an initial state that is bound with the ionization potential I_p, multi-photon absorption (yellow vertical arrows) populates a virtual intermediate state. The green horizontal arrow indicate the change of the position coordinate which occurs in the classically allowed region.

Finally, it should be mentioned that there is another chapter in this thesis for which OBI has a certain relevance. Chapter 6 deals with non-sequential double ionization upon recollisional excitation of singly charged argon ions in CRTC fields. In chapter 6 non-adiabatic corrections or (NA)OBI are not considered. However, some of the laser parameters that are listed in Tab. 6.2 are slightly above the threshold for OBI. This could affect the initial momentum distribution at the tunnel exist and the recollision probability. Hence, non-sequential double ionization in two-color fields could be used to quantitatively benchmark theoretic models that include an offset of the initial momentum distribution along the tunneling direction.

[149] The existence of momentum offsets and a non-zero width of the initial momentum distribution along the tunneling direction were already discussed in the literature (see chapter 8.1 and Refs. [11, 47, 124, 126, 130, 131, 134, 159, 160]).

11. Summary, Conclusion and Outlook

This thesis demonstrates that tailored intense two-color fields are a versatile tool in studying non-adiabatic tunneling. Characteristic processes in strong field ionization including recollision dynamics, interferences, non-adiabatic tunneling, and the transport of the electron's initial angular momentum in the classical forbidden region have been analyzed. The four main projects of this thesis have been realized using circularly polarized two-color fields and are illustrated in Fig. 11.1.

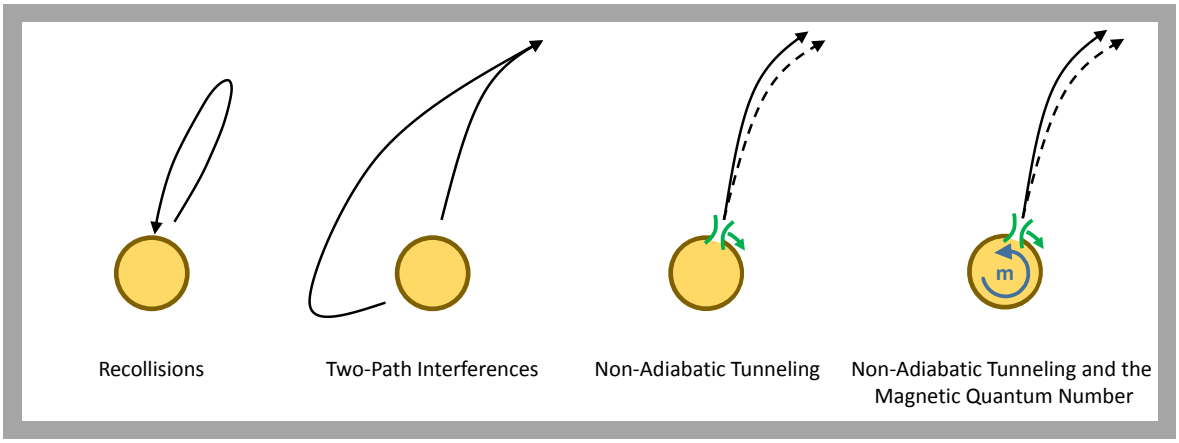


Figure 11.1: Illustration of the four main topics of this thesis.

For each project one control parameter and/or one variable was varied while one or more observables were investigated. In each case, this allowed to explore a certain aspect of strong field ionization. The central control parameters and the most important observables for the individual projects are:

- Recollisions (see chapter 6): the relative field strength of the two single-color laser fields (control parameter) was varied and the ratio of double to single ionization (observable) was measured.
- Two-path interferences (see chapter 7): an unexpected intensity (observable) modulation along the light propagation direction in momentum space (variable) was observed.
- Non-adiabatic tunneling (see chapter 8): depending on the relative helicity (control parameter) of the two laser pulses (with temporal overlap) the radial momentum changes (observable).
- Non-adiabatic tunneling and the magnetic quantum number (see chapter 9): depending on the relative helicity (control parameter) of the two laser pulses (without temporal

overlap) the yield of double ionization and the electron momentum distribution changes (observables).

The results from chapter 6 and 7 show that electron wave packets that are emitted by noble gases through non-adiabatic tunneling can be approximated as classical particles that possess semi-classical phases. It has been demonstrated that the electron possesses particle properties (allowing for recollisions) as well as wave properties (allowing for interference). The results from chapter 8 and chapter 9 illustrate the importance of the conservation of angular momentum including the angular momentum of the bound electron and allow for the introduction of a mechanistic model regarding non-adiabatic tunneling.

The mechanistic model is consistent with saddle point strong field approximation. It correctly predicts that for typical laser parameters and circularly polarized light at 780 nm about 0.2 a.u. of the total radial momentum of 1.0 a.u. are due to non-adiabatic effects. Moreover, the mechanistic model qualitatively explains why electrons with $m = -1$ are preferred for ionization.

The preference of electrons with $m = -1$ has been investigated in detail and they can be used to prepare and detect ring currents on ultrafast timescales. Ring currents in singly charged argon ions were prepared and detected. The sign of the ring current does not change over time due to the conservation of angular momentum. Thus, it has been demonstrated experimentally that it is possible to save and read one bit of information. The variable that stores the information is encoded in the sign of the quantum mechanical phase of an electron in a single atom.

Chapter 10 presents further experimental findings that cannot be easily explained by the mechanistic model of non-adiabatic tunneling. A new ionization channel is proposed which is referred to as non-adiabatic over-the-barrier ionization (NAOBI).

11.1. In Short: Boiling all Observations Down to One Model

All observations[150] made throughout this thesis can be understood using the following model:

- The initial state of the electron possesses a well-defined momentum distribution, a well-defined energy level and a well-defined angular momentum.
- Non-adiabatic tunneling can be viewed as a two-step process. In the first step the momentum distribution of the bound electron does not change but the energy and the

[150] Except for the observations that are discussed in chapter 10, these observations do not contradict the model of non-adiabatic tunneling, but suggest that the adiabatic tunneling step has to be replaced by an over-the-barrier ionization in certain conditions.

angular momentum can be modified by the absorption of photons. The modified initial state can be viewed as a virtual intermediate state. For single-color circularly polarized light the modification in energy divided by the photon energy defines the change of angular momentum.

- The second step of non-adiabatic tunneling is equivalent to adiabatic tunneling from the virtual intermediate state. This results in an offset of the initial momentum distribution due to the conservation of angular momentum during tunneling.
- After the electron wave packet has left the tunnel exit, it can be approximated as a classical particle with a semi-classical phase that moves in a time-dependent potential which is defined by the laser electric field and the Coulomb potential.

11.2. Limitations and Shortcomings

This subchapter deals with the limitations and shortcomings of the results that are presented in this thesis.

A very obvious experimental shortcoming is that the mirror inside the vacuum chamber was vibrating for the project that is presented in chapter 6. This oscillatory motion significantly affects the quality of the tomographically reconstructed undetected electron (see discussion regarding Fig. A.28). Another shortcoming of this project was that the intensities were not identical for all two-color field ratios that were used (see Tab. 6.2). The discussion in chapter 6.4.1 shows that this does not affect any conclusions that are drawn.

The original goal of the project described in chapter 7 and chapter A.6 was the comparison of helium and neon. However, the two data sets showed only small differences. The exact reason for the differences is not fully understood and needs further theoretical modeling. It appears plausible that for helium and neon similar virtual intermediate states are populated.

As described in chapter 9.11 the temporal evolution of the electron hole occurs on a time scale of about 23 fs. The duration of the laser pulses used is longer[151] than 35 fs. Thus, any fingerprints of the temporal evolution of the electron hole average out. The pulse duration could be improved by balancing the optical dispersion in the two arms of the interferometer. However, even pulse durations of about 35 fs would not allow any new conclusions to be drawn. A new class of experiments could be performed if the temporal evolution of the electron hole could be analyzed.

The speculative conclusions that are drawn in chapter 10.2 need further theoretic modeling.

[151] The cross-correlation that is depicted in Fig. 9.7 can be used to estimate the pulse duration.

One should not claim to have observed a new ionization channel, namely “non-adiabatic over-the-barrier ionization”, without theoretic support.

A limitation of the semi-classical two-step (SCTS) model is that the semi-classical phase can only be calculated in a Coulomb potential. This does not allow for the inclusion of real atomic potentials, polarization effects or multi-electron dynamics.

Finally, the mechanistic picture (see chapter 8.5) is only able to link the non-adiabatic offset with the number of absorbed photons for almost circularly polarized and almost single-color fields. This is because for elliptically polarized light the number of virtually absorbed photons cannot be derived from the value of the magnetic quantum number of the virtually populated state.

11.3. Perspective

Besides the physical insights, this thesis describes new techniques that might be useful for future experimental and theoretical works:

- Double ionization: using coincidence detection and a tomographic reconstruction of the second electron allows for the reconstruction of the undetected electron (see chapter 6.5.2).
- Visualization: new methods to visualize three-dimensional data are presented (see chapter 7.7.1).
- Non-adiabatic tunneling: the effective angular frequency can be tuned by changing the relative helicity of the two colors and the two-color field ratio (see chapter A.8).
- Sequential double ionization: using two-color laser pulses with suitable polarization and coincidence detection allows one to distinguish the electrons that are emitted from the pump-pulse and the probe-pulse on fs-timescales (although the time resolution of the electron detector is in the ns-range).
- Active stabilization of the relative phase: a concept for the closed-loop stabilization of the relative phase of the two laser pulses is implemented and tested. It is shown that slow phase drifts can be eliminated (see chapter A.4).
- Simulation: the method of “phase compression” is introduced allowing for the improvement of the convergence of the semi-classical two-step model (see chapter 5.3).

What is missing to understand the physics of strong field ionization even better? Future experiments might build on the physical insights gained on how non-adiabatic tunneling and

the propagation of electron wave packets can be modeled in the strong field regime. The control parameters found that proved to be useful in studying atoms could be applied to molecules.[152]

More complex two-color fields could be realized using other fields than CRTC or CoRTC fields (see e.g. chapter A.3). This class of two-color fields does not allow for an offline compensation of the phase drifts of the two laser pulses (see chapter A.2) and an active stabilization of the relative phase is needed (see e.g. chapter A.4).

Shorter laser pulses might allow one to resolve ultrafast dynamics such as the temporal evolution of the electron hole. A better momentum resolution for the detected ions for (non-) sequential double ionization is promising for the study of the correlation of the two emitted electron wave packets. Finally, outstanding questions such as the momentum-offset along the direction of tunneling that are described in chapter 10.2 should be further investigated.

[152] Some interesting experiments using molcules have alredy been done. Examples are found in Refs. [55, 121, 161–163].

A. Appendix

A.1. The Laser Intensity in the Interaction Region

In this subchapter the expected properties of the two single-color laser pulses in the vicinity of the laser focus are investigated[153]. Fig. A.1 shows the typical beam profiles of the light intensity in position space in front of the vacuum chamber.

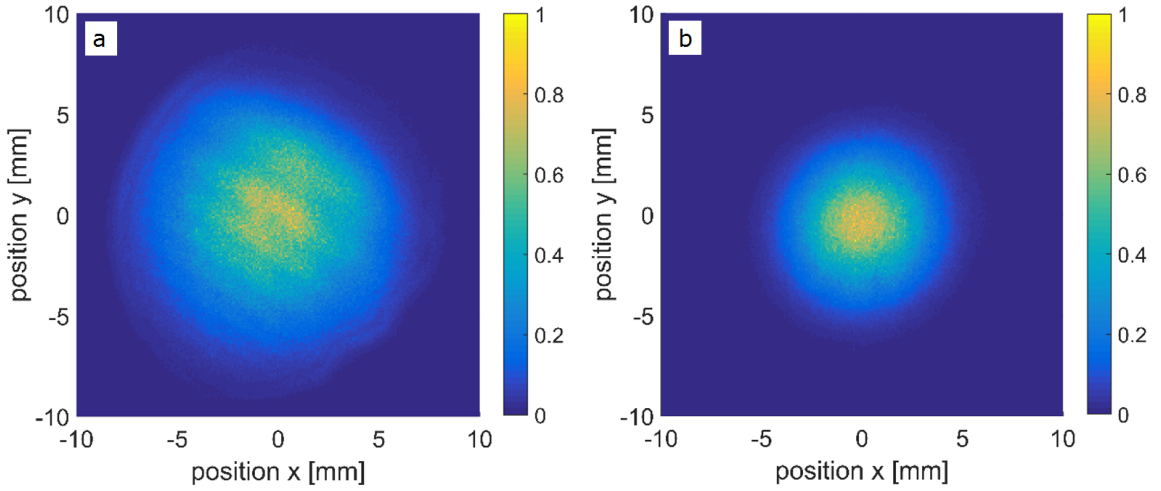


Figure A.1: The beam profiles in front of the vacuum chamber are depicted for the beam at a wavelength of 780 nm and the beam at a wavelength of 390 nm. The normalized light intensity is color-coded. The figure has been part of the answer to the referees regarding the publication Eckart et al. [24]. The layout and labels have been changed.

The beam diameter (full width at half maximum) of the beam at a wavelength of 780 nm [390 nm] is 8 mm [5 mm]. The reason why the beam at a wavelength of 780 nm has a larger beam diameter is because the generation of the second harmonic is proportional to the square of the intensity. This results in an expected beam diameter for the beam at a wavelength of 390 nm which is smaller by a factor of $\sqrt{2}$ compared to the beam at a wavelength of 780 nm. This is consistent with the measured beam profiles.

In a next step an assumption about the beam quality factor M^2 has to be made[154]. Assuming a perfect beam quality ($M^2 = 1$) results in beam waists of 5.9 µm [4.7 µm] for the beam at a wavelength of 780 nm [390 nm]. The dependence of the beam radius[155] on the distance to the focus along the light propagation direction is shown in Fig. A.2.

[153] Chapter A.1 is based on the answer to the referees regarding the publication Eckart et al. [24].

[154] For the modeling the Gaussian TEM00 mode is used. The formulas to describe a Gaussian TEM00 mode can be found in most books about optics (see e.g. Ref. [164]).

[155] The beam radius is defined as the distance to the optical axis at which the intensity is $1/e^2$ of the value on the optical axis. The beam waist is the minimal beam radius multiplied with two.

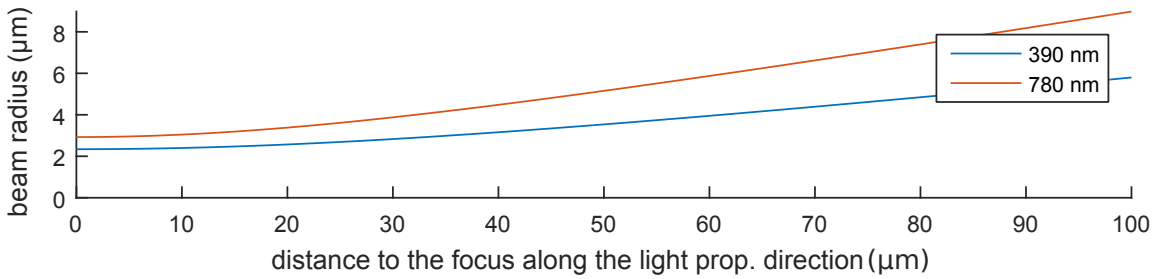


Figure A.2: The beam radius is plotted as a function of the distance to the focus along the light propagation direction for the beam at a wavelength of 780 nm (upper line) and 390 nm (lower line). The panel has been part of a figure which has been part of the answer to the referees regarding the publication Eckart et al. [24] in an almost identical version. The layout and labels have been changed.

Besides the beam radius, the value for the Gouy phase can also be plotted as a function of the distance to the focus along the light propagation direction. The result is shown in Fig. A.3 and it is evident that the Gouy phases of the two beams are almost identical.

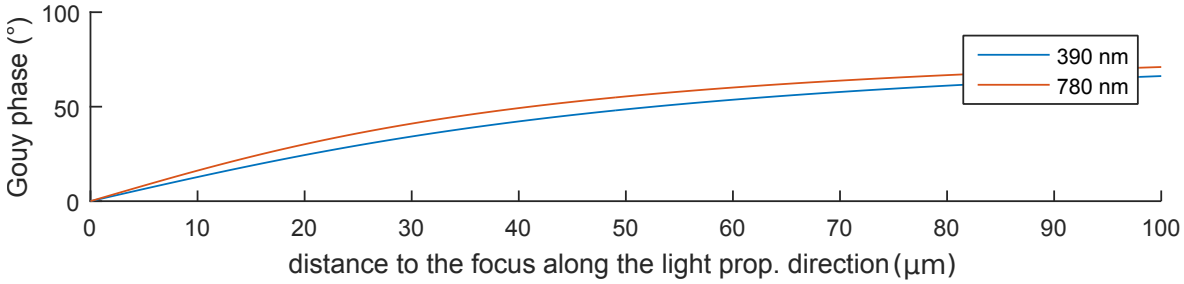


Figure A.3: The gouy phase is plotted as a function of the distance to the focus along the light propagation direction for the beam at a wavelength of 780 nm (upper line) and 390 nm (lower line). The panel has been part of a figure which has been part of the answer to the referees regarding the publication Eckart et al. [24] in an almost identical version. The layout and labels have been changed.

Using the symmetry of the Gaussian TEM00 mode the three-dimensional focal volume can be visualized in two dimensions using cylindrical coordinates. Choosing a peak intensity of $1 \cdot 10^{14}\mathrm{W/cm^2}$ for both single-color pulses in the focus results in the position-dependent intensity distribution that is shown in Fig. A.4.

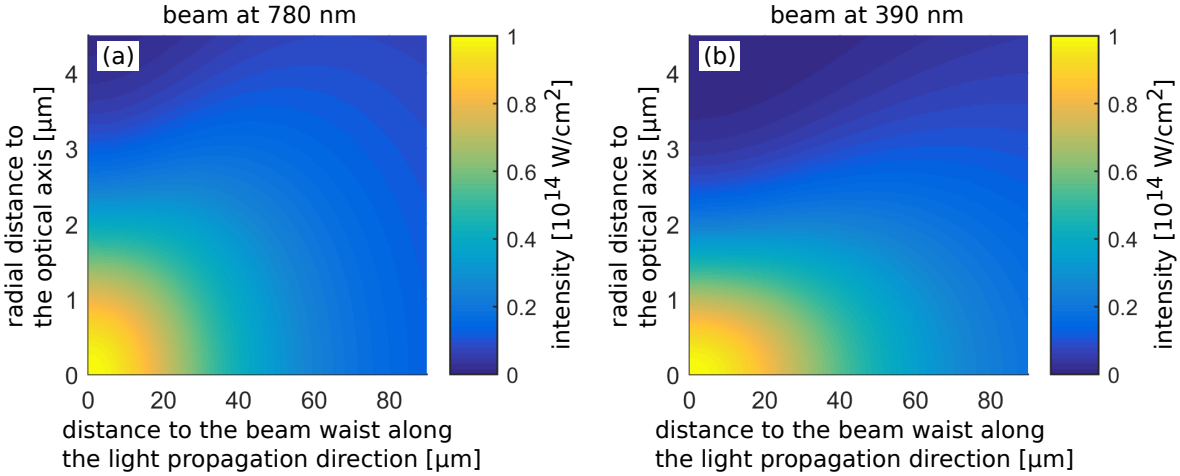


Figure A.4: The position-dependent light intensity $I_{780\,\mathrm{nm}}$ [$I_{390\,\mathrm{nm}}$] for the beam at a wavelength of 780 nm [390 nm] is depicted in (a) [(b)]. The figure has been part of the answer to the referees regarding the publication Eckart et al. [24]. The layout and labels have been changed.

Building on this result the combined intensity of the two-color laser field[156] can be calculated which is shown in Fig. A.5(a). The combined intensity is defined by $I_{\mathrm{combined}} = \left(\sqrt{I_{780\,\mathrm{nm}}} + \sqrt{I_{390\,\mathrm{nm}}}\right)^2$. Moreover, for each position in the interaction region the nonlinear ionization rate can be calculated[157]. The result is shown in Fig. A.5(b).

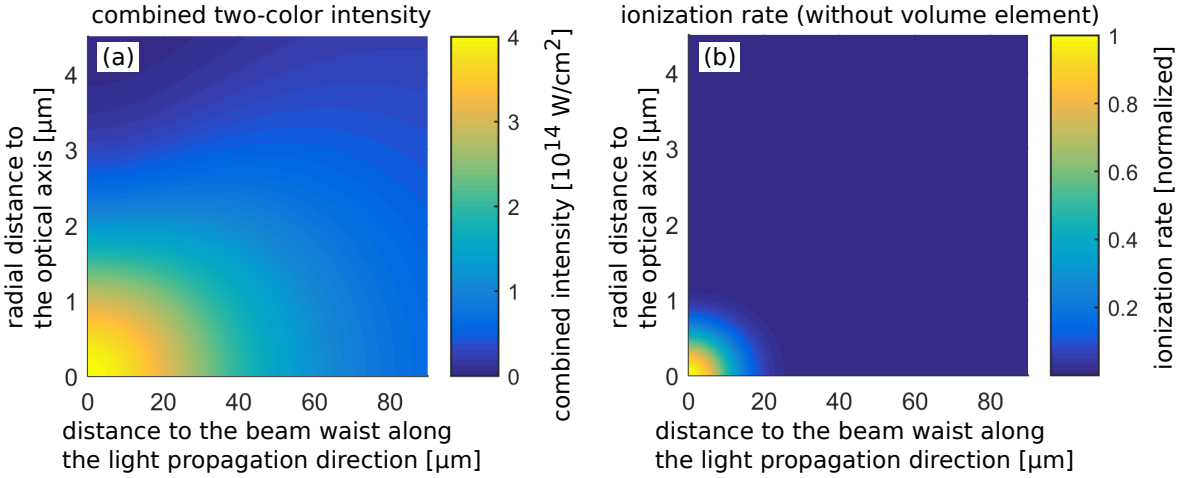


Figure A.5: In (a) the position-dependent combined light intensity I_{combined} for the two-color laser beam is shown. (b) shows the ionization rate at each position without taking the volume element into account. The figure has been part of the answer to the referees regarding the publication Eckart et al. [24]. Here, the ionization rate is approximated for helium using Eq. 5.

The results in Fig. A.5(b) are shown in cylindrical coordinates but neglect the volume element. Taking the volume element into account results in Fig. A.6(a). For Fig. A.6(b) at each

[156] Only those parts of the laser beam that intersect the gas target can contribute to the experiment. This allows one to minimize the range of intensities that contribute to the experiment (focal averaging) by collimating the gas target along the light propagation direction using metal plates that crop the gas jet in those directions.

[157] The ionization rate is approximated for helium using Eq. 5.

position in the interaction region the two-color field ratio E_{390}/E_{780} is plotted. It is seen that the two-color field ratio does not vary significantly in the region that is contributing to the ionization rate.

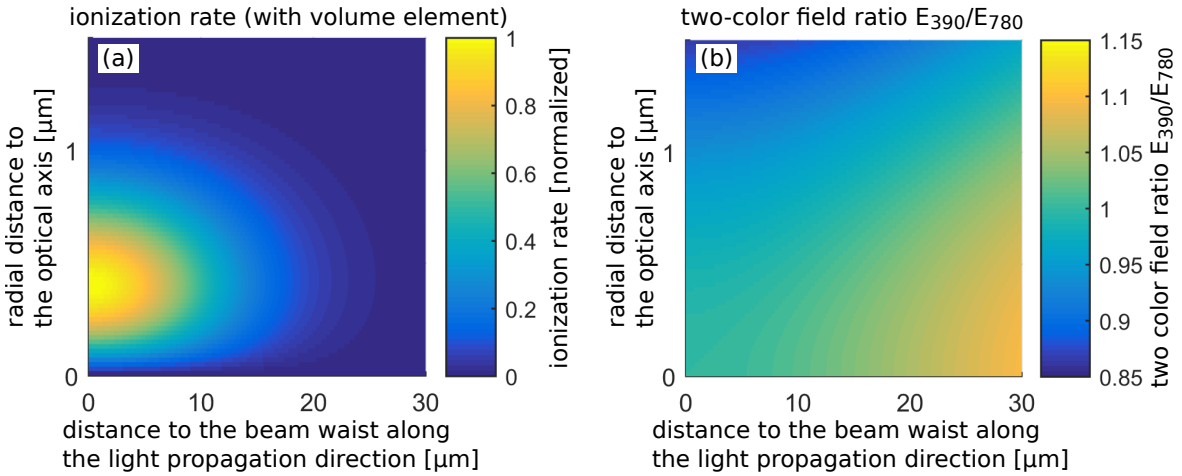


Figure A.6: In (a) the ionization rate at each position is shown taking the volume element into account. (b) shows the position dependent two-color field ratio. The figure has been part of the answer to the referees regarding the publication Eckart et al. [24]. Here, the ionization rate is approximated for helium using Eq. 5.

Using the result shown in Fig. A.6(a) as a weight for each point in the focal volume a histogram can be generated that reveals which two-color field ratios contribute to the total ionization rate. The result is shown in Fig. A.7(a). Fig. A.7(b) and Fig. A.7(c) show the same histogram for the Gouy phase and the combined intensity. It is seen that the field ratio, the Gouy phase and the combined intensity all have distributions with a moderate width. The deviation of the mean of the two-color field ratio to the two-color field ratio comparing the peak electric fields is only 1%. The mean of the combined intensity is about 10% below the peak of the combined intensity of $4 \cdot 10^{14}\mathrm{W/cm^2}$ for the given focal geometry.

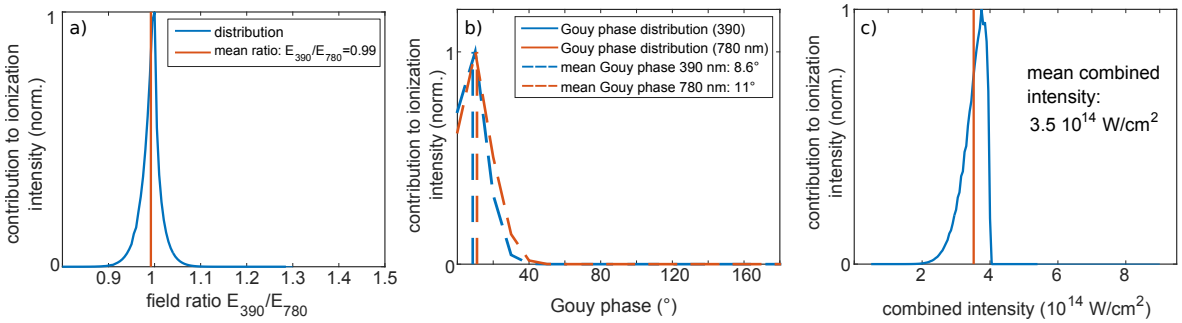


Figure A.7: (a), (b) and (c) show the contributions of various field ratios, Gouy phases and combined intensities to the overall ionization rate. The figure has been part of the answer to the referees regarding the publication Eckart et al. [24] in an almost identical version. Here, the ionization rate is approximated for helium using Eq. 5. The layout and labels have been changed.

A.2. Offline Compensation of the Drifts of the Relative Phase

The relative phase of the two individual laser pulses Φ is very sensitive to changes of the temperature and the humidity in the laboratory. Both laser pulses are spatially separated in the interferometric two-color setup (see chapter 4.1.2). The temperature in the laboratory is actively stabilized by an air conditioning system and typically temperature changes are below 0.1 °C. The humidity is not stabilized. The procedure[158] that is described in the remainder of this subchapter is very similar to the method used in Ref. [36].

Using circularly polarized counter-rotating two-color (CRTC) fields or circularly polarized co-rotating two-color (CoRTC) fields a change of the relative phase results in a rotation of the electron momentum distribution in the plane of polarization (see chapter 6). This property can be used for an offline[159] compensation of the drifts of the relative phase. Since the drifts of the relative phase are almost[160] unavoidable, the nm-delay stage is intentionally moved in most cases. This creates an additional, "controlled change of the relative phase" $\Delta\Phi_{\text{stage}}$ which can be easily corrected for. The active variation of Φ_{stage} minimizes systematic errors that are due to detector inefficiencies. As a result very accurate final electron momentum distributions can be obtained.

Fig. A.8(a) shows the measured electron momentum in the laboratory system. The data is the same that is presented in chapter 8 but here a different binning is used. All data was taken within 5 hours and the relative phase of the two laser pulses was adjusted every 4 minutes using the nm-delay stage. The nm-delay stage was moved to 40 equidistant position within a range of 389 nm (one moving-sequence takes 160 minutes). After one moving-sequence was complete the moving-sequence restarted from the beginning.

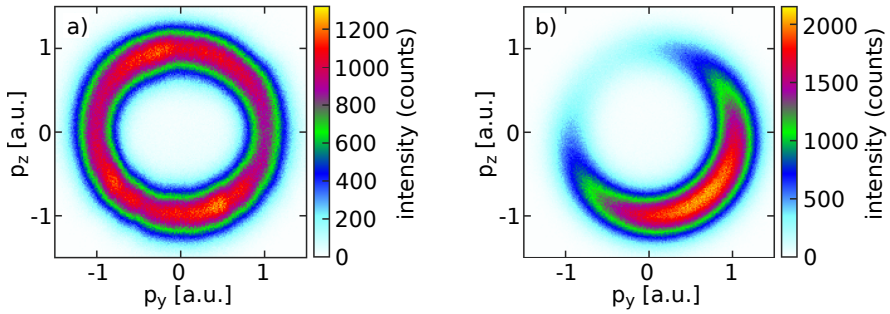


Figure A.8: The measured electron momentum distribution is shown before (a) and after (b) the changes of the relative phase $\Delta\Phi$ have been compensated for. The momentum in the plane of polarization is shown for the field geometry that is depicted in Fig. 8.3(a).

[158] In the supplementary material of Ref. [112] a method for the offline compensation of the drifts of the relative phase of orthogonal two-color laser pulses is described.

[159] "Offline" means that the method is applied after the process of data taking is completed.

[160] In chapter A.4 it is demonstrated how the relative phase of the two individual laser pulses can be actively stabilized.

Compensating for all phase changes $\Delta\Phi$ the final electron momentum distribution shown in Fig. A.8(b) is obtained. There are two contributions to $\Delta\Phi$. One contribution is $\Delta\Phi_{\text{stage}}$ which is due to the position of the nm-delay stage. This contribution is precisely known and can easily be compensated for. The second contributions is $\Delta\Phi_{\text{parasitic}}$. $\Delta\Phi_{\text{parasitic}}$ is due to phase drifts that depend on the temperature and the humidity in the laboratory. Therefore, changes of the relative phase of the two individual laser pulses $\Delta\Phi$ are the sum of the actively controlled changes of the relative phase $\Delta\Phi_{\text{stage}}$ and the parasitic phase drifts $\Delta\Phi_{\text{parasitic}}$:

$$\Delta\Phi = \Delta\Phi_{\text{stage}} + \Delta\Phi_{\text{parasitic}} \tag{58}$$

The phase drifts $\Delta\Phi_{\text{parasitic}}$ are shown in Fig. A.9 as a function of the eventcounter (see chapter 4.1.3). How were the phase drifts $\Delta\Phi_{\text{parasitic}}$ determined?

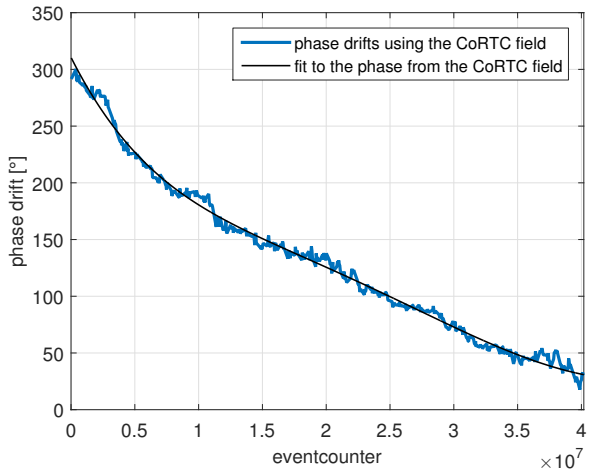


Figure A.9: The phase drifts $\Delta\Phi_{\text{parasitic}}$ are shown as a function of the eventcounter (which is in a good approximation linear to the absolute measurement time). A fit of a fifth order polynomial to the data is shown as a black line.

Fig. A.10(a) shows a subset of the data from Fig. A.8(a): the angle in momentum space in the plane of polarization is calculated for every event that has a final radial momentum $\left(p_r = \sqrt{p_y^2 + p_z^2}\right)$ that fulfills $0.65\,\text{a.u.} < p_r < 1.2\,\text{a.u.}$ It is seen that the most probable angle in momentum space in the plane of polarization evolves with the eventcounter (which is approximately linear in time). This is equivalent to a rotation of the electron momentum distribution in the plane of polarization. Compensating the displacement of the nm-delay stage leads to the result shown in Fig. A.10(b).

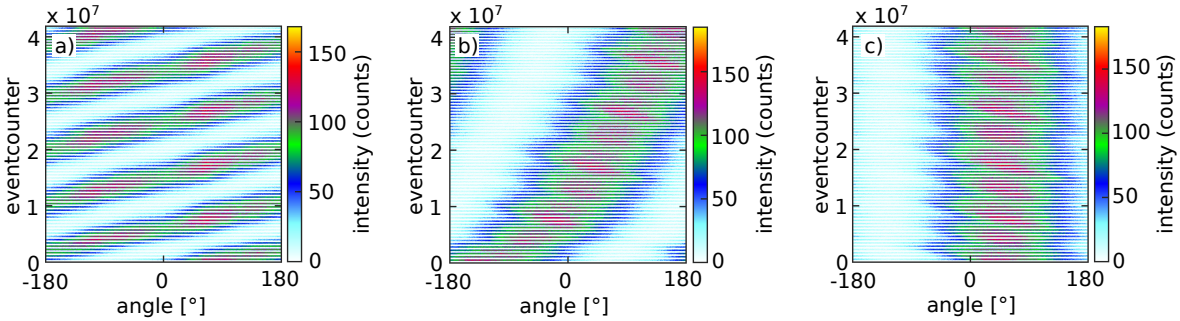


Figure A.10: In (a) a subset of the data from Fig. A.8(a) that fulfills $0.65\,\text{a.u.} < p_r < 1.2\,\text{a.u.}$ is presented. The angle is the angle in the plane of polarization and calculated by $\text{atan2}(p_z, p_y)$ for every detected electron. The eventcounter is approximately linear in time. The duration of the measurement was 5 hours. The horizontal white stripes indicate times for which the CRTC field was used. Here, only the data for the CoRTC field is shown. In (b) the same data is shown as in (a) but the phase changes $\Delta\Phi_{\text{stage}}$ due to the displacement of the nm-delay stage are compensated for. (c) shows the same as (a) but here the phase changes of the nm-delay stage $\Delta\Phi_{\text{stage}}$ and the phase phase drifts $\Delta\Phi_{\text{parasitic}}$ are corrected for. For the correction of the phase drifts the fifth order polynomial from Fig. A.9 is used.

Each row in Fig. A.10(b) can be used to perform a Fourier transform and the phase of the onefold symmetry is extracted and shown as the value for the phase drift $\Delta\Phi_{\text{parasitic}}$ in Fig. A.9. The result from the fit of the fifth order polynomial is used to compensate for the phase drifts $\Delta\Phi_{\text{parasitic}}$. This allows for the correction of all phase changes $\Delta\Phi$ which leads to the result that is shown in Fig. A.10(c) and Fig. A.8(b). Fig. A.10(c) shows 9 diagonal substructures that indicate that the phase compensation does not work perfectly. At close examination these structures are already seen in Fig. A.10(a). The structures are probably due to local inefficiencies of the electron detector.

The horizontal white stripes which are seen in Fig. A.10 reflect the changes of the relative helicity. The helicity of the laser pulse at a central wavelength of 390 nm was inverted every 2 minutes. In Fig. A.10 only those events are shown that were recorded using the CoRTC field. Hence, there is a complementary data set which has been measured during the same time period which can be analyzed as well in order to validate the method for retrieving the phase drifts $\Delta\Phi_{\text{parasitic}}$.

Fig. A.11 and Fig. A.12 show the data for the CRTC field in analogy to the discussion that was done for the CoRTC field. The white stripes in Fig. A.10 are complementary to those in Fig. A.12. The phase drifts $\Delta\Phi_{\text{parasitic}}$ that are extracted using the CRTC field (Fig. A.12(b)) are shown in Fig. A.13 together with the data from the CoRTC field (Fig. A.9). In Fig. A.13 the values that are retrieved for the phase drift $\Delta\Phi_{\text{parasitic}}$ are compared. The data shown as blue (red) line was obtained using the CRTC (CoRTC) field. It is evident that the two results are consistent.

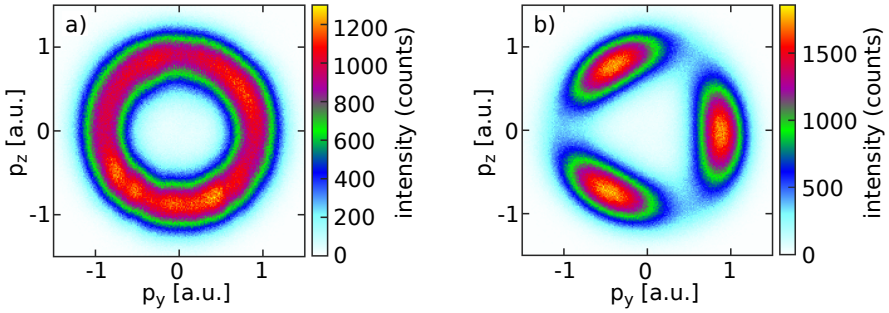


Figure A.11: The measured electron momentum distribution is shown before (a) and after (b) the changes of the relative phase have been compensated for in analogy to Fig. A.8. The momentum in the plane of polarization is shown for the field geometry is shown in Fig. 8.3(b).

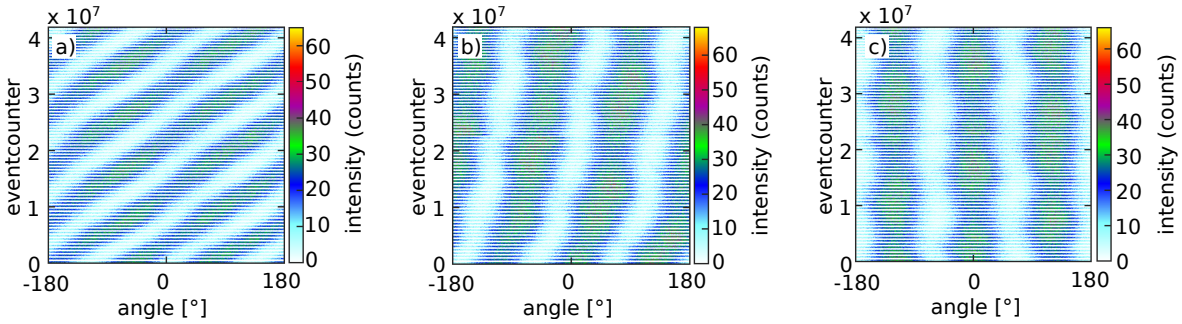


Figure A.12: The data from Fig. A.11(a) that fulfills 0.5 a.u. $< p_r <$ 0.8 a.u. is presented in analogy to Fig. A.10. Here the data belonging to the CRTC field is shown.

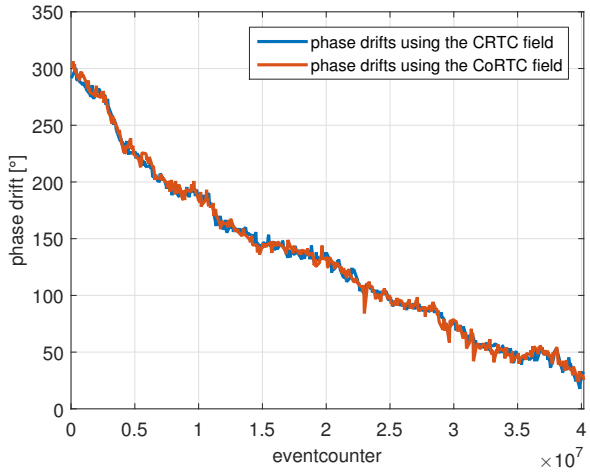


Figure A.13: The drifts of the relative phase are shown as a function of the eventcounter (which is in a good approximation linear to the absolute measurement time) for the CoRTC and the CRTC field. The retrieved phase drifts are consistent.

The method that is described in this subchapter uses a Fourier transform to extract the phase and afterwards a polynomial fit is done to extract the phase drifts $\Delta\Phi_{\text{parasitic}}$. The polynomial fit provides the phase drift as a function of the eventcounter. Using this approach, in the analysis the phase drift for every measured event is known. This method is very similar to the procedure described in Ref. [36]. In Ref. [36] the peak of the angular distribution

(similar to Fig. A.12(a)) is tracked continuously using a moving average to obtain $\Delta\Phi$. Both methods provide similar results. In this thesis one of the two methods is chosen if the relative phase of the two single-color laser pulses has to be compensated for.

Finally, as a side product of this subchapter the stability of the interferometric two-color setup has been characterized. For a measurement with a duration of 5 hours the phase drifts were about 280°. This corresponds to a change of the relative phase that is less than 60° per hour[161].

[161] For the CoRTC field the value of the rotation angle is the same as the value of the relative phase of the two single-color laser pulses. For the CRTC field the value of the rotation angle is only $\frac{1}{3}$ of the value of the relative phase of the two laser pulses.

A.3. Two-Color Fields Composed of Non-Circularly Polarized Single-Color Fields

In chapter 6, 7, 8 and 10 circularly polarized counter-rotating two-color (CRTC) fields or circularly polarized co-rotating two-color (CoRTC) fields are used. The only case in which one of the two laser pulses is not circularly polarized is found in chapter 9. However, in chapter 9 the two laser pulses do not overlap temporally.

This subchapter[162] show examples of two-color fields that are composed of a linearly polarized laser pulse at a central wavelength of 390 nm and a circularly polarized laser pulse at a central wavelength of 780 nm. The advantage of this special type of a two-color field is that both individual polarization states can be set with high accuracy in the experiment (see chapter 4.1.5). This in in contrast to elliptically polarized light. Although elliptically polarized light can be set experimentally, it is not trivial to retrieve the exact ellipticity and the orientation of the main axis of the ellipse in the laser focus (see e.g. Ref. [56]).

In order to find the setting for the wave plates in the arm of the laser pulse at a central wavelength of 390 nm an average power of 68 mW was set in front of the vacuum chamber and an argon target was used. The positions of the wave plates were optimized to maximize non-sequential double ionization (the ratio of double to single ionization, see also chapter 6). The measured electron momentum distribution is shown in Fig. A.14. The electrons were not measured in coincidence with argon ions.

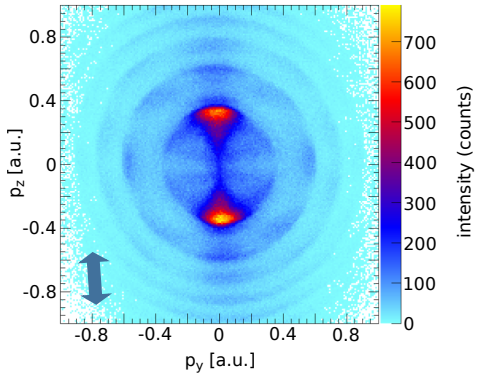


Figure A.14: Ionization of argon using linearly polarized light at 390 nm. The total measurement-time was only 11 minutes. The polarization is indicated by a blue arrow and the polarization axis is tilted by 4° with respect to the p_z-direction.

The orientation of the polarization axis can be obtained from the experimental data. To this end the electron momentum distribution in the plane of polarization is analyzed. The radial momentum $\left(p_r = \sqrt{p_y^2 + p_z^2}\right)$ in the plane of polarization is restricted to $0.8\,\text{a.u.} < p_r <$

[162] Nico Strenger and Andreas Pier contributed to this project. Both are students that were supervised by the author of this thesis.

1.0 a.u. The resulting subset is analyzed and it is found that there is a peak at an angle of $\varphi = 94°$ in the angular distribution plotting $\varphi = \text{atan2}(p_z, p_y)$. This defines the polarization axis of the linearly polarized laser pulse at a central wavelength of 390 nm.

In order to find the settings for the wave plates in the arm of the laser pulse at a central wavelength of 780 nm the laser pulse was set to an average power of 337 mW in front of the vacuum chamber and helium was used as target. Two settings were found that lead to circularly polarized light which have opposite helicities. The two resulting electron momentum distributions, which were measured in coincidence with helium atoms, are depicted in Fig. A.15. Helium was used because it has the highest ionization potential for single ionization. Therefore, the electron momentum distribution would deviate from the "donut-like" distributions already for small deviations from perfect circularly polarized light. Since such deviations cannot be seen in Fig. A.15(a) and A.15(b) it can be concluded that in both cases the laser pulse is almost perfectly circularly polarized.

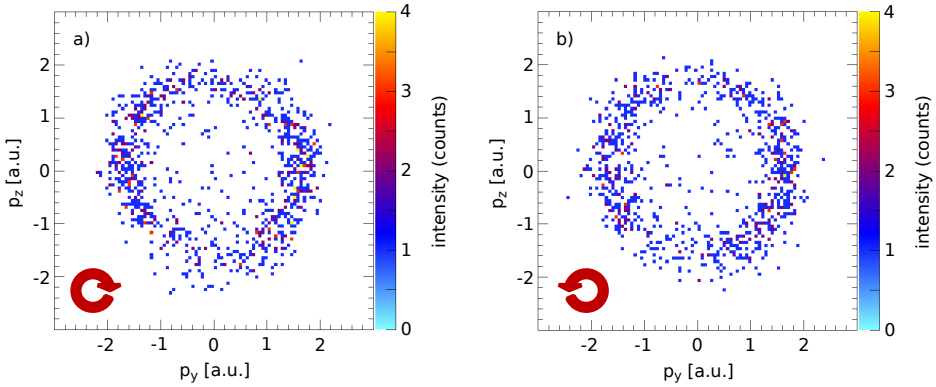


Figure A.15: Ionization of helium using clockwise rotating (a) and anti-clockwise rotating (b) circularly polarized light at a central wavelength of 780 nm. The total measurement-time was only six minutes. The data sets that are shown in (a) and in (b) were both measured for equal acquisition times (each data set for three minutes). The helicity is indicated by red arrows in (a) and (b).

For the measurement using the two-color field the average powers were adjusted to 175 mW for the laser pulse at a central wavelength of 390 nm and 210 mW for the laser pulse at a central wavelength of 780 nm. The intensities were calibrated using circularly polarized light measuring the radius of the "donut-like" distribution (see chapter 4.1.5). The peak electric field for the laser pulse at a central wavelength of 390 nm (780 nm) was found to be $E_{390} = 0.15$ a.u. ($E_{780} = 0.08$ a.u.).

The circularly polarized light pulse at a central wavelength of 780 nm with a clockwise rotating electric field (see Fig. A.15(a)) was temporally and spatially overlapped with the linearly polarized laser pulse at a central wavelength of 390 nm and the nm-delay stage was

set to 210 positions within a range of 257 nm. At each position data was recorded for 10 s resulting in a total measurement time of 35 minutes. The result of this measurement is shown in Fig. A.16(a). The presented electron momentum distribution was measured in coincidence with helium. For Fig. A.16(b) the helicity of the electric field of the light pulse at a central wavelength of 780 nm was inverted and thus set as for Fig. A.15(b). Everything else remained unchanged compared to Fig. A.16(a).

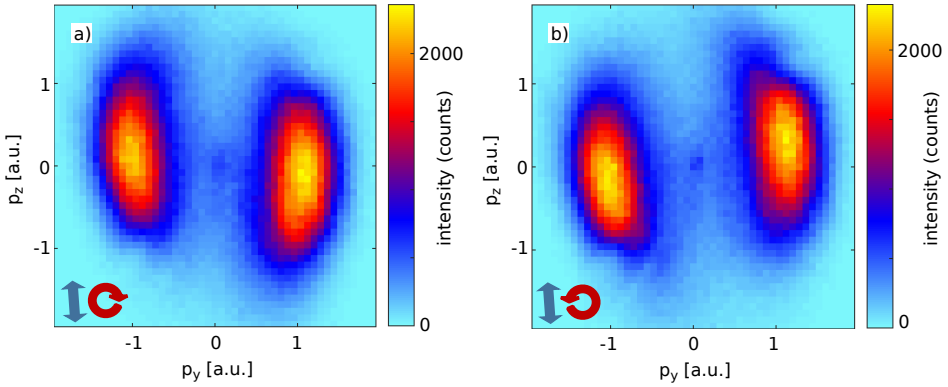


Figure A.16: The electron momentum distributions upon the ionization of helium by a two-color field consisting of a circularly polarized laser pulse at a central wavelength of 780 nm and a linearly polarized laser pulse at a central wavelength of 390 nm are shown. For both electron momentum distributions many relative phases of the two laser pulses contribute. Both electron momentum distributions were measured in coincidence with helium. In (a) [(b)] the light pulse at a central wavelength of 780 nm has a clockwise [counter-clockwise] rotating electric field. The axis of polarization for the linearly polarized laser pulse at a central wavelength of 390 nm is tilted by 4° with respect to the p_z-direction. The polarization properties of the two single-color laser pulses are illustrated by colored arrows.

The data shown in Fig. A.16 is not resolved on the relative phase of the two laser pulses. It can be shown that the differences of Fig. A.16(a) and Fig. A.16(b) are not due to differences of the negative vector potentials: The negative vector potential for several relative phases of the two laser pulses is shown in Fig. A.17(a)-A.17(d) for the case in which the circularly polarized light pulse at a central wavelength of 780 nm has a clockwise rotating electric field. The difference of the relative phase is given by Δt which indicates the temporal delay of the two laser pulses. It is evident that complicated Lissajou curve emerge. Fig. A.17(e)-A.17(h) show that for a circularly polarized light pulse at a central wavelength of 780 nm with a counter-clockwise rotating electric field the same vector potentials can be produced as in Fig. A.17(a)-A.17(d). Comparing the electric fields in Fig. A.17(a)-A.17(d) with the electric fields in Fig. A.17(e)-A.17(h) it is seen that the electric fields are point reflected at the origin. This leads to the following conclusion: if the final electron momentum were only given by the value of the negative vector potential, the electron momentum distributions in Fig. A.16(a) and Fig. A.16(b) would be identical (see “simple man’s model” in chapter 3).

The fact that the measured distributions are different shows that the temporal evolution of the laser electric field and the interaction with the Coulomb potential cannot be neglected. This is an expected result (see e.g. Refs. [8, 122]) and it is difficult to separate (trivial) Coulomb interaction after tunneling from interesting quantities such as non-adiabatic offsets (see chapter 8).

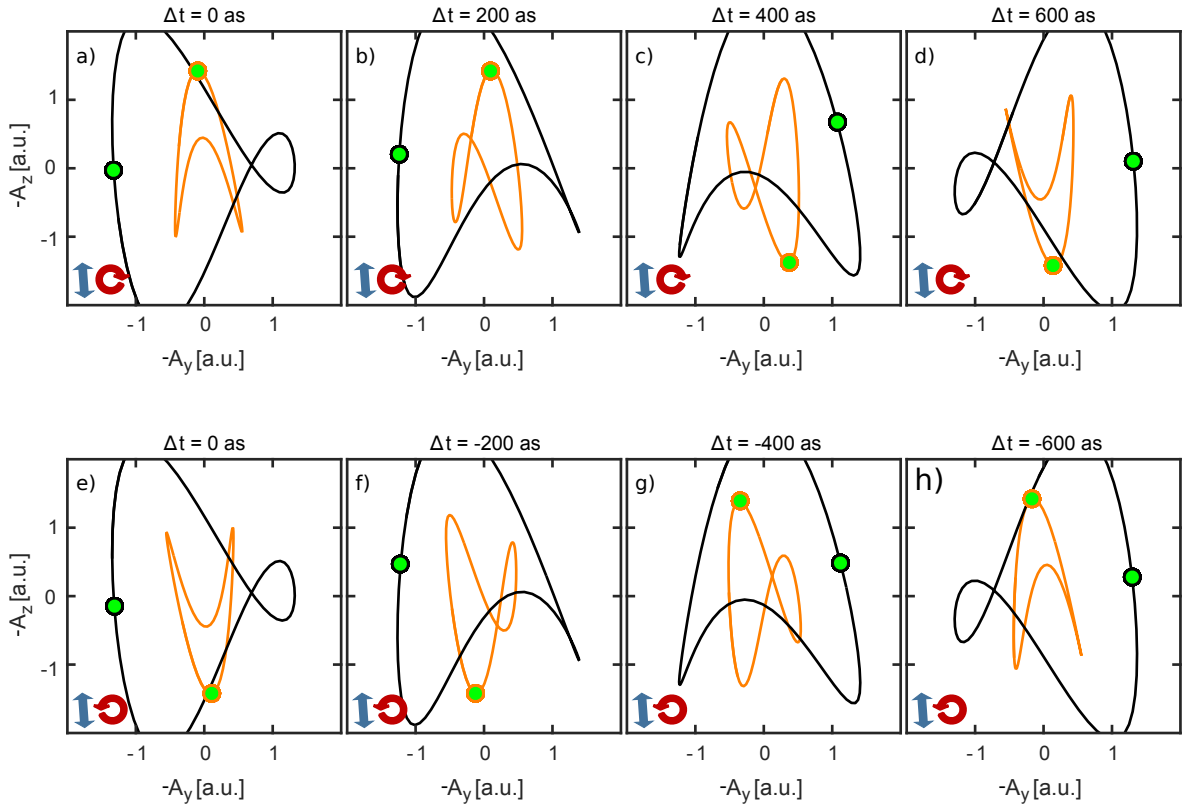


Figure A.17: (a)-(d) shows the Lissajou curves for the electric field and the negative vector potential. The time delay, that defines the relative phase of the two laser pulses, is indicated as temporal delay Δt above each panel. The circularly polarized light pulse at a central wavelength of 780 nm has a clockwise rotating electric field and the light pulse at a central wavelength of 390 nm is linearly polarized. The highest absolute value of the electric field in the shown Lissajou curve and the corresponding negative vector potential is highlighted by a green dot. The electric field is shown as an orange line in arbitrary units. The polarization properties of the two single-colors are illustrated by colored arrows. For (e)-(h) the circularly polarized light pulse at a central wavelength of 780 nm has an anti-clockwise rotating electric field. The delays Δt in (e)-(h) are chosen such that the shape of the negative vector potential is as in (a)-(d).

In a next step the electron momentum distributions from Fig. A.16(a) is resolved on the relative phase[163] of the two laser pulses. Here, the temporal delay of the two laser pulses is equivalent to the relative phase. The delay of the two laser pulses Δt is calculated from the displacement of the nm-delay stage Δx using

$$\Delta t = \frac{2 \cdot \Delta x}{c} \tag{59}$$

[163] All data shown in Fig. A.16 was recorded within 35 minutes. The drifts of the relative phase are expected to be less than 33° which corresponds to 120 as (see chapter A.2).

where c is the speed of light. Each panel from Fig. A.18 was recorded within 10 seconds at one single position of the nm-delay stage. The Lissajou curves for the electric field and the negative vector potential are also depicted.

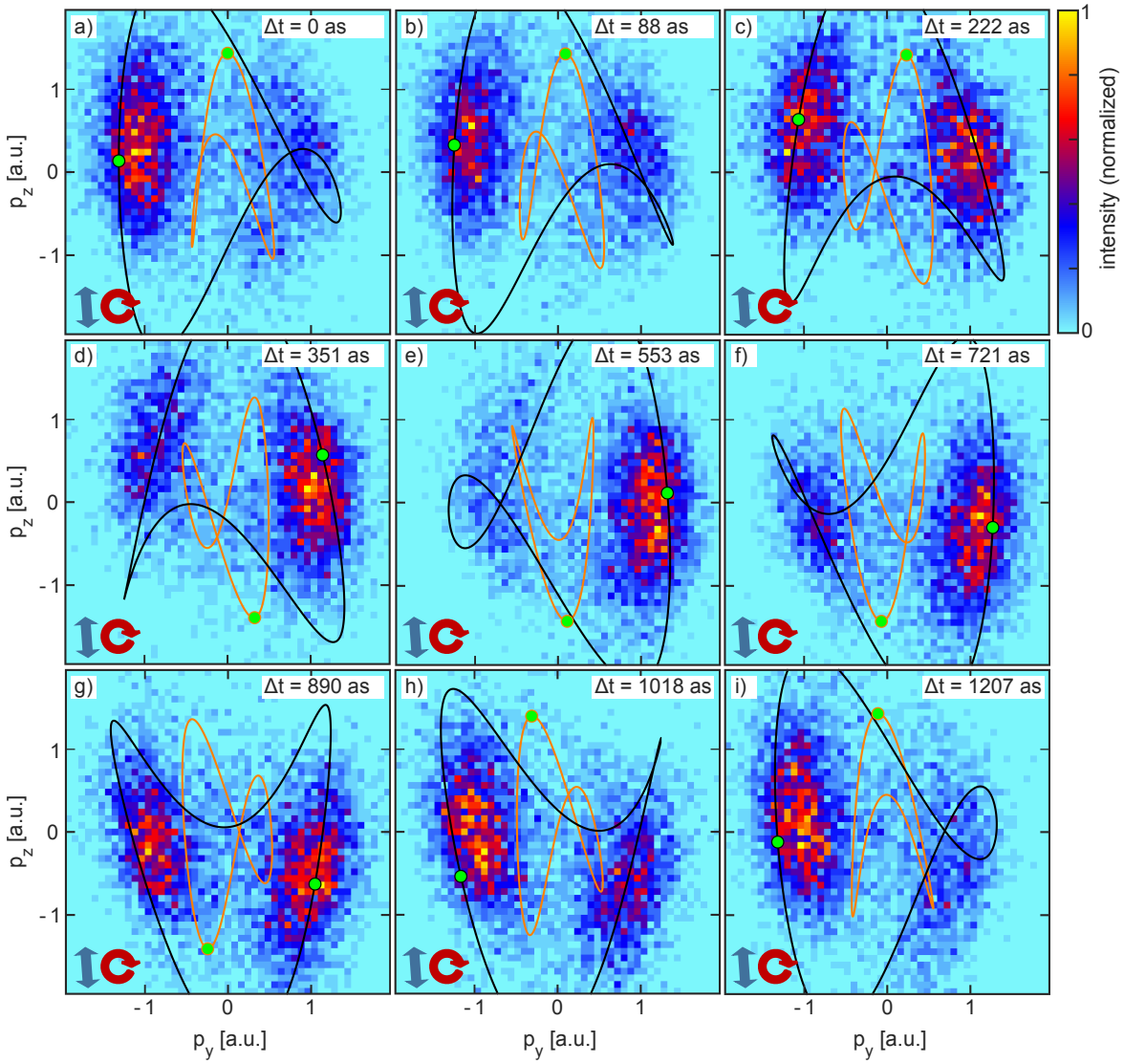


Figure A.18: All panels show subsets of the data from Fig. A.16(a). The measurement time for the data in each panel data was 10 s and during this time the nm-delay stage was not moved. The temporal delays Δt are shown in the insets. The negative vector potential is shown as a black line in atomic units. The electric field is shown as an orange line in arbitrary units. The highest absolute value of the electric field in the shown Lissajou curve and the corresponding negative vector potential is highlighted by a green dot. The polarization properties of the two single-colors are illustrated by colored arrows. Here, typically the absolute value of the most intense pixel corresponds to about 30 counts.

It has to be noted that the absolute phase is not exactly known in the experiment and was estimated using the following method: Fig. A.18(f), A.18(g) and A.18(h) were analyzed. In Fig. A.18(f) [(h)] the peak at the right [left] half of the electron momentum distribution is more prominent. In Fig. A.18(g) both peaks have equal intensity. It was concluded that for the stage position that belongs to Fig. A.18(g) the absolute value of the combined laser

electric fields must have two different maxima within one laser cycle with similar absolute value of the laser electric field. Fig. A.18 can be interpreted as a movie that shows how the electron momentum distribution and the field properties change as the delay of the two laser pulses Δt is varied. It is clearly seen that the negative vector potential that belongs to the highest electric field (both are marked as green dots) is always found in the region in momentum space in which many events were recorded. This underlines that the approach to resolve the electron momentum distribution on the relative phase of the two laser pulses was successful. Further quantitative insights cannot be easily gained. This is because drifts of the relative phase (see chapter A.2) make a precise assignment of the measured data for a given stage position to an exact relative phase impossible.

In the following chapter (chapter A.4) a method for the active stabilization of the relative phase of the two single-color laser pulses is presented.

A.4. Active Stabilization of the Relative Phase

For CRTC and CoRTC field slow drifts of the relative phase of the two laser pulses can be compensated for during the analysis (see chapter A.2). For non-circularly polarized fields the changes of the relative phase cannot be easily compensated for because the phase changes do not lead to a rotation of the electron momentum distribution in the plane of polarization (see chapter A.3).

This motivates to develop a method to actively stabilize the phase of the two laser pulses which is independent of the measurement inside the vacuum chamber. This subchapter explains how a feedback loop can be realized that allows for the active stabilization of the relative phase of the two laser pulses. The basic idea is to use an interference signal that is measured using an optical spectrometer outside the vacuum chamber to adjust the position of the nm-delay stage employing a closed loop control scheme.

The project of building the active stabilization of the relative phase was realized in two steps. First a proof of concept was done neglecting all intensity and polarization characteristics of the two laser pulses. In a second step the active stabilization was implemented in a way that allows for the use of tailored intense two-color fields inside the vacuum chamber.

A.4.1. Active Stabilization: Proof of Concept

The experimental setup that was used to test the idea for the active stabilization is shown in Fig. A.19. Upto the beam splitter "BS2" everything is the same as in Fig. 4.6.

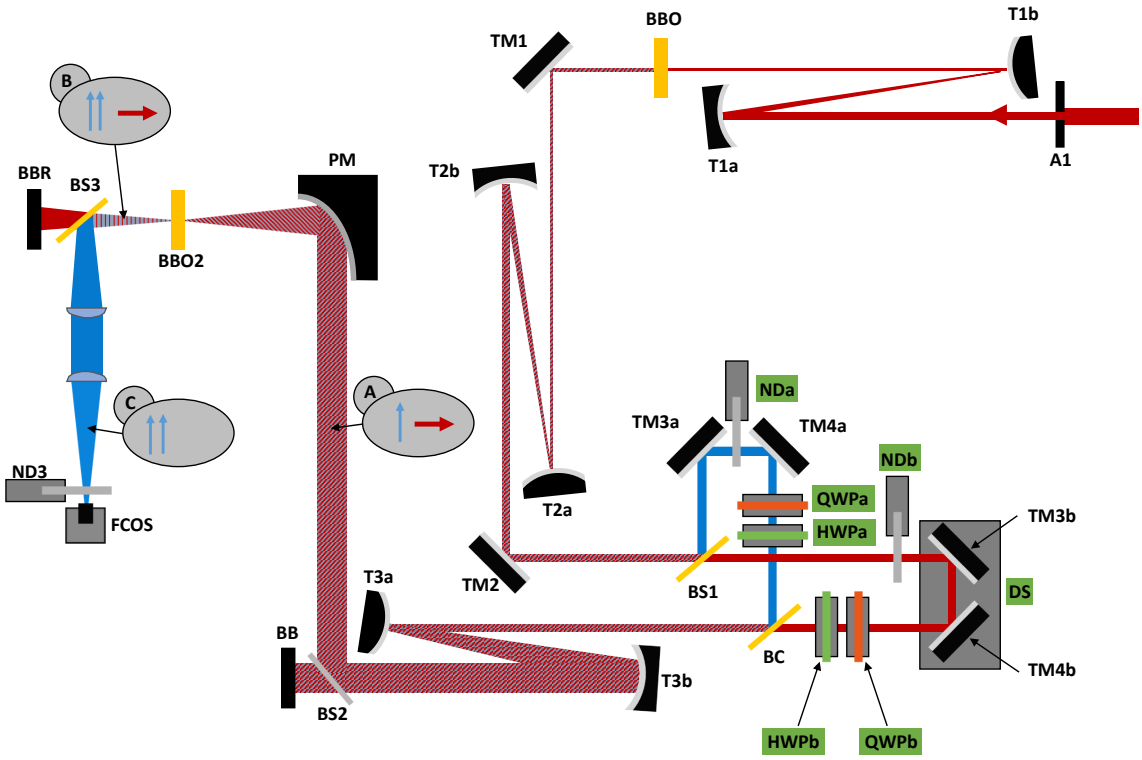


Figure A.19: The experimental setup for the stabilization of the relative phase of the two laser pulses in the interferometer is schematically shown. The first part of the setup is as in Fig. 4.6. In front of the vacuum chamber a window (UV fused silica) acts as a beam splitter ("BS2"). A beamblock is inserted ("BB") to absorb the light that is transmitted through "BS2". The light that is reflected at "BS2" is focuses using an off-axis parabolic mirror. A BBO ("BBO2") frequency doubles the p-polarized component of the light at 780 nm. Afterwards, a beam splitter ("BS3") reflects only the light at 390 nm which is transmitted through a neutral density filter ("ND3") and coupled into a fiber-coupled optical spectrometer ("FCOS"). The polarization states are indicated by the vertical and horizontal arrows in the gray shaded ellipses that are labeled with "A", "B" and "C".

For the beam splitter "BS2", a window, which is made of UV fused silica window[164] with a thickness of 1 mm, is used. The window is inserted under almost zero degrees. The transmitted light is absorbed by a beam block ("BB" in Fig. A.19). The reflected light was used for the active stabilization. On the way to the parabolic mirror[165] that focused the two-color beam into a BBO (see "BBO2" in Fig. A.19) a UV-enhanced aluminum mirror[166] was used for alignment, which is not shown in Fig. A.19. The BBO was not positioned exactly in the focus of the parabolic mirror. The BBO generates a beam at a central wavelength of

[164] The product with the code "WG41010" from Thorlabs GmbH was used.
[165] The product with the code "MPD169-F01" from Thorlabs GmbH was used.
[166] For the mirror "TM5" the UV-enhanced aluminum mirror with the product code "PF10-03-F01" from Thorlabs GmbH was used.

390 nm from the incident light at a central wavelength of 780 nm. Afterwards, a beam splitter ("BS3" in Fig. A.19, "BS3" is identical to "BS1" and "BC") separates the light at around 780 nm and the light at around 390 nm. The laser pulses at a central wavelength of 780 nm are transmitted and absorbed on a beam block ("BBR" in Fig. A.19). The reflected light is collimated and focused by two lenses made of fused silica that is transparent to light with a wavelength of about 390 nm. Before the light is sent into a fiber-coupled optical spectrometer[167] ("FCOS" in Fig. A.19) it is attenuated using a neutral density filter "ND3" (the same as "NDa").

A typical polarization state that could be used is indicated by the vertical (indicating s-polarized light) and horizontal (indicating p-polarized light) arrows in the gray shaded ellipse that is labeled with "A". The colors of the arrows correspond to the color of the laser beam (blue (red) for the laser pulses with a central wavelength of 390 nm (780 nm)). In "A" the beam at 780 nm is p-polarized and very intense (indicated by a bold arrow) and the beam at 390 nm is s-polarized and possesses less intensity (indicated by a thin arrow). After the BBO part of the light at 780 nm is frequency-doubled to 390 nm. The frequency-doubled light is also s-polarized (see "B" in Fig. A.19). Since the light at a central wavelength of 780 nm is transmitted through "BS3" there is only light at a wavelength of about 390 nm detected in the fiber-coupled optical spectrometer. The polarization state in front of the fiber-coupled optical spectrometer is indicated in the gray shaded ellipse that is labeled with "C".

The working principle of the active stabilization is that the detected photons at about 390 nm have two possible origins. They can be generated in the first or the second BBO. If they are generated in the first BBO, the photons were reflected at "BS1" and if they were generated in the second BBO they were transmitted through "BS1" (see chapter 4.1.2). This leads to a two-path interference of photons that have traveled the two different arms of the interferometric setup. Changes of the relative phase of the two laser pulses (one at a central wavelength of 780 nm and the other at a central wavelength of 390 nm) result in a change of the relative phase of the two laser pulses at a central wavelength of 390 nm that arrive at the fiber-coupled optical spectrometer.

The measured optical spectra for three different delays, that were set using the nm-delay stage, are presented in Fig. A.20. It is evident that the measured optical spectrum shows a modulation. The modulation depends on the delay of the two laser pulses that are interfering (the two laser pulses can be viewed as a double slit in time giving rise to a two-path interference in energy). The phase of the modulation of the optical spectra depends on the phase of

[167] The model "SM242" from Spectral Products is used. Typically 50 ms were used as an integration time.

the two laser pulse at a central wavelength of 390 nm and the laser pulse at a central wavelength of 780 nm at the second BBO (see "BBO2" in Fig. A.19). Accordingly, the phase of the blue line (delay stage position of 99 nm) and the yellow (delay stage position of 0 nm) line in Fig. A.20 differ by 180°. This is expected because a displacement of the delay stage by a quarter wavelength of the laser pulse at a central wavelength of 390 nm corresponds to a phase shift of the relative phase of the two single-color laser pulses of 180°.

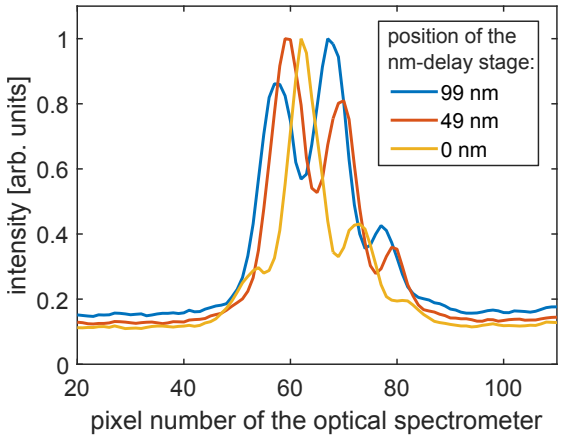


Figure A.20: Measured optical spectra showing two-path interferences for three different positions of the nm-delay stage.

However, it should be noted that the horizontal axis in Fig. A.20 shows the pixel number of the spectrometer which must not be linear in the wavelength. This is also a shortcoming of the procedure that is described in the remainder of chapter A.4. Each of the three measured spectra from Fig. A.20 is Fourier transformed and the result is shown in Fig. A.21. Fig. A.21(a) [(b)] shows the amplitude [phase] of the Fourier transformed data.

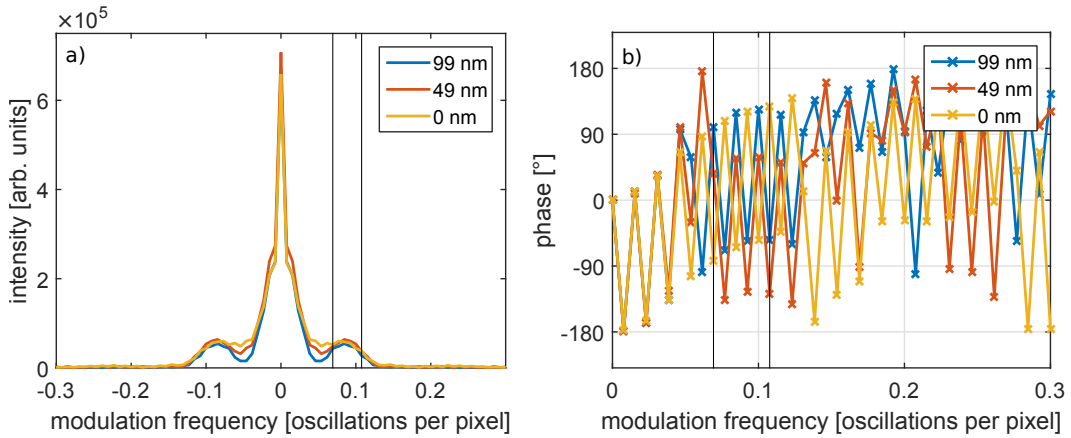


Figure A.21: (a) [(b)] shows the amplitude [phase] of the measured spectra from Fig. A.20. The vertical black lines are drawn at identical modulation frequencies in (a) and (b) to guide the eye.

The side-band at about 0.08 oscillations per pixel in Fig. A.21(a) is due to the observed

modulations in Fig. A.20. The phase around this modulation frequency shows a clear dependence on the displacement of the nm-delay stage in Fig A.21(b). This finding can be seen even more clearly inspecting Fig. A.22 which shows the differences of the phases from Fig. A.21(b) using the data for a displacement of the nm-delay stage of 99 nm as a reference. It is evident that the phase in Fig. A.22 provides a very sensitive signal to changes of the relative length of the two arms of the interferometer.

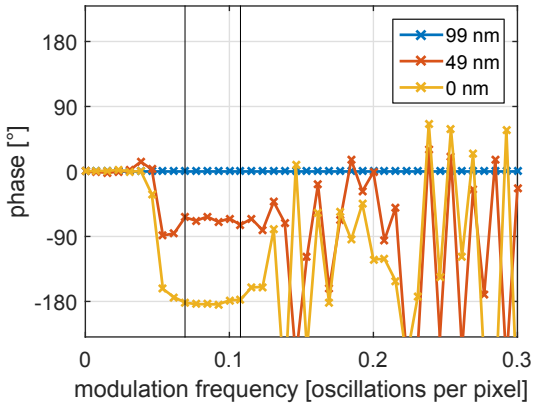


Figure A.22: The differences of the phases from Fig. A.21(b) are shown using the data for a displacement of 99 nm as a reference. The vertical black lines are drawn at identical modulation frequencies as in Fig. A.21 to guide the eye.

However, it is also evident that the phase changes are not perfectly linear. One reason for this are drifts of the relative phase between the three individual measurements. Another possibility is that this is due to the approximation that the wavelength of the spectrometer is linear in the pixel number. Nevertheless, it is obvious that the signal shown in Fig. A.21(b) can be used to stabilize the relative phase of the two laser pulses. To further illustrate this, Fig. A.23(a) shows the value of the phase that is extracted at a given modulation frequency on the side-band as a function of time.

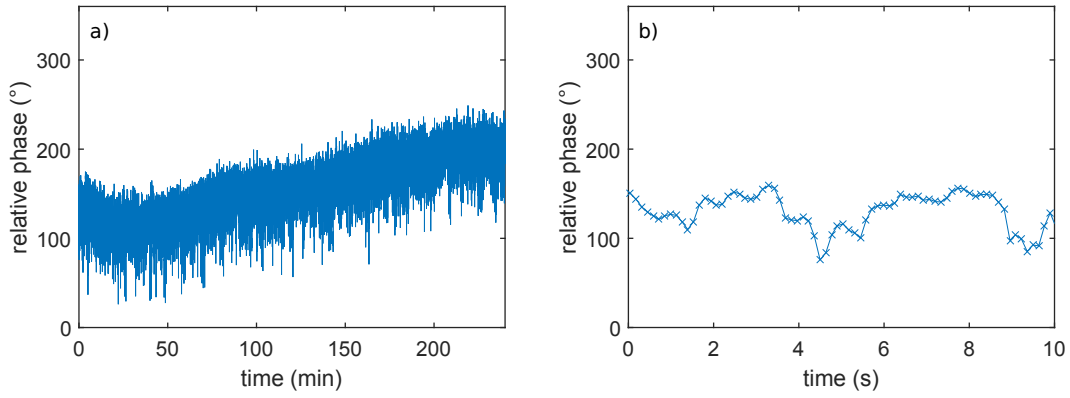


Figure A.23: (a) shows the drifts of the relative phase that are extracted from the modulations in the optical spectrum as a function of time. (b) shows a subset of (a) to illustrate that the phase drifts occur on long and short time scales.

Fig. A.23(b) shows a subset of Fig. A.23(a) to illustrate the phase drifts on short time scales. Fig. A.23 illustrates that the relative phase of the two laser pulses can be measured several times per second. Thus, the deviations from a desired phase can be calculated and this error signal can be used to move the nm-delay stage such that the relative phase is actively stabilized. This has been done about 16 times per second to actively stabilize the relative phase. Fig. A.24 shows the measured phases using this approach.

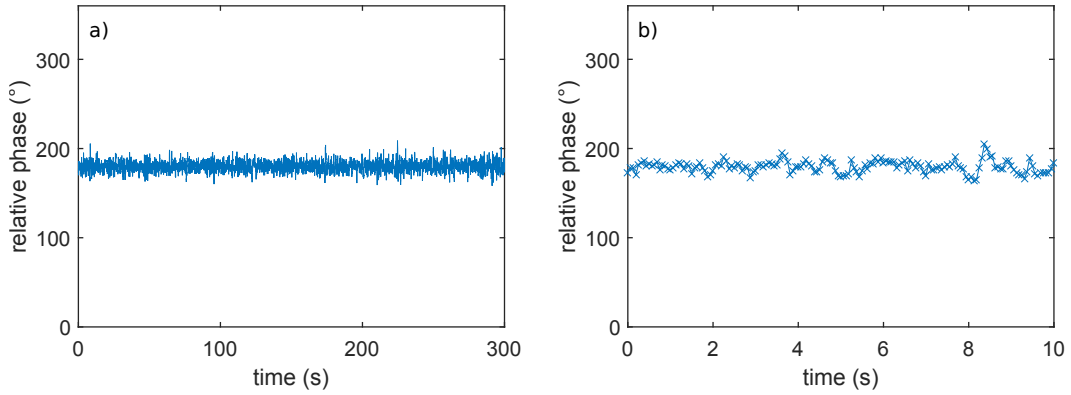


Figure A.24: a) shows the relative phase as a function of time while a computer program uses the nm-delay stage to actively stabilize the relative phase. (b) shows a subset of (a) to illustrate that the phase drifts occur on long and short time scales.

It is evident that the slow drifts of the relative phase are completely corrected for. Moreover, also the stability of the relative phase on short time scales (below 10 seconds) is improved.

For the proof of concept the polarization of the two laser pulses and their individual intensities were optimized to generate a very high modulation depth of the optical spectra. Is it possible to implement an active stabilization of the relative phase that can be used for a broad range of tailored intense light fields? The solution is presented in the next subchapter.

A.4.2. Active Stabilization: Implementation

The setup in chapter A.4.1 allows for the active stabilization of orthogonally polarized two-color fields if the intensity of the laser pulse at a central wavelength of 390 nm is weaker than the intensity at the laser pulse at a central wavelength of 780 nm. How to implement the active stabilization in a way that allows one to stabilize more than just a limited range of two-color fields? The scheme which is presented in Fig. A.25 shows a possible approach.

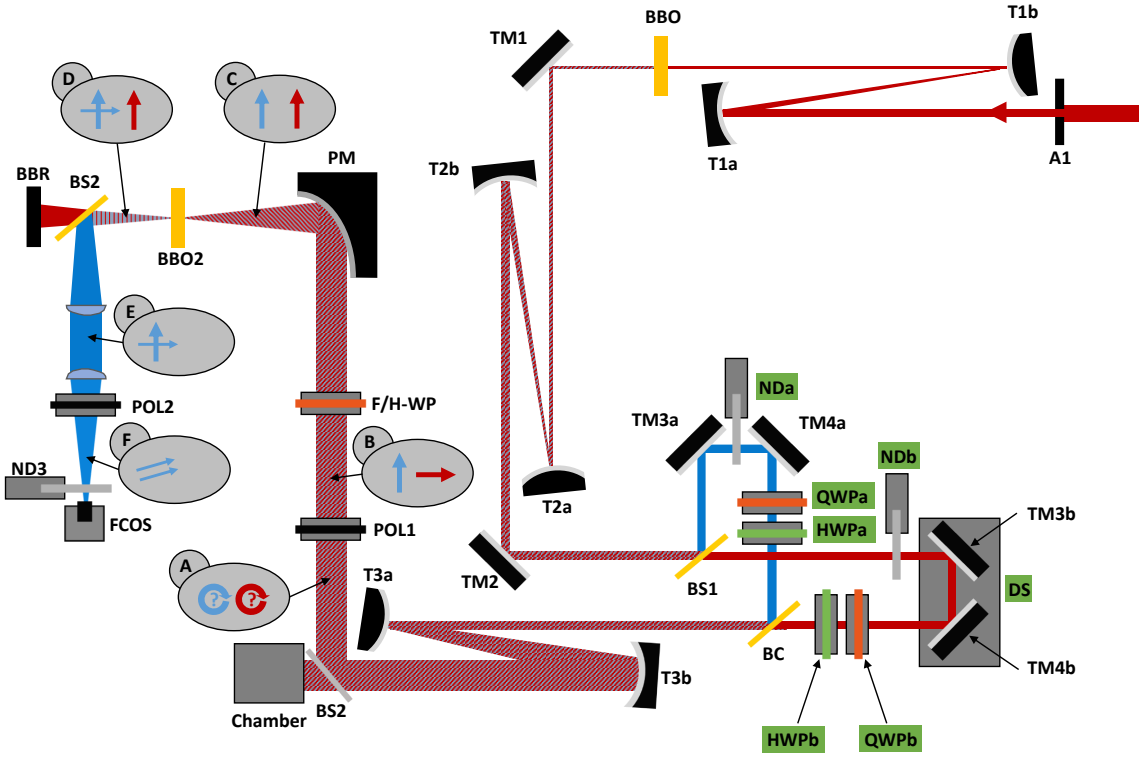


Figure A.25: The extended experimental setup is shown schematically. The extended setup allows for the measurement of momentum distributions using phase-locked tailored intense two-color laser pulses. The depicted setup is very similar to the one shown in Fig. A.19. Here the beam block behind the beam splitter "BS2" is removed. Additionally, two polarizers ("POL1" and "POL2") and a half wave plate for 780 nm that acts as a full wave plate for 390 nm ("F/H-WP") are inserted. The polarization states are indicated by the vertical and horizontal arrows in the gray shaded ellipses that are labeled with "A", "B", "C", "D", "E" and "F" (see text).

A polarizer[168] ("POL1" in Fig. A.25) is placed behind "BS2" that projects an arbitrary polarization state[169] (indicated by "A" in Fig. A.25) to a well-defined polarization state by projecting the field at 390 nm to its s-polarized state and the field at 780 nm to its p-polarized state. The well-defined polarization state is indicated in the gray shaded ellipse in "B" in Fig. A.25 and corresponds to an orthogonally polarized two-color field. Afterwards, a special wave plate ("F/H-WP" in Fig. A.25) is used that acts as a half wave plate for light at a

[168] The polarizer is the commercial product "UV 375 BC5" from CODIXX AG.

[169] A prerequisite is that the field at 390 nm must not be perfectly p-polarized and the field at 780 nm must not be perfectly p-polarized.

wavelength of 780 nm and as a full wave plate for light at a wavelength of 390 nm in order to rotate the polarization of the beam at 780 nm by 90°. The BBO generates a p-polarized beam at 390 nm from the incident light at 780 nm leading to two orthogonally polarized beams at 390 nm that are illustrated in "E". A second polarizer ("POL2" which is identical to "POL1") is used to project the two polarization states to a common polarization direction. This final step allows for the observation of interferences. The angle of the second polarizer ("POL2") can be tuned to vary the mixing ratio of the two polarization states shown in "E" in Fig. A.25. This allows one to optimize the modulation-depth of the optically measured spectrum in the fiber-coupled optical spectrometer.

To include the active stabilization seamlessly into the existing control scheme (see Fig. 4.11) the sub-thread that is usually controlling the nm-delay stage is modified. The modified control scheme is depicted in Fig. A.26.

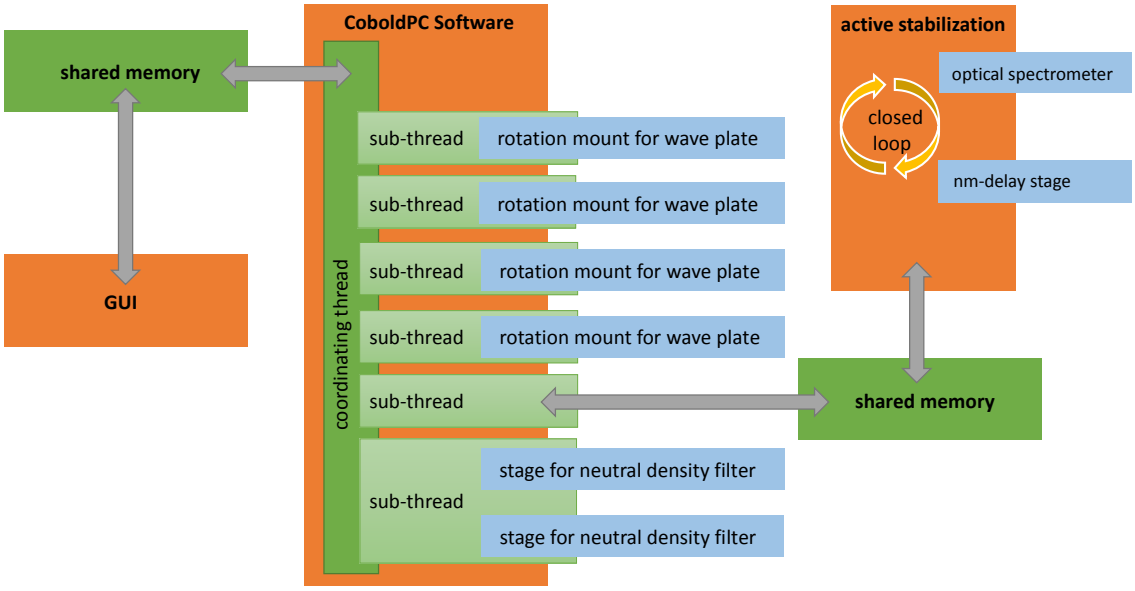


Figure A.26: The control scheme is an extension to Fig. 4.11. The sub-thread for the nm-delay stage is adapted and communicates with a third independent application that can adapt the position of the nm-delay stage after reading the measured optical spectra from the fiber-coupled optical spectrometer resulting in a closed-loop stabilization of the relative phase.

The nm-delay stage is not controlled directly by the sub-thread of the CoboldPC Software anymore. Instead, the sub-thread writes a set point for the relative phase to a second shared memory interface. A third application is used to actively stabilize the relative phase of the two laser pulses. The application realizes a closed-loop controller that adjusts the position for the nm-delay stage to minimize the deviations of the relative phase from the set point. The relative phase is calculated from the measured optical spectrum as described in chapter

A.4.1. Using the scheme shown in Fig. A.25 and Fig. A.26 it has been shown that the side-bands in the optical spectrum are sufficient to stabilize the relative phase for average powers of $I_{390} = 8\,\mathrm{mW}$ and $I_{780} = 70\,\mathrm{mW}$ in front of the vacuum chamber[170]. A momentum measurement has not yet been conducted while the fully implemented phase stabilization was running. However, it is expected that this scheme allows for the generation of phase-locked tailored intense two-color laser pulse.

Finally, it should be noted that the demonstrated method stabilizes the relative phase at the second BBO ("BBO2" in Fig. A.25). Any changes that occur between "BC" and the interaction region inside the vacuum chamber or between "BC" and "BBO2" are not accounted for. However, those changes are expected to be very small because both single-color laser pulses propagate co-linearly after the beam combiner ("BC"). Moreover, here it is assumed that the retrieved phase is not subject to any systematic errors. An outstanding task is to show that the optically measured phase and the phase in the interaction region in the vacuum chamber are phase-locked with respect to each other[171].

[170] This range could probably be extended towards higher ratios of I_{390}/I_{780} using a high reflector for light at wavelengths around 390 nm that is transparent for light at wavelengths around 780 nm. The high reflector could be placed in front of "POL1".

[171] A preliminary measurement, using the COLTRIMS reaction microscope and the active stabilization of the relative phase simultaneously, has already been done. For this measurement, the setup from Fig. A.19 was modified by placing a high reflector ("DMLP567" from Thorlabs GmbH) for 390 nm and an α-BBO (to compensate the dispersion of the high reflector) in front of the parabolic mirror. The electron momentum distribution upon the ionization by a two-color field (the field geometry was very close to a circularly polarized two-color field) showed no obvious time-dependent rotation of the electron momentum distribution in a measurement with a duration of 15 hours.

A.5. Appendix for Non-Sequential Double Ionization

This part of the appendix provides details and supplementary information for chapter 6.

A.5.1. Absolute Yield of Ar^{2+} and Ar^{1+}

The absolute yield of Ar^{2+} and Ar^{1+} in chapter 6 is difficult to determine for several reasons. One reason is that the probability to detect an electron, ion or doubly charged ion depends on the trigger method. Triggering on electrons overestimates the ratio of double to single ionization. This is because if a doubly charged ion is produced two electrons are available. (The probability to detect one electron out of one is lower than detecting at least one electron out of two.)

Table A.1: Comparison of different trigger methods. The measurement for which the signal from the photo diode was used as trigger was done directly after the measurement for which the signal of the electron detector was used as trigger. Both measurements accumulated data for about 2 minutes. The Ar^{1+} were determined using a gate on the ion time-of-flight. The Ar^{2+} were gated on the time-of-flight and the position on the ion detector.

trigger method	Ar^{1+} (counts)	Ar^{2+} (counts)	Ratio Ar^{2+}/Ar^{1+}
signal of MCP (electron detector)	16096	358	0.022
signal of the photo diode	26563	469	0.018

The data shown in Fig. 6.6 was obtained by triggering the data acquisition on having detected at least one electron while Fig. 6.7 was taken triggering on each and every single laser shot (trigger on photo diode). For Fig. 6.11 different triggering methods were used to be able to perform cross checks. It was found that the obtained results do not depend on the trigger-method. To improve statistics all measurements were combined. Table A.1 shows the ratio of double to single ionization Ar^{2+}/Ar^{1+} for identical laser parameters (close to the parameters used for Fig. 6.7). This allows one to quantify that the ratio Ar^{2+}/Ar^{1+} is overestimated by a factor of 1.26 if the signal of the MCP on the electron side of the spectrometer is used as trigger. Since this is a systematic error and in Fig. 6.6 the signal of the MCP on the electron side of the spectrometer was used as a trigger this error was corrected[172] for by scaling the results in 6.6(a).

Another reason is that the MCP efficiency depends on the position on the MCP. For typical spectrometer setting the spot sizes of argon on the MCPs is only about 0.3 mm in diameter. The efficiency of the MCP reduces with time and inefficient spots (“holes”) emerge. To investigate this effect quantitatively several measurements were performed. During all those measurements all parameters remained untouched but the impact position of the ions was

[172] Fig. 6.6(a) shows the corrected values.

moved across the detector. Calculating the ratio of detected ions relative to the number of detected electrons the local efficiency for Ar^{2+} and for Ar^{1+} was quantified. The results for Ar^{1+} and Ar^{2+} are then normalized individually to a maximum value of one. The result is shown in Fig. A.27.

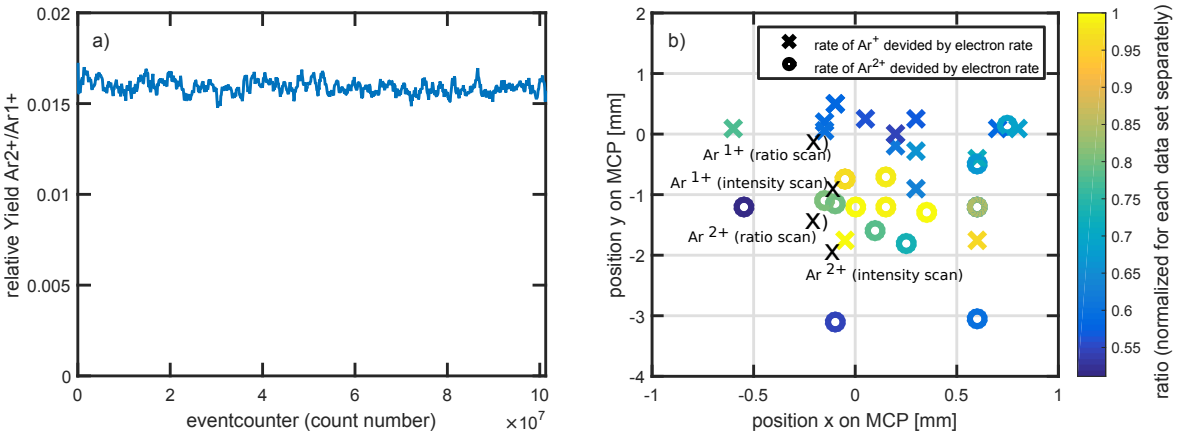


Figure A.27: (a) Shows the ratio of detected doubly charged ions divided by the ratio of detected singly charged ions (Ar^{2+}/Ar^{1+}) as a function of the eventcounter for a measurement with a duration of 18 hours. (The eventcounter is in a good approximation linear to time since during the measurement there was a constant rate of about 1500 Hz on the electron detector. The electron detector was used as trigger (see chapter 4.1.3).) (b) MCP detection efficiency as a function of position on the detector (x points along the direction of laser propagation and y points along the jet-direction). The maximum ratio in (b) prior to normalization for Ar^{1+} (Ar^{2+}) is 0.3 ($6.9 \cdot 10^{-4}$). (The content of panels (a) and (b) has been part of the answer to the referees regarding the publication Eckart et al. [23]. Labels and layout have been adapted.)

Fig. A.27(a) nicely illustrates that the relative yield Ar^{2+}/Ar^{1+} is stable as a function of time for a typical duration of a measurement[173]. Fig. A.27(b) shows the detection efficiency as a function of the position on the MCP (the x-direction points along the laser propagation direction and the y-direction points along the direction of the gas jet). Depending on the position on the MCP the detection efficiency varies by a factor of approximately two. However, it should be noted that the data for Fig. A.27 was taken after the measurement for the data that led to Ref. [23] and chapter 6 and cannot be used to estimate the absolute detection efficiency for the other projects that are presented in this thesis. All other projects were conducted after the project that led to chapter 6. In general, it is expected that the detection efficiency slightly decreases with every detected event.

[173] The results shown in Fig. 6.11 are based on the same measurement. 18 hours of the measurement are shown. The average power was measured before (17.8 mW for the fundamental 46.7 mW for the second harmonic) and after (17.3 mW for the fundamental 44.8 mW for the second harmonic) this period.

A.5.2. False Electron-Ion Coincidences and Momentum Conservation

In chapter 6, some measured electron momentum distribution for the single ionization of argon are corrected for false electron-ion coincidences (see e.g. Fig. 6.9(a) and Fig. 6.9(b)). A false electron-ion coincidence is an event where an electron has been detected that does not belong to the detected ion. The false[174] electron can stem from ionization of another argon atom in the same laser shot or from the ionization of residual gas.

To quantify false electron-ion coincidences the momentum conservation for the single ionization of argon in the time-of-flight direction is used as a benchmark in Fig. A.28. The histogram shows two diagonal lines. Ideally a single, very sharp diagonal line would be seen and its width would be related to the momentum resolution. However, a double hump structure is seen which indicates a problem resolving the momentum of the ions or the electrons.

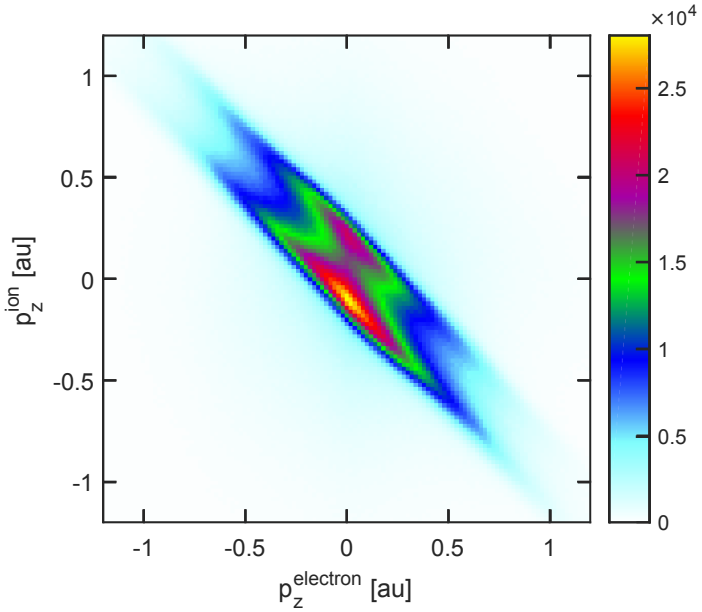


Figure A.28: Based on the same data set as Fig. 6.11. The width of the observed diagonal line is related to the momentum resolution. The double line in vertical direction with a spacing of about 0.3 au corresponds to a time-of-flight difference of about 4 ns. This corresponds to a displacement of 80 µm of the interaction region in the spectrometer. This experimental shortcoming was only relevant for the experiment described in chapter 6. (Fig. 9.13 shows a measurement without this problem.)

At the time of the measurement the origin of this double line was not understood. It took several weeks to understand that the double line vanishes if a vacuum pump was slightly displaced. Afterwards, the pump could not transfer vibrations to the main chamber anymore. From this observation we concluded that the origin of the double line is due to the vibrations

[174] Of course, the electron is a real electron but is called "false" electron here for brevity. "False" electrons are electrons that stem from another ion than the one which has been detected as the first hit on the ion detector.

of the mirror that is mounted inside the vacuum chamber. Due to the vibrating mirror the interaction region of the laser focus and the gas target moved sinusoidally in the time-of-flight direction. A projection of a sinusoidal movement appears like a double hump structure. The spacing of the double hump structure of about 0.3 au is equivalent to a time-of-flight difference of about 4 ns which corresponds to an amplitude of about 80 µm in the time-of-flight direction of the sinusoidal movement. Anyway, momentum conservation can be used to infer the contribution of false electron-ion coincidences. To achieve this the sum of the ion and electron momentum are plotted (see Fig. A.29).

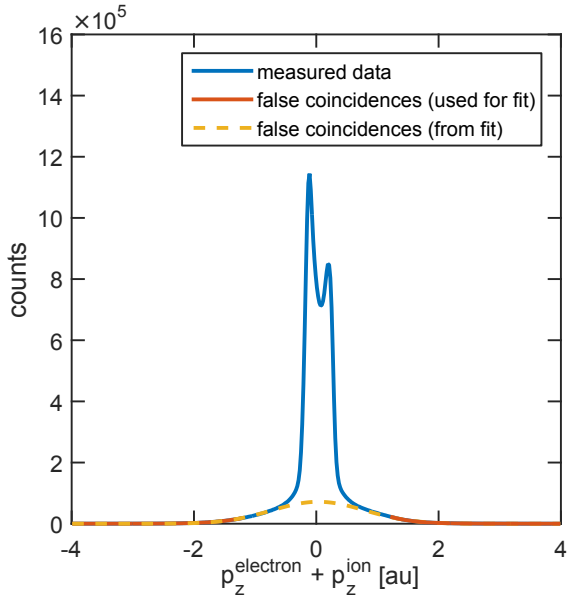


Figure A.29: The data shown as a blue line is based on the same data set as Fig. A.28. The momentum-mismatch $p_z^{\text{electron}} + p_z^{\text{ion}}$ is depicted. The region $|p_z^{\text{electron}} + p_z^{\text{ion}}| > 1.2$ a.u. is assumed to be due to false coincidences only (red line). A Gaussian fit to the data fulfilling $|p_z^{\text{electron}} + p_z^{\text{ion}}| > 1.2$ a.u. results in the dashed yellow line. The integral of the data belonging to the dashed yellow line (false coincidences) is divided by the integral of the blue line (measured data) and the result is found to be 25%. Thus the contribution of false electron-ion coincidences is quantified to be 25%.

Ideally this sum is a very sharp peak at a sum momentum of zero due to momentum conservation. In the present case the sharp peak is a double hump structure that is caused by vibrations of the focusing mirror inside the vacuum chamber. However, two contributions can be distinguished. There is a broad distribution and the sharp double hump structure. The broad (Gaussian-like) distribution is due to the false electron-ion coincidences and is used to fit a Gaussian distribution (see Fig. A.29). The integral of the Gaussian fit (dashed yellow curve) is divided by the integral of all electrons recorded in coincidence with singly charged ions (blue curve). The resulting ratio is $\frac{1}{4}$. This means that the contribution of false electron-ion coincidences for the single ionization of argon is 25%.

How can this insight be used to estimate the contribution of false electron-ion coincidences for double ionization? To this end Tab. A.2 shows the conditional probability for the existence of "good" electrons and "false" electrons[175] for double and single ionization. In the case of single ionization there is always exactly one "good" electron available and in the case of double ionization there are always two "good" electrons available. It is assumed that the existence probability for a "false" electron is independent of the detected ion ($P(\mathrm{e}^-_{\mathrm{false}}|\mathrm{Ar}^{1+}) = P(\mathrm{e}^-_{\mathrm{false}}|\mathrm{Ar}^{2+}) = x$) and only the first detected electron is considered. Building on the situation described by Tab. A.2 the probability to detect the "false" electron can be expressed as shown in Tab. A.3.

Table A.2

has been detected	electron existence probabilities		
Ar^{1+}	$P(1^{\mathrm{st}}\mathrm{e}^-_{\mathrm{good}}\|\mathrm{Ar}^{1+}) = 1$	$P(2^{\mathrm{nd}}\mathrm{e}^-_{\mathrm{good}}\|\mathrm{Ar}^{1+}) = 0$	$P(\mathrm{e}^-_{\mathrm{false}}\|\mathrm{Ar}^{1+}) = x$
Ar^{2+}	$P(1^{\mathrm{st}}\mathrm{e}^-_{\mathrm{good}}\|\mathrm{Ar}^{2+}) = 1$	$P(2^{\mathrm{nd}}\mathrm{e}^-_{\mathrm{good}}\|\mathrm{Ar}^{2+}) = 1$	$P(\mathrm{e}^-_{\mathrm{false}}\|\mathrm{Ar}^{2+}) = x$

Table A.3

has been detected	probability for a false electron-ion coincidence
Ar^{1+}	$P(\text{"false coincidence"}\|\mathrm{Ar}^{1+}) = \frac{P(\mathrm{e}^-_{\mathrm{false}}\|\mathrm{Ar}^{1+})}{P(1^{\mathrm{st}}\mathrm{e}^-_{\mathrm{good}}\|\mathrm{Ar}^{1+})+P(\mathrm{e}^-_{\mathrm{false}}\|\mathrm{Ar}^{1+})} = \frac{x}{1+x}$
Ar^{2+}	$P(\text{"false coincidence"}\|\mathrm{Ar}^{2+}) = \frac{P(\mathrm{e}^-_{\mathrm{false}}\|\mathrm{Ar}^{2+})}{P(1^{\mathrm{st}}\mathrm{e}^-_{\mathrm{good}}\|\mathrm{Ar}^{2+})+P(2^{\mathrm{nd}}\mathrm{e}^-_{\mathrm{good}}\|\mathrm{Ar}^{2+})+P(\mathrm{e}^-_{\mathrm{false}}\|\mathrm{Ar}^{2+})} = \frac{x}{2+x}$

From the analysis of Fig. A.29 it is known that $P(\text{"false coincidence"}|\mathrm{Ar}^{1+}) = \frac{1}{4}$. Using the relations presented in Tab. A.2 and A.3 the relation $P(\text{"false coincidence"}|\mathrm{Ar}^{1+}) = \frac{x}{1+x}$ allows one to determine $x = \frac{1}{3}$. This can be used to calculate the value of the variable $P(\text{"false coincidence"}|\mathrm{Ar}^{2+}) = \frac{x}{2+x} = \frac{1}{7}$. The fact the contribution of false electron-ion coincidences for double ionization is smaller than for single ionization is not surprising. For double ionization there are two "good" electrons which stem from the same doubly charged ion.

The values $P(\text{"false coincidence"}|\mathrm{Ar}^{1+})$ and $P(\text{"false coincidence"}|\mathrm{Ar}^{2+})$ allow for the correction of the measured electron momentum distribution by the false electron-ion coincidence assuming that the electron momentum distribution without condition on the ion has the same shape as the electron momentum distribution that is due to false electron-ion

[175] "Good" electrons and "false" electrons are all real electron. An electron is called "false" if it stems from another ion than the one which has been detected as the first hit on the ion detector. If an electron is not a "false" electron it is called a "good" electron.

coincidence. For the measurement regarding Fig. 6.8 this implies that the electron momentum distribution shown in Fig. 6.8(b) can be used to correct for the false electron-ion coincidences starting with the uncorrected data shown in Fig. 6.8(c) and Fig. 6.8(d).

To this end the distribution shown in Fig. 6.8(c) is normalized to an integral of 1 and the distribution shown in Fig. 6.8(b) is normalized to an integral of $P(\text{“false coincidence”}|\text{Ar}^{1+}) = 0.25$. The second distribution is subtracted from the first. The result is shown in Fig. A.30(a). The same procedure is done for the case of double ionization using the data from Fig. 6.8(d) and $P(\text{“false coincidence”}|\text{Ar}^{1+}) = 0.14$. The result is shown in Fig. A.30(b).

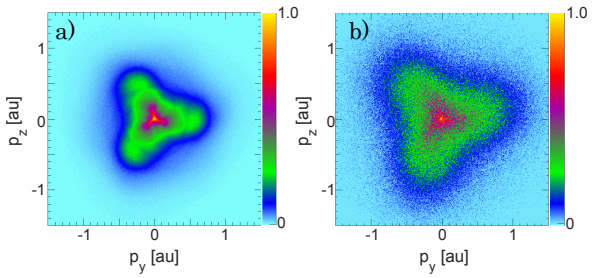


Figure A.30: (a) [(b)] is based on the same data as Fig. 6.8(c) [Fig. 6.8(d)] but the data in (a) [(b)] has been corrected for false electron-ion coincidences and normalized afterwards. Hence, (a) and (b) are the same as Fig. 6.9(a) and Fig. 6.9(b). The definition of the laser electric field is given in Fig. 6.8(a).

Fig. A.30(a) and Fig. A.30(b) show the normalized electron momentum distribution for the single and double ionization of argon. Fig. A.30(a) and Fig. A.30(b) are the same as Fig. 6.9(a) and Fig. 6.9(b). The corresponding definition of the laser electric field can be found in Fig. 6.8(a).

A.5.3. Tomographic Reconstruction - Validating the Method

The procedure to tomographically reconstruct[176] the undetected electron, which is used in chapter 6, will be demonstrated using the single ionization of argon. In this case for every event the electron is restricted to a region in final momentum space after the offline compensation of the relative phase has already been performed (see chapter A.2). The remaining electron momentum distribution is shown in Fig. A.31(a).

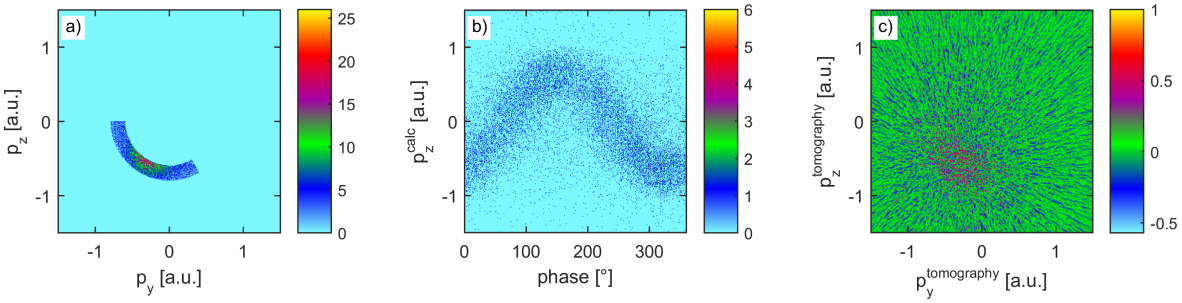


Figure A.31: (a) shows a subset of Fig. 6.8(c) taking only 1% of the events from Fig. 6.8 and restricting the momentum to a given region in momentum space. (b) shows $p_z^{calc} = -p_z^{ion}$ in dependence of the relative phase of the two single-color laser pulses. (c) shows the tomographic reconstructed electron momentum distribution based on the projection data shown in (b).

The momentum in time-of-flight direction p_z^{ion} of the argon ion can be used to calculate the momentum of the undetected electron in that direction using momentum conservation:

$$p_z^{calc} = -p_z^{ion} \tag{60}$$

The calculated momentum p_z^{calc} is plotted for all phases in Fig. A.31(b). The phases in Fig. A.31(b) are the relative phases of the two single-color laser pulses and equivalent to a rotation of the electron momentum distribution in the laboratory system[177]. The distribution in Fig. A.31(c) is obtained by performing an inverse radon transformation[178] of the sinogram shown in Fig. A.31(b) using a value for the low-pass filter of 1 with means that the low-pass filter is not filtering anything. In Fig. A.31(c) the reconstructed momentum distribution is very noisy and shows negative intensities as an artifact of the reconstruction.

[176] An important prerequisite is that the zero point of the ion momentum has to be well calibrated. The calibration of the zero point in momentum space can be checked by plotting the ion momentum in time-of-flight direction of the singly charged ions in a one dimensional histogram and fitting a gaussian distribution to it. The mean of the gaussian distribution should be zero. This check should be performed for singly charged and double charged argon ions separately.

[177] This is the same phase that was used for the offline compensation of the relative phase (see chapter A.2) in order to obtain the electron momentum distribution shown in Fig. A.31(a).

[178] The matlab-function iradon is used with linear interpolation and for the filtered backprojection the Ram-Lak filter is multiplied with a Hamming window. The filter is applied in Fourier space. The Ram-Lak filter ensures that the high frequency components are not underestimated due to the geometry of the projection data. The Hamming window removes high frequency components that are sensitive to noise.

Fig. A.32 shows the same as Fig. A.31 but uses a value for the low-pass filter of 0.09. The result in Fig. A.32(c) looks similar to the distribution in Fig. A.32(a).

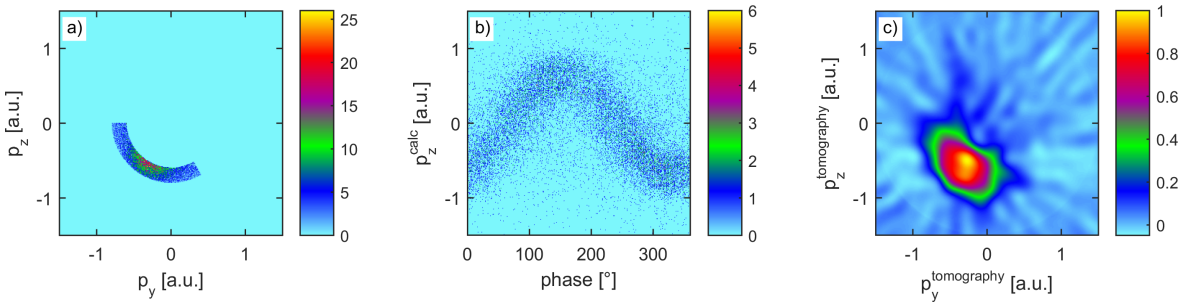


Figure A.32: (a) and (b) are the same as in Fig. A.31(a) and Fig. A.31(b). (c) shows the tomographic reconstructed electron momentum distribution. In contrast to Fig. A.31 a low-pass filter of 0.09 is used for the tomographic reconstruction.

The result of the reconstruction can be further improved by using all the available information. The sum momentum of electron and ion are not a sharp peak (see Fig. A.29). Therefore, every column in Fig. A.32(b) is deconvolved[179] with the distribution shown in Fig. A.29. The result is shown in Fig. A.33(b).

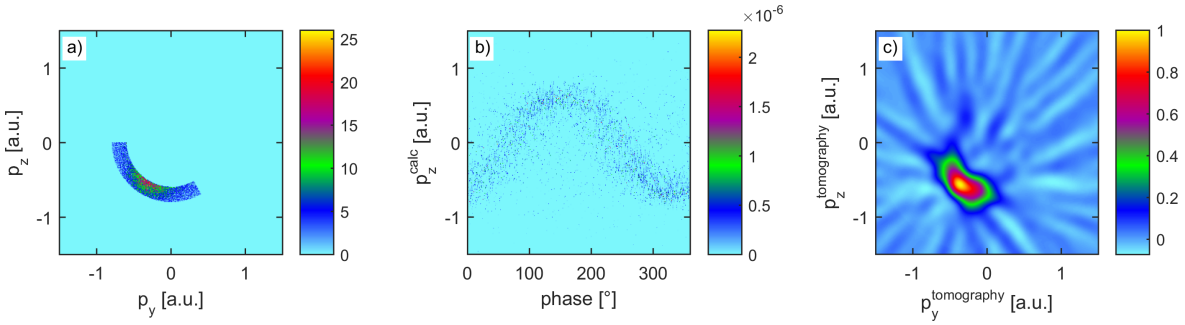


Figure A.33: Shows the same as Fig. A.32 but using a deconvolution algorithm making use of the known double hump stucture (see Fig. A.29). The sinogram in (b) is already deconvolved. The tomographically reconstructed electron momentum distribution in (c) is very similar to (a) validating the method.

The tomographically reconstructed distribution Fig. A.33(c), which is based on the ion momentum in time-of-flight direction and the knowledge about the relative phase of the two single-color laser pulses, reaches good agreement with the directly detected electrons (see Fig. A.33(a)).

[179] For the deconvolution the matlab-function deconvlucy is used with 100 iterations.

A.5.4. Tomographically Reconstructed Second Electron - Details

In order to test the validity of the tomographically reconstructed electron momentum distribution shown in Fig. 6.11(d) a cross check has been performed which is explained in the following. For Fig. 6.11(d) the three fold symmetry was used to increase statistics. Alternatively the three fold symmetry can be used as a cross check. For Fig. A.34, Fig. A.35 and Fig. A.36 a different lobe of the measured electron momentum distribution is used for the tomographic reconstruction of the undetected electron.

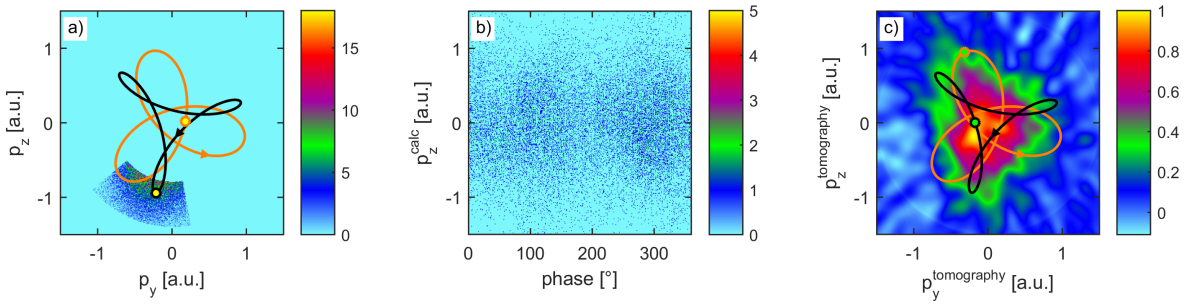


Figure A.34: (a) shows the data from Fig. 6.11(b) after restricting the electron momentum distribution to the given region in momentum space (without combing all three lobes to increase statistics (see chapter 6.5.2)). (b) shows $p_z^{calc} = -p_z^{ion} - p_z^{electron}$ in dependence of the phase as in chapter A.5.3. (c) shows the tomographic reconstructed electron momentum distribution based on the projection data shown in (b). A low-pass filter of 0.09 is used for the tomographic reconstruction but no deconvolution is used. The yellow dots indicate the assumed recollision phase and the green dot indicates the ionization phase of the second electron that is liberated from argon.

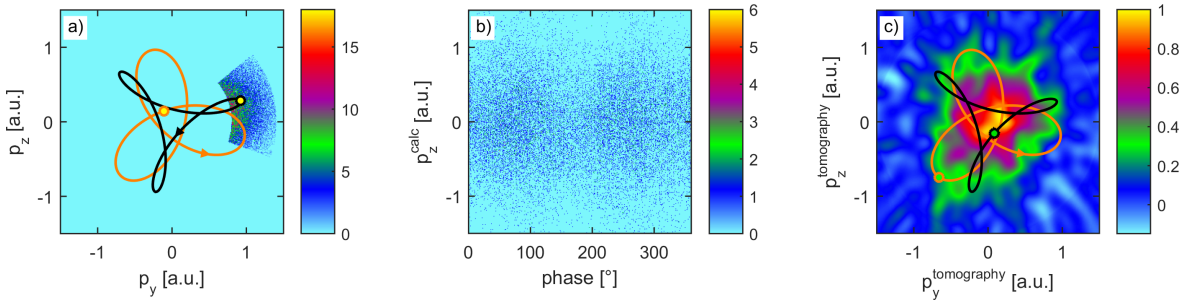


Figure A.35: The same as Fig. A.34 but using a different region in momentum space (see panel (a)).

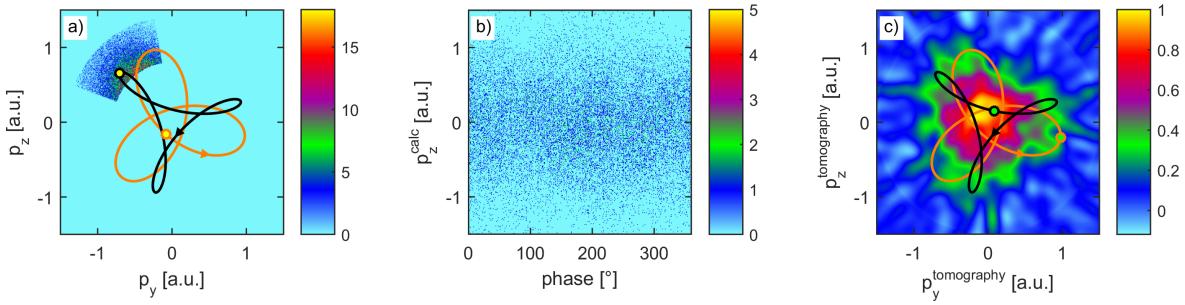


Figure A.36: The same as Fig. A.34 and A.35 but using a different region in momentum space (see panel (a)).

In all three cases a low-pass filter (parameter 0.09) was used. The deconvolution that is described in chapter A.5.3 is not used. It can be seen that the brightest region in the tomographically reconstructed momentum distribution moves as expected and coincides with the phase of the vector potential that is marked with a green dot in Fig. A.34, Fig. A.35 and Fig. A.36 indicating the ionization phase of the second electron. Making use of the symmetry the distributions in Fig. A.35 and Fig. A.36 can be rotated by 240°and 120°, respectively, and both rotated distributions are added to Fig. A.34. The result is shown in Fig. A.37.

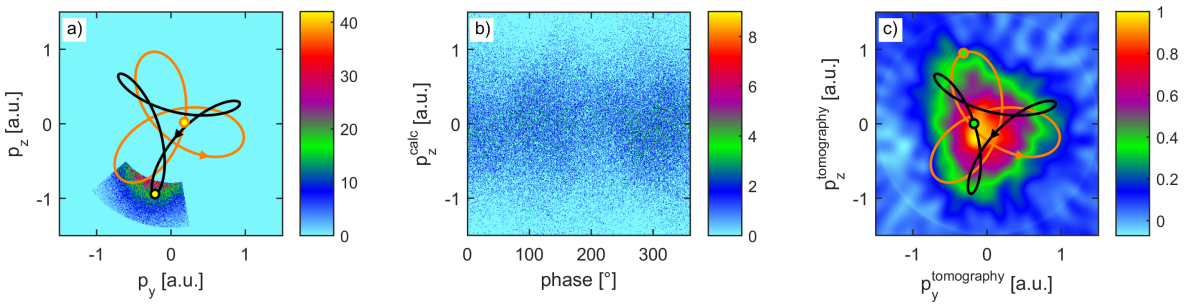


Figure A.37: Conceptually the same as Fig. A.34, Fig. A.35, Fig. A.36 but the symmetry of those three figures is used and the results are combined to increase statistics.

To illustrate the effect of the used devonvolution one can compare Fig. A.37 with Fig. A.38. The only difference of those two figures is that for Fig. A.38 the data used for the tomographic reconstruction has been devonvolved. Fig. A.37(b) [Fig. A.38(b)] shows the data before [after] the devonvolution which has been done as explained for Fig. A.33. The tomographically reconstructed result shown in Fig. A.38(c) appears to have a better resolution.

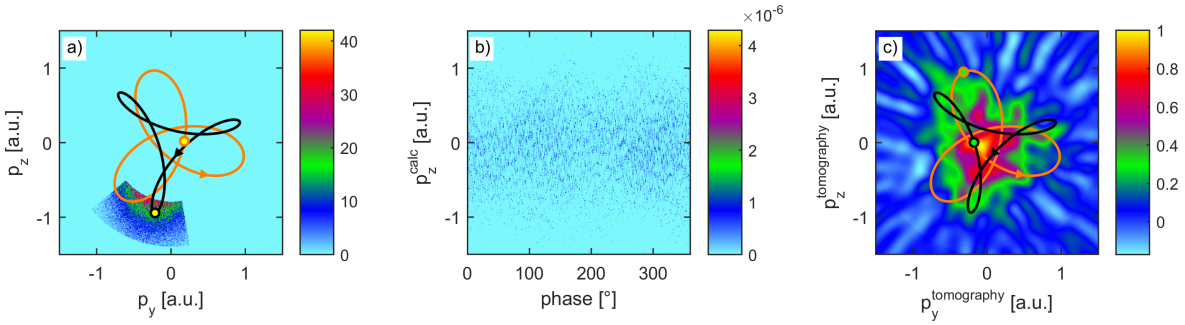


Figure A.38: The same as Fig. A.37 but the sinogram in (b) has been deconvolved as explained for Fig. A.33 which provides a higher resolution compared to Fig. A.37.

Moreover, in some cases two electrons are detected in coincidence with the doubly charged argon ion. Usually, in those cases only the first detected electron is used. However, the second electron can also be used handling one event with two detected electrons as two events where one time the first electron is used and one time the second electron is used. Using this approach Fig. A.39 is generated in analogy to the previous figures. Almost no

change is observed for the tomographically reconstructed result.

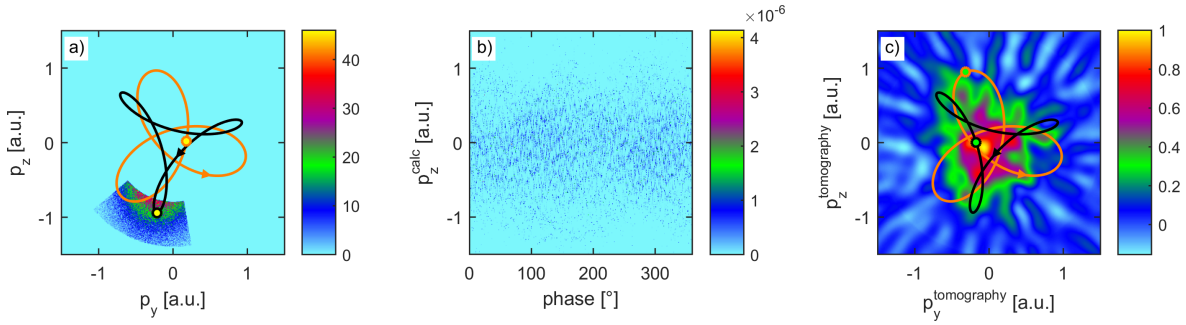


Figure A.39: The same as Fig. A.38 but taking into account the second detected electron, if present. This result is identical to the result shown in Fig. 6.11(d).

The tomographic reconstruction is sensitive to noise. Therefore, in the analysis only events are used where all used particles have a reconstruction method smaller 15 which indicates the quality of the detected signals on the delay-line anode on the single particle level which has nothing to do with the tomographic reconstruction itself but might lead to more noise regarding the underlying data. Details are described in Ref. [54] on page 110 and onwards. For comparison Fig. A.40 shows the same as Fig. A.38 without restricting the detector-method to values smaller than 15. The deviations comparing Fig. A.38 and Fig. A.40 are small and the total number of events changes only by about 20%.

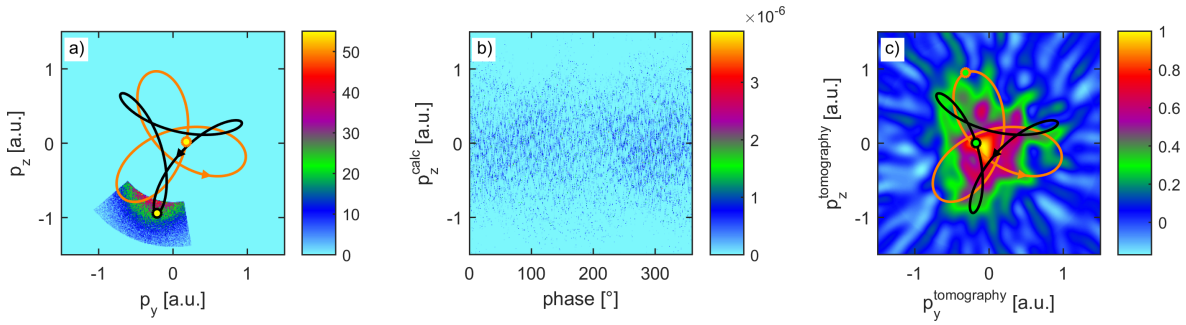


Figure A.40: The same as Fig. A.38 but without an additional condition on the quality of the detected signals on the delay-line anode.

A.6. Supplementary 2D Maps of the Electron's Angle in Momentum Space

Following the procedure described in chapter 7.7.1 more "phase maps" are generated using the available data. The results are shown without conclusion.

Fig. A.41 shows the "phase map" for the data which is presented in Fig. 7.2(a).

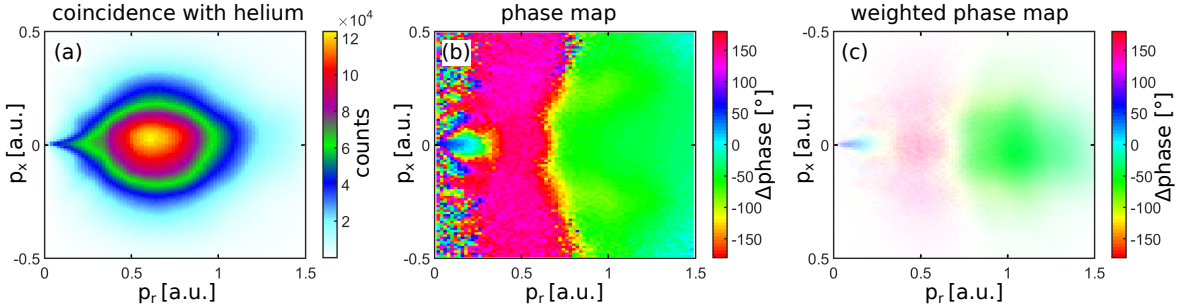


Figure A.41: (a) shows the intensity after projecting out the angle in the plane of polarization for the data from Fig. 7.2(a). (b) and (c) show the corresponding "phase map" (see chapter 7.7.1 for details).

Furthermore, in Fig. A.42 the same "phase map" using two different restrictions on the range of the differences (Δphases) are shown. The color map in Fig. A.42(a) is restricted in order to allow to investigate high energy electrons and in Fig. A.42(b) the emission angle in the plane of polarization of electrons with $p_r \approx 0.5$ a.u. can be examined.

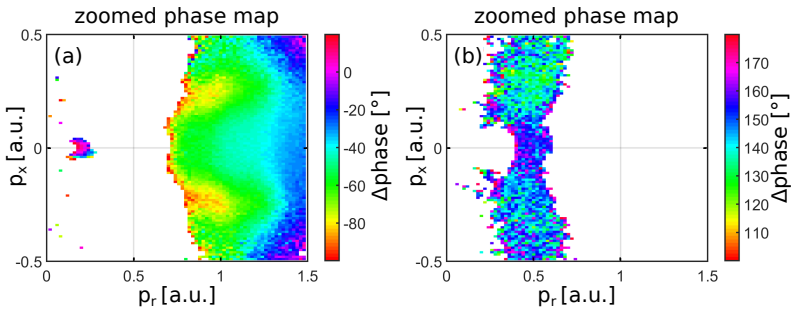


Figure A.42: (a) and (b) show two differently zoomed "phase maps" representing the same data as Fig. A.41(b).

Fig. A.43 shows the same as Fig. A.41 but for the ionization of neon. Fig. A.43 is based on the same data set as Fig. 7.13(a).

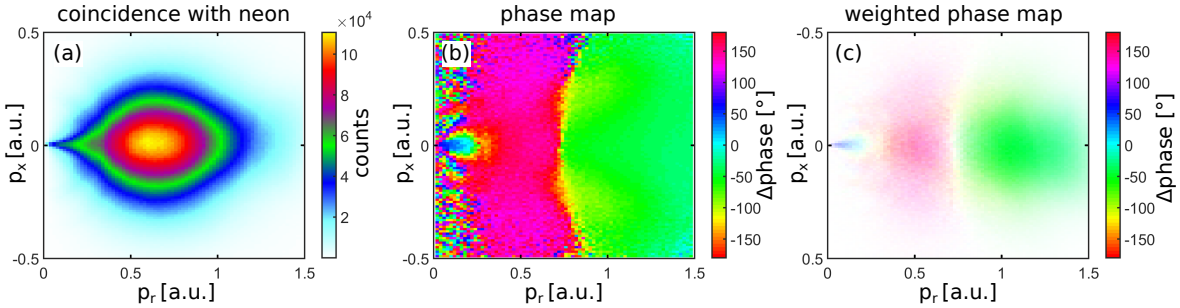


Figure A.43: a) shows the intensity after projecting out the angle in the plane of polarization for the data from Fig. 7.13(a). (b) and (c) show the corresponding "phase map" (see chapter 7.7.1 for details).

In Fig. A.44 the differences in the phase maps of Fig. A.41 and Fig. A.43 are depicted. The differences are most prominent at about $p_r \approx 0.7$ a.u.

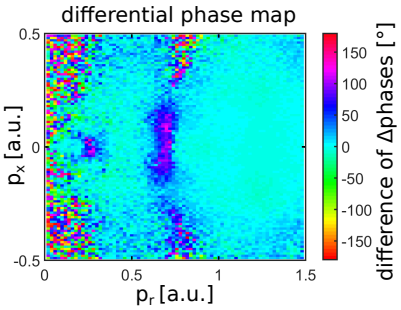


Figure A.44: The difference of the phases from Fig. A.41(b) and Fig. A.43(b) are shown. Differences of about $\pm 120°$ are evident for $p_r \approx 0.7$ a.u.

The "phase map"-approach can also be applied to the data from the single ionization of argon (see Fig. 6.11(a)) resulting in the "phase map" shown in Fig. A.45.

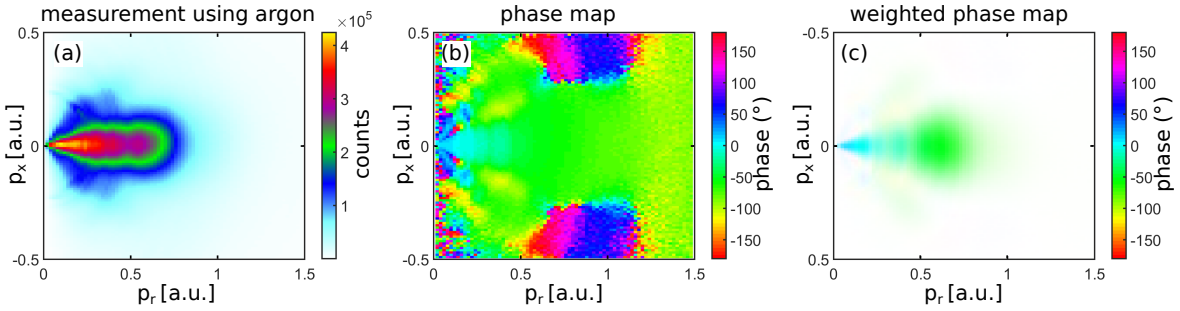


Figure A.45: The data that is shown is based on the measurement that belongs to Fig. 6.11. (a) shows the intensity after projecting out the angle in the plane of polarization. The data was measured using argon but without condition on the ion. Considering only electrons that are detected in coincidence with argon does not change the result and only reduces statistics. (b) and (c) show the corresponding "phase map" (see chapter 7.7.1 for details).

There is a highly speculative interpretation of the results shown in Fig. A.45(b) that should be considered with care: The blue area at small values of p_r are direct electrons that only weakly interact with their ionic core. The green area belongs to elastically scattered electrons. The

yellow stripes are interference of elastically scattered and direct electrons. The purple and dark blue areas for large values of $|p_x|$ are due to inelastic recollisions or related interference because for argon inelastic recollisions are possible (in contrast to helium, see chapter 6). This feature is not observed in Fig. 7.21 for a similar combined electric field.

A.7. Uncertainty of the Experimentally Determined Two-Color Ratio

The two-color field ratio is defined by

$$R_{\text{twocolor}} = \frac{E_{390\,\text{nm}}}{E_{780\,\text{nm}}} = \left(\frac{I_{390\,\text{nm}}}{I_{780\,\text{nm}}}\right)^{0.5} \tag{61}$$

where $E_{390\,\text{nm}}$ [$E_{780\,\text{nm}}$] is the electric field amplitude of the single-color laser pulse at a central wavelength of 390 nm [780 nm]. $I_{390\,\text{nm}}$ and $I_{780\,\text{nm}}$ are the corresponding intensities with the absolute uncertainties $\Delta I_{780\,\text{nm}} = 0.1 \cdot I_{780\,\text{nm}}$ and $\Delta I_{390\,\text{nm}} = 0.2 \cdot I_{390\,\text{nm}}$ (see chapter 4.1.5 for details). This allows for the calculation of the absolute uncertainty of the two-color field ratio:

$$\begin{aligned}
\Delta R_{\text{twocolor}} &= 0.5 \cdot \left(\frac{I_{390\,\text{nm}}}{I_{780\,\text{nm}}}\right)^{-0.5} \cdot \sqrt{\left(\frac{\Delta I_{390\,\text{nm}}}{I_{780\,\text{nm}}}\right)^2 + \left(\frac{\Delta I_{780\,\text{nm}} \cdot I_{390\,\text{nm}}}{I_{780\,\text{nm}}^2}\right)^2} \\
&= \frac{1}{2R_{\text{twocolor}}} \cdot \sqrt{\left(\frac{0.2 \cdot I_{390\,\text{nm}}}{I_{780\,\text{nm}}}\right)^2 + \left(\frac{0.1 \cdot I_{390\,\text{nm}}}{I_{780\,\text{nm}}}\right)^2} \\
&= \frac{R_{\text{twocolor}}}{2} \cdot \sqrt{0.2^2 + 0.1^2} \\
&\approx 0.11 \cdot R_{\text{twocolor}}
\end{aligned} \tag{62}$$

This shows that the relative uncertainty of R_{twocolor} is approximately 11% which is relevant in chapter 6.4.

A.8. The Effective Angular Frequency in Circularly Polarized Two-Color Fields

In two-color circularly polarized fields the instantaneous effective angular velocity is of interest because it is relevant for the non-adiabaticity of tunneling. The analytical result[180] for the effective angular velocity at the field maxima in CRTC fields and the field minimum in CoRTC fields has been derived before by an anonymous referee regarding the project presented in chapter 8. The absolute magnitude of the field does not matter for the discussion of the effective angular velocity. For simplicity the magnitude of the low frequency field (ω, with $\omega > 0$ a.u.) is set to 1. The unit of the electric field is neglected in this chapter. The magnitude of the high frequency field (2ω) is defined by η. In this thesis the fundamental wavelength is 780 nm and the second harmonic is 390 nm and their (non-negative, real valued) amplitudes are E_{780} and E_{390}. Thus, the two-color ratio reads $\eta = E_{390}/E_{780}$ and is always non-negative. The corresponding combined two-color field is defined by:

$$\vec{E}(t) = \begin{pmatrix} E_x \\ E_y \\ E_z \end{pmatrix} = \begin{pmatrix} 0 \\ \sin(\omega \cdot t) + H \cdot \eta \cdot \sin(2 \cdot \omega \cdot t) \\ \cos(\omega \cdot t) + \eta \cdot \cos(2 \cdot \omega \cdot t) \end{pmatrix} \tag{63}$$

In the plane defined by E_y (abscissa) and E_z (ordinate) the polarization vector of the fundamental frequency (ω) rotates clockwise with time (t). Further H is one or minus one and defines the helicity of the second harmonic. For $H = 1$ ($H = -1$) the polarization vector of the second harmonic rotates clockwise (counter-clockwise) with time t. A clockwise rotation corresponds to a negative effective angular velocity using the following definition:

$$\omega_{\text{eff}} = \frac{\mathrm{d}\,\mathrm{atan}\left(\frac{E_z}{E_y}\right)}{\mathrm{d}t} \tag{64}$$

[180] The anonymous referee presented the results as in Eq. 79 and Eq. 83 but only for $0 \leq \eta < 0.5$ and neglecting the absolute values of numerator and denominator.

The definition given in Eq. 64 can be used to derive[181] the effective angular frequency for the field defined in Eq. 63.

$$\begin{aligned}
\omega_{\text{eff}} &= \frac{1}{1+\left(\frac{E_z}{E_y}\right)^2}\frac{\dot{E}_z\cdot Ey - E_z\cdot\dot{E}_y}{E_y^2} \\
&= \frac{-\left[\omega\sin(\omega t)+2\omega\eta\sin(2\omega t)\right]\cdot\left[\sin(\omega t)+H\cdot\eta\sin(2\omega t)\right]}{\left|\vec{E}(t)\right|^2} \\
&\qquad - \frac{\left[\cos(\omega t)+\eta\cos(2\omega t)\right]\cdot\left[\omega\cos(\omega t)+2\omega H\eta\cos(2\omega t)\right]}{\left|\vec{E}(t)\right|^2} \\
&= -\omega\frac{\sin^2(\omega t)+2\eta\sin(2\omega t)\sin(\omega t)}{\left|\vec{E}(t)\right|^2} \\
&\qquad - \omega\frac{\sin(\omega t)H\eta\sin(2\omega t)+2H\eta^2\sin^2(2\omega t)}{\left|\vec{E}(t)\right|^2} \\
&\qquad - \omega\frac{\cos^2(\omega t)+\eta\cos(2\omega t)\cos(\omega t)}{\left|\vec{E}(t)\right|^2} \\
&\qquad - \omega\frac{\cos(\omega t)2H\eta\cos(2\omega t)+2H\eta^2\cos^2(2\omega t)}{\left|\vec{E}(t)\right|^2}
\end{aligned} \tag{65}$$

This can be reduced to:

$$\begin{aligned}
\omega_{\text{eff}} &= -\omega\frac{1+2H\eta^2+(2\eta+H\eta)\sin(2\omega t)\sin(\omega t)}{\left|\vec{E}(t)\right|^2} \\
&\qquad - \omega\frac{(\eta+2H\eta)\cos(2\omega t)\cos(\omega t)}{\left|\vec{E}(t)\right|^2}
\end{aligned} \tag{66}$$

For the case of circularly polarized counter-rotating two-color fields (CRTC, $H=-1$) Eq. 66 can be simplified to:

$$\omega_{\text{eff}}^{CRTC} = -\omega\frac{1-2\eta^2+\eta\left[\sin(2\omega t)\sin(\omega t)-\cos(2\omega t)\cos(\omega t)\right]}{\left|\vec{E}(t)\right|^2} \tag{67}$$

[181] The derivative of arctangent is: $\frac{\mathrm{d}\,\mathrm{atan}(x)}{\mathrm{d}x} = \frac{1}{1+x^2}$

which can be written[182] as:

$$\omega_{\text{eff}}^{CRTC} = -\omega \frac{1-2\eta^2-\eta\cos(3\omega t)}{\left|\vec{E}(t)\right|^2} \tag{68}$$

At the maximum of $\left|\vec{E}(t)\right|$ there are $\cos(3\omega t) = 1$ and $\left|\vec{E}(t)\right|^2 = (1+\eta)^2$. Hence, at the peak electric field in a CRTC field the effective angular frequency is:

$$\begin{aligned}\omega_{\text{eff}}^{\text{CRTC}_{\text{maximum_electric_field}}} &= -\omega \frac{1-2\eta^2-\eta}{(1+\eta)^2} \\ &= -\omega \frac{(1+\eta)\cdot(1-\eta)-\eta\cdot(1+\eta)}{(1+\eta)^2} \\ &= -\omega \frac{1-2\eta}{1+\eta}\end{aligned} \tag{69}$$

The same derivation can be done for the minimum of $\left|\vec{E}(t)\right|$ for a CRTC field using $\cos(3\omega t) = -1$ and $\left|\vec{E}(t)\right|^2 = (1-\eta)^2$ which leads to the effective angular frequency:

$$\begin{aligned}\omega_{\text{eff}}^{\text{CRTC}_{\text{minimum_electric_field}}} &= -\omega \frac{1-2\eta^2+\eta}{(1-\eta)^2} \\ &= -\omega \frac{(1+\eta)\cdot(1-\eta)+\eta\cdot(1-\eta)}{(1-\eta)^2} \\ &= -\omega \frac{1+2\eta}{1-\eta}\end{aligned} \tag{70}$$

For the case of circularly polarized co-rotating two-color (CoRTC, $H = 1$) fields Eq. 66 can be simplified to:

$$\omega_{\text{eff}}^{CoRTC} = -\omega \frac{1+2\eta^2+3\eta\sin(2\omega t)\sin(\omega t)+3\eta\cos(2\omega t)\cos(\omega t)}{\left|\vec{E}(t)\right|^2} \tag{71}$$

which can be written[183] as:

$$\omega_{\text{eff}}^{CoRTC} = -\omega \frac{1+2\eta^2+3\eta\cos(\omega t)}{\left|\vec{E}(t)\right|^2} \tag{72}$$

[182] The identity $\sin(2\omega t)\sin(\omega t) - \cos(2\omega t)\cos(\omega t) = -\cos(3\omega t)$ is used.
[183] The identity $\sin(2\omega t)\sin(\omega t) + \cos(2\omega t)\cos(\omega t) = \cos(\omega t)$ is used.

At the minimum of $\left|\vec{E}(t)\right|$ there are $\cos(\omega t) = -1$ and $\left|\vec{E}(t)\right|^2 = (1-\eta)^2$. Hence, at the minimum electric field in a CoRTC field the effective angular frequency is:

$$\begin{aligned}\omega_{\text{eff}}^{\text{CoRTC}_{\text{minimum_electric_field}}} &= -\omega\frac{1+2\eta^2-3\eta}{(1-\eta)^2} \\ &= -\omega\frac{(1-\eta)^2-\eta\cdot(1-\eta)}{(1-\eta)^2} \\ &= -\omega\frac{1-2\eta}{1-\eta}\end{aligned} \tag{73}$$

The same derivation can be done for the maximum of $\left|\vec{E}(t)\right|$ for a CoRTC field using $\cos(\omega t) = 1$ and $\left|\vec{E}(t)\right|^2 = (1+\eta)^2$ which leads to the effective angular frequency:

$$\begin{aligned}\omega_{\text{eff}}^{\text{CoRTC}_{\text{maximum_electric_field}}} &= -\omega\frac{1+2\eta^2+3\eta}{(1+\eta)^2} \\ &= -\omega\frac{(1+\eta)\cdot(1-\eta)+3\eta\cdot(1+\eta)}{(1+\eta)^2} \\ &= -\omega\frac{1+2\eta}{1+\eta}\end{aligned} \tag{74}$$

To summarize the results of this chapter Tab. A.4 provides the effective angular frequencies at the minimum and the maximum of the absolute value of the laser electric field in CRTC and CoRTC fields. The result of Tab. A.4 is plotted in Fig. A.46 as a function of the two-color field ratio η.

Table A.4: Overview of the effective angular frequency ω_{eff} in two-color counter-rotating and co-rotating fields where ω is the angular frequency of the fundamental color.

	CRTC	CoRTC
minimum of the absolute value of the combined laser electric field	$-\omega\frac{1+2\eta}{1-\eta}$	$-\omega\frac{1-2\eta}{1-\eta}$
maximum of the absolute value of the combined laser electric field	$-\omega\frac{1-2\eta}{1+\eta}$	$-\omega\frac{1+2\eta}{1+\eta}$

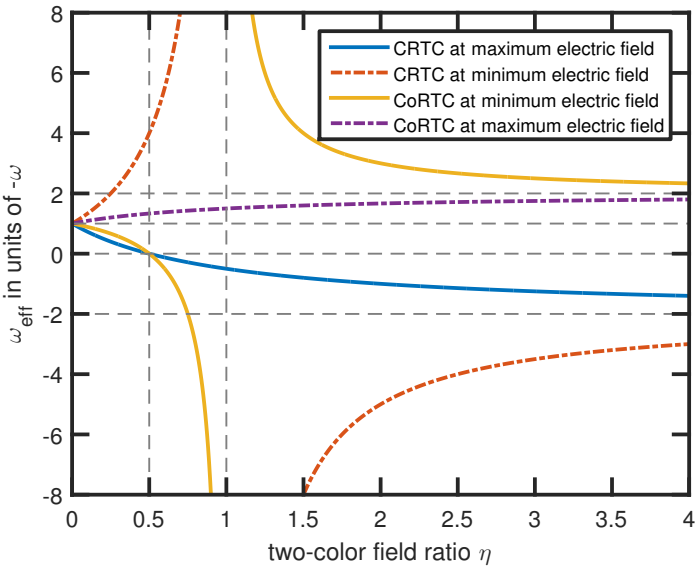


Figure A.46: The result of Tab. A.4 is shown. Vertical and horizontal gray dashed lines guide the eye. It is nicely seen that for $\eta = 0$ and very high η single color fields are realized. Interestingly in all cases, except at the maximum of the CoRTC field, the direction of rotation changes its sign as η is varied. The unit of the ordinate is chosen to be $-\omega$. In this convention a clockwise rotating field as described by Eq. 64 leads to positive values.

Fig. A.46 illustrates that for $\eta = 0$ and very high η single-color fields are realized and the corresponding effective angular frequency and its direction of rotation are entirely determined by the dominating single-color laser pulse. The sign changes near $\eta = 0.5$ are due to inversions of the direction of rotation (with non-vanishing field amplitude) and related to loops in the corresponding Lissajous curves for $\eta > 0.5$. In contrast, the sign changes near $\eta = 1$ occurs because the combined field crossing the origin.

A.8.1. The Effective Keldysh-Parameter

Based on the results shown in Fig. A.46 the effective Keldysh-parameter γ_{eff} can be calculated. The result is presented in Fig. A.47. It should be noted that the diverging values of γ_{eff} are only reached at minima of the combined electric field that are close to zero. This means that in these cases the ionization rate vanishes. According to chapter 8.4 the effective Keldysh-parameter (see Ref. [1] and chapter 3) is

$$\gamma_{\text{eff}} = \frac{|\omega_{\text{eff}}|}{|E|} \cdot \sqrt{2I_p} \tag{75}$$

where ω_{eff} is the instantaneous effective angular frequency, E is the instantaneous combined electric field and I_p is the time independent ionization potential[184]. The effective Keldysh-

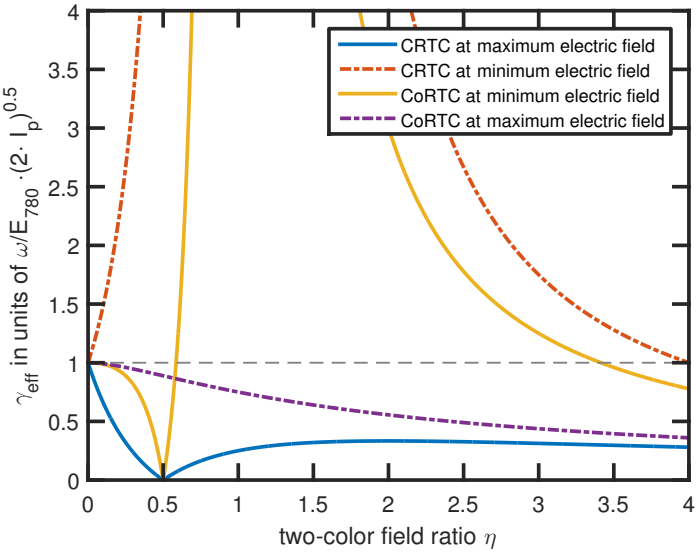


Figure A.47: The effective Keldysh-parameter γ_{eff} is calculated as a function of the two-color ratio η. The value of γ_{eff} is plotted in units of $\omega/E_{780}\cdot(2\cdot I_p)^{0.5}$ in order to obtain the most general result possible.

parameter is an instantaneous quantity. At minima or maxima of the combined electric field there exists strong evidence that γ_{eff} is a good figure of merit describing the non-adiabaticity of strong-field tunnel-ionization (see chapter 8). However, it is not obvious if and how this concept can be extended to "birth-times" of the electron other than those corresponding to the extrema of $|E|$. In those cases the electric field vector and its derivative are not orthogonal and further research is necessary to reach conclusions regarding the description of those scenarios. The results shown in chapter 10.1 are a first step into this direction.

[184] Here, the momentum in the light propagation direction p_x is set to zero. In chapter 8.4 a generalized version of the effective Keldysh-parameter γ_{eff} is presented including cases with non-zero momentum in the light propagation direction. The results presented here can be generalized to this form by substituting I_p with $I_p^{\text{eff}} = I_p + \frac{1}{2}p_x^2$.

A.8.2. Alternative Derivation of the Effective Angular Frequency

To obtain the absolute value of the effective angular frequency ω_{eff} at the minima or maxima of the combined electric field the simple expression

$$|\omega_{\text{eff}}^{\text{extrema}}| = \frac{|\dot{E}|}{|E|} \tag{76}$$

can be used where E is the instantaneous combined electric field and $\dot{E}$ is its derivative. Starting from Eq. 63 the squared absolute value of the temporal derivative reads:

$$\begin{aligned}
|\dot{E}|^2 &= \omega^2[\cos^2(\omega\cdot t) + 4H\cdot\eta\cos(\omega\cdot t)\cos(2\cdot\omega\cdot t) + (2H\cdot\eta)^2\cdot\cos^2(2\cdot\omega\cdot t) \\
&\qquad + \sin^2(\omega\cdot t) + \sin(\omega\cdot t)(4\eta)\cdot\sin(2\cdot\omega\cdot t) + (2\eta)^2\cdot\sin^2(2\cdot\omega\cdot t)] \\
&= \omega^2[1 + H4\eta\cos(\omega\cdot t)\cos(2\cdot\omega\cdot t) + H^2(2\eta)^2\cdot\cos^2(2\cdot\omega\cdot t) \\
&\qquad + 4\eta\sin(\omega\cdot t)\sin(2\cdot\omega\cdot t) + (2\eta)^2\cdot\sin^2(2\cdot\omega\cdot t)]
\end{aligned} \tag{77}$$

For $H = 1$ (CoRTC field) this leads to[185]:

$$\begin{aligned}
|\dot{E}| &= \omega\sqrt{1 + 4\eta^2 + 4\eta[\cos(\omega\cdot t)\cos(2\cdot\omega\cdot t) + \sin(\omega\cdot t)\cdot\sin(2\cdot\omega\cdot t)]} \\
&= \omega\sqrt{1 + 4\eta^2 + 4\eta\cos(\omega\cdot t)}
\end{aligned} \tag{78}$$

At the minimum of $|E|$ there are $\cos(\omega t) = -1$ and $|E| = (1-\eta)$. Hence, at the minimum electric field in a CoRTC field the absolute value of the effective angular frequency is:

$$|\omega_{\text{eff}}^{\text{CoRTC}_{\text{minimum_electric_field}}}| = \frac{|\dot{E}|}{|E|} = \omega\frac{\sqrt{1 + 4\eta^2 - 4\eta}}{|1-\eta|} = \omega\frac{|1-2\eta|}{|1-\eta|} \tag{79}$$

At the maximum of $|E|$ there are $\cos(\omega t) = 1$ and $|E| = (1+\eta)$:

$$|\omega_{\text{eff}}^{\text{CoRTC}_{\text{maximum_electric_field}}}| = \frac{|\dot{E}|}{|E|} = \omega\frac{\sqrt{1 + 4\eta^2 + 4\eta}}{|1+\eta|} = \omega\frac{|1+2\eta|}{|1+\eta|} \tag{80}$$

For $H = -1$ (CRTC field) Eq. 77 leads to[186]:

$$\begin{aligned}
|\dot{E}| &= \omega\sqrt{1 + 4\eta^2 + 4\eta[-\cos(\omega\cdot t)\cos(2\cdot\omega\cdot t) + \sin(\omega\cdot t)\cdot\sin(2\cdot\omega\cdot t)]} \\
&= \omega\sqrt{1 + 4\eta^2 - 4\eta\cos(3\omega\cdot t)}
\end{aligned} \tag{81}$$

[185] The identity $\sin(2\omega t)\sin(\omega t) + \cos(2\omega t)\cos(\omega t) = \cos(\omega t)$ is used.
[186] The identity $\sin(2\omega t)\sin(\omega t) - \cos(2\omega t)\cos(\omega t) = -\cos(3\omega t)$ is used.

At the minimum of $|E|$ there are $\cos(3\omega t) = -1$ and $|E| = (1-\eta)$. Hence, at the minimum of the absolute value of the combined electric field in a CRTC field the absolute value of the effective angular frequency is:

$$|\omega_{\text{eff}}^{\text{CRTC}_{\text{minimum_electric_field}}}| = \frac{|\dot{E}|}{|E|} = \omega\frac{\sqrt{1+4\eta^2+4\eta}}{|1-\eta|} = \omega\frac{|1+2\eta|}{|1-\eta|} \tag{82}$$

At the maximum of $|E|$ there are $\cos(3\omega t) = 1$ and $|E| = (1+\eta)$:

$$|\omega_{\text{eff}}^{\text{CRTC}_{\text{maximum_electric_field}}}| = \frac{|\dot{E}|}{|E|} = \omega\frac{\sqrt{1+4\eta^2-4\eta}}{|1+\eta|} = \omega\frac{|1-2\eta|}{|1+\eta|} \tag{83}$$

These results are consistent with the values that were presented in Tab. A.4 but are less general because they only describe the absolute value of ω_{eff}.

References

[1]L. V. Keldysh, "Ionization in the field of a strong electromagnetic wave", Sov. Phys. JETP **20**, 1307 (1965) (cit. on pp. 1, 10, 34, 47, 118, 129, 231).

[2]J. D. Jackson, *Classical electrodynamics*, ISBN 047130932X, 3rd ed., 1999 (cit. on p. 1).

[3]W. Demtröder, *Laser spectroscopy 2*, ISBN 9783662446409, 5th ed. (Springer, 2015) (cit. on p. 1).

[4]L. A. MacColl, "Note on the transmission and reflection of wave packets by potential barriers", Phys. Rev. **40**, 621 (1932) (cit. on p. 1).

[5]T. E. Hartman, "Tunneling of a wave packet", J. Appl. Phys. **33**, 3427 (1962) (cit. on p. 1).

[6]M. Büttiker and R. Landauer, "Traversal time for tunneling", Phys. Rev. Lett. **49**, 1739 (1982) (cit. on p. 1).

[7]A. M. Steinberg, P. G. Kwiat, and R. Y. Chiao, "Measurement of the single-photon tunneling time", Phys. Rev. Lett. **71**, 708 (1993) (cit. on p. 1).

[8]P. Eckle, A. N. Pfeiffer, C. Cirelli, A. Staudte, R. Dörner, H. G. Muller, M. Büttiker, and U. Keller, "Attosecond ionization and tunneling delay time measurements in helium", Science **322**, 1525 (2008) (cit. on pp. 1, 90, 92, 101, 125, 199).

[9]L. Torlina, F. Morales, J. Kaushal, I. Ivanov, A. Kheifets, A. Zielinski, A. Scrinzi, H. G. Muller, S. Sukiasyan, M. Ivanov, and S. Olga, "Interpreting attoclock measurements of tunnelling times", Nat. Phys. **11**, 503 (2015) (cit. on pp. 1, 125).

[10]H. Ni, U. Saalmann, and J.-M. Rost, "Tunneling ionization time resolved by backpropagation", Phys. Rev. Lett. **117**, 023002 (2016) (cit. on pp. 1, 100, 101).

[11]N. Teeny, E. Yakaboylu, H. Bauke, and C. H. Keitel, "Ionization time and exit momentum in strong-field tunnel ionization", Phys. Rev. Lett. **116**, 063003 (2016) (cit. on pp. 1, 101, 180).

[12]N. Camus, E. Yakaboylu, L. Fechner, M. Klaiber, M. Laux, Y. Mi, K. Z. Hatsagortsyan, T. Pfeifer, C. H. Keitel, and R. Moshammer, "Experimental evidence for quantum tunneling time", Phys. Rev. Lett. **119**, 023201 (2017) (cit. on pp. 1, 90, 101).

[13]K. Liu, H. Ni, K. Renziehausen, J.-M. Rost, and I. Barth, "Deformation of atomic $p_\pm$ orbitals in strong elliptically polarized laser fields: ionization time drifts and spatial photoelectron separation", Phys. Rev. Lett. **121**, 203201 (2018) (cit. on pp. 1, 101, 126, 165, 167).

[14]G. Binnig, H. Rohrer, C. Gerber, and E. Weibel, "Tunneling through a controllable vacuum gap", Appl. Phys. Lett. **40**, 178 (1982) (cit. on p. 1).

[15]G. Binnig, H. Rohrer, C. Gerber, and E. Weibel, "Surface studies by scanning tunneling microscopy", Phys. Rev. Lett. **49**, 57 (1982) (cit. on p. 1).

[16]R. H. Fowler and L. Nordheim, "Electron emission in intense electric fields", Proceedings of the Royal Society of London. Series A, Containing Papers of a Mathematical and Physical Character **119**, 173 (1928) (cit. on p. 1).

[17]J. C. Fisher and I. Giaever, "Tunneling through thin insulating layers", J. Appl. Phys. **32**, 172 (1961) (cit. on p. 1).

[18]P. Cappelletti, C. Golla, P. Olivo, and E. Zanoni, *Flash memories*, ISBN 9780792384878 (Springer Science & Business Media, 1999) (cit. on p. 1).

[19]G. Gamow, "Zur Quantentheorie des Atomkernes", Zeitschrift für Physik **51**, 204 (1928) (cit. on p. 1).

[20]G. Gamow, "The quantum theory of nuclear disintegration", Nature **122**, 805 (1928) (cit. on p. 1).

[21]G. L. Yudin and M. Ivanov, "Nonadiabatic tunnel ionization: looking inside a laser cycle", Phys. Rev. A **64**, 013409 (2001) (cit. on pp. 1, 100, 102).

[22]M. Y. Ivanov, M. Spanner, and O. Smirnova, "Anatomy of strong field ionization", J. Mod. Opt. **52**, 165 (2005) (cit. on pp. 1, 10, 11, 34, 100–102, 114, 119).

[23]S. Eckart, M. Richter, M. Kunitski, A. Hartung, J. Rist, K. Henrichs, N. Schlott, H. Kang, T. Bauer, H. Sann, L. P. H. Schmidt, M. Schöffler, T. Jahnke, and R. Dörner, "Nonsequential double ionization by counterrotating circularly polarized two-color laser fields", Phys. Rev. Lett. **117**, 133202 (2016) (cit. on pp. 3, 44, 45, 48, 55, 58, 65, 212, 249).

[24]S. Eckart, M. Kunitski, I. Ivanov, M. Richter, K. Fehre, A. Hartung, J. Rist, K. Henrichs, D. Trabert, N. Schlott, L. P. H. Schmidt, T. Jahnke, M. S. Schöffler, A. Kheifets, and R. Dörner, "Subcycle interference upon tunnel ionization by counter-rotating two-color fields", Phys. Rev. A **97**, 041402 (2018) (cit. on pp. 3, 69, 71, 75, 78, 83, 187–190, 249, 252).

[25]S. Eckart, K. Fehre, N. Eicke, A. Hartung, J. Rist, D. Trabert, N. Strenger, A. Pier, L. P. H. Schmidt, T. Jahnke, M. S. Schöffler, M. Lein, M. Kunitski, and R. Dörner, "Direct experimental access to the nonadiabatic initial momentum offset upon tunnel ionization", Phys. Rev. Lett. **121**, 163202 (2018) (cit. on pp. 3, 78, 97–99, 101–103, 108, 110, 112, 114, 116, 118, 119, 148, 169, 170, 249).

[26]S. Eckart, M. Kunitski, M. Richter, A. Hartung, J. Rist, F. Trinter, K. Fehre, N. Schlott, K. Henrichs, L. H. Schmidt, T. Jahnke, M. Schöffler, K. Liu, I. Barth, J. Kaushal, F. Morales, M. Ivanov, O. Smirnova, and R. Dörner, "Ultrafast preparation and detection of ring currents in single atoms", Nat. Phys. **14**, 701 (2018) (cit. on pp. 3, 123, 125, 126, 129, 132, 133, 136–140, 142, 143, 147, 151, 154–158, 161, 163, 165, 249).

[27]A. Staudte, "Subfemtosecond electron dynamics of H_2 in strong fields", Dissertation, Johann Wolfgang Goethe-Universität Frankfurt am Main (2005) (cit. on pp. 5, 24).

[28]I. Velchev, W. Hogervorst, and W. Ubachs, "Precision VUV spectroscopy of Ar I at 105 nm", J. Phys. B **32**, L511 (1999) (cit. on p. 5).

[29]A. Einstein, "Über einen die Erzeugung und Verwandlung des Lichtes betreffenden heuristischen Gesichtspunkt", Ann. Phys. **322**, 132 (1905) (cit. on p. 6).

[30]M. Göppert-Mayer, "Über Elementarakte mit zwei Quantensprüngen", Ann. Phys. **401**, 273 (1931) (cit. on p. 6).

[31]W. Kaiser and C. G. B. Garrett, "Two-photon excitation in CaF_2:Eu^{2+}", Phys. Rev. Lett. **7**, 229 (1961) (cit. on p. 6).

[32]G. S. Voronov and N. B. Delone, "Many-photon ionization of the xenon atom by ruby laser radiation", Sov. Phys. JETP **23**, 54 (1966) (cit. on pp. 6, 47).

[33]P. Agostini, F. Fabre, G. Mainfray, G. Petite, and N. K. Rahman, "Free-free transitions following six-photon ionization of xenon atoms", Phys. Rev. Lett. **42**, 1127 (1979) (cit. on pp. 7, 70).

[34]G. Petite, P. Agostini, and H. Muller, "Intensity dependence of non-perturbative above-threshold ionisation spectra: experimental study", J. Phys. B **21**, 4097 (1988) (cit. on pp. 7, 70).

[35]R. R. Freeman, P. H. Bucksbaum, H. Milchberg, S. Darack, D. Schumacher, and M. E. Geusic, "Above-threshold ionization with subpicosecond laser pulses", Phys. Rev. Lett. **59**, 1092 (1987) (cit. on p. 7).

[36]M. C. Richter, "Ionisation in Zwei-Farben-Laserfeldern: Steuerung von Elektronenwellenpaketen", Dissertation, Johann Wolfgang Goethe-Universität Frankfurt am Main (2016) (cit. on pp. 7, 14, 15, 21–24, 32, 38, 56, 57, 79, 88, 191, 194).

[37]S. L. Chin, F. Yergeau, and P. Lavigne, "Tunnel ionisation of Xe in an ultra-intense CO_2 laser field (10^{14}Wcm^{-2}) with multiple charge creation", J. Phys. B **18**, L213 (1985) (cit. on p. 8).

[38]N. I. Shvetsov-Shilovski, M. Lein, L. B. Madsen, E. Räsänen, C. Lemell, J. Burgdörfer, D. G. Arbó, and K. Tőkési, "Semiclassical two-step model for strong-field ionization", Phys. Rev. A **94**, 013415 (2016) (cit. on pp. 8, 38, 76).

[39]L. D. Landau and E. M. Lifshitz, *Quantum mechanics non- relativistic theory*, 2nd ed. (Pergamon Press, 1965) (cit. on p. 8).

[40]A. M. Perelomov, V. S. Popov, and M. V. Terent'ev, "Ionization of atoms in an alternating electrical field", Sov. Phys. JETP **23**, 924 (1966) (cit. on pp. 8, 101).

[41]M. V. Ammosov, N. B. Delone, and V. P. Krainov, "Tunnel ionization of complex atoms and of atomic ions in an alternating electromagnetic field", Sov. Phys. JETP **64**, 1191 (1986) (cit. on p. 8).

[42]S. Augst, D. D. Meyerhofer, D. Strickland, and S. L. Chin, "Laser ionization of noble gases by Coulomb-barrier suppression", J. Opt. Soc. Am. B **8**, 858 (1991) (cit. on p. 9).

[43]A. Hartung, S. Eckart, S. Brennecke, J. Rist, D. Trabert, K. Fehre, M. Richter, H. Sann, S. Zeller, K. Henrichs, G. Kastirke, J. Hoehl, A. Kalinin, M. S. Schöffler, T. Jahnke, L. P. H. Schmidt, M. Lein, M. Kunitski, and R. Dörner, "Magnetic fields alter tunneling in strong-field ionization", arXiv preprint arXiv:1902.07278 (2019) (cit. on p. 9).

[44]P. B. Corkum, "Plasma perspective on strong field multiphoton ionization", Phys. Rev. Lett. **71**, 1994 (1993) (cit. on pp. 9, 47, 48).

[45]M. Kitzler and S. Gräfe, *Ultrafast dynamics driven by intense light pulse*, ISBN 9783319201726 (Springer, 2015) (cit. on p. 10).

[46]S. V. Popruzhenko, "Keldysh theory of strong field ionization: history, applications, difficulties and perspectives", J. Phys. B **47**, 204001 (2014) (cit. on pp. 10, 34).

[47]M. Klaiber, K. Z. Hatsagortsyan, and C. H. Keitel, "Tunneling dynamics in multiphoton ionization and attoclock calibration", Phys. Rev. Lett. **114**, 083001 (2015) (cit. on pp. 10, 11, 100, 102, 119–121, 180, 254).

[48]M. Klaiber and J. S. Briggs, "Crossover from tunneling to multiphoton ionization of atoms", Phys. Rev. A **94**, 053405 (2016) (cit. on pp. 10, 102, 119–121, 167, 175, 180, 254).

[49]O. Jagutzki, A. Cerezo, A. Czasch, R. Dörner, M. Hattas, M. Huang, V. Mergel, U. Spillmann, K. Ullmann-Pfleger, T. Weber, H. Schmidt-Böcking, and G. D. W. Smith, "Multiple hit readout of a microchannel plate detector with a three-layer delay-line anode", IEEE Trans. Nucl. Sci. **49**, 2477 (2002) (cit. on pp. 21, 22).

[50]J. Ullrich, R. Moshammer, A. Dorn, R. Dörner, L. P. Schmidt, and H. Schmidt-Böcking, "Recoil-ion and electron momentum spectroscopy: reaction-microscopes", Rep. Prog. Phys. **66**, 1463 (2003) (cit. on p. 21).

[51]T. Jahnke, "'Interatomic Coulombic Decay' - Experimentelle Untersuchung eines neuartigen, interatomaren Abregungsmechanismus", Dissertation, Johann Wolfgang Goethe-Universität Frankfurt am Main (2005) (cit. on p. 21).

[52]M. Meckel, "Laser-Induced Electron Tunneling and Diffraction", Dissertation, Johann Wolfgang Goethe-Universität Frankfurt am Main (2011) (cit. on pp. 23, 24).

[53]M. S. Schöffler, "Grundzustandskorrelationen und dynamische Prozesse untersucht in Ion-Helium-Stößen", Dissertation, Johann Wolfgang Goethe-Universität Frankfurt am Main (2005) (cit. on p. 24).

[54]S. Voss, "Koinzidente Photoelektronenspektroskopie an Supraleitern", Dissertation, Johann Wolfgang Goethe-Universität Frankfurt am Main (2011) (cit. on pp. 24, 221).

[55]N. Schlott, "In situ Charakterisierung von Laserfeldern und Starkfeldionisation von Argon in Zwei-Farben-Laserfeldern", Masterarbeit, Goethe-Universität Frankfurt am Main (2017) (cit. on pp. 30, 31, 74, 130, 185).

[56]C. Wang, X. Li, X.-R. Xiao, Y. Yang, S. Luo, X. Yu, X. Xu, L.-Y. Peng, Q. Gong, and D. Ding, "Accurate in situ measurement of ellipticity based on subcycle ionization dynamics", Phys. Rev. Lett. **122**, 013203 (2019) (cit. on pp. 31, 196).

[57]C. Smeenk, J. Z. Salvail, L. Arissian, P. B. Corkum, C. T. Hebeisen, and A. Staudte, "Precise in-situ measurement of laser pulse intensity using strong field ionization", Opt. Express **19**, 9336 (2011) (cit. on p. 31).

[58]A. S. Alnaser, X. M. Tong, T. Osipov, S. Voss, C. M. Maharjan, B. Shan, Z. Chang, and C. L. Cocke, "Laser-peak-intensity calibration using recoil-ion momentum imaging", Phys. Rev. A **70**, 023413 (2004) (cit. on p. 31).

[59]W. C. Wallace, O. Ghafur, C. Khurmi, S. Sainadh U, J. E. Calvert, D. E. Laban, M. G. Pullen, K. Bartschat, A. N. Grum-Grzhimailo, D. Wells, H. M. Quiney, X. M. Tong, I. V. Litvinyuk, R. T. Sang, and D. Kielpinski, "Precise and accurate measurements of strong-field photoionization and a transferable laser intensity calibration standard", Phys. Rev. Lett. **117**, 053001 (2016) (cit. on p. 31).

[60]D. Milošević, G. G. Paulus, and W. Becker, "Phase-dependent effects of a few-cycle laser pulse", Phys. Rev. Lett. **89**, 153001 (2002) (cit. on p. 34).

[61]T.-M. Yan, S. V. Popruzhenko, M. J. J. Vrakking, and D. Bauer, "Low-energy structures in strong field ionization revealed by quantum orbits", Phys. Rev. Lett. **105**, 253002 (2010) (cit. on pp. 34, 114).

[62]E. Hasović, W. Becker, and D. B. Milošević, "Electron rescattering in a bicircular laser field", Opt. Express **24**, 6413 (2016) (cit. on p. 34).

[63]D. Bauer, D. B. Milošević, and W. Becker, "Strong-field approximation for intense-laser–atom processes: The choice of gauge", Phys. Rev. A **72**, 023415 (2005) (cit. on p. 34).

[64]L. Torlina, "The analytical R-matrix approach to strong field dynamics", Dissertation, Technische Universität Berlin (2016) (cit. on p. 34).

[65]D. Bauer, "Strong-field few-body dynamics", Talk at the annual QUTIF meeting in Dornburg (Germany) (2016) (cit. on pp. 34–36, 104).

[66]D. Milošević, G. Paulus, D. Bauer, and W. Becker, "Above-threshold ionization by few-cycle pulses", J. Phys. B **39**, R203 (2006) (cit. on p. 34).

[67]S. V. Popruzhenko, G. G. Paulus, and D. Bauer, "Coulomb-corrected quantum trajectories in strong-field ionization", Phys. Rev. A **77**, 053409 (2008) (cit. on pp. 34, 122).

[68]S. Popruzhenko and D. Bauer, "Strong field approximation for systems with Coulomb interaction", J. Mod. Opt. **55**, 2573 (2008) (cit. on pp. 34, 102).

[69]I. Barth and O. Smirnova, "Nonadiabatic tunneling in circularly polarized laser fields: Physical picture and calculations", Phys. Rev. A **84**, 063415 (2011) (cit. on pp. 36, 37, 101, 118, 122, 125, 126, 138, 167).

[70]C. Hofmann, A. S. Landsman, A. Zielinski, C. Cirelli, T. Zimmermann, A. Scrinzi, and U. Keller, "Interpreting electron-momentum distributions and nonadiabaticity in strong-field ionization", Phys. Rev. A **90**, 043406 (2014) (cit. on pp. 37, 102).

[71]C. Hofmann, T. Zimmermann, A. Zielinski, and A. S. Landsman, "Non-adiabatic imprints on the electron wave packet in strong field ionization with circular polarization", New J. Phys. **18**, 043011 (2016) (cit. on pp. 37, 102).

[72]M. Li, J.-W. Geng, H. Liu, Y. Deng, C. Wu, L.-Y. Peng, Q. Gong, and Y. Liu, "Classical-quantum correspondence for above-threshold ionization", Phys. Rev. Lett. **112**, 113002 (2014) (cit. on p. 38).

[73]A. N. Pfeiffer, C. Cirelli, M. Smolarski, D. Dimitrovski, M. Abu-Samha, L. B. Madsen, and U. Keller, "Attoclock reveals natural coordinates of the laser-induced tunnelling current flow in atoms", Nat. Phys. **8**, 76 (2012) (cit. on p. 38).

[74]H. Ni, U. Saalmann, and J.-M. Rost, "Tunneling exit characteristics from classical backpropagation of an ionized electron wave packet", Phys. Rev. A **97**, 013426 (2018) (cit. on pp. 38, 100, 101, 120).

[75]C. A. Mancuso, K. M. Dorney, D. D. Hickstein, J. L. Chaloupka, J. L. Ellis, F. J. Dollar, R. Knut, P. Grychtol, D. Zusin, C. Gentry, M. Gopalakrishnan, H. C. Kapteyn, and M. M. Murnane, "Controlling nonsequential double ionization in two-color circularly polarized femtosecond laser fields", Phys. Rev. Lett. **117**, 133201 (2016) (cit. on pp. 45, 48, 57).

[76]J. L. Chaloupka and D. D. Hickstein, "Dynamics of strong-field double ionization in two-color counterrotating fields", Phys. Rev. Lett. **116**, 143005 (2016) (cit. on pp. 45, 48, 57).

[77]A. L'Huillier, L. A. Lompre, G. Mainfray, and C. Manus, "Multiply charged ions formed by multiphoton absorption processes in the continuum", Phys. Rev. Lett. **48**, 1814 (1982) (cit. on p. 47).

[78]D. N. Fittinghoff, P. R. Bolton, B. Chang, and K. C. Kulander, "Observation of nonsequential double ionization of helium with optical tunneling", Phys. Rev. Lett. **69**, 2642 (1992) (cit. on p. 47).

[79]B. Walker, B. Sheehy, L. F. DiMauro, P. Agostini, K. J. Schafer, and K. C. Kulander, "Precision measurement of strong field double ionization of helium", Phys. Rev. Lett. **73**, 1227 (1994) (cit. on pp. 47, 58).

[80]B. Feuerstein, R. Moshammer, D. Fischer, A. Dorn, C. D. Schröter, J. Deipenwisch, J. R. Crespo Lopez-Urrutia, C. Höhr, P. Neumayer, J. Ullrich, H. Rottke, C. Trump, M. Wittmann, G. Korn, and W. Sandner, "Separation of recollision mechanisms in nonsequential strong field double ionization of Ar: the role of excitation tunneling", Phys. Rev. Lett. **87**, 043003 (2001) (cit. on p. 47).

[81]V. L. B. D. Jesus, B. Feuerstein, K. Zrost, D. Fischer, A. Rudenko, F. Afaneh, C. D. Schröter, R. Moshammer, and J. Ullrich, "Atomic structure dependence of nonsequential double ionization of He, Ne and Ar in strong laser pulses", J. Phys. B **37**, L161 (2004) (cit. on pp. 47, 55, 57, 93).

[82]T. Weber, H. Giessen, M. Weckenbrock, G. Urbasch, A. Staudte, L. Spielberger, O. Jagutzki, V. Mergel, M. Vollmer, and R. Dörner, "Correlated electron emission in multiphoton double ionization", Nature **405**, 658 (2000) (cit. on p. 48).

[83]Y. Liu, S. Tschuch, A. Rudenko, M. Dürr, M. Siegel, U. Morgner, R. Moshammer, and J. Ullrich, "Strong-field double ionization of Ar below the recollision threshold", Phys. Rev. Lett. **101**, 053001 (2008) (cit. on p. 48).

[84]B. Bergues, M. Kübel, N. G. Johnson, B. Fischer, N. Camus, K. J. Betsch, O. Herrwerth, A. Senftleben, A. M. Sayler, T. Rathje, T. Pfeifer, I. Ben-Itzhak, R. R. Jones, G. G. Paulus, F. Krausz, R. Moshammer, J. Ullrich, and M. F. Kling, "Attosecond tracing of correlated electron-emission in non-sequential double ionization", Nat. Commun. **3**, 813 (2012) (cit. on p. 48).

[85]N. Camus, B. Fischer, M. Kremer, V. Sharma, A. Rudenko, B. Bergues, M. Kübel, N. G. Johnson, M. F. Kling, T. Pfeifer, J. Ullrich, and R. Moshammer, "Attosecond correlated dynamics of two electrons passing through a transition state", Phys. Rev. Lett. **108**, 073003 (2012) (cit. on p. 48).

[86]M. Kübel, K. J. Betsch, N. G. Kling, A. Alnaser, J. Schmidt, U. Kleineberg, Y. Deng, I. Ben-Itzhak, G. G. Paulus, T. Pfeifer, J. Ullrich, R. Moshammer, M. Kling, and B. Bergues, "Non-sequential double ionization of Ar: from the single- to the many-cycle regime", New J. Phys. **16**, 033008 (2014) (cit. on p. 48).

[87]M. Kübel, "Single-cycle non-sequential double ionization", Dissertation, Ludwig-Maximilians-Universität (2014) (cit. on p. 48).

[88]A. N. Pfeiffer, C. Cirelli, M. Smolarski, X. Wang, J. H. Eberly, R. Dörner, and U. Keller, "Breakdown of the independent electron approximation in sequential double ionization", New J. Phys. **13**, 093008 (2011) (cit. on p. 48).

[89]A. H. Winney, S. K. Lee, Y. F. Lin, Q. Liao, P. Adhikari, G. Basnayake, H. B. Schlegel, and W. Li, "Attosecond electron correlation dynamics in double ionization of benzene probed with two-electron angular streaking", Phys. Rev. Lett. **119**, 123201 (2017) (cit. on p. 48).

[90]T. Brabec and F. Krausz, "Intense few-cycle laser fields: frontiers of nonlinear optics", Rev. Mod. Phys. **72**, 545 (2000) (cit. on p. 48).

[91]W. Becker, F. Grasbon, R. Kopold, D. B. Milošević, G. G. Paulus, and H. Walther, "Above-threshold ionization: from classical features to quantum effects", Adv. At. Mol. Opt. Phy. **48**, 35 (2002) (cit. on p. 48).

[92]C. Francesca, S. Giuseppe, S. Salvatore, V. Caterina, and N. Mauro, "Advances in attosecond science", J. Phys. B **49**, 062001 (2016) (cit. on p. 48).

[93]J. L. Krause, K. J. Schafer, and K. C. Kulander, "High-order harmonic generation from atoms and ions in the high intensity regime", Phys. Rev. Lett. **68**, 3535 (1992) (cit. on p. 48).

[94]M. Lewenstein, P. Balcou, M. Y. Ivanov, A. L'Huillier, and P. B. Corkum, "Theory of high-harmonic generation by low-frequency laser fields", Phys. Rev. A **49**, 2117 (1994) (cit. on p. 48).

[95]B. Walker, E. Mevel, B. Yang, P. Breger, J. P. Chambaret, A. Antonetti, L. F. DiMauro, and P. Agostini, "Double ionization in the perturbative and tunneling regimes", Phys. Rev. A **48**, R894 (1993) (cit. on p. 48).

[96]H. Eichmann, A. Egbert, S. Nolte, C. Momma, B. Wellegehausen, W. Becker, S. Long, and J. K. McIver, "Polarization-dependent high-order two-color mixing", Phys. Rev. A **51**, R3414 (1995) (cit. on p. 48).

[97]W. Becker, B. N. Chichkov, and B. Wellegehausen, "Schemes for the generation of circularly polarized high-order harmonics by two-color mixing", Phys. Rev. A **60**, 1721 (1999) (cit. on p. 48).

[98]D. B. Milošević, W. Becker, and R. Kopold, "Generation of circularly polarized high-order harmonics by two-color coplanar field mixing", Phys. Rev. A **61**, 063403 (2000) (cit. on p. 48).

[99]A. Fleischer, O. Kfir, T. Diskin, P. Sidorenko, and O. Cohen, "Spin angular momentum and tunable polarization in high-harmonic generation", Nat. Photonics **8**, 543 (2014) (cit. on p. 48).

[100]C. A. Mancuso, D. D. Hickstein, P. Grychtol, R. Knut, O. Kfir, X.-M. Tong, F. Dollar, D. Zusin, M. Gopalakrishnan, C. Gentry, E. Turgut, J. L. Ellis, M.-C. Chen, A. Fleischer, O. Cohen, H. C. Kapteyn, and M. M. Murnane, "Strong-field ionization with two-color circularly polarized laser fields", Phys. Rev. A **91**, 031402 (2015) (cit. on pp. 48, 64).

[101]C. A. Mancuso, D. D. Hickstein, K. M. Dorney, J. L. Ellis, E. Hasović, R. Knut, P. Grychtol, C. Gentry, M. Gopalakrishnan, D. Zusin, F. J. Dollar, X.-M. Tong, D. B. Milošević, W. Becker, H. C. Kapteyn, and M. M. Murnane, "Controlling electron-ion rescattering in two-color circularly polarized femtosecond laser fields", Phys. Rev. A **93**, 053406 (2016) (cit. on pp. 56, 67).

[102]A. Müller, N. Djurić, G. H. Dunn, and D. S. Belić, "Absolute detection efficiencies of microchannel plates for 0.1–2.3 keV electrons and 2.1–4.4 keV Mg^+ ions", Rev. Sci. Instrum. **57**, 349 (1986) (cit. on p. 63).

[103]K. Henrichs, S. Eckart, A. Hartung, D. Trabert, J. Rist, H. Sann, M. Pitzer, M. Richter, H. Kang, M. S. Schöffler, M. Kunitski, T. Jahnke, and R. Dörner, "Experimental evidence for selection rules in multiphoton double ionization of helium and neon", Phys. Rev. A **97**, 031405 (2018) (cit. on p. 63).

[104]T.-M. Yan and D. Bauer, "Sub-barrier Coulomb effects on the interference pattern in tunneling-ionization photoelectron spectra", Phys. Rev. A **86**, 053403 (2012) (cit. on pp. 70, 122).

[105]D. G. Arbó, . L. Ishikawa, K. Schiessl, E. Persson, and J. Burgdörfer, "Intracycle and intercycle interferences in above-threshold ionization: the time grating", Phys. Rev. A **81**, 021403 (2010) (cit. on p. 70).

[106]F. Lindner, M. G. Schätzel, H. Walther, A. Baltuška, E. Goulielmakis, F. Krausz, D. B. Milošević, D. Bauer, W. Becker, and G. G. Paulus, "Attosecond double-slit experiment", Phys. Rev. Lett. **95**, 040401 (2005) (cit. on p. 70).

[107]R. Gopal, K. Simeonidis, R. Moshammer, T. Ergler, M. Dürr, M. Kurka, K.-U. Kühnel, S. Tschuch, C.-D. Schröter, D. Bauer, J. Ullrich, A. Rudenko, O. Herrwerth, T. Uphues, M. Schultze, E. Goulielmakis, M. Uiberacker, M. Lezius, and M. F. Kling, "Three-dimensional momentum imaging of electron wave packet interference in few-cycle laser pulses", Phys. Rev. Lett. **103**, 053001 (2009) (cit. on p. 70).

[108]J. W. Geng, W. H. Xiong, X. R. Xiao, L. Y. Peng, and Q. Gong, "Nonadiabatic electron dynamics in orthogonal two-color laser fields with comparable intensities", Phys. Rev. Lett. **115**, 193001 (2015) (cit. on pp. 70, 102).

[109]L. Yue and L. B. Madsen, "Inter- and intracycle interference effects in strong-field dissociative ionization", Phys. Rev. A **93**, 031401 (2016) (cit. on p. 70).

[110]A. Gramajo, R. D. Picca, S. D. López, and D. Arbó, "Intra- and intercycle interference of angle-resolved electron emission in laser-assisted XUV atomic ionization", J. Phys. B **51**, 055603 (2018) (cit. on p. 70).

[111]L. Zhang, X. Xie, S. Roither, D. Kartashov, Y. L. Wang, C. L. Wang, M. Schöffler, D. Shafir, P. B. Corkum, A. Baltuška, I. Ivanov, A. Kheifets, X. J. Liu, A. Staudte, and M. Kitzler, "Laser-sub-cycle two-dimensional electron-momentum mapping using orthogonal two-color fields", Phys. Rev. A **90**, 061401 (2014) (cit. on p. 70).

[112]M. Richter, M. Kunitski, M. Schöffler, T. Jahnke, L. P. H. Schmidt, M. Li, Y. Liu, and R. Dörner, "Streaking temporal double-slit interference by an orthogonal two-color laser field", Phys. Rev. Lett. **114**, 143001 (2015) (cit. on pp. 70, 191).

[113]X. Xie, T. Wang, S. Yu, X. Lai, S. Roither, D. Kartashov, A. Baltuška, X. Liu, A. Staudte, and M. Kitzler, "Disentangling intracycle interferences in photoelectron momentum distributions using orthogonal two-color laser fields", Phys. Rev. Lett. **119**, 243201 (2017) (cit. on p. 70).

[114]X. Xie, S. Roither, D. Kartashov, E. Persson, D. G. Arbó, L. Zhang, S. Gräfe, M. S. Schöffler, J. Burgdörfer, A. Baltuška, and M. Kitzler, "Attosecond probe of valence-electron wave packets by subcycle sculpted laser fields", Phys. Rev. Lett. **108**, 193004 (2012) (cit. on pp. 70, 85).

[115]M. Han, P. Ge, Y. Shao, M.-M. Liu, Y. Deng, C. Wu, Q. Gong, and Y. Liu, "Revealing the sub-barrier phase using a spatiotemporal interferometer with orthogonal two-color laser fields of comparable intensity", Phys. Rev. Lett. **119**, 073201 (2017) (cit. on p. 70).

[116]T. Nubbemeyer, K. Gorling, A. Saenz, U. Eichmann, and W. Sandner, "Strong-field tunneling without ionization", Phys. Rev. Lett. **101**, 233001 (2008) (cit. on p. 76).

[117]T. Brabec, M. Y. Ivanov, and P. B. Corkum, "Coulomb focusing in intense field atomic processes", Phys. Rev. A **54**, R2551 (1996) (cit. on p. 76).

[118]L. Arissian, C. Smeenk, F. Turner, C. Trallero, A. V. Sokolov, D. M. Villeneuve, A. Staudte, and P. B. Corkum, "Direct test of laser tunneling with electron momentum imaging", Phys. Rev. Lett. **105**, 133002 (2010) (cit. on pp. 78, 102).

[119]M. Richter, M. Kunitski M.and Schöffler, T. Jahnke, L. P. H. Schmidt, and R. Dörner, "Ionization in orthogonal two-color laser fields: origin and phase dependences of trajectory-resolved Coulomb effects", Phys. Rev. A **94**, 033416 (2016) (cit. on p. 79).

[120]M. Pitzer, M. Kunitski, A. S. Johnson, T. Jahnke, H. Sann, F. Sturm, L. P. H. Schmidt, H. Schmidt-Böcking, R. Dörner, J. Stohner, J. Kiedrowski, M. Reggelin, S. Marquardt, A. Schießer, R. Berger, and M. S. Schöffler, "Direct determination of absolute molecular stereochemistry in gas phase by Coulomb explosion imaging", Science **341**, 1096 (2013) (cit. on p. 85).

[121]M. Han, P. Ge, Y. Shao, Q. Gong, and Y. Liu, "Attoclock photoelectron interferometry with two-color corotating circular fields to probe the phase and the amplitude of emitting wave packets", Phys. Rev. Lett. **120**, 073202 (2018) (cit. on pp. 92, 118, 185).

[122]A. W. Bray, S. Eckart, and A. S. Kheifets, "Keldysh-Rutherford model for the attoclock", Phys. Rev. Lett. **121**, 123201 (2018) (cit. on pp. 92, 199).

[123]Y. Huismans, A. Rouzée, A. Gijsbertsen, J. H. Jungmann, A. S. Smolkowska, P. S. W. M. Logman, F. Lépine, C. Cauchy, S. Zamith, T. Marchenko, J. M. Bakker, G. Berden, B. Redlich, A. F. G. van der Meer, H. G. Muller, W. Vermin, K. J. Schafer, M. Spanner, M. Y. Ivanov, O. Smirnova, D. Bauer, S. V. Popruzhenko, and M. J. J. Vrakking, "Time-resolved holography with photoelectrons", Science **331**, 61 (2011) (cit. on p. 94).

[124]R. Xu, T. Li, and X. Wang, "Longitudinal momentum of the electron at the tunneling exit", Phys. Rev. A **98**, 053435 (2018) (cit. on pp. 100, 180).

[125]B. Feuerstein and U. Thumm, "On the computation of momentum distributions within wavepacket propagation calculations", J. Phys. B **36**, 707 (2003) (cit. on p. 100).

[126]J. Tian, X. Wang, and J. H. Eberly, "Numerical detector theory for the longitudinal momentum distribution of the electron in strong field ionization", Phys. Rev. Lett. **118**, 213201 (2017) (cit. on pp. 100, 180).

[127]X. Wang, J. Tian, and J. H. Eberly, "Extended virtual detector theory for strong-field atomic ionization", Phys. Rev. Lett. **110**, 243001 (2013) (cit. on p. 100).

[128]H. Ni, N. Eicke, C. Ruiz, J. Cai, F. Oppermann, N. I. Shvetsov-Shilovski, and L.-W. Pi, "Tunneling criteria and a nonadiabatic term for strong-field ionization", Phys. Rev. A **98**, 013411 (2018) (cit. on p. 100).

[129]I. Barth and O. Smirnova, "Nonadiabatic tunneling in circularly polarized laser fields. II. Derivation of formulas", Phys. Rev. A **87**, 013433 (2013) (cit. on pp. 101, 118, 125, 126, 167).

[130]A. N. Pfeiffer, C. Cirelli, A. S. Landsman, M. Smolarski, D. Dimitrovski, L. B. Madsen, and U. Keller, "Probing the longitudinal momentum spread of the electron wave packet at the tunnel exit", Phys. Rev. Lett. **109**, 083002 (2012) (cit. on pp. 102, 180).

[131]X. Sun, M. Li, J. Yu, Y. Deng, Q. Gong, and Y. Liu, "Calibration of the initial longitudinal momentum spread of tunneling ionization", Phys. Rev. A **89**, 045402 (2014) (cit. on pp. 102, 180).

[132]J.-W. Geng, L. Qin, M. Li, W.-H. Xiong, Y. Liu, Q. Gong, and L.-Y. Peng, "Nonadiabatic tunneling ionization of atoms in elliptically polarized laser fields", J. Phys. B **47**, 204027 (2014) (cit. on p. 102).

[133]E. E. Serebryannikov and A. M. Zheltikov, "Strong-field photoionization as excited-state tunneling", Phys. Rev. Lett. **116**, 123901 (2016) (cit. on p. 102).

[134]M. Li, J.-W. Geng, M. Han, M.-M. Liu, L.-Y. Peng, Q. Gong, and Y. Liu, "Subcycle nonadiabatic strong-field tunneling ionization", Phys. Rev. A **93**, 013402 (2016) (cit. on pp. 102, 180).

[135]M.-M. Liu, M. Li, Y. Shao, M. Han, Q. Gong, and Y. Liu, "Effects of orbital and Coulomb potential in strong-field nonadiabatic tunneling ionization of atoms", Phys. Rev. A **96**, 043410 (2017) (cit. on pp. 102, 126, 167).

[136]C. A. Mancuso, K. M. Dorney, D. D. Hickstein, J. L. Chaloupka, X.-M. Tong, J. L. Ellis, H. C. Kapteyn, and M. M. Murnane, "Observation of ionization enhancement in two-color circularly polarized laser fields", Phys. Rev. A **96**, 023402 (2017) (cit. on p. 105).

[137]J. Kaushal and O. Smirnova, "Nonadiabatic Coulomb effects in strong-field ionization in circularly polarized laser fields", Phys. Rev. A **88**, 013421 (2013) (cit. on p. 122).

[138]I. Barth and J. Manz, "Electric ring currents in atomic orbitals and magnetic fields induced by short intense circularly polarized π laser pulses", Phys. Rev. A **75**, 012510 (2007) (cit. on p. 123).

[139]T. Herath, L. Yan, S. K. Lee, and W. Li, "Strong-field ionization rate depends on the sign of the magnetic quantum number", Phys. Rev. Lett. **109**, 043004 (2012) (cit. on pp. 124, 125).

[140]S. Eckart, M. Kunitski, and R. Dörner, "Ringströme in einzelnen Atomen", Physik in unserer Zeit **49**, 162 (2018) (cit. on pp. 124, 128, 131, 145).

[141]X. Zhu, P. Lan, K. Liu, Y. Li, X. Liu, Q. Zhang, I. Barth, and P. Lu, "Helicity sensitive enhancement of strong-field ionization in circularly polarized laser fields", Opt. Express **24**, 4196 (2016) (cit. on p. 125).

[142]J. H. Bauer, F. Mota-Furtado, P. F. O'Mahony, B. Piraux, and K. Warda, "Ionization and excitation of the excited hydrogen atom in strong circularly polarized laser fields", Phys. Rev. A **90**, 063402 (2014) (cit. on pp. 125, 168).

[143]I. Barth and O. Smirnova, "Comparison of theory and experiment for nonadiabatic tunneling in circularly polarized fields", Phys. Rev. A **87**, 065401 (2013) (cit. on p. 125).

[144]B. Bergues, Y. Ni, H. Helm, and I. Y. Kiyan, "Experimental study of photodetachment in a strong laser field of circular polarization", Phys. Rev. Lett. **95**, 263002 (2005) (cit. on pp. 126, 167).

[145]J. Kaushal, F. Morales, and O. Smirnova, "Opportunities for detecting ring currents using an atto-clock setup", Phys. Rev. A **92**, 063405 (2015) (cit. on pp. 126, 167).

[146]Y. Li, P. Lan, H. Xie, M. He, X. Zhu, Q. Zhang, and P. Lu, "Nonadiabatic tunnel ionization in strong circularly polarized laser fields: counterintuitive angular shifts in the photoelectron momentum distribution", Opt. Express **23**, 28801 (2015) (cit. on pp. 126, 167).

[147]I. Barth and O. Smirnova, "Spin-polarized electrons produced by strong-field ionization", Phys. Rev. A **88**, 013401 (2013) (cit. on p. 126).

[148] A. Hartung, F. Morales, M. Kunitski, K. Henrichs, A. Laucke, M. Richter, T. Jahnke, A. Kalinin, M. Schöffler, L. P. H. Schmidt, M. Ivanov, O. Smirnova, and R. Dörner, "Electron spin polarization in strong-field ionization of xenon atoms", Nat. Photonics **10**, 526 (2016) (cit. on p. 126).

[149] D. Trabert, A. Hartung, S. Eckart, F. Trinter, A. Kalinin, M. Schöffler, L. P. H. Schmidt, T. Jahnke, M. Kunitski, and R. Dörner, "Spin and angular momentum in strong-field ionization", Phys. Rev. Lett. **120**, 043202 (2018) (cit. on pp. 126, 168).

[150] M.-M. Liu, Y. Shao, M. Han, P. Ge, Y. Deng, C. Wu, Q. Gong, and Y. Liu, "Energy- and momentum-resolved photoelectron spin polarization in multiphoton ionization of Xe by circularly polarized fields", Phys. Rev. Lett. **120**, 043201 (2018) (cit. on p. 126).

[151] H. Haken and H. Wolf, *"Atom-und Quantenphysik"*, ISBN 3540612378, 6th ed. (Springer, 1996) (cit. on p. 147).

[152] L. Torlina and O. Smirnova, "Time-dependent analytical R-matrix approach for strong-field dynamics. I. One-electron systems", Phys. Rev. A **86**, 043408 (2012) (cit. on p. 157).

[153] I. Barth and O. Smirnova, "Hole dynamics and spin currents after ionization in strong circularly polarized laser fields", J. Phys. B **47**, 204020 (2014) (cit. on p. 159).

[154] A. N. Pfeiffer, S. G. Sayres, and S. R. Leone, "Calculation of valence electron motion induced by sequential strong-field ionisation", Mol. Phys. **111**, 2283 (2013) (cit. on p. 159).

[155] A. Fleischer, H. J. Wörner, L. Arissian, L. R. Liu, M. Meckel, A. Rippert, R. Dörner, D. M. Villeneuve, P. B. Corkum, and A. Staudte, "Probing angular correlations in sequential double ionization", Phys. Rev. Lett. **107**, 113003 (2011) (cit. on p. 161).

[156] L. Fechner, N. Camus, J. Ullrich, T. Pfeifer, and R. Moshammer, "Strong-field tunneling from a coherent superposition of electronic states", Phys. Rev. Lett. **112**, 213001 (2014) (cit. on p. 161).

[157] M. Ilchen, N. Douguet, T. Mazza, A. J. Rafipoor, C. Callegari, P. Finetti, O. Plekan, K. C. Prince, A. Demidovich, C. Grazioli, L. Avaldi, P. Bolognesi, M. Coreno, M. Di Fraia, M. Devetta, Y. Ovcharenko, S. Düsterer, K. Ueda, K. Bartschat, A. N. Grum-Grzhimailo, A. V. Bozhevolnov, A. K. Kazansky, N. M. Kabachnik, and M. Meyer, "Circular dichroism in multiphoton ionization of resonantly excited He^+ ions", Phys. Rev. Lett. **118**, 013002 (2017) (cit. on p. 168).

[158] D. Ayuso, A. Jiménez-Galán, F. Morales, M. Ivanov, and O. Smirnova, "Attosecond control of spin polarization in electron–ion recollision driven by intense tailored fields", New J. Phys. **19**, 073007 (2017) (cit. on p. 168).

[159] D. Shafir, H. Soifer, B. D. Bruner, M. Dagan, Y. Mairesse, S. Patchkovskii, M. Ivanov, O. Smirnova, and N. Dudovich, "Resolving the time when an electron exits a tunnelling barrier", Nature **485**, 343 (2012) (cit. on p. 180).

[160]M. Li, M.-M. Liu, J.-W. Geng, M. Han, X. Sun, Y. Shao, Y. Deng, C. Wu, L.-Y. Peng, Q. Gong, and Y. Liu, "Experimental verification of the nonadiabatic effect in strong-field ionization with elliptical polarization", Phys. Rev. A **95**, 053425 (2017) (cit. on p. 180).

[161]S. Beaulieu, A. Comby, A. Clergerie, J. Caillat, D. Descamps, N. Dudovich, B. Fabre, R. Géneaux, F. Légaré, S. Petit, B. Pons, G. Porat, T. Ruchon, R. Taïeb, V. Blanchet, and Y. Mairesse, "Attosecond-resolved photoionization of chiral molecules", Science **358**, 1288 (2017) (cit. on p. 185).

[162]J. Vos, L. Cattaneo, S. Patchkovskii, T. Zimmermann, C. Cirelli, M. Lucchini, A. Kheifets, A. S. Landsman, and U. Keller, "Orientation-dependent stereo wigner time delay and electron localization in a small molecule", Science **360**, 1326 (2018) (cit. on p. 185).

[163]K. Fehre, S. Eckart, M. Kunitski, M. Pitzer, S. Zeller, C. Janke, D. Trabert, J. Rist, M. Weller, A. Hartung, L. P. H. Schmidth, T. Jahnke, R. Berger, R. Dörner, and M. S. Schöffler, "Enantioselective fragmentation of an achiral molecule in a strong laser field", Sci. Adv. **5**, eaau7923 (2019) (cit. on p. 185).

[164]A. M. Weiner, *Ultrafst optics*, ISBN 9780471415398 (John Wiley & Sons, 2009) (cit. on p. 187).

Deutsche Zusammenfassung

Die vorliegende Arbeit basiert auf vier Publikationen des Autors dieser Arbeit [23–26], wobei die vorliegende Arbeit ausführlicher ist und die Erkenntnisse zusammenhängend diskutiert werden. Die experimentellen Details, die verwendeten theoretischen Methoden, der Stand der Forschung und die physikalischen Grundlagen werden ausführlicher beschrieben und anhand zusätzlicher Abbildungen illustriert.

Die grundlegende Frage der vorliegenden Arbeit ist: Was passiert, wenn hochintensives Licht mit einer Spitzenintensität von etwa $10^{15}\mathrm{W/cm^2}$ dazu führt, dass ein Elektron aus einem Atom herausgelöst wird?

In der Einleitung zu der vorliegenden Arbeit wird das Thema dieser Arbeit, die nicht-adiabtische Tunnelionisation in hochintensiven, maßgeschneiderten Zwei-Farben-Laserfeldern motiviert und in Kapitel 2 werden einige relevante Beispiele für die Umrechnung von SI-Einheiten zu atomaren Einheiten gezeigt.

Anschließend werden in Kapitel 3 die grundlegenden Konzepte der Starkfeldionisation, die Multi-Photonen-Ionisation, die adiabatische Tunnelionisation und die nicht-adiabatische Tunnelionisation unter Verweis auf die Literatur eingeführt.

Die verwendeten experimentellen Methoden und der experimentelle Aufbau werden in Kapitel 4 vorgestellt. Die nötigen, hohen Lichtintensitäten werden im Rahmen dieser Arbeit experimentell durch Femtosekunden-Laserpulse erreicht. Die resultierenden Starkfeldionisationsprozesse finden im Regime des nicht-adiabatischen Tunnelns statt, wobei jeweils Helium, Neon oder Argon ionisiert werden. Die Ionisation findet in einer Vakuumapparatur statt, in der die erzeugten Laserpulse in einen kalten Edelgasstrahl fokussiert werden. Das Volumen, in dem der Gasstrahl mit dem Laserfokus überlappt, wird Interaktionsvolumen genannt. Der experimentelle Aufbau besteht somit aus drei Komponenten: Einem kommerziellen Lasersystem, einem interferometrischen Zwei-Farben-Aufbau und einem COLTRIMS[187] Reaktionsmikroskop. Bei der Beschreibung des Aufbaus liegt der Fokus auf dem interferometrischen Zwei-Farben-Aufbau, da dieser Aufbau die Grundlage für die Experimente legt und im Rahmen des Projekts, welches zu dieser Arbeit geführt hat, geplant und gebaut wurde. Der interferometrische Aufbau ermöglicht es, aus linear polarisierten Femtosekunden-Laserpulsen bei einer Zentralwellenlänge von 780 nm zwei neue Femtosekunden-Laserpulse zu erzeugen. Einer der Laserpulse hat eine Zentralwellenlänge von 390 nm und der andere

[187] COLTRIMS ist ein Akronym für “COLd Target Recoil Ion Momentum Spectroscopy”.

Laserpuls hat eine Zentralwellenlänge von 780 nm. Für beide Laserpulse kann der Polarisationszustand und die Intensität präzise eingestellt werden. Darüber hinaus können die beiden erzeugten Laserpulse auch zeitlich überlappt und die relative Phase zwischen den beiden Laserpulsen kann präzise eingestellt werden. Es ergeben sich sieben Freiheitsgrade, mit denen polarisationsgeformte Femtosekunden-Zwei-Farben-Laserfelder mit nicht-trivialen Feldgeometrien erzeugt werden können. Alle sieben Freiheitsgrade sind im Experiment motorisiert ansteuerbar und können mit einem speziell entwickelten Computerprogramm reproduzierbar und präzise eingestellt werden. Schließlich wird dargelegt, wie herausgefunden wurde, welche Laborparameter gesetzt werden müssen, damit im Interaktionsvolumen in der Vakuumapparatur ein definiertes, maßgeschneidertes, elektrisches Feld erzeugt werden kann. Zwei wichtige Kategorien von Zwei-Farben-Laserfeldern sind entgegengesetzt-rotierende zirkular polarisierte Zwei-Farben-Felder (CRTC Felder, englisch für "counter-rotating circularly polarized two-color laser fields") und in-die-gleiche-Richtung-rotierende zirkular polarisierte Zwei-Farben-Felder (CoRTC Felder, englisch für "co-rotating circularly polarized two-color laser fields"), wobei in beiden Fällen die beiden einfarbigen Laserpulse zeitlich überlappen, sodass ein Zwei-Farben Laserfeld entsteht.

In Kapitel 5 werden die relevanten theoretischen Grundlagen vorgestellt. Diese sind die Sattelpunkt-Starkfeldnäherung (SFA, englisch für "saddle point strong field approximation") und ein semi-klassisches, zweistufiges trajektorienbasiertes Model (SCTS[188], englisch für "Semi-Classical Two-Step"). Die SFA ist ein weit verbreiteter, quantenmechanischer Ansatz, der unter Verweis auf die Literatur eingeführt wird und anschließend genutzt wird, um den Übergang vom adiabatischen Tunneln zum nicht-adiabatischen Tunneln in Ein- und Zwei-Farben-Feldern zu illustrieren. Anschließend wird das SCTS Model unter Verweis auf die Literatur eingeführt. Im SCTS Model wird Tunnelionisation als ein adiabatischer Tunnelvorgang und eine anschließende klassische Propagation des Elektrons im Summenpotential aus Laserpotential und Atompotential beschrieben, wobei der resultierenden Elektronentrajektorie im Ortsraum an jedem Punkt eine semi-klassische Phase zugeordnet werden kann. Dies ermöglicht die Modellierung von Interferenzeffekten im Endimpulsraum. Es werden Beispiele für einfarbige Laserfelder sowie eine neue Methode zur Konvergenzverbesserung vorgestellt. Weiterhin werden je eine Trajektorien in einem Ein- und einem Zwei-Farben-Feld gezeigt. Das Zwei-Farben-Feld ist ein CRTC Feld, bei dem das Elektron nach dem Tunnelprozess noch einmal sehr nah an dem Ionenrumpf vorbeikommt und somit gestreut

[188] Außerdem wird auch ein CTS Modell eingeführt, das äquivalent zum SCTS Modell ist, aber die semi-klassische Phase vernachlässigt.

wird.

Im Kern der vorliegenden Arbeit werden vier Experimente diskutiert, die im Regime der nicht-adiabatischen Tunnelionisation durchgeführt wurden. Nachdem das Elektron den Tunnelausgang mit einem gegebenen Startimpuls verlassen hat, wird es durch das polarisationsgeformte Femtosekunden-Zwei-Farben-Feld getrieben, wobei auch das langreichweitige Potential des verbleibenden Ions noch einen Einfluss auf das Elektron hat. Die dreidimensionale Impulsverteilung des Elektrons bzw. der Elektronen und der Ladungszustand des Ions sowie eine Impulskomponente des erzeugten Ions werden mit einem COLTRIMS Reaktionsmikroskop detektiert. Um den Prozess des nicht-adiabatischen Tunnelns zu untersuchen, werden die Eigenschaften des polarisationsgeformten Femtosekunden-Zwei-Farben-Laserfeldes variiert und die Änderungen der mit dem COLTRIMS Reaktionsmikroskop gemessenen Größen werden analysiert.

In Kapitel 6 wird untersucht unter welchen Bedingungen es zur nicht-sequentiellen Doppelionisation von Argon bzw. der Elektronenrückstreuung in CRTC-Feldern kommt. Das Verhältnis von Zweifach- zu Einfachionisation wird in Abhängigkeit des Feldverhältnisses der beiden einfarbigen Laserpulse untersucht. Es wird gefolgert, dass die nicht-sequentielle Doppelionisation von Argon am wahrscheinlichsten ist, wenn die Feldamplitude des Laserpulses mit der Zentralwellenlänge von 390 nm etwa $\frac{3}{2}$-mal so groß ist wie die Feldamplitude des Laserpulses mit der Zentralwellenlänge von 780 nm. Mit Hilfe eines trajektorienbasierten, theoretischen Modells kann gezeigt werden, dass die Doppelionisation folgendermaßen abläuft: Nachdem das erste Elektron Argon durch einen Tunnelprozess verlassen hat, wird es vom Zwei-Farben-Laserpuls zurück zu seinem Ionenrumpf getrieben und es kommt zu einer inelastischen Rückstreuung am einfach geladenen Ion, wobei das Ion angeregt wird. Der Endimpuls des streuenden Elektrons kann durch das negative Vektorpotential zum Zeitpunkt der Rückstreuung angenähert werden. In einem darauffolgenden Feldmaxima des kombinierten elektrischen Feldes kann aus dem angeregten Ion ein Elektron gelöst werden, wobei der Endimpuls dieses Elektrons durch das negative Vektorpotential zum Zeitpunkt der Ionisation des zweiten Elektrons angenähert werden kann. In den durchgeführten Experimenten wird nur der Impuls eines Elektrons direkt gemessen. Unter der Annahme, dass das zweite Elektron bei der nicht-sequentiellen Doppelionisation von Argon die gleiche Verteilung hat wie das erste Elektron bei der Einfachionisation von Argon, kann die Impulsverteilung des ersten Elektrons, das bei der nicht-sequentiellen Doppelionisation von Argon entsteht, berechnet werden. Die beiden so gewonnenen Verteilungen beinhalten allerdings keine Information über die Korrelation der beiden Elektronen. Dieses Problem kann dadurch gelöst

werden, dass das Impulsspektrum des nicht direkt gemessenen Elektrons in der Polarisationsebene anhand des gemessenen zweifach geladenen Argon Ions und unter Ausnutzung der Impulserhaltung tomographisch rekonstruiert wird und für die tomographische Rekonstruktion nur Ereignisse verwendet werden, für die das direkt gemessene Elektron in einem vorher festgelegten Teilbereich des Endimpulsraums liegt. Wählt man hierzu einen Bereich, in den das Elektron nur durch eine Rückstreuung kommen kann, so ergibt sich für das tomographisch rekonstruierte Elektron ein Impulsspektrum und es ist bekannt, dass dieses Elektron dem zeitlich später emittierten Elektron zugeordnet werden kann. Da der wahrscheinlichste Endimpuls in dem so gewonnenen Impulsspektrum mit dem negativen Vektorpotential des Feldmaximums übereinstimmt, bestätigt dieses Ergebnis das zuvor aufgestellte Modell. Weiterhin werden in Kapitel 6 zweidimensionale Projektionen in Zylinderkoordinaten und einige zweidimensionale Schnitte aus dem dreidimensionalen Impulsraum gezeigt.

In Kapitel 7 wird eine ausgeprägte und charakteristische Struktur im Endimpulsraum für niedrige Elektronenenergien sowie eine Zwei-Wege Interferenz in der dreidimensionalen Impulsverteilung als Intensitätsmodulation entlang der Lichtausbreitungsrichtung für die Ionisation von Helium in einem CRTC Feld beobachtet. Der Ursprung der ausgeprägten und charakteristischen Struktur im Endimpulsraum für niedrige Elektronenenergien und der Ursprung der Zwei-Wege Interferenz wird unter Zuhilfenahme des SCTS Modells ergründet. Die charakteristische Struktur im Endimpulsraum für niedrige Elektronenenergien wird darauf zurückgeführt, dass nach Ende des Femtosekunden-Laserpulses die Elektronen vom langreichweitigen atomaren Potential abgebremst werden. Außerdem wird gezeigt, dass die Zwei-Wege Interferenz zwei Tunnelzeitpunkten zugeordnet werden kann, die weniger als eine drittel Lichtschwingung (866 as) auseinanderliegen. Außerdem wird deutlich, dass sowohl der Einfluss des Coulombpotential als auch die Startimpulse am Tunnelausgang berücksichitgt werden müssen, um die Interferenz zu beschreiben. Weiterhin wird eine Methode vorgestellt, die auf einer Fouriertransformation beruht und die Drehwinkel der dreizählig symmetrischen Endimpulsverteilung in Abhängigkeit der Impulskomontente in der Lichtausbreitungsrichtung und der radialen Impulskomonte in der Polarisationsebene als zweidimensionale Verteilung farbkodiert. Die Messkampanie für Ref. [24] wurde mit einem kombinierten Gasjet aus Helium und Neon durchgeführt. In Ref. [24] werden nur die Daten für Helium gezeigt. In der vorliegenden Arbeit werden auch die Daten für Neon diskutiert. Weiterhin wird auf die Unterschiede in den Impulsspektren für die beiden Edelgase eingegangen und festgestellt, dass die Unterschiede klein sind.

In Kapitel 8 wird ein experimenteller Zugang zur Bestimmung des Versatzes der Endimpulsverteilung am Tunnelausgang vorgestellt, der dazu führt, dass die radiale Impulsverteilung in der Polarisationsebene bei größeren Impulsen zu finden ist, als es aufgrund des negativen Vektorpotentials zu erwarten wäre. Für typische Laserparameter und Wellenlängen um 780 nm sowie Endimpulsverteilungen mit Radialimpulsen von etwa 1 a.u. ergibt sich ein Impulsversatz am Tunnelausgang von etwa $\frac{2}{10}$ a.u. Die verwendete experimentelle Strategie nutzt den Vergleich von CRTC mit CoRTC Feldern, die fast zirkular polarisiertem Licht entsprechen. Die Feldstärke des Laserpulses mit einer Zentralwellenlänge von 780 nm ist dabei etwa 10-mal stärker als die des Laserpulses bei einer Zentralwellenlänge von 390 nm. Die Helizität des Laserpulses mit einer Zentralwellenlänge von 780 nm wird im Verlauf des Experiments nicht verändert. Durch Invertieren der Helizität des Laserpulses bei der Zentralwellenlänge von 390 nm wird zwischen dem CRTC und dem CoRTC Feld umgeschaltet. Der Vergleich der beiden resultierenden Elektronenimpulsverteilungen erlaubt es Elektronen zu vergleichen, für die die Vektorpotentiale zum Zeitpunkt des Tunnelns identisch waren, wobei jedoch unterschiedliche effektive Drehgeschwindigkeiten vorlagen. Als effektive Drehgeschwindigkeit wird die Winkelgeschwindigkeit des Tunnelausgangs in der Polarisationsebene bezeichnet. Es wird gezeigt, dass die effektive Drehgeschwindigkeit einen großen Einfluss auf den nicht-adiabatischen Versatz der Startimpulse am Tunnelausgang hat. Die Ergebnisse werden mit den Ergebnissen des SCTS Modells und der SFA verglichen. Das SCTS Modell ist nicht in der Lage die experimentellen Ergebnisse zu erklären. Im Gegensatz dazu kann die SFA die experimentellen Ergebnisse sehr gut beschreiben. Das ist bemerkenswert, da beide Modelle als komplementär angesehen werden können. Im SCTS Modell wird der Tunnelprozess adiabatisch beschrieben und nach dem Tunneln wird das Coulomb Potential berücksichtigt. In SFA werden nicht-adiabatische Prozesse nicht vernachlässigt, allerdings wird das Coulomb-Potential nach dem Tunnelprozess nicht berücksichtigt. In einem nächsten Schritt wird in Kapitel 8 die dreidimensionale Impulsverteilung für ein Ein-Farben-Laserfeld bei einer Zentralwellenlänge von 780 nm untersucht. Es wird gezeigt, dass die Nicht-Adiabatizität vom Betrag des Impulses in der Lichtausbreitungsrichtung abhängt und geschlussfolgert, dass die Energie der Impulskomponente in Lichtausbreitungsrichtung ($\frac{1}{2}p_x^2$) einen äquivalenten Einfluss auf die Nicht-Adiabatizität hat wie eine Erhöhung des Ionisationspotentials. Der Einfluss der effektiven Drehgeschwindigkeiten des elektrischen Feldes und der Betrag der Impulskomponente in der Lichtausbreitungsrichtung werden verwendet, um den Keldysh-Parameter, der üblicherweise mit der Nicht-Adiabatizität in Zusammenhang

gebracht wird, zu verallgemeinern. Aufbauend auf den Messdaten, die für das Ein-Farben-Laserfeld erhoben wurden, wird ein mechanistisches Modell eingeführt, dass auf Ideen von Klaiber et al. [47, 48] zurückgeht und in dem nicht-adiabatisches Tunneln als ein zweistufiger Prozess beschrieben wird. Im ersten Schritt wird ein virtuelles Zwischenniveau durch einen Multi-Photonenprozess populiert. Im zweiten Schritt findet ein adiabatischer Tunnelprozess von diesem virtuellen Zwischenniveau aus statt. In Kapitel 8 wird durch einen Vergleich mit SFA Rechnungen gezeigt, dass so die Magnetquantenzahl des virtuell populierten Zwischenniveaus experimentell zugänglich wird.

In Kapitel 9 wird der Einfluss der Magnetquantenzahl auf die Ionisationswahrscheinlichkeit und die Elektronenimpulsverteilung mit einem Anrege-Abfrage Experiment untersucht. Es wird experimentell gezeigt, dass Elektronen mit $m = -1$ bevorzugt ionisiert werden[189]. Da das Fehlen eines Elektrons mit einer definierten Magnetquantenzahl in einem sonst voll besetzten p-Orbital einen Netto-Ringstrom zur Folge hat, wurde gezeigt, dass sich Ringströme auf ultrakurzen Zeitskalen präparieren und abfragen lassen. Der Anregepuls ist ein zirkular polarisierter Femtosekunden-Laserpuls mit einer Zentralwellenlänge von 390 nm. Die Abfrage wird 200 Femtosekunden später durch einen elliptisch polarisierten Femtosekunden-Laserpuls bei einer Zentralwellenlänge von 780 nm realisiert. Beide Laserpulse sind zeitlich getrennt, wie durch eine experimentell gemessene Kreuzkorrelation gezeigt wird. Der Anregepuls löst eine Einfachionisation von Argon aus. Der Abfragepuls löst die Doppelionisation des einfach geladenen Argon-Ions sequentiell aus. Es wird beobachtet, dass die Wahrscheinlichkeit ein doppelt geladenes Argon Ion zu messen von der Helizität des Anregepulses abhängt. Daraus kann gefolgert werden, dass das einfach geladene Ion einen Zustand aufweist, in dem die Helizität des Anregepulses im Vorzeichen der Magnetquantenzahl kodiert ist. Diese Einsicht wird verwendet, um den Doppelionisationsschritt genauer zu untersuchen und die Impuls- und Energiespektren für das im Abfrageschritt emittierte Elektron in Abhängigkeit der Magnetquantenzahl dieses Elektrons im gebundenen Zustand zu messen. Die gemessenen Energie- und Impulsspektren für Elektronen mit $m = -1$ und $m = +1$ im gebundenen Zustand werden diskutiert. Unter der Annahme, dass Drehimpulserhaltung näherungsweise auch während des Tunnelprozesses gilt, wird aus den Messdaten gefolgert, dass Elektronen mit $m = -1$ bevorzugt das Atom verlassen. Dieses experimentelle Ergebnis kann durch das zweistufige, mechanistische Modell des nicht-adiabatischen Tunnelns erklärt werden: Für nahezu zirkular polarisiertes Licht und die Absorption von

[189] Elektronen mit $m = -1$ sind hier Elektronen, deren semi-klassiche Drehrichtung der Drehrichtung des elektrischen Feldes des ionisierenden Laserpulses entgegengesetzt ist.

n Photonen im ersten Schritt ergibt sich der Betrag der Magnetquantenzahl des virtuellen Zwischenniveaus zu $|m+n|$. Folglich ist für $n > 0$ die Magnetquantenzahl und damit der Startimpuls am Tunnelausgang für $m = -1$ kleiner als für $m = +1$. Da höhere Startimpulse am Tunnelausgang, wie in Kapitel 8 beschrieben, äquivalent zu einer Erhöhung des Ionisationspotentials sind, ist plausibel, warum Elektronen mit $m = -1$ bevorzugt aus dem Atom gelöst werden. Abschließend werden Winkelunterschiede in der Elektronenimpulsverteilung für $m = -1$ und $m = +1$ diskutiert.

In Kapitel 10 werden Anhaltspunkte für einen Versatz der Startimpulsverteilung entlang der Richtung diskutiert, in die das Laserfeld zu dem Zeitpunkt zeigt, in dem das Elektron seinen gebundenen Zustand verlässt. Dazu werden die Messdaten aus Kapitel 8 aus einer neuen Perspektive analysiert, sodass der Startimpuls entlang der Tunnelrichtung zugänglich wird. Dies ist interessant, da ein solcher endliche Impulsversatz ein Widerspruch zur Tunnelionisation darstellt. Es wird gezeigt, dass das CTS Modell nicht in der Lage ist, die experimentellen Beobachtungen zu erklären. Der Unterschied zwischen dem CTS Modell und dem Experiment ist für das CRTC Feld ausgeprägter als für das CoRTC Feld. Allerdings kann durch einen ad hoc eingeführten Startimpuls in Tunnelrichtung, der von der Ableitung des elektrischen Feldes abhängt, eine bessere Übereinstimmung von CTS und Experiment erreicht werden. Anschließend wird das mechanistische Modell zur nicht-adiabatischen Tunnelionisation verwendet und es werden damit hohe radiale Impulse in der Polarisationsebene analysiert. Es ergibt sich, dass die resultierenden hohen Werte für die Magnetquantenzahl nur möglich sind, wenn das virtuelle Zwischenniveau energetisch über dem Maximum der Potentialbarriere liegt, welche eigentlich durch den Tunnelprozess überwunden wird. Dies legt nahe, dass eine Über-die-Barriere-Ionisation möglich ist und keine Tunnelionisation stattfindet. Es wird spekuliert, dass es somit denkbar wäre, dass eine "nicht-adiabatische Über-die-Barriere-Ionisation" (NAOBI, englisch für "non-adiabatic over-the-barrier ionization") stattfindet. Die Voraussetzungen für diesen Ionisationskanal werden abgeschätzt und es wird begründet, warum ein solcher Prozess in CRTC Feldern wahrscheinlicher wäre als in einem CoRTC Feld.

Abschließend werden in Kapitel 11 die Ergebnisse und die neu entwickelten Methoden zusammengefasst, die experimentellen Unzulänglichkeiten beschrieben und ein Ausblick gegeben.

Im Anhang wird, neben weiteren Details, auch ein Zusatz zum interferometrischen Laseraufbau beschrieben, mit dem die relative Phase zwischen den beiden Laserpulsen mit optischen Methoden aktiv stabilisiert werden kann (Kapitel A.4.1). Weiterhin sind im Appendix

weitere Details zur Geometrie des Laserstrahls im Interaktionsvolumen (Kapitel A.1) und der Korrektur der relativen Phase zwischen dem Laserpuls bei einer zentralen Wellenlänge von 390 nm und dem Laserpuls bei einer zentralen Wellenlänge von 780 nm zu finden (Kapitel A.2). Zusätzlich werden Messdaten für ein Zwei-Farben-Laserfeld gezeigt, bei dem der Laserpuls bei der Zentralwellenlänge von 390 nm linear polarisiert ist und der Laserpuls bei der Zentralwellenlänge von 780 nm weiterhin zirkular polarisiert ist. Die gemessenen Impulsspektren sind für verschiedene relative Phasen zwischen den beiden Ein-Farben-Laserpulsen gezeigt (Kapitel A.3). Darüber hinaus sind weitere Details zu den Ergebnissen aus Kapitel 6 und 7 im Appendix zu finden.

Acknowledgments

Research is a team effort. Without the help of many others it would not have been possible to obtain the results that are presented in this thesis.

First and foremost, I would like to extend my sincere gratitude to Prof. **Reinhard Dörner** for the opportunity to be part of his research group and for his trust. I would like to thank him for his feedback during all stages of the projects that led to this thesis and his intuition for studying two-color tailored intense light fields. I am indebted to him for many exciting discussions and the continuous exchange of ideas. Finally, I would like to thank him for gathering so many motivated and outstanding physicists who enjoy being part of a team, which is the essential ingredient for the outstanding atmosphere in the group.

I am indebted to **Maksim Kunitski** for sharing his expertise about COLTRIMS reaction microscopes and lasers, for helping me to find my place within the group and for many discussions about ideas regarding the best way to build a fully-automated interferometric two-color setup. Moreover, I would like to thank him for aligning the oscillator and the amplifier of the laser system that was used for this thesis. He developed the initial first version of the semi-classical simulation that all the classical simulations that are shown in this thesis are built on. Finally, I greatly appreciated his professional attitude and his valuable feedback during all stages of the work for this thesis.

I would like to thank **Martin Richter** for sharing his two-color laser know-how and introducing many basic concepts of strong field physics to me. I would like to thank him for his calm and professional attitude and for everything I was able to learn from him.

A huge thank you to **Markus Schöffler** for his ongoing support, especially on the long road to discovering the origin of the „banana-like distribution“and for the great time we had organizing cake for 400 people and editing the daily conference-newspaper during the conference ECAMP12 in Frankfurt.

I would like to thank Prof. **Till Jahnke** for the way he is, supportive and genuinely interested in each and every student. I valued his advice and his sharing of his perspective on strong field physics. He taught me to always strive for the highest scientific standards and to never rest until the best possible explanation for a given problem has been found.

Lothar Schmidt kept the group's hardware running. I would like to thank him for his help with the electronics and many discussions about atoms, electrons, electronic signals, numerical simulations and safety in the lab.

Prof. **Horst Schmidt-Böcking** founded the atomic physics group in Frankfurt many years

ago. I would like to thank him for establishing the positive atmosphere in the group. Further, I am grateful for many discussions about his perspective on atoms, electrons and angular momentum. I would like to thank him for questioning everything which is not obviously true and for never giving up trying to find a deeper understanding of how the world works.
Alex Hartung and **Jonas Rist** are the best office neighbors one can imagine. I would like to thank them for many discussions during countless group barbecue events and unforgettable times in Cairns, Berkeley and Shanghai. I would like to thank **Kilian Fehre** for many discussions that not only led to the discovery of the "banana-like distribution", but also made huge amounts of chocolate disappear.
I am grateful to **Nikolai Schlott**, **Andreas Pier**, **Nico Strenger**, and **Daniel Pitters** for their contributions while they were working on their theses. It was great being your supervisor and I learned at least as much as you did.
I am indebted to **Marianne Frey** for her help with many organizational issues from my employment contract to travel billing.

I greatly appreciated **Manfred Lein** and **Nicolas Eicke** sharing their expertise about saddle point strong field approximation and providing a computer program to perform calculations using the saddle point strong field approximation.

I would like to thank **Achim Czasch**, **Tobias Bauer**, **Hendrik Sann**, and **Klaus Ullmann-Pfleger** for their help during the implementation of the software that controlled the motorized translation stages.

A huge thank you to **Daniel Trabert**, **Florian Trinter**, **Markus Waitz**, **Christian Janke**, **Kevin Henrichs**, **Miriam Weller**, **Gregor Kastirke**, **Sven Schößler**, **Tobias Bauer**, **Hendrik Sann**, and **Sven Grundmann** for the great time at beamtimes, conferences and group events. I would like to thank **Gregor Kastirke** for organizing many of the group events.

I am indebted to Prof. **Heinz Hänel** for his invaluable advice not to underestimate the Goethe University Frankfurt during my search for a Ph.D. position.

I am sincerely grateful to **Edda Krücke** for her advice regarding the layout of text and figures. I would like to thank **Kilian Fehre** for partial proofreading and providing comments. I would like to express the deepest appreciation to **Linda Liebers** and **Cynthia Trendafilova** for partial proofreading regarding the English language and for providing comments. I would like to thank **Edith Eckart**, **Christine Eckart**, and **Thomas Eckart** for proofreading the German summaries. I admit that it was my choice whether or not to follow their suggestions. All remaining mistakes are solely my responsibility.

Last, but certainly not least, I would like to acknowledge the love and support of my family and friends. Without them this thesis would not have been possible.

Publications

- C. Riek, D. V. Seletskiy, A. S. Moskalenko, J. F. Schmidt, P. Krauspe, S. Eckart, S. Eggert, G. Burkard, and A. Leitenstorfer, "Direct sampling of electric-field vacuum fluctuations", Science **350**, 420 (2015)
- S. Eckart, M. Richter, M. Kunitski, A. Hartung, J. Rist, K. Henrichs, N. Schlott, H. Kang, T. Bauer, H. Sann, L. P. H. Schmidt, M. Schöffler, T. Jahnke, and R. Dörner, "Nonsequential double ionization by counterrotating circularly polarized two-color laser fields", Phys. Rev. Lett. **117**, 133202 (2016)
- C. W. McCurdy, T. N. Rescigno, C. S. Trevisan, R. R. Lucchese, B. Gaire, A. Menssen, M. S. Schöffler, A. Gatton, J. Neff, P. M. Stammer, J. Rist, S. Eckart, B. Berry, T. Severt, J. Sartor, A. Moradmand, T. Jahnke, A. L. Landers, J. B. Williams, I. Ben-Itzhak, R. Dörner, A. Belkacem, and T. Weber, "Unambiguous observation of F-atom core-hole localization in CF_4 through body-frame photoelectron angular distributions", Phys. Rev. A **95**, 011401 (2017)
- D. Trabert, A. Hartung, S. Eckart, F. Trinter, A. Kalinin, M. Schöffler, L. P. H. Schmidt, T. Jahnke, M. Kunitski, and R. Dörner, "Spin and angular momentum in strong-field ionization", Phys. Rev. Lett. **120**, 043202 (2018)
- S. Eckart, M. Kunitski, M. Richter, A. Hartung, J. Rist, F. Trinter, K. Fehre, N. Schlott, K. Henrichs, L. H. Schmidt, T. Jahnke, M. Schöffler, K. Liu, I. Barth, J. Kaushal, F. Morales, M. Ivanov, O. Smirnova, and R. Dörner, "Ultrafast preparation and detection of ring currents in single atoms", Nat. Phys. **14**, 701 (2018)
- K. Henrichs, S. Eckart, A. Hartung, D. Trabert, J. Rist, H. Sann, M. Pitzer, M. Richter, H. Kang, M. S. Schöffler, M. Kunitski, T. Jahnke, and R. Dörner, "Experimental evidence for selection rules in multiphoton double ionization of helium and neon", Phys. Rev. A **97**, 031405 (2018)
- S. Eckart, M. Kunitski, I. Ivanov, M. Richter, K. Fehre, A. Hartung, J. Rist, K. Henrichs, D. Trabert, N. Schlott, L. P. H. Schmidt, T. Jahnke, M. S. Schöffler, A. Kheifets, and R. Dörner, "Subcycle interference upon tunnel ionization by counter-rotating two-color fields", Phys. Rev. A **97**, 041402 (2018)
- H. Kang, K. Henrichs, M. Kunitski, Y. Wang, X. Hao, K. Fehre, A. Czasch, S. Eckart, L. P. H. Schmidt, M. Schöffler, T. Jahnke, X. Liu, and R. Dörner, "Timing recollision

in nonsequential double ionization by intense elliptically polarized laser pulses", Phys. Rev. Lett. **120**, 223204 (2018)

- H. Kang, K. Henrichs, Y. Wang, X. Hao, S. Eckart, M. Kunitski, M. Schöffler, T. Jahnke, X. Liu, and R. Dörner, "Double ionization of neon in elliptically polarized femtosecond laser fields", Phys. Rev. A **97**, 063403 (2018)

- S. Eckart, M. Kunitski, and R. Dörner, "Ringströme in einzelnen Atomen", Physik in unserer Zeit **49**, 162 (2018)

- A. W. Bray, S. Eckart, and A. S. Kheifets, "Keldysh-Rutherford model for the attoclock", Phys. Rev. Lett. **121**, 123201 (2018)

- S. Zeller, M. Kunitski, J. Voigtsberger, M. Waitz, F. Trinter, S. Eckart, A. Kalinin, A. Czasch, L. P. H. Schmidt, T. Weber, M. Schöffler, T. Jahnke, and R. Dörner, "Determination of interatomic potentials of He_2, Ne_2, Ar_2, and H_2 by wave function imaging", Phys. Rev. Lett. **121**, 083002 (2018)

- K. Henrichs, S. Eckart, A. Hartung, D. Trabert, K. Fehre, J. Rist, H. Sann, M. Pitzer, M. Richter, H. Kang, M. S. Schöffler, M. Kunitski, T. Jahnke, and R. Dörner, "Multiphoton double ionization of helium at 394 nm: A fully differential experiment", Phys. Rev. A **98**, 043405 (2018)

- S. Eckart, K. Fehre, N. Eicke, A. Hartung, J. Rist, D. Trabert, N. Strenger, A. Pier, L. P. H. Schmidt, T. Jahnke, M. S. Schöffler, M. Lein, M. Kunitski, and R. Dörner, "Direct experimental access to the nonadiabatic initial momentum offset upon tunnel ionization", Phys. Rev. Lett. **121**, 163202 (2018)

- S. Grundmann, F. Trinter, A. W. Bray, S. Eckart, J. Rist, G. Kastirke, D. Metz, S. Klumpp, J. Viefhaus, L. P. H. Schmidt, J. B. Williams, R. Dörner, T. Jahnke, M. S. Schöffler, and A. S. Kheifets, "Separating dipole and quadrupole contributions to single-photon double ionization", Phys. Rev. Lett. **121**, 173003 (2018)

- A. Mhamdi, J. Rist, D. Aslitürk, M. Weller, N. Melzer, D. Trabert, M. Kircher, I. Vela-Pérez, J. Siebert, S. Eckart, S. Grundmann, G. Kastirke, M. Waitz, A. Khan, M. S. Schöffler, F. Trinter, R. Dörner, T. Jahnke, and P. V. Demekhin, "Breakdown of the spectator concept in low-electron-energy resonant decay processes", Phys. Rev. Lett. **121**, 243002 (2018)

- A. Hartung, S. Eckart, S. Brennecke, J. Rist, D. Trabert, K. Fehre, M. Richter, H. Sann, S. Zeller, K. Henrichs, G. Kastirke, J. Hoehl, A. Kalinin, M. S. Schöffler, T. Jahnke, L. P. H. Schmidt, M. Lein, M. Kunitski, and R. Dörner, "Magnetic fields alter tunneling in strong-field ionization", arXiv preprint arXiv:1902.07278 (2019)

- K. Fehre, S. Eckart, M. Kunitski, M. Pitzer, S. Zeller, C. Janke, D. Trabert, J. Rist, M. Weller, A. Hartung, L. P. H. Schmidth, T. Jahnke, R. Berger, R. Dörner, and M. S. Schöffler, "Enantioselective fragmentation of an achiral molecule in a strong laser field", Sci. Adv. **5**, eaau7923 (2019)

Contributions to Conferences

11/2018 **International Symposium on Light Driven Dynamics**, Shanghai (China), Invited talk with the title: "*Non-Adiabatic Tunnel Ionization with Tailored Two-Color Laser Fields*"

03/2018 **Spring Meeting of the German Physical Society**, Erlangen (Germany), Invited talk with the title: "*Magnetic Quantum Number in Strong Field Ionization*"

02/2018 **QUTIF*** **Annual Meeting**, Hamburg (Germany)

09/2017 **QUTIF*** **International Conference**, Bad Honnef (Germany), Talk with the title: "*Strong-Field Ionization with Counterrotating Circularly Polarized Two-Color Laser Fields*"

08/2017 **International Symposium on (e,2e), Double Photoionization and Related Topics**, Palm Cove (Australia), Invited talk with the title: "*Double Ionization in Shaped Laser Fields*"

07–08/2017 **ICPEAC (International Conference on Photonic Electronic and Atomic Collisions)**, Cairns (Australia)

02–03/2017 **QUTIF*** **Annual Meeting**, Dresden (Germany), Talk with the title: "*Strong-Field Ionization with Tailored Two-Color Laser Fields*"

09/2016 **ECAMP (European Conference on Atoms Molecules and Photons)**, Frankfurt am Main (Germany)

05/2016 **QUTIF*** **Annual Meeting**, Jena (Germany), Talk with the title: "*Strong-Field Ionization with Tailored Two-Color Laser Fields*"

11-12/2015 **QUTIF*** **Kick-off Meeting**, Hannover (Germany), Talk with the title: "*Imaging Electrons and Ions by Two-Color Counterrotating Laser Fields of variable Ellipticity*"

*QUTIF is a Priority Programme of the German Research Foundation on Quantum Dynamics in Tailored Intense Fields.

Practical Experience related to Atomic Physics

since 2015 **Tutoring of undergraduate students**, Atomic and Quantum Physics at the Goethe University Frankfurt, weekly in winter semesters starting in 2015, 2016 and 2018

03/2019 **European XFEL (Free Electron Laser)**, Hamburg (Germany), one week

02/2019 **European XFEL (Free Electron Laser)**, Hamburg (Germany), one week

05/2018 **BESSY II (Synchrotron)**, Berlin (Germany), 1 week

03/2017 **Photonics Institute**, University of Technology in Vienna (Austria), 2 weeks

03/2017 **SOLEIL (Synchrotron)**, Saint-Aubin (France), 1 week

05/2016 **BESSY II (Synchrotron)**, Berlin (Germany), 1 week

03–04/2016 **PETRA III (Synchrotron)**, Hamburg (Germany), 1 week

08/2015 **ALS (Synchrotron)**, Berkeley (USA), 2 weeks